Fluidic Nozzles for Automotive Washer Systems

Computational Fluid Dynamics and Experimental Analysis

Submitted to Swansea University in fulfilment of the requirements for the Degree of Materials, Modelling and Manufacturing Engineering

Doctor of Engineering

Zara Louise Sheady
M2A SWANSEA UNIVERSITY, KAUTEX TEXTRON CVS LTD.

Abstract

One of the main goals of this project was to cultivate an understanding of fluidic nozzle geometries and characteristic flow. Through this knowledge, three new fluidic nozzle concepts were developed to be used as components in several windscreen washer systems for an automotive part supplier, Kautex Textron CVS Ltd.

Accurate and conclusive visualisation of flow through fluidic nozzles was vital in understanding how they can be best utilised for different applications. Over the past century, the specific needs of automotive cleaning systems have greatly developed with new technological discoveries, these advances allow the driver further knowledge of their surroundings. These specialised systems each require a different type of maintenance and cleaning system depending on their usage and the different size and shape of the vehicle. By completing this project, it is hoped to allow manufacturers to accurately identify what sort of fluidic nozzles are best for windscreen cleaning systems for a vehicle and how to design a nozzle to suit their specification. Fluidic nozzles have been researched experimentally and computationally to ensure an accurate comparison of results. By guaranteeing a precise comparison it will negate the need for high volume testing of nozzles in experimental situations, greatly reducing time and resources required to analyse a fluidic nozzle.

The fluidic nozzles that are investigated and developed in this project were modelled and examined both experimentally and computationally, this ensured valid and accurate results were achieved by both the computational modelling and experimental testing. The development of the nozzles within this project was conducted using several experimental and computational setups to analyse the spray distribution, angle and oscillatory frequency amongst other parameters significant to the nozzle usage on a vehicle. Through this it was possible to tailor nozzle dimensions to allow for a streamlined design approach, this increased efficiency in fluidic nozzle development for any specification given by a vehicle manufacturing company customer. In addition to this the water flow emitted from the outlet was experimentally tested and modelled with both stationary and high surrounding velocities to examine how external variables affect the flow of the water from the nozzle.

This project has been useful in the design manufacturing process of fluidic nozzles, by utilising computational modelling it has allowed a faster and cheaper method of analysing the effect of design alterations to fluidic nozzles. There is a greatly reduced frequency required for rapid prototyping of an array of fluidic chips with minimal dimensional differences to be used in the experimental stages of design, as once the inlet boundary conditions are established the nozzle can be redesigned completely within reason without the need for additional material wastage. This ensures a more easy and precise method of testing the manufacturing tolerances of a fluidic nozzle with a target of reaching customer specifications are always achieved.

Three nozzles were aimed developed to satisfy conditions set by the customers, the vehicle manufacturers at which the new nozzle designs are aimed at are Honda, Nissan and Toyota. The nozzles to be established were designed for use on windscreen washer systems with a varying number of nozzles and with diverse windscreen sizes for different vehicles, resulting in a wide variety of specifications that must be met for each vehicle manufacturer. This meant that a single nozzle could not be utilised for all vehicles, instead a base model of fluidic chip was developed for the Nissan vehicle which was then dimensionally changed to suit the other vehicles.

Throughout this project there were design specifications changes and ambiguities from the automotive company customers, leading to redesigns of the fluidic chips designed in this project. This means that although only two of the three fluidic nozzle designs are successfully in production, a much greater understanding of the mechanics of the fluid flow within the fluidic nozzle was achieved.

Keywords – fluidic, nozzle, automotive, system, cleaning, windscreen, experimental, computational, comparison, oscillation, frequency, droplet, distribution, angle

Table of Contents

List of Tables

List of Figures

Acknowledgments

Thank you to the Innovation team and Core Engineering team at Kautex Textron CVS Ltd. for the support in completing some of the later portions of the experimental testing in this project.

I want to heartily thank my mother, Sharon Sheady, and my close family and friends for supporting and motivating me through this project work, without you all I would have never been able to finish.

1. Introduction

The goal of this project was to develop three different fluidic chips to be used in nozzles for automotive windscreen washing applications. This venture was completed through a partnership between Swansea University and Kautex Textron CVS Ltd. The first chapter covers some of the research already in circulation regarding automotive nozzles. There is a particular focus upon the fluidic nozzle, and the principal differences in performance between this type of nozzle and other automotive nozzles currently in use. From this data it was possible to draw a conclusion that the best suited nozzle type for the applications required from Kautex Textron CVS Ltd. were those utilising a fluidic chip concept.

A fluidic nozzle in Kautex Textron CVS Ltd. is comprised of three separate parts: the nozzle main body, an eyeball, and a fluidic chip. The nozzle main body is the component which is connected to a hose to supply water to the nozzle and provide a housing for the eyeball and fluidic chip. The eyeball is an almost spherical part with an opening at the back to allow the inflow of fluid and in this case a hollow at the front to house a fluidic chip. The eyeball is implemented in the design of the nozzle as it facilitates the adjustment of the area of interest to suit different vehicle shapes. The fluidic chip is the smallest part which comprises of microchannels in the form of a fluidic oscillator on the top portion of the chip. Utilising a chip in the nozzle design achieves two outcomes, it decreases the complexity of dimensional adjustments in the fluidic component as only a new chip is required rather than a whole nozzle. Additionally, this means that the same nozzle body and eyeball can be utilised for several systems with only a separate fluidic chip being produced to suit different customer specifications.

1.1. Introduction and Objectives

In 1986 washer jets or washer nozzles became a legal and vital requirement of almost all road using automotive vehicles with a windscreen. This law was introduced to ensure that when used in conjunction with windscreen wipers the area swept by the wiper could be cleaned of mud, dust or similar substances to provide clear vision to a driver for safe driving conditions [1].

Throughout history a wide variety of complex systems involving different types of nozzles have been developed for use in windscreen washer systems. This originated

with the first production of a water-based cleaning system in 1938 by James S Dimukes [2].

These nozzle types include but are not constrained to straight jets, fan nozzles and fluidic nozzles, Figure 1-1 shows how the fluid emitted from each of these nozzle types differs. The first nozzle is known as a straight jet or pencil jet, with this nozzle the water projected travels through the nozzle outlet with 0° of diffusion of spray. The second nozzle variety is the fan jet, this nozzle type emits a spray with a diffusion angle greater than 0°. The final nozzle type is the fluidic jet, this jet produces a spray distribution with peaks of water at the external points of its spray angle through oscillatory motion.

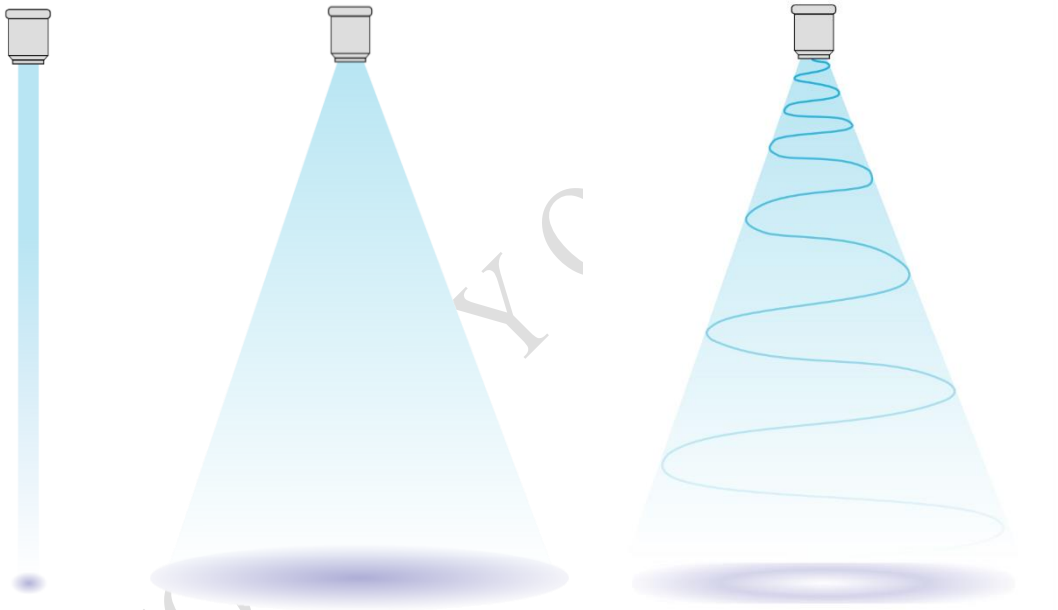

Figure 1-1: Straight jet (left), fan jet (centre) and fluidic oscillating jet (right)

The goal of any system is to ensure that the optimum product for an application is always used. In this case, the goal for windscreen washer systems is to have the best nozzle type and configuration for a wide coverage of water droplets, with the optimum amount of water being used to ensure a thorough clean at all velocities encountered in a vehicle. Currently, there is an increase in uptake of the fluidic nozzle as the predominant nozzle utilised in automotive windscreen systems (9.1 Appendix A). Due to this fact and the benefits found with fluidic nozzles discussed in Section 1.3.3 Fluidic Oscillating Nozzles, a focus upon this nozzle was placed for this project. Therefore, the mechanics of the fluidic nozzle and how to tailor them to different customer specifications is the main investigation of this research.

1.2. Windscreen Washer Systems

Windscreen washer systems have evolved greatly from their initial conception in order to maintain safety standards and improve overall efficiency. This thesis discusses the ways in which the evolution of technology in fluid dynamics and construction engineering has affected the way in which windscreen washer systems have progressed throughout history.

Several features have been added to systems to ensure that they are operational in all conditions. These include a heated component to ensure it is operational during cold weather conditions, additionally the fact that the speed of the vehicle affects the drop-down, where the spray delivered from the nozzle hits the windscreen, resulting in an adjustable spray angle is taken into consideration.

1.2.1. What makes the best windscreen washer nozzle?

An important part of this project is investigating which type of nozzle or nozzles are the most ideal for automotive cleaning system applications. Therefore, in addition to researching and analysing fluidic nozzles, there will also be data collected and examined from fan nozzles for the same multiple situations recorded for the fluidic nozzles.

The method of analysing which nozzle system is the optimum for the stated customers is through comparison of the actual nozzle to a combined specification set out by the consumer. Each car manufacturer and OEM (original equipment manufacturer) customer has a differing specification to hit predetermined spots on their differently shaped and sized vehicles, therefore it is difficult to analyse which system is actually the best. Therefore, within this investigation process three different specifications given by manufacturers are examined.

Windscreen washer nozzle systems are not always able to operate in predetermined ideal operating conditions; therefore, it is necessary to analyse them when the temperature is low for winter conditions, or if there is a drop in pressure. This will ensure that the nozzles will be operable in cold weather or low pressure conditions at a level that is required to provide sufficient clear visibility as specified by the customers.

In addition to normal and cold weather situation testing the project will also analyse the effect that the vehicles velocity has on the spray emitting from the nozzles. The current method of specifying whether a windscreen washer nozzle is operating

sufficiently well to be installed on a vehicle is if it is hitting the 'C-zones' specified by the customer (Figure 1-2).

The fluid from the nozzle must hit the area of the windscreen in the C-zone in order to qualify, if the height at which the nozzle hits the windscreen differs too greatly due to vehicle velocity then a redesign of the system is required. Additionally, if a

Figure 1-2: C-Zones on Vehicle Windscreens

nozzle is not distributing the fluid sufficiently wide then a full clean may not be achieved.

There are a couple of methods in which this can be examined experimentally, one of which is by analysing the water distribution on the windscreen with UV (ultra-violet) paint and photography. The UV paint fluid is sprayed onto the windscreen and then cleaned with the washer system and wiper blades, if any of the UV fluid remains in the C-Zones then there will be a need for readjustment of the nozzle positioning.

A second method can be utilised in which the C-zones are marked onto a windscreen without causing an obstruction to the driver view, and a recording is taken of the spray hitting the surface of the windscreen. This can be used for both stationary and at velocity driving conditions and is the method used by Kautex Textron CVS Ltd to test nozzles.

1.2.2. History of the Windscreen Washer System

Some of the first windshield washer systems in 1915 and 1923 did not use a fluid in their operation, instead utilising a system that would transmit redundant engine heat to the windshield either directly or with heated air [3] [4] (Figure 1-3). However, the heating structure was not a sustainable mechanism due to the poor conductivity of

the windshield. This meant that for the driver to have a clean, rain and ice-free window, the heating system would need to be in front of them; therefore, obstructing the driver vision. This meant that this system needed redevelopment and redesign to make it safer to use before it could be used on a wider variety of cars.

Another early invention designed for cleaning vehicle windscreens was designed by

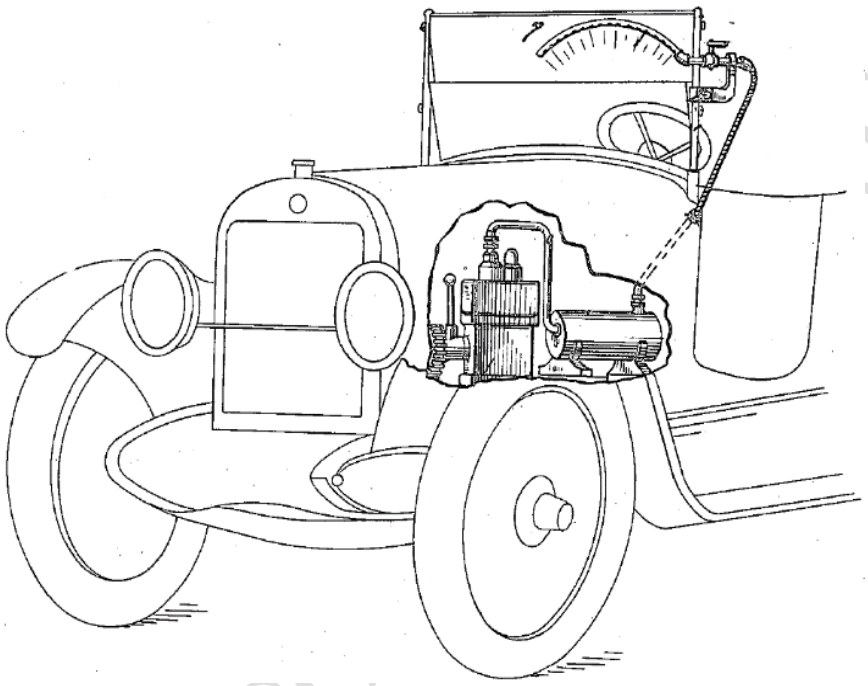

Figure 1-3: 1923 Windshield Cleaner System [4]

Herman Klatt in 1921. This device comprised of a mechanical roller system that is moved over the windscreen to remove dust, moisture and other foreign bodies that

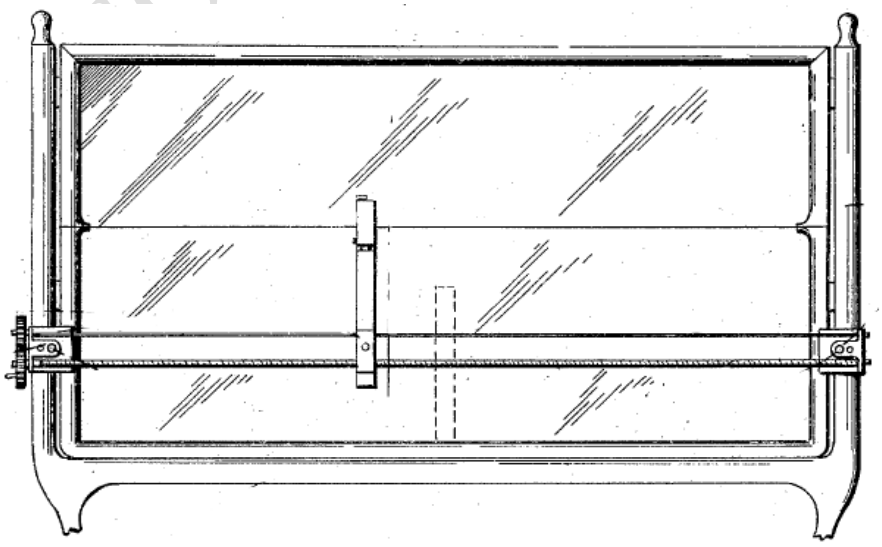

Figure 1-4: 1921 Windshield Wiper System [5]

impede vision through the glass (Figure 1-4) [5]. This design worked well as it allowed the driver to choose whether the whole of the windscreen or just his/her side in addition to not permanently obstructing the view through the windscreen. However, the problem with this apparatus is that it is quite heavy and bulky, meaning that it would need strong reinforcement around the window, and this is not always possible with some vehicles.

The first step towards the system that is used in the present day with fluid systems incorporated into the mechanism was patented in 1933 [6]. The arrangement involved a mechanism to deliver a fluid (such as water) to the windscreen by way of a pump hidden beneath the bonnet of the vehicle. The fluid is then used to clean the windscreen with the assistance of a conventional windscreen wiper. The main difference with this design from the conventional one now used to be that the water was pumped out through a number of pipes at the top of the windscreen operated through a manual foot pump. However, it was likely too distracting to have to press and hold the foot pedal to clean the windscreen system therefore this method of operation needed to be altered.

The first assembly incorporating a nozzle to spray the fluid at the windscreen from a position on the bonnet was utilised in 1938 [2] (Figure 1-5). This revelation meant that the fluid output could be more precisely controlled to ensure that the flow would reach the correct position on the windshield. This mechanism still used the foot pedal method of operation as seen in the previous system as at this point there was little knowledge on how to give a predefined amount of power to a piece of apparatus from a single short press of a button.

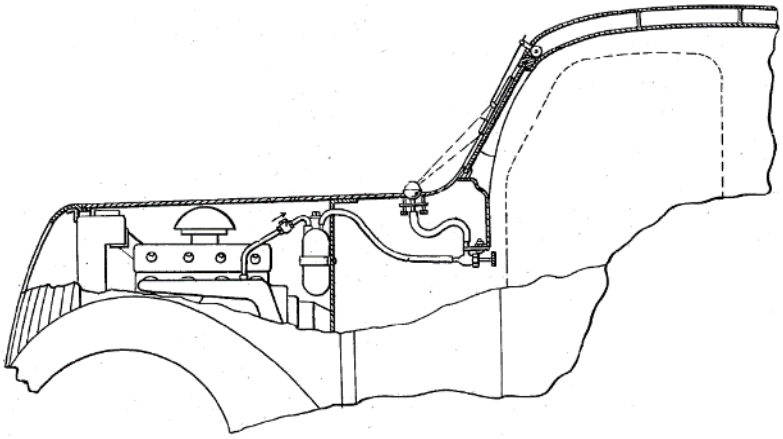

Figure 1-5: 1938 Windshield Cleaning Apparatus [2]

In 1939 a system was patented that allowed the vehicle user to operate the spray device to give a predefined length of time of spray with the touch of a button, similar to the one used in present day [7]. In addition to the innovative operation of the windscreen cleaning system, this apparatus was designed to be used in cold weather and hence it is supplied with a warm fluid to aid in removing ice and snow from the windscreen. The fluid in this arrangement is warmed by the heat emanating from the vehicle engine and radiator. The fluid heating method was updated in 1941 to utilise a separate heating coil in the engine jacket [8]. Although the method of heating the fluid prior to spray is not used in present day cleaning systems, there is an option for a heating component to ensure that the nozzle does not become blocked due to poor weather conditions. The systems that will be designed in this project will have the option of including this heating element if desired by the customer.

In the 1950s there was a new development in what type of nozzle outlets were used for the windscreen washer operation. Similar to the norm, these nozzle outlets were of the straight jet form, in that they output of fluid was a straight stream. However, instead of requiring at least two nozzles to clean the entire windscreen a dual output was developed so that one nozzle could discharge water from two outlets positioned side by side to target the whole windscreen [9]. This meant that the pipe and nozzle system could be condensed into one line, and hence there would be a reduction of overall weight and space taken for the apparatus. This system is still used today by a number of vehicle manufacturers, such as Audi, Fiat, Mercedes and Renault (9.1 Appendix A).

During the 1960s two new types of nozzles started to be used for windscreen washing applications, these are the fan and fluidic type [10] [11]. These nozzles

differ greatly from the usual straight jets in that the outlet spray from the nozzle was delivered over a greater area. This meant that instead of having a dense distribution of water in one area, the spray distribution was much finer and uniform. Consequently, this meant that there was less risk of obstructing the driver's vision with the blur from the puddle of water aimed at his eye-level. The main difference between fan and fluidic nozzles is that fan nozzles have a continuous ovular distribution with a mostly uniform distribution of water droplets, fluidic nozzles have a dynamic oscillatory spray distribution. Fluidic nozzles are designed to give two peaks of spray distribution at the eye-level of the driver and passenger of the vehicle, with a less dense distribution between the two peaks. This dissemination of water can be seen as being almost equivalent to two pencil nozzles aimed at the passenger and the driver in terms of where the majority of water is sprayed.

1975 saw a novel way to distribute water to a windscreen, this method involved a pair of nozzles that were attached to the wiper arm [12] (Figure 1-6). This delivery system gives rise to a great reduction in puddles and streaks on the windscreen as the water droplets are wiped away subsequent to their delivery. There will also be a reduction in waste with this mechanism as the projected aim is much closer to the nozzle exit. There has been a redevelopment of this system recently in 2014, with a more streamlined structure [13] and a similar method of water delivery is now used today on Toyota's Aygo and Yaris.

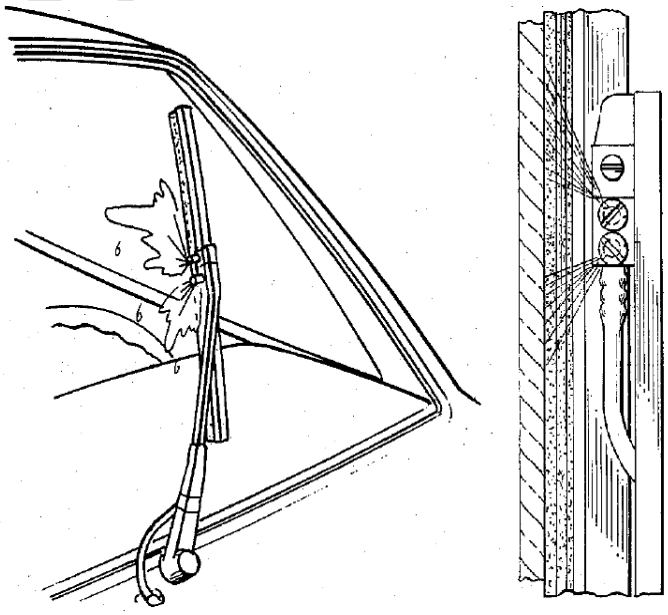

Figure 1-6: 1975 Windshield Washer Nozzle

When travelling at low velocities the windscreen washer nozzle output tends to be projected fairly high on the windscreen, and for high speeds the opposite occurs. This is due to the pressure of the air system around the windscreen and it can cause a large waste of water due to it not reaching the drivers vision or going over the vehicle. A number of solutions have been proposed to combat this including air deflectors [14],

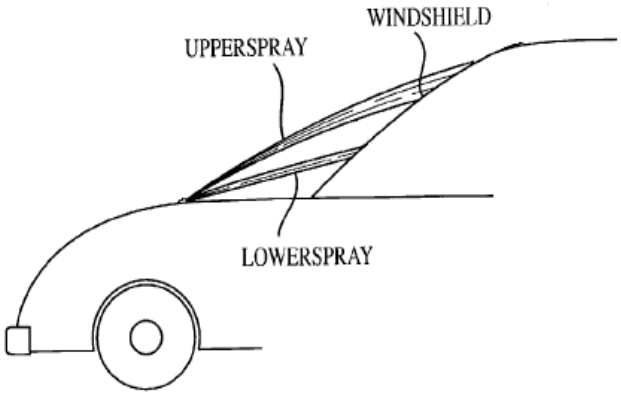

Figure 1-7: 2003 High Speed Dual Nozzle System [16]

a pressure sensitive dual nozzle [15] and an integrated dual nozzle [16] (Figure 1-7). In this project the effect of surrounding conditions will be investigated to ensure that an adequate and accurate distribution will be dispensed at high velocities. This will be investigated experimentally in two different manners, one experiment to analyse the spray distribution of the nozzles designed in a wind tunnel situation and the other will be in a real-life situation on a vehicle travelling at speed.

In addition to the windscreen washer system developments there has been an innovative design first established in 1965 by A. L. Ludwig in the US [17] and developed in Japan by K. Motoda [18] which incorporates sound waves to remove precipitation and other forms of debris from the windscreen. This would remove the need for water in windscreen cleaning system completely, resulting in reduced space required for the system as there is no need to carry a container and piping to transport the washer fluid or water. This system would not require windscreen wipers or nozzles to eject the water, eliminating a part of plastic usage in the car and allowing the vehicle to become more environmentally friendly. There is some redevelopment of this system occurring presently using ultrasonic waves completed Echovista Systems Limited in the UK [19]. This would result in windscreen wipers and hence windscreen washer systems becoming redundant.

However, current legislation means that all vehicles with a windscreen must have at least one efficient automatic windscreen wipers, unless the driver can see adequately

the road in front without using the windscreen. It also explains that all vehicles with a windscreen wiper, apart from pre-1986 agricultural vehicles, tracked vehicles and vehicles that cannot surpass 20 mph, must have a windscreen washer [20]. Therefore, this legislation must be overcome before this can be put into action.

1.3. Nozzles

There are a large variety of nozzles used in diverse applications, from spraying paint [21] or pesticides [22], to aircraft propulsion [23], to delivering viscous material to on a production line in a factory [24]. These nozzle types comprise but are not limited to fan, straight and fluidic nozzles; these are the nozzles which are the most predominantly used in the automotive industry for onboard vehicle cleaning systems.

Within each of these nozzle configurations there are many different sub-categories and varying complex geometries that can be produced to develop a nozzle to suit a given application. Each application will have a different optimum performance level dependent on the specification for the washer system design and the customer performance focus.

There are three main characteristic fluid flows for nozzles given by different types of nozzles: straight jet, fan jet and fluidic. A straight jet nozzle emits fluid in a relatively thin concentrated jet, a large area circular or elliptical flow is expected for a fan nozzle and a fluidic jet forms an oscillatory flow forming a line or curve. The distribution of fluid from each of these nozzle type differs, with fan and straight jets having concentrated spray in the centre and a fluidic nozzle likely to have the densest spray area at the edge of the distribution area and less fluid to the centre where there is a lighter deposition.

1.3.1. Straight (pencil) Jet Nozzle

A straight jet nozzle is the simplest in terms of fluid dynamics, the water that is discharged from the jet travels in a straight line with 0° spray angle to a specified target as shown in Figure 1-1. The main use for straight jet nozzles is for precision work where there should be no overlap of the target area and other areas in the vicinity. These jets also tend to have a greater amount of pressure concentration due to the percentage of the water directed into one jet, this helps for long distance targets or those objectives requiring a greater amount of force. Some applications using straight jets are high pressure cleaning [25] and water-cutting [26].

1.3.2. Fan Nozzle

Fan nozzles differ greatly to straight jet nozzles in that instead of the spray angle being 0°, the water dispersal is much more spread out giving a large circular or elliptical spray pattern. This results in a lower pressure force behind the water spray, so these nozzles are utilised in closer distance applications, this type of nozzle is illustrated in Figure 1-1. Fan nozzles are primarily used in applications requiring a light distribution over a large area, such as in agriculture to spray crops [27] or for spray painting vehicles [28]. There are several different outlets that can be used for a fan nozzle giving diverse spray distributions and pressures to suit many functions, a variety of examples are shown below in Figure 1-8.

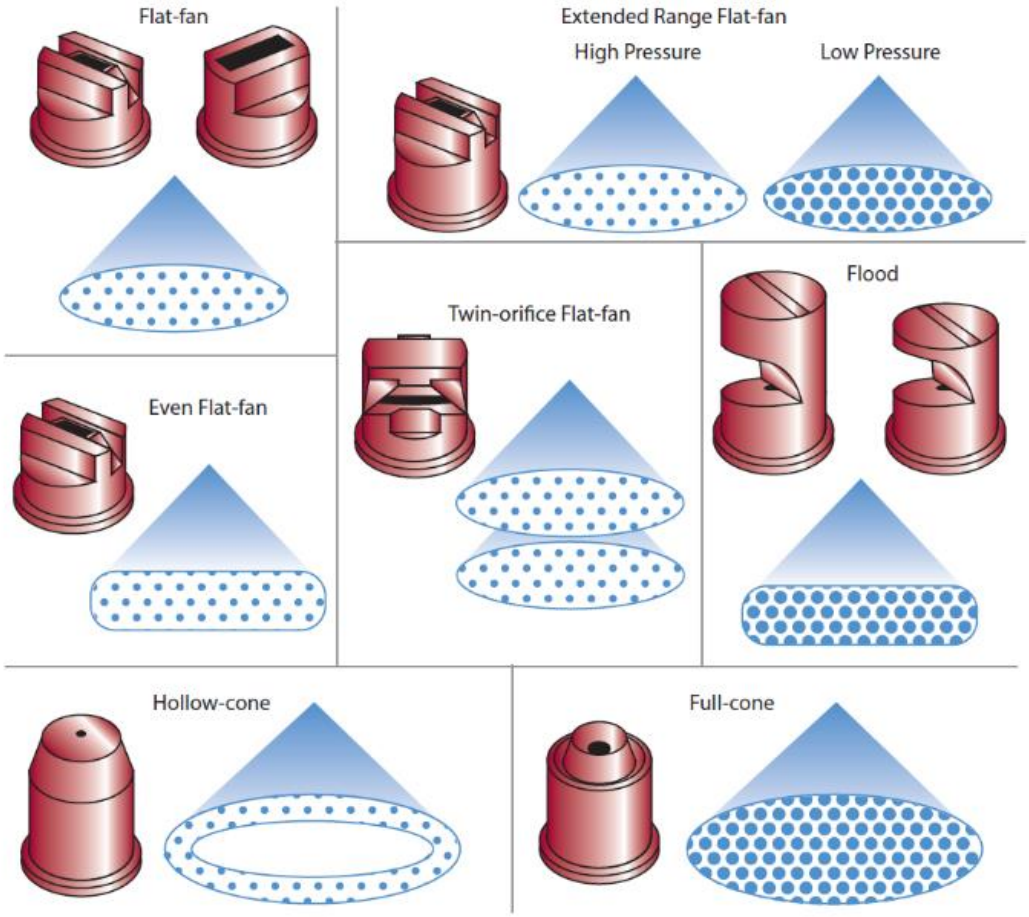

Figure 1-8: Fan Nozzle Outlets [82]

Fluidic nozzles are a combination of both straight jet and fan jet but with an amalgamation of the two types' advantages and disadvantages. A fluidic spray

distribution has two concentrated peaks similar to what would be expected from a set of two straight jet nozzles, however it also has a dispersal of fluid between the two peaks giving a rectangular-elliptical distribution as shown in Figure 1-1.

Unlike both the fan jet and straight jet nozzles however, the spray emitted from the orifice is not at a constant angle, instead oscillating between the two sides with a pause between arriving and departing from the most extreme angles. This is what gives the concentrated distribution and the less dense water dispersal in the centre and around the edges. These features make oscillating fluidic nozzles ideal in turbomachinery [29], flow control [30], fluid logic arrangements [31], automotive cleaning systems and including liquid atomization [32].

Out of the three nozzles described the one that typically uses the most liquid is the fan nozzle and the least is the straight jet with the fluidic nozzle somewhere between these two. However, this does depend on the application. The fan and fluidic nozzles provide a large area of droplet coverage with varied density of droplet landing sites, whereas the role of the straight jet nozzle is to direct spray in a concentrated relatively small zone meaning the straight jet is more practical at longer distances.

The main feature and benefit of the nozzles described is that they all have no moving parts, meaning that they are reliable and relatively cheap and easy to produce as very will need to be replaced or maintained in to ensure efficient spray. This includes the fluidic nozzle with the oscillatory outlet spray, instead it utilises vorticial effects to control spray direction.

1.3.3. Fluidic Oscillating Nozzles

The nozzle focused upon in this report is the fluidic oscillating nozzle. Fluidic devices are based on transistors in fluid logic, an area greatly detailed by Morris [33], Moylan [34] and Kirshner and Katz [35]; and more specifically fluidic or suction amplifiers [36] [37]. A fluidic oscillator has no moving parts, instead utilising vorticial effects formed through complex fluid dynamics within the internal chamber, to create a rapidly oscillating jet output.

There are two main types of fluidic oscillator, a wall-attachment form [38] and a feedback-free [39] class. The geometries of each of these oscillators are completely different as they utilise different vorticial principles to create the oscillating flow. The two types are the wall-attachment oscillator, and the feedback-free oscillator.

The wall-attachment fluidic oscillator utilises the Coanda effect of wall attachment to oscillate the fluid flow between two walls, forming vortices in the internal mixing chamber, the fluid is fed through the system by feedback channels (Figure 1-9).

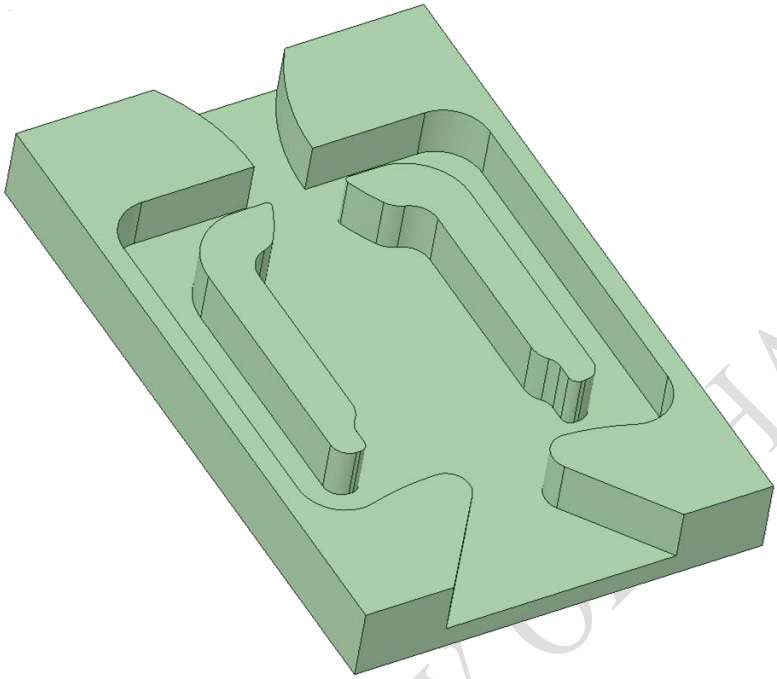

Figure 1-9: Feedback-channel fluidic oscillator chip

Feedback-free fluidic oscillators use the energy of two jet streams impinging off each other, with the dominant flow forcing the other away from the outlet, as the deflected flow collects and grows its size then diverts the main flow and the process repeats (Figure 1-10). Jet interaction fluidic oscillators can also be used to mix two different fluids as the fluid enters the mixing chamber at two separate points.

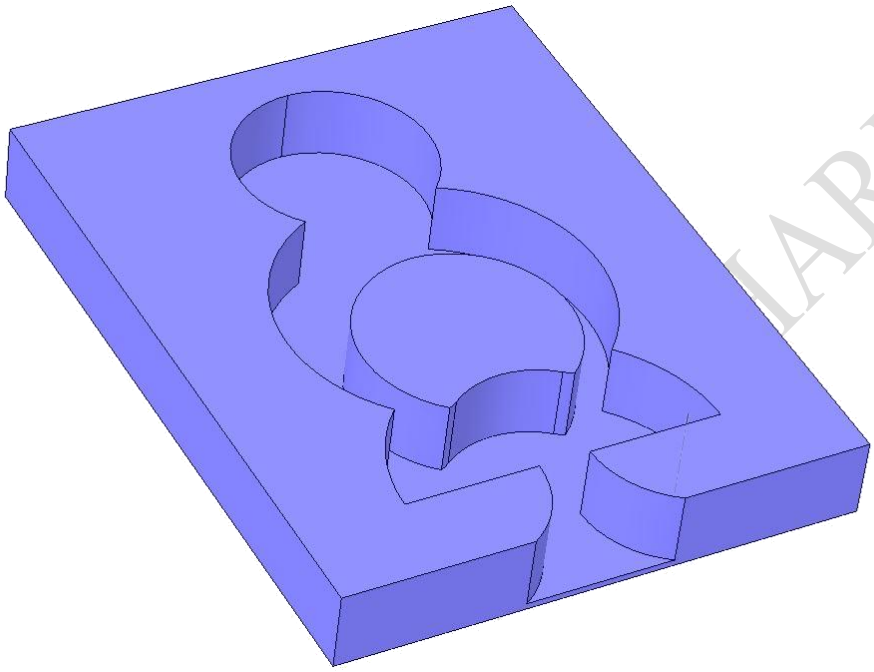

Figure 1-10: Jet interaction fluidic oscillator chip

1.3.3.1. Wall-Attachment Fluidic Oscillators

A wall-attachment fluidic oscillator is comprised of an inlet, an interaction chamber, attachment walls and an outlet as seen in Figure 1-11. The fluid enters through the inlet and is fed into the internal mixing chamber where the stream of flow bends at the inner walls and part of the flow is forced through the attachment walls whilst the remainder exits through the outlet [38].

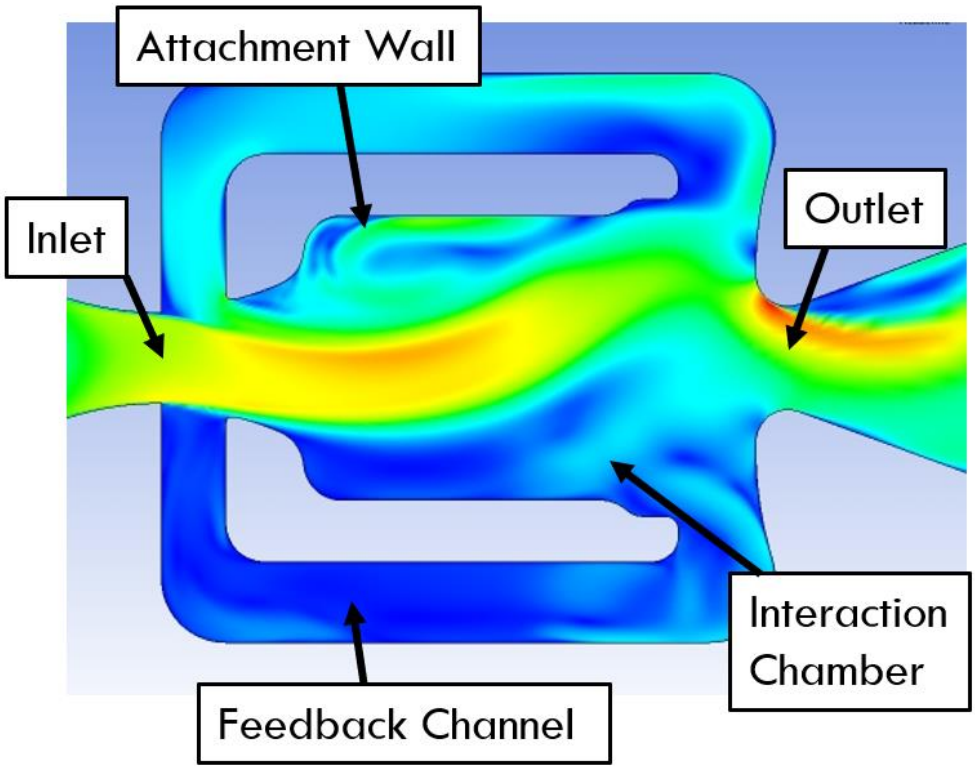

Figure 1-11: Fluidic oscillator chip with feedback channels - labelled

The interior walls of the oscillator form feedback channels for fluid that has been through the interaction chamber, the feedback channels lead back to the area between the inlet and the internal mixing chamber and the fluid re-joins the main fluid flow at an earlier point. The changes in direction of the fluid creates drops in pressure in areas of low velocity in the internal chamber which perpetuate low pressure vortices to influence the flow within the internal chamber. It is these vortices connected to and affecting one another that cause the fluid to oscillate from one side to the other as the flow is emitted from the outlet.

The main principle behind wall-attachment fluidic oscillators is the use and manipulation of the Coanda effect. This effect used in conjunction with the feedback channels produces an oscillatory output. The Coanda effect is described further in the next section of this section.

1.3.3.1.1. *The Coanda Effect*

Henri Coanda first discovered the Coanda effect 1910, Henri was a student at the Ecole Supérieure Aéronautique in Paris and an aircraft designer and builder. At this time, he was constructing a plywood aircraft with two jet engines, to ensure the jet exhaust did not cause the fuselage to ignite he used a curved metal buffer to deflect the exhaust. However instead of the hot exhaust air deflecting away from the aircraft,

the curved surface caused the hot air to bend towards the fuselage. After discussing the incident with Theodor von Kármán, the leading aerodynamicist at the time the Coanda effect was proposed as the name of the phenomenon [40].

The Coanda effect is the phenomenon described as when a free stream of a fluid jet emerges from a nozzle, and it tends to follow a nearby inclined or curved surface. The stream will attach itself to the surface if the angle between the stream and the surface is sufficiently small and the gap between the jet outlet and the surface is sufficiently small if present. This propensity is caused by the jet stream absorption of neighbouring fluid molecules, attracting the atoms of the fixed solid curved surface through frictional force, however due to the inability of the surface to move the water is forced to bend towards the surface to equalise the attractive force.

This causes a partial vacuum to develop between the stream and the surface, which if it remains constant will influence the stream to bend or attach itself to the surface [41]. Provided the adjacent surface is within a sufficiently small tangential angle, the fluid will remain at the same angle of flow due to surface friciton. This prevents the fluid velocity from decreasing and prevents it from diverting back to the original stream [34].

The Coanda effect can be seen below in Figure 1-12 and Figure 1-13, where the flow direction changes where it has met either a curved or inclined surface and followed the direction of that plane. Figure 1-12 displays velocity of flow in coloured streamlines and pressure in a grayscale contour plot, the figure clearly shows an increase in pressure at upper half of the front of the surface hole and a drop of pressure at the upper rear half of the semi-circular orifice.

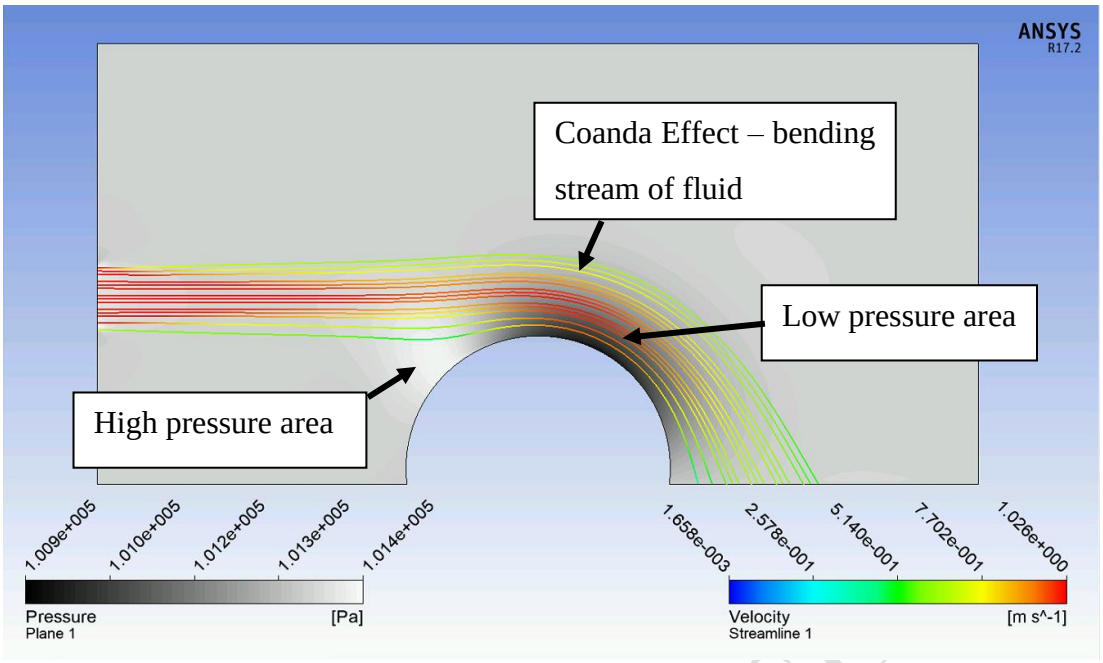

Figure 1-12: Coanda effect shown on a plate with a single hole

There is a rise in pressure where the particles from the fluid stream encounters the surrounding particles of the wall, competing for the space and increasing the density of fluid and therefore increasing the pressure. As the fluid flows along the upper surface of the semicircle it becomes more attached to the particles in the vicinity of the wall and is unable to generate the energy required to move away from the fixed surface. This results in the fluid following the wall surface to a certain angular velocity at which point it requires less energy to separate than to follow the wall surface.

The Coanda effect is seen in Figure 1-13 at the inlet to the internal chamber of a wall-attachment fluidic oscillator. Although there is a section of the fluid stream that

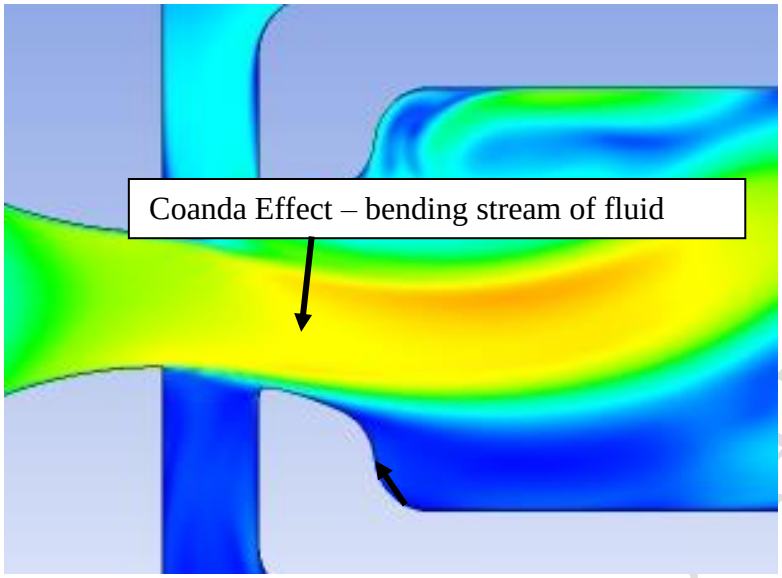

Figure 1-13: Coanda effect in wall-attachment microfluidic oscillator

does not have a wall surface to follow, the inner wall surface is sufficiently proximal for the water to tend towards and imitate the curvature. As the surface of the inner wall becomes more obtuse to the initial free stream velocity the flow is released, due to the external forces on the pressure flow this influences the flow to react to the distortion of the Coanda effect, forcing the fluid flow to tend against initial direction of the Coanda effect.

1.3.3.1.2. *Switching Process*

A wall-attachment fluidic oscillator utilises the Coanda effect to form the oscillatory output. As the water enters through the inlet it curves to either of the inner attachment walls due to the surface friction of the inclined wall, causing an area of low pressure further along the wall. Flow separation occurs when the momentum of the fluid becomes greater than the constant forces attracting the fluid to the surface. The fluid is then able to flow unconstrained.

Once the fluid is released from the inclined wall it bends back away from the surface as a low-pressure vortex has developed on the reverse side to the attachment wall and the pressure is able to flow most easily into the low-pressure area. As the fluid reaches the end of the interaction chamber most of it exits the nozzle through the outlet, however some flows back towards the inlet and is recirculated with the mainstream. This increases the pressure greatly at this side of the fluidic oscillator meaning that the pressure on the opposite becomes lower causing a low-pressure

vortex. This results in the opposite attachment wall becoming more suitable for the Coanda effect, and the fluid switches sides, starting the process again [42].

1.3.3.2. Jet-Interaction (Feedback-Free) Fluidic Oscillators

Jet-interaction fluidic oscillators differ from wall-attachment oscillators in that they use jet interaction instead of using the Coanda effect and feedback channels. There is an internal chamber in the fluidic chip in which two jets collide and the unsteady

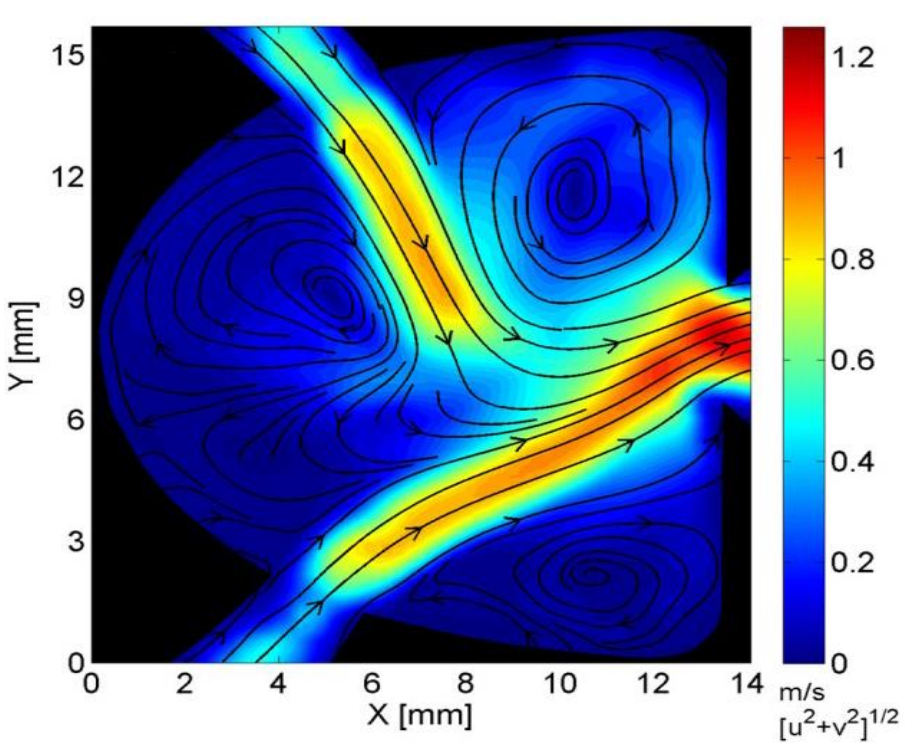

Figure 1-14: Streamlines superimposed over velocity contour plot [42]

interactions cause the desired oscillatory output (Figure 1-14).

The dual nozzle is special in that the water from the nozzle flows through two back-to-back fluidic chips creating two separate fluidic outputs.

1.3.3.2.1. *Switching Process*

Due to the unsteady nature of the jet collisions in the interaction chamber, a few large vortices are formed. The vortices formed are unsteady and intrinsically linked which results in the ability to change the direction of travel of the two jets from one side to the other in a cyclical mode. Whilst the jet feeding in from one side is dominant and feeding the outlet, the other is deflected upwards causing and/or enlarging a vortex in this area. Two side vortices are also formed and fed when the jet is displaced, this ensures that the jet output is positioned at the outlet for the dominant jet. Once the upper vortex becomes sufficiently strong and large it

bifurcates the first jet and hence changes the direction of the jet output. This process then repeats and gives the fluidic oscillating output [42].

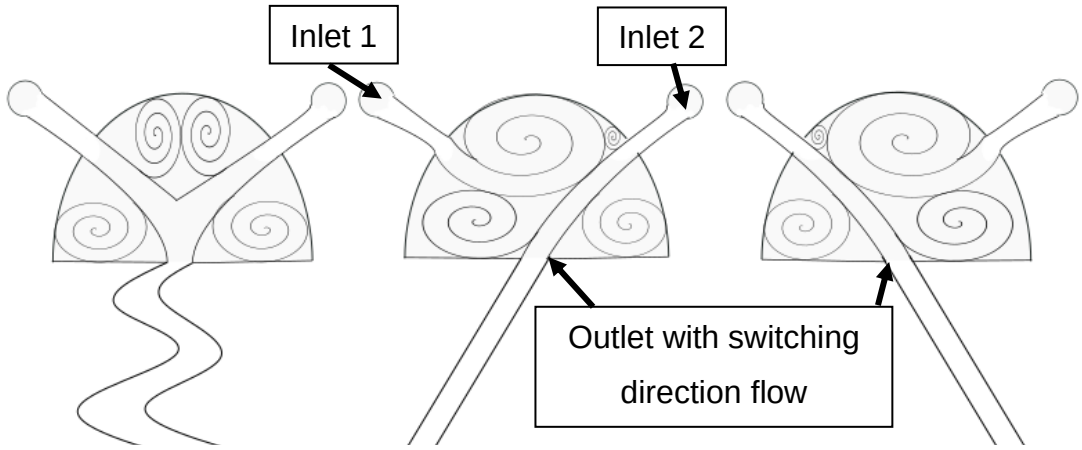

Figure 1-15: Jet-interaction fluidic oscillator internal sequence

1.4. Project Goals

The main goals of this project are the following:

- To develop an understanding of a range of nozzle types that can be used for automotive applications, focusing primarily on fluidic nozzles
- To redesign and improve the performance of three fluidic nozzles for screen wash cleaning applications
- To ensure that the fluidic nozzles can be used when stationary and at high velocities
- To compare the performance of fluidic nozzles to more conventional straight and fan nozzles

Although there has been a lot of development with regards to how automotive windscreens are cleaned, there is still progress that can be made. There is an increasing move towards utilising fluidic nozzles as they are able to provide a wide but focused area of coverage on the windscreen, therefore it is important to further the knowledge on the subject through this project. There is a lack of understanding of how the internal geometry of a fluidic chip can be changed to influence the output and every vehicle manufacturer requires a different specification for their vehicle. This means that it is vital to know how to tailor a fluidic chip to suit a vehicle manufacturer's needs.

1.5. Thesis Structure

The first chapter in this research covered the history of windscreen washer systems and an overview on how different types of nozzles can be used for automotive cleaning applications with a primary focus on fluidic nozzles. Through this review of current technology and historical data an understanding of how fluidic oscillators work and other cleaning systems that have been used in automotive cleaning systems previously.

The next chapter will discuss competitor fluidic nozzles and the approach of experimental testing undertaken in this research. In this chapter a series of experiments are undertaken to study the mass flow rate, spray angles and distribution, droplet sizing and oscillatory rate.

The following chapters will discuss the methodology and implementation of computational fluid dynamics (CFD) in the research. Chapter 3 discusses the theoretical equations behind the CFD utilised in the two following chapters. In chapter 4 a study into the internal fluid mechanics of the fluidic nozzle operates is conducted in addition to an investigation into possible defects that could occur due to manufacturing method. Chapter 5 is comprised of a study into how to apply the data discovered from the internal CFD analysis to an external multiphase problem to examine how the fluidic oscillator performs in air.

The final chapter of the thesis describes the development of three fluidic nozzles designed for customers of Kautex Textron CVS Ltd.

2. Experimental Benchmarking Analysis

To analyse what makes the optimum fluidic nozzle for windscreen and camera cleaning it is necessary to study those already on the market and see where improvements can be made. As the vehicles that the windscreen cleaning system are being redesigned and enhanced for already have standard fluidic nozzles it is important to understand the mechanics of these nozzles before developing anything new. It is vital to be able to compare the current data to the criteria given in a customer specification as it gives a clear picture of exactly what a company requires and what it is currently utilising and the gap between these two aspects.

The experiments conducted in this section were repeated for more successful prototype designs that were taken forward into either batch- or mass-production for testing or mass-manufacture, the results and conclusions of these results are found in Chapter 5.

2.1. Competitor Nozzle Descriptions

The four vehicles from which the competitor fluidic nozzles were studied are Ford's B-Max and Ecosport, all Nissan vehicles, and the Toyota RAV4. These vehicles have been specified as they cover the full range of current fluidic nozzles from these companies which were initially intended to be replaced by Kautex nozzles. The automotive companies originally bought these nozzles from a competing automotive cleaning company or the fluidic nozzle parts were bought from a competitor by Kautex and integrated into company cleaning systems.

The three nozzles initially tested are completely fluidic, with three being wall-attachment, and one being jet-interaction application based.

The Ford B-Max nozzle has a fluidic chip with one tall, narrow aperture as shown in Figure 2-1. The hypothesised spray distribution for this nozzle was that the outlet

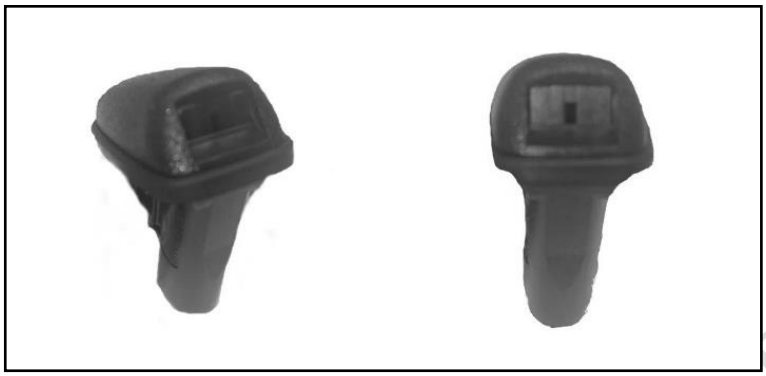

Figure 2-1: Ford B-Max nozzle

would emit a narrow but tall spray distribution. The spray outlet area is relatively small in comparison to the Nissan nozzle, Ford Ecosport nozzles therefore a mass flow rate at the lower range of these nozzles would be expected.

Unfortunately it was not possible to photograph the internal part of the Ford B-Xax nozzle as it was difficult to dissasemble the nozzle without causing damage to the fluidic chip. However it is believed that this nozzle utilised a wall-attachment fluidic chip.

The Nissan nozzle has a simple wall-attachment fluidic chip with a single almost square aperture as shown in the fluidic chip in Figure 2-2. This nozzle would be expected to have a wider spray angle with less height than the previous Ford B-Max nozzle as the outlet has a larger area for the outlet, and a relatively similar but marginally increased mass flow rate in comparison to the Ford-B-Max nozzle but lower than the Nissan nozzle.

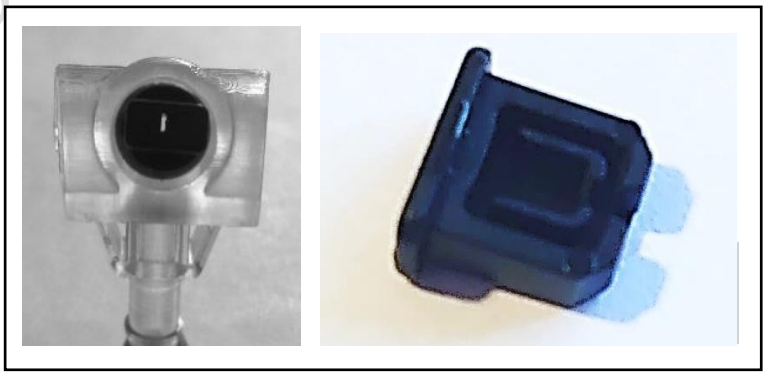

Figure 2-2: Nissan nozzle (left) and fluidic chip (right)

The Ford Ecosport nozzle is unique in this investigation in that it comprises a fluidic chip with two back-to-back jet-interaction fluidic chips with fluid flowing through two separate apertures giving a dual level stream with two different spray angles (Figure 2-3).

Figure 2-3: Ford Ecosport nozzle (top) and both fluidic chip inner surfaces (bottom)

The benefit of this fluidic chip is that it enables a concentrated spray at two different spray angles to ensure a throrough clean of a specified area prescribed prior to the nozzle design and manufacture. The spray would be expected to have a higher mass flow rate than that for the single-sided, single-outlet fluidic chips however likely at a decreased velocity due to sharing the external pressure forces between two chip sides. It would be possible for this nozzle to have both a decreased and increased spray angle in comparison to the prior nozzles.

The Toyota nozzle investigated has a wall-attachment fluidic chip as shown in Figure 2-4, but it is distinctive in that the aperture is a stepped shape which gives two different streams with separate spray angles similarly to the Ford Ecosport nozzle. This nozzle has the smallest outlet area of all competitor nozzles studied so the lowest mass flow rate is predicted with this nozzle. The angle within the outlet of the nozzle on the fluidic chip is relatively wide in comparison to those of the other fluidic nozzles so this nozzle is estimated to have a wider spray angle than most of the other nozzles.

Figure 2-4: Toyota Nozzle (top) and Fluidic Chip (bottom)

In addition to experimentally analysing and benchmarking these nozzles, computational fluid dynamic modelling and testing are completed for the nozzles. This ensured that there is a correlation between the computational fluid dynamics (CFD) data and real-world situations and enabled a fast analysis of the fluidic nozzles. This means that it could be quicker and easier to examine the tolerances and defects of any fluidic nozzles developed in the future.

2.2. Testing

Extensive testing had previously been conducted on the Nissan/Kautex nozzle by Kautex, therefore some testing was conducted to reinforce the data found and ensure that there were no errors in test equipment or CFD. Three additional nozzles were acquired for benchmarking, one manufactured by Toyota and two by Ford, so testing was required for these nozzles in the same manner as the Nissan/Kautex nozzle. Retesting of the Nissan/Kautex nozzle was also performed to ensure that the data from previous work was reliable and to guarantee present data was precise and accurate.

Each of the nozzles are mounted in different positions on the vehicles, and the vehicles themselves are differently shaped. Therefore, as a guideline Table 2-1 is included below stating the width of the vehicle, the number of nozzles on the vehicle and approximate positioning (for the Nissan vehicle an average of the length of all vehicles width and nozzle quantity and positioning is made).

Table 2-1: Nozzle and vehicle details for benchmarking nozzles

Vehicle	Width (mm)	Nozzle Quantity	Nozzle Approximate Positioning
Ford B-Max	1751	2	1/3 down bonnet
Ford Ecosport	1765	2	1/3 down bonnet
Nissan	1790	3	Under Bonnet
Toyota RAV4	1845	3	Under Bonnet

The testing was conducted at room temperature with water as the operating fluid for simplicity and due to the density and viscosity of any coolant mixtures being similar to water [43]. Subsequent testing involved the system being tested with dynamic operating conditions to mimic usage with the vehicle at different velocities to investigate the effect of the water in a much higher velocity airstream (6.2.2.2). The dynamic testing enables Kautex and the customers to reliably know that the water emitted from the nozzles hits the windscreen at the prescribed area, despite any velocity disruptions.

2.2.1. Spray Distribution and Volumetric Flow Rate

The objective of this experiment is to calculate the spray distribution and volumetric flow rates for the four different fluidic nozzles, made by Ford, Nissan/Kautex and Toyota when using water as the operating fluid. From this data it is possible to compare the competitor nozzles in the conditions typically experienced when in use on an automobile.

The spray distribution emitted from a nozzle is important as it gives a visualisation of what will occur when the nozzle is used to spray water at a car windscreen when the vehicle is stationary and allows a prediction for dynamic use. By visualising and analysing this data it is possible to ensure thorough and accurate cleaning coverage of the pertinent areas of the windscreen. Calculating where the peak fluid coverage is for the nozzle aids in the positioning of the nozzle on the vehicle and ensuring the correct angle of spray is discharged from the nozzle for a thorough an efficient clean.

It is expected that the nozzles with the narrower apertures would have a denser distribution due to the allowable angle of flow from the nozzle. A second hypothesis is that the larger the area of the aperture of the nozzle, the more fluid that would be discharged from the nozzle.

2.2.1.1. Spray Distribution Method

A schematic and image of the experimental apparatus is shown below (Figure 2-5). The apparatus used in the experiment are listed below:

- Spray distribution measurement device
- Three samples of four different fluidic nozzles
- Clamp and stand
- Frequency generator
- Power supply
- Water pump
- Multi-meter
- Metre rule (millimetre unit)

On a vehicle the spray is directed upwards and laterally from the windscreen coving onto the windscreen, however due to the complexity of the problem it is not feasible to design a catchment device that would allow this orientation. Therefore, it is deemed possible and most practical to use a vertically down orientation for this investigation. The distance from the nozzle aperture to the catchment device is the same distance between a mounted nozzle and the vehicle windscreen, to more accurately model and examine the pattern formed by the nozzle and the overall distribution of the water.

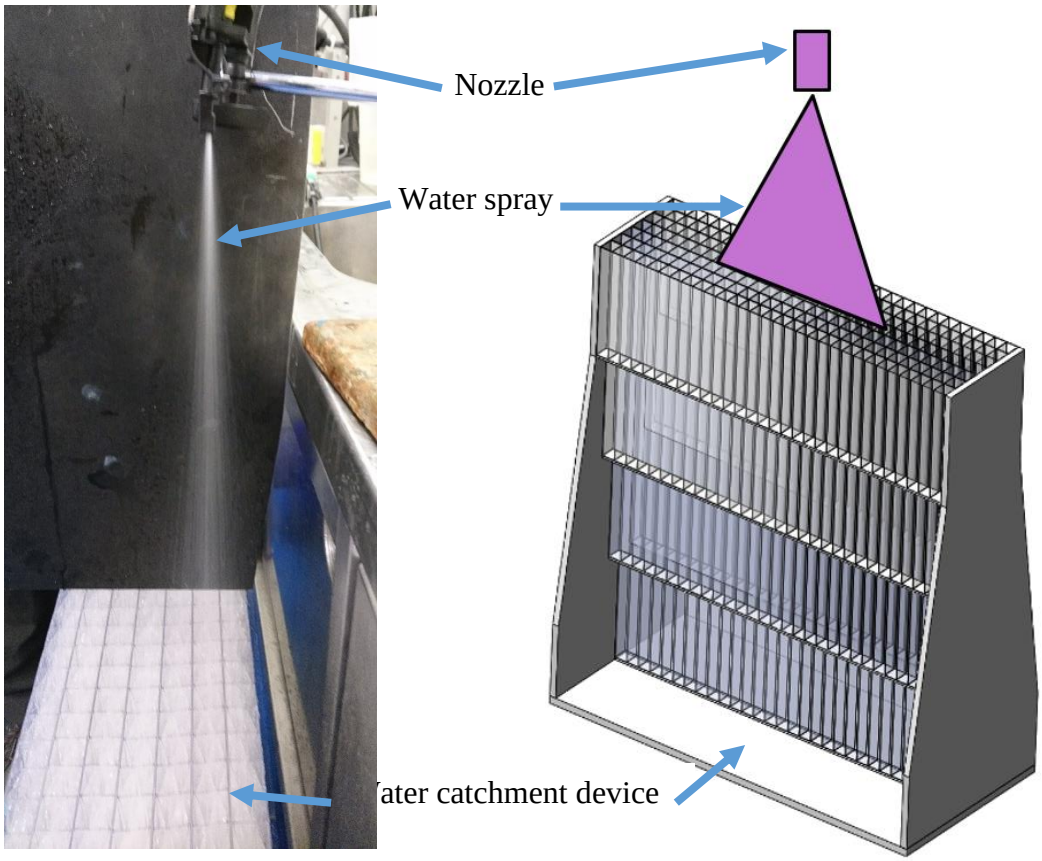

Figure 2-5: Experimental Apparatus (graphic from Astute-Kautex iii presentation – results 2015)

The spray distribution device was designed by Kautex specifically to measure the spray distribution of fluidic devices. The dimensions of each container in the equipment are 20mm by 20mm and marks on the containers discretising each ml of water are included, this cross-sectional area gives a reasonable height for the columns to show the volume of water in each container without interfering with the other rows.

The initial design of the apparatus involved measuring by hand the distance from the water catchment device to the fluidic nozzle aperture and mounting a clamp device to hold the nozzle, however partway through the research duration an additional attachment was added to ensure that the nozzle would always be tested at the same position relative to the device. This negated the need to adjust any recordings from the analysis to ensure the distribution was central and minimised any errors in recording.

In order to moderate the input for the system so that it could be tested with the correct time duration, a frequency generator was used, this is connected to an external power supply to ensure that the correct pressure over the issued time is achieved. Two different pressures of 4 Bar and 2.5 Bar were chosen for

benchmarking analysis as there have been studies conducted by Kautex that show that these are the average specified pressure supplied to a nozzle of this variety by manufacturers. 2.5 Bar pressure is usually used for nozzles that are used in a pair system as seen on typical vehicle windscreen cleaning systems, and 4 Bar is typically the value of pressure felt by a single nozzle system when one nozzle is non-functioning. By testing at 4 Bar pressure it is possible to analyse the effect that a blockage of one nozzle of a pair has on spray distribution and volumetric flow rate. Initial testing was conducted by Kautex Textron to ensure that these voltages and pressure rates allowed the nozzle to still behave as an oscillatory flow.

The frequency generator is then connected to an adaptor on the water tank which allows water through the tubing connected to the nozzle for the time duration set on the frequency generator. The frequency generator was set to allow a 30 second pulse of power from the generator which allowed a 30 second burst of water to be sprayed at the spray distribution measurement device.

A 30 second standard burst is utilised as this allows the fluidic nozzle to repeat through multiple cycles to find an accurate average over a period of time. It is possible that initial start-up and finishing flow rates in a nozzle usage cycle would have different flow rates and spray distributions however the proportion of time spent in these cycle portions was negligible in comparison to the main operation of use. It is also the standard test used by Kautex Textron CVS Ltd for all fan and fluidic nozzles.

To ensure that the correct pressure is achieved for the experiment, a multi-meter is attached to the tubing between the water tank and the fluidic nozzle and monitored to ensure there is no voltage change between test operations. This is attached to an electronic pressure gauge connected just prior to the fluidic nozzle, the gauge is wrapped in waterproofing to protect the equipment and minimise any hazards.

The nozzle is fastened to a stationary clamp and board to ensure that it does not move during the experiment. The distance between the nozzle and the catchment device by utilising the metre ruler and the nozzle is aimed vertically down, this allows for an accurate visualisation of the spray with no angular deflection and no other outside conditions distorting the flow.

A risk assessment was performed to ensure that the experiment was conducted safely. Ensuring that the electronic components were not positioned to receive spray or backsplash from the water. A restriction was placed in that the catchment device could only be emptied by two or more people due to the shape and weight of the measurement instrument. Once the 30 second pulse is complete the amount of water in each section of the fluid spray distribution measurement device is calculated and inputted onto a table the same as the one shown below (Table 2-2).

Table 2-2: Experiment data table (set up details)

Set-Up Details:																														
Fan	N		Fluidic	Y		Part No			Flow (cc/sec)																					
			Spray Height (mm)	400		**Cycle Time**	30 seconds		**Pressure (Bar)**																					
NOTE: INPUT VOLUME = CC																					***VIEW FROM ABOVE***								
0	0	0	0	0	0	0	0	0	0	0	0	0	0	0	0	0	0	0	0	0	0	0	0	0	0	0	0	0	0	0
0	0	0	0	0	0	0	0	0	0	0	0	0	0	0	0	0	0	0	0	0	0	0	0	0	0	0	0	0	0	0
0	0	0	0	0	0	0	0	0	0	0	0	0	0	0	0	0	0	0	0	0	0	0	0	0	0	0	0	0	0	0
0	0	0	0	0	0	0	0	0	0	0	0	0	0	0	0	0	0	0	0	0	0	0	0	0	0	0	0	0	0	0
0	0	0	0	0	0	0	0	0	0	0	0	0	0	0	0	0	0	0	0	0	0	0	0	0	0	0	0	0	0	0
0	0	0	0	0	0	0	0	0	0	0	0	0	0	0	0	0	0	0	0	0	0	0	0	0	0	0	0	0	0	0
0	0	0	0	0	0	0	0	0	0	0	0	0	0	0	0	0	0	0	0	0	0	0	0	0	0	0	0	0	0	0
0	0	0	0	0	0	0	0	0	0	0	0	0	0	0	0	0	0	0	0	0	0	0	0	0	0	0	0	0	0	0

The spray distribution measurement device is then emptied of the fluid and the experiment is repeated. This test is conducted three times with each of the nozzles at 2.5 Bar and 4 Bar pressures to obtain accurate results. These pressures are chosen as the each of the systems has a standard pump for the vehicle and when operating correctly will be able to supply a steady water supply of 2.5 Bar pressure to each of the nozzles in the system. However, when a system becomes blocked and one of the channels receives the full pressure of the pump this does not generally exceed 4.0 Bar pressure.

The volumetric flow rate (ml/sec) is measured, in addition to the pressure at which the nozzle is operated to ensure that the nozzle is behaving correctly. The volumetric flow rate is measured by calculating the total amount of water dispersed during the 30 second distribution test by adding all of the values collected from the water dispersion table. This value is then divided by 30, the duration of time in seconds that

the nozzle was operated in the experiment, to find the volumetric flow per second in ml/s.

2.2.1.2. Volumetric flow rate setup

The measurement of the volumetric flow rate was similar to the spray distribution test; however the results were much less involved, it required the following apparatus:

- Three samples of four different fluidic nozzles
- Frequency generator
- Power supply
- Water pump
- Multi-meter
- Clamp stand
- Bucket
- Mass measurement scales with tearing function

The setup for the power supply, frequency generator, water pump, multi-meter, clamp stand, and nozzles was the same as for the previous experiment. However instead of clamping the nozzles to a stand to examine the distribution, the jet was clamped so that it was facing downwards into a bucket.

The procedure for this test was to weigh the bucket on the scales and tear it so that the scales would equal zero with the bucket on them. This bucket would then be placed below the nozzle and the nozzle activated for the thirty second standard testing period used by the Kautex laboratory, ensuring all water was caught within the bucket. The bucket would then be reweighed with the water inside the vessel, this value in grams was then divided by thirty and divided by the density of water, 0.997 g/ml.

2.2.1.3. Variables

The fixed variables in the experiment are the positioning of the nozzle relative to the spray distribution measurement device (central), the pressure delivered from the pump, the fluid being used in the nozzle and the amount of time that the water was sprayed at the catchment device.

The dependent variables measured are the amount of fluid discharged from the nozzle for a ten second burst of flow, the amount of water caught in each of the

sections of the spray distribution device after a 30 second release and the pressure level flowing through the circuit during the operation of the experiment.

The independent variables for this experiment is the pressure, the nozzles and the distance from the nozzle to the water catchment device. The reason for the adjustment in distance was due to the fact that the Ford Ecosport nozzle has a much wider distribution of water in comparison to the two other nozzles, requiring less distance to the device to ensure all water is caught when tested at 4 Bar pressure. These are the only variable changes, everything else was kept constant in order to provide an accurate measurement.

By testing and analysing several samples of the same nozzle, it ensures that the results from experimentation were accurate and that the testing is consistent. This enables accurate prediction of a range of values for a particular nozzle, considering any defects formed in production. This will allow for prediction of whether there is a defect in a part and demonstrate how different defects can affect the spray distribution and volumetric flow rate.

2.2.1.4. Results

Table 2-3 shows the volumetric flow rates for each of the nozzles at both 2.5 Bar and 4 Bar pressures. In addition to measuring the volumetric flow rate within the spray catchment device, the nozzles were activated for a 30 second period and sprayed into a vessel as detailed in the above section. This meant that if any water falls outside the catchment device during the distribution testing, this would not affect the volumetric flow rate recorded of the nozzle as this was examined separately.

Table 2-3: Volumetric Flow Rates at 2.5 and 4 Bar Pressures

Nozzle	2.5 Bar case (ml/s)	4 Bar case (ml/s)
Ford B-Max	18.2	24.7
Ford Ecosport	19.2	25.8
Nissan	22.1	25.6
Toyota	13.7	18.4

The data from the spray distribution test is inputted into a number of Microsoft Excel spreadsheets, the template of which was based on one used by Kautex Textron CVS (Table 2-2), the table is part of a worksheet which contains formulae and charts to

instantly transform the raw data into a series of graphs. A spreadsheet for each of the 24 benchmarking tests, showing the distributions found, further spreadsheets are then formed from these showing the averages for each nozzle at the pressures measured (9.2 Appendix B).

In the tests there is very little variance in the positioning and height of the peaks and dips of flow for each of the nozzles therefore the tests were considered precise enough to calculate an average. The average is found by taking the value from the same slot in each of the distribution tables for a particular nozzle type at a given pressure and calculating the mean of these values.

Due to a customer preference of fluid distribution graphs being symmetrical and smooth, the spray volume distributions are averaged around the central point to suit this criterion in their final spreadsheets (9.2 Appendix B)). The symmetrical values are found by taking the mean of the cells in the table that are symmetric around the midpoint, meaning that the first and last cell in a particular row are summed and divided by two and the value found is recorded in the cells that the input came from.

The graphs of the symmetrical averages of each nozzle at both pressures are displayed below, they show the overall volume distribution in two viewing angles: from the side and the top (Figure 2-6 - Figure 2-9). The contour plot represents the amount of water collected in each of the slots in the water catchment device and the colour indicates the amount of water in cm^3 or equivalent ml. The bar graph shows the volume of water collected in each row to give a volumetric profile distribution.

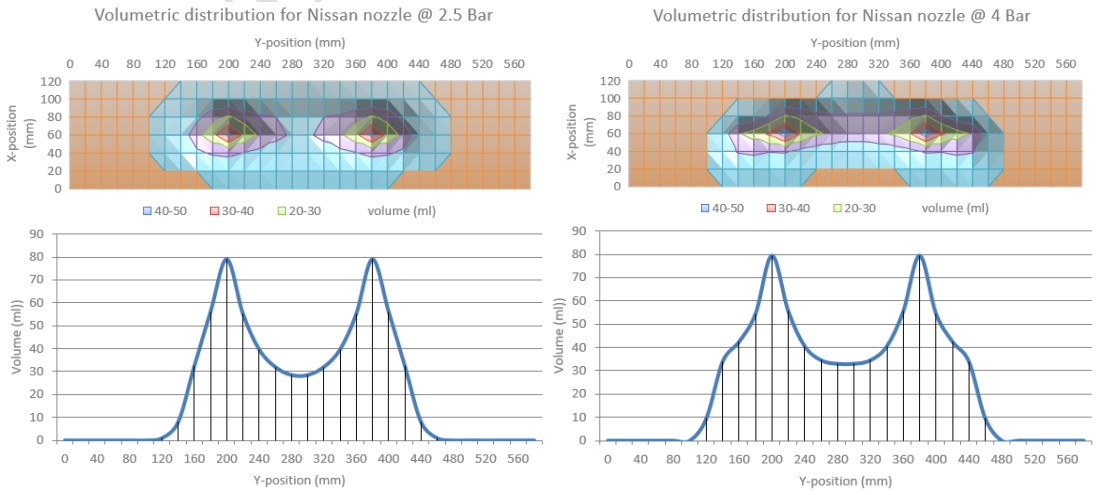

Figure 2-6: Nissan Spray Distribution at 2.5 Bar (left) and 4 Bar (right)

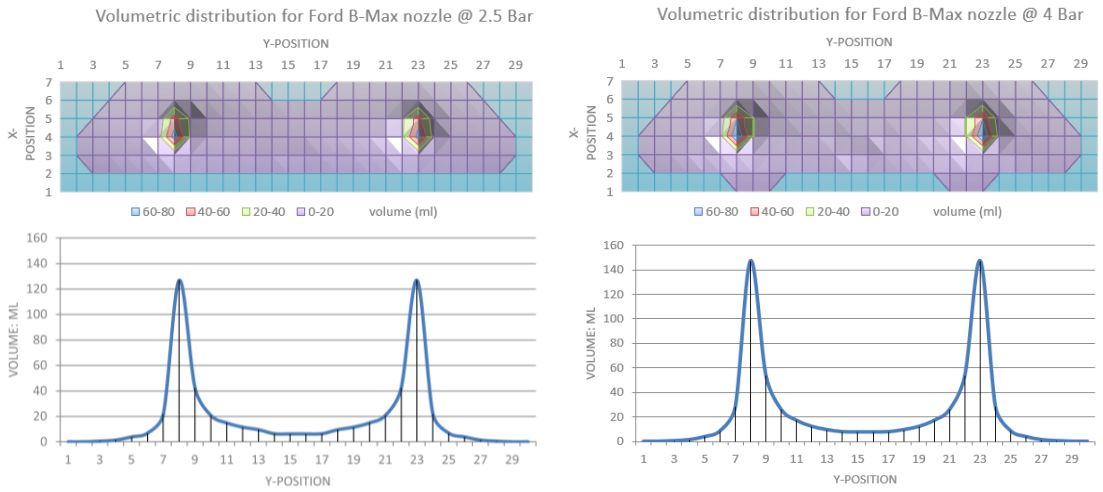

Figure 2-7: Ford B-Max Spray Distribution at 2.5 Bar (left) and 4 Bar (right)

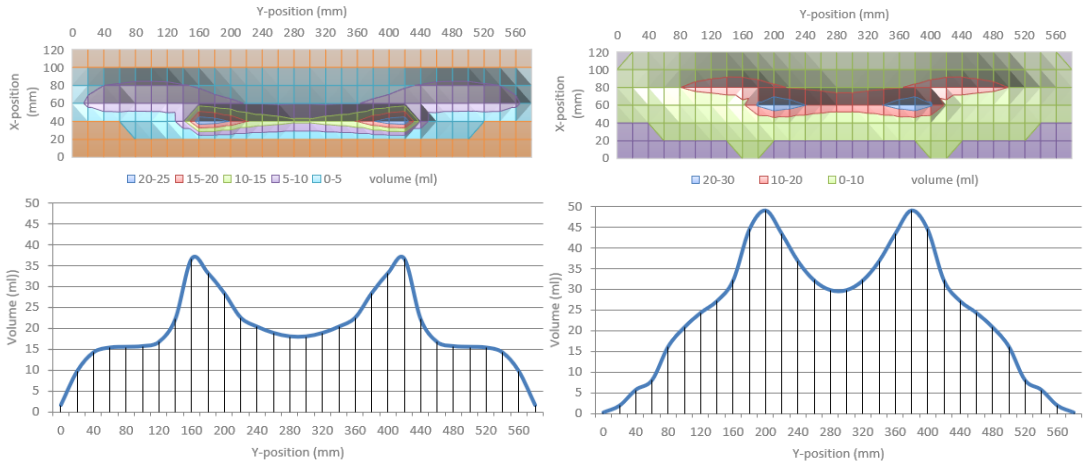

Figure 2-8: Ford Eco Spray Distribution at 2.5 Bar (left) and 4 Bar (right)

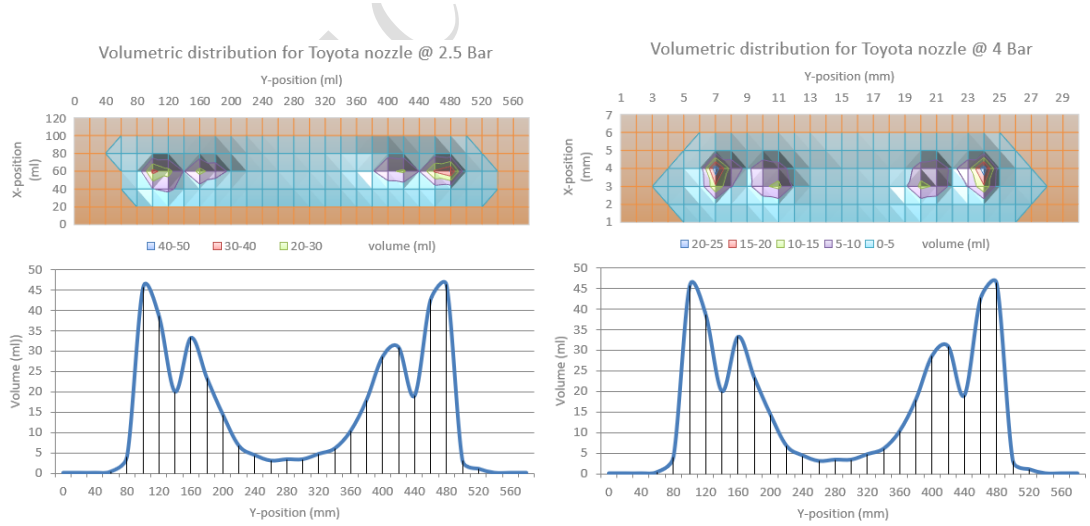

Figure 2-9: Toyota Distribution at 2.5 Bar (left) and 4 Bar (right)

of the water flows, therefore different ranges of axes are used in the graphs to most easily see the shape of the distribution of water.

In addition to the distribution graphs, below is Figure 2-10 which shows the relationship between the outlet area size and the volumetric flow rate for each of the nozzles in the study at the pressures 2.5 and 4 Bar.

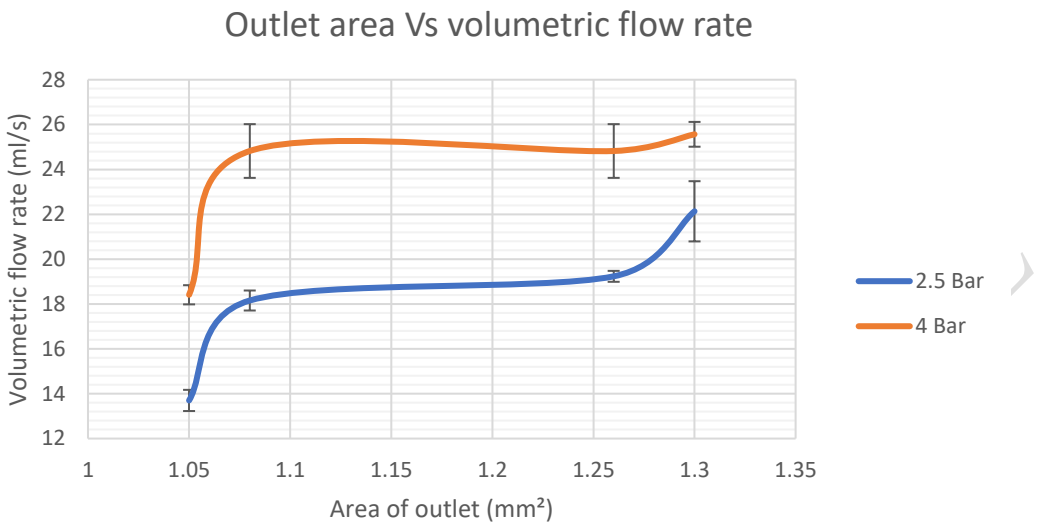

Figure 2-10: Graph showing Outlet Area vs Mass Flow Rate

2.2.1.5. Discussion and Conclusions

2.2.1.5.1. *Spray Distribution*

Two Ford B-Max nozzles are mounted on the vehicle bonnet a third of the way down the windscreen. This explains the need for the fairly wide spray distribution found, with the fluid predominantly concentrated at the two peaks on the far ends of the distribution. This nozzle gives a good approximation to what would be found if two pencil jets were used rather than one fluidic, therefore by utilising a fluidic nozzle there is a reduction of cost than if two systems were used. This distribution is useful to have as the fluid is projected at both sides of each C-zone, one for the driver and the other for the passenger, with minimal wastage between the two zones. The difference in the graphs at different pressures is very small, with only the overall volume at the peaks and surrounding areas increasing.

The Ford Ecosport has two nozzles positioned similarly to those for the Ford B-Max, however the Ford Ecosport is wider than the B-Max hence the wider spray distribution [44]. It can be seen on the graph above that the Ford Ecosport has two pairs of peaks, in order to view this more clearly the graphs showing volume per row for the central rows the Ford Ecosport nozzle are shown below (Figure 2-11). The cause for the two separate peaked distributions in this case is due to the Ford

Ecosport having a set of two back-to-back fluidic chips feeding fluid into two separate apertures, this gives a broader range of coverage ensuring that all the windscreen is cleaned.

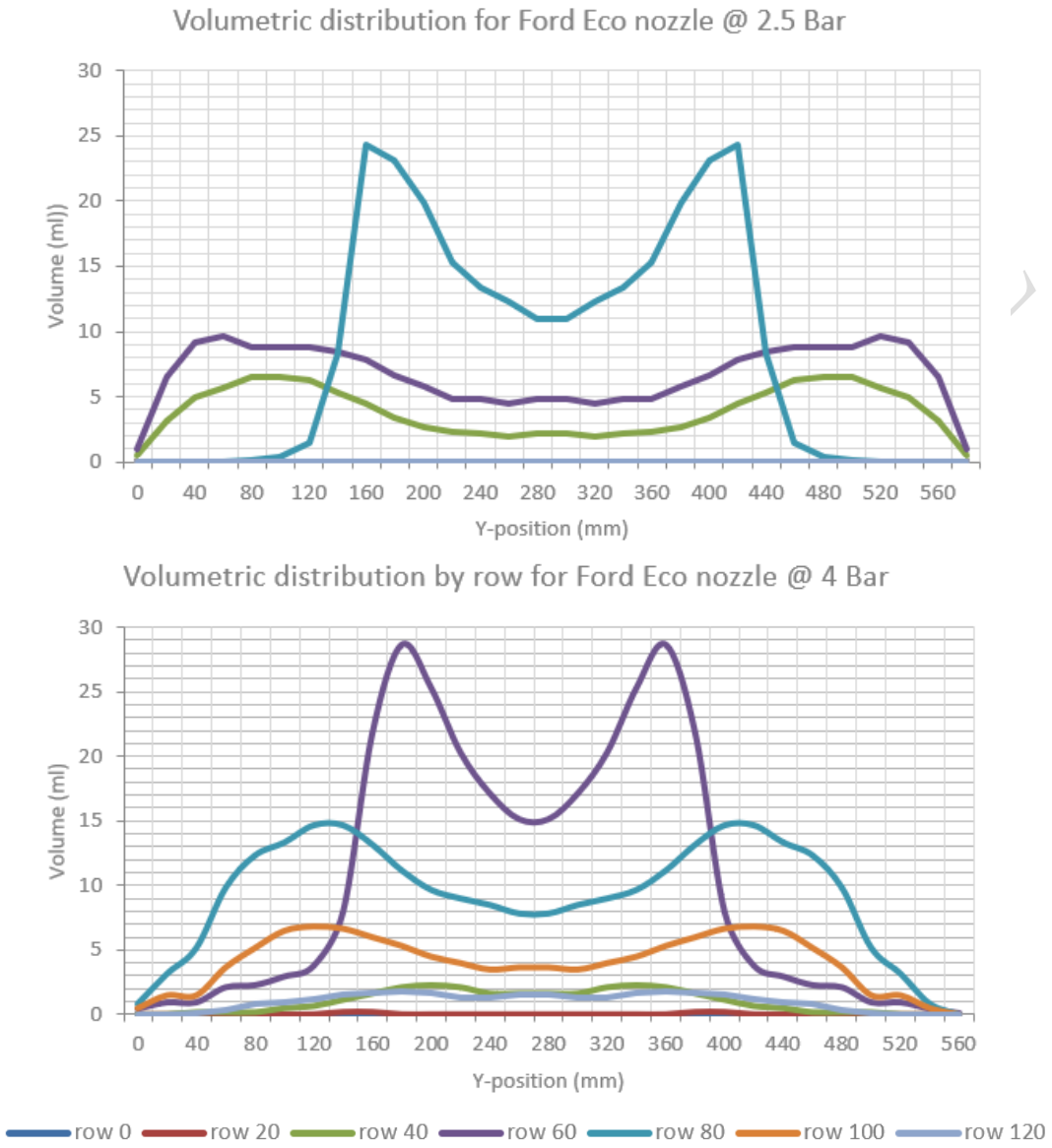

Figure 2-11: Volumetric distribution by row for Ford Eco nozzle at 2.5 Bar (top) and 4 Bar (bottom)

The distribution is dissimilar for the two different pressures, most noticeably the wider distribution at 4 Bar pressure. The water catchment area was much wider at 4 Bar pressure, resulting in a requirement of moving the nozzle closer to the device to be able to view the distribution as a whole. Secondly the volume distribution shape is altered for the two pressures, it is possible to see the two peaks given by the inner fluidic chip with the peaks higher in volume for the 4 Bar pressure as would be expected, however the surrounding fluid is distributed in diverse ways. The

surrounding fluid for the lower pressure distribution has peaks further apart than those given at the higher pressure, this has resulted in a merged peak for the higher pressure and a smooth curve with a more even distribution width-ways for the lower pressure.

The nozzles for Nissan vehicles are mounted under the bonnet, as an average due to the width of the vehicle the estimated number of nozzles per vehicle is three. In comparison to all of the other nozzles tested the Nissan nozzle has the narrowest distribution, this is possible due to there being three nozzles positioned sufficiently far from the windscreen. With three nozzles rather than two there is less need for a wide spray angle. The overall distribution shape is similar to that found for the Ford B-Max with two peaks, however there is more fluid sprayed in the central area for this nozzle. This is because with there being three nozzles on Nissan vehicles it will give a more consistent clean over the whole of the windscreen. The spray distributions for the different pressures are very similar, with the same peak volume and very comparable overall distributions. The main difference is that the peaks for the 4 Bar pressure test are wider than those for the 2.5 Bar pressure test.

The Toyota RAV4 has three nozzles positioned on the cowling under the bonnet of the vehicle, this means that there is less distance from the nozzle to the windscreen than both of the Ford nozzles. The spray angle for the Toyota RAV4 nozzle is the narrowest of all of the nozzles tested, this is due to there being three nozzles used rather than two, the number of nozzles found on the other vehicles. The data shows that the Toyota nozzle gives four peaks of spray distribution, this is due to the aperture shape on the Toyota nozzle having a step in the outlet shape allowing the outlet angle of the nozzle to be set at two different values for the top and bottom of the outlet (Figure 2-12).

Figure 2-12: Toyota outlet nozzle shape

The likely reason why a double distribution is uses is to ensure that the maximum amount of fluid reaches the target areas on the windscreen. The overall shape of the spray distribution is similar for both 2.5 and 4 Bar pressures, with the 4 Bar graph having higher volumes for all values than the 2.5 Bar graph. In both the two sets of peak volumes are very visible, however the peak volume increase for the outer peaks is much greater than the inner peaks for the flow at a pressure of 4 Bar, this means that this is most likely the dominant fluidic chip, the outer chip.

2.2.1.5.2. *Volumetric Flow Rate*

Figure 2-10 shows that there is a correlation between the area of the outlet of the nozzle and the volumetric flow rate. Where a larger outlet area generally results in a higher volumetric flow rates in the cases investigated in this project. The small downtrend at the end of the 4 Bar pressure graph is due to a smaller increase in flow rate in the Toyota nozzle from 2 Bar pressure. It is not possible to conclusively say why this occurs however due to this outlet being differently shaped than the other simple rectangular outlets, this could be part of the reason why this occurs. Further research into differently shaped outlet nozzles would be required to come to an improved hypothesis.

The results show that there is a much higher flow rate of the Nissan nozzle than the Toyota nozzle, with the two Ford nozzles having very similar volumetric flow rates in-between. This could be due to the size and shape of the outlet, or the internal geometry of the fluidic chip.

All nozzles experience a greater volumetric flow rate at 4 Bar pressure than at 2.5 Bar pressure. This is to be expected as the greater pressure forces the water through the fluidic chip at a faster rate.

The smallest variation in flow rate with pressure change is experienced by the Nissan nozzle and the largest in the Ford Ecosport nozzle. At the time of experimental testing, it was uncertain what the main factor in what affects the volumetric flow rate with regard to pressure as it was not possible to see inside the fluidic nozzle to view the flow patterns, therefore this required further investigation through computational fluidic modelling.

2.2.2. Spray Angle

The object of this experiment was to calculate the spray angles given by the three different fluidic nozzles, made by Nissan/Kautex, Toyota and Ford. From this data it was possible to compare the four nozzles in the conditions typically experienced when in use in an automobile.

Spray angle is vital as it gives a visualisation of where the fluid spray will terminate when the nozzle is sprayed towards a windscreen. Through visualisation and examination, it is possible to ensure that all of the critical parts of the windscreen are completely cleaned. Calculating the extreme external spray angles for the nozzles helps to calculate the number of nozzles required for a specified windscreen and the positioning of the nozzles required. This reinforces the data gathered from the spray distribution analysis.

Two hypotheses related to this testing were posed. Hypothesis 1 stated that it was expected that the nozzles with the thinner apertures would have narrower spray angles due to the allowable angle of flow from the nozzle. Hypothesis 2 predicted that the higher the volumetric flow rate a nozzle has the wider the angle of spray produced.

2.2.2.1. **Method**

A schematic of the main part the apparatus is shown below (Figure 2-13), there is also a list of equipment used:

- Black backdrop
- Camera
- Fluidic nozzle (x3)
- Clamp and stand
- Frequency generator
- Power supply
- Water pump

The setup for the nozzle was the same as for the previous spray distribution tests however the nozzle was used horizontally instead of vertically for this experiment. A risk assessment was performed to ensure that the experiment was conducted safely. Instead of using the spray distribution measurement device, a black back-drop and a bucket to collect the water was used, the back-drop allowed the spray angle to be

more visible and hence easier to measure. The frequency generator was not specified to spray a quantified amount of time, instead allowed to spray until a sufficiently precise photograph was achieved. This experiment was conducted with the Nissan/Kautex nozzle in order to verify the past data, and with the Toyota and Ford nozzles.

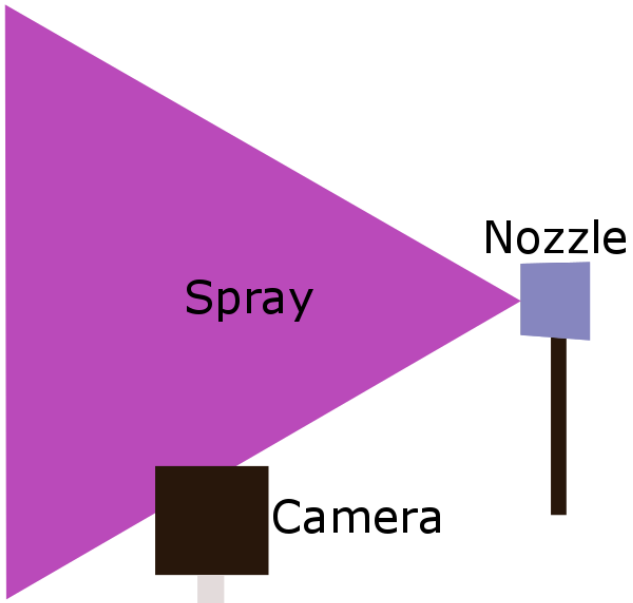

Figure 2-13: Spray angle testing apparatus

2.2.2.2. Variables

The fixed variables in the experiment were the angle of the nozzle relative to the horizontal (kept at 0°), the voltage delivered to the pump, the fluid being used in the nozzle and the camera used to capture the spray angle. This test used a horizontal axis rather than the vertical downwards axis used in the previous test as it was the easiest method for capturing the image and due to the proximity to the nozzle body the amount of deflection due to gravity would be negligible.

The dependent variable measured was the angle of the water projected from the nozzle outlet.

The independents for this experiment were the nozzles. These were the only variable changes, everything else was kept constant in order to provide an accurate measurement.

2.2.2.3. **Results**

The photographs taken during the experiment were uploaded to a computer and analysed by a program called ImageJ [45] to find the angle of the spray distribution. Several photos were captured of each nozzle at both side and above angles, and an average was taken in order to ensure that the data was accurate.

The images are shown below in ImageJ with superimposed circle sectors to display the angle of spray (Figure 2-16 - Figure 2-18). A table has been constructed showing the spray angles for all nozzles at both pressures and is shown below (Table 2-4). In the table there are 'inner' and 'outer' columns for the nozzles whose outputs give two distinct streams, those whose don't have the above stream in the outer column for easy comparison of maximum spray angle.

Additionally, a graph that shows the relationship between the height of a nozzle and the resulting spray height is included alongside a graph with the association of the nozzle widths with the spray angle widths (Figure 2-14 - Figure 2-15).

Table 2-4: Spray angles for all nozzles at 2.5 Bar and 4 Bar pressure

Nozzle	2.5 Bar pressure			4 Bar pressure		
	Outer	Inner	Side	Outer	Inner	Side
Ford B-Max	43.7	N/A	4.2	45.1	N/A	5.3
Ford Eco-Sport	67.2	40.7	7.4	70.8	43.7	8.9
Nissan	35.7	N/A	7.6	33.3	N/A	5.7
Toyota	51.8	33.4	4.9	45.6	28.5	3.9

Figure 2-14: Graph showing relationship between nozzle outlet height and spray height

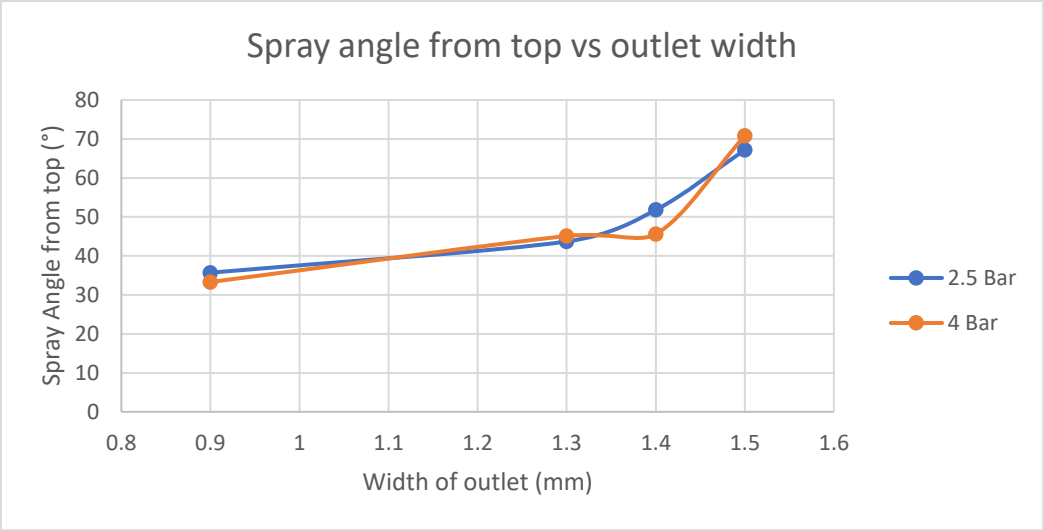

Figure 2-15: Graph showing relationship between nozzle outlet width and spray width

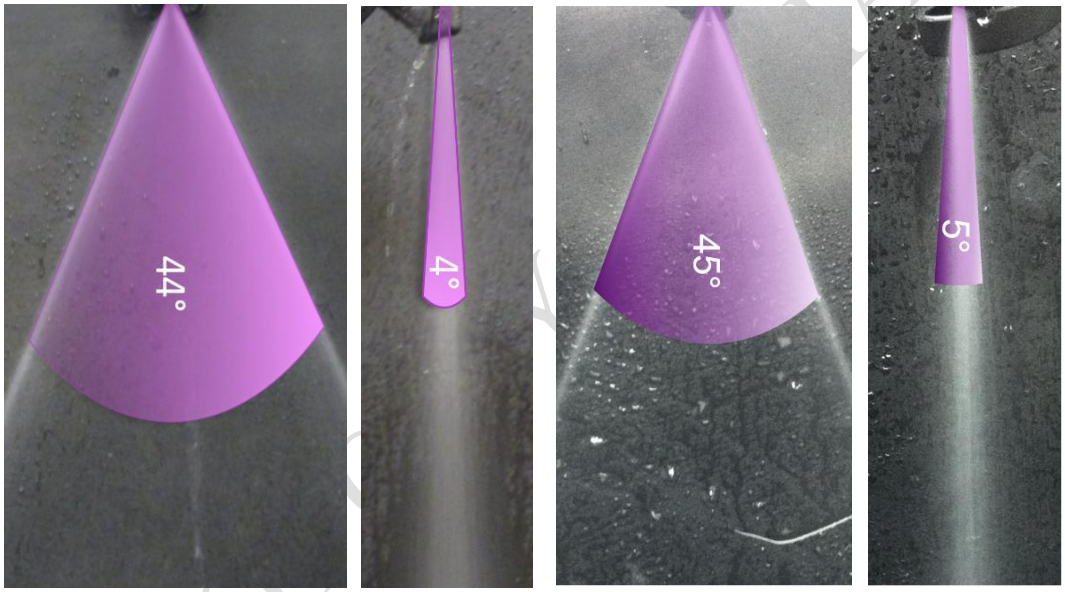

Figure 2-16: Ford B-Max spray angles from the top (left) and side (right) at 2.5 Bar (left) and 4 Bar (right)

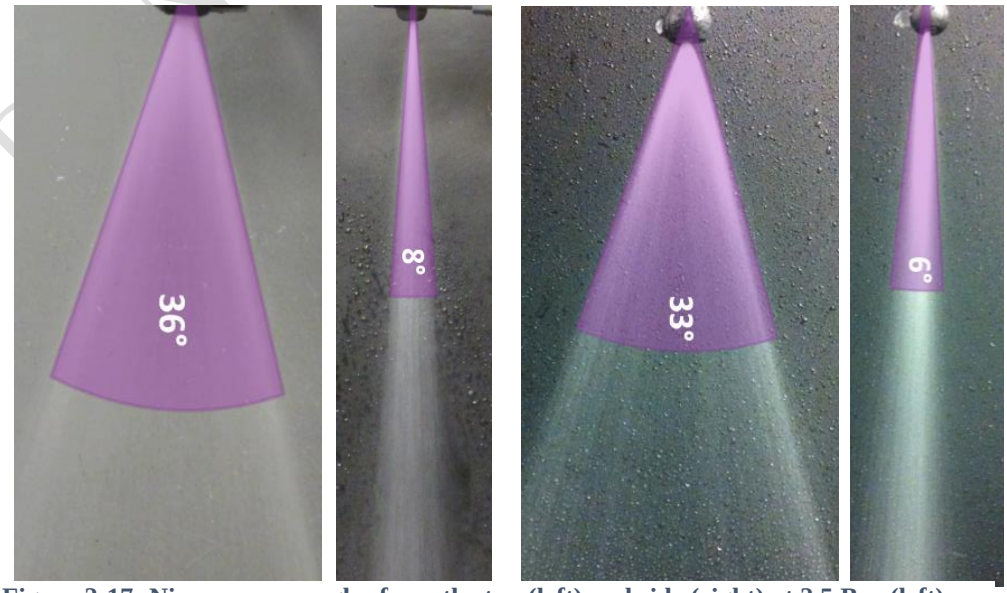

Figure 2-17: Nissan spray angles from the top (left) and side (right) at 2.5 Bar (left)

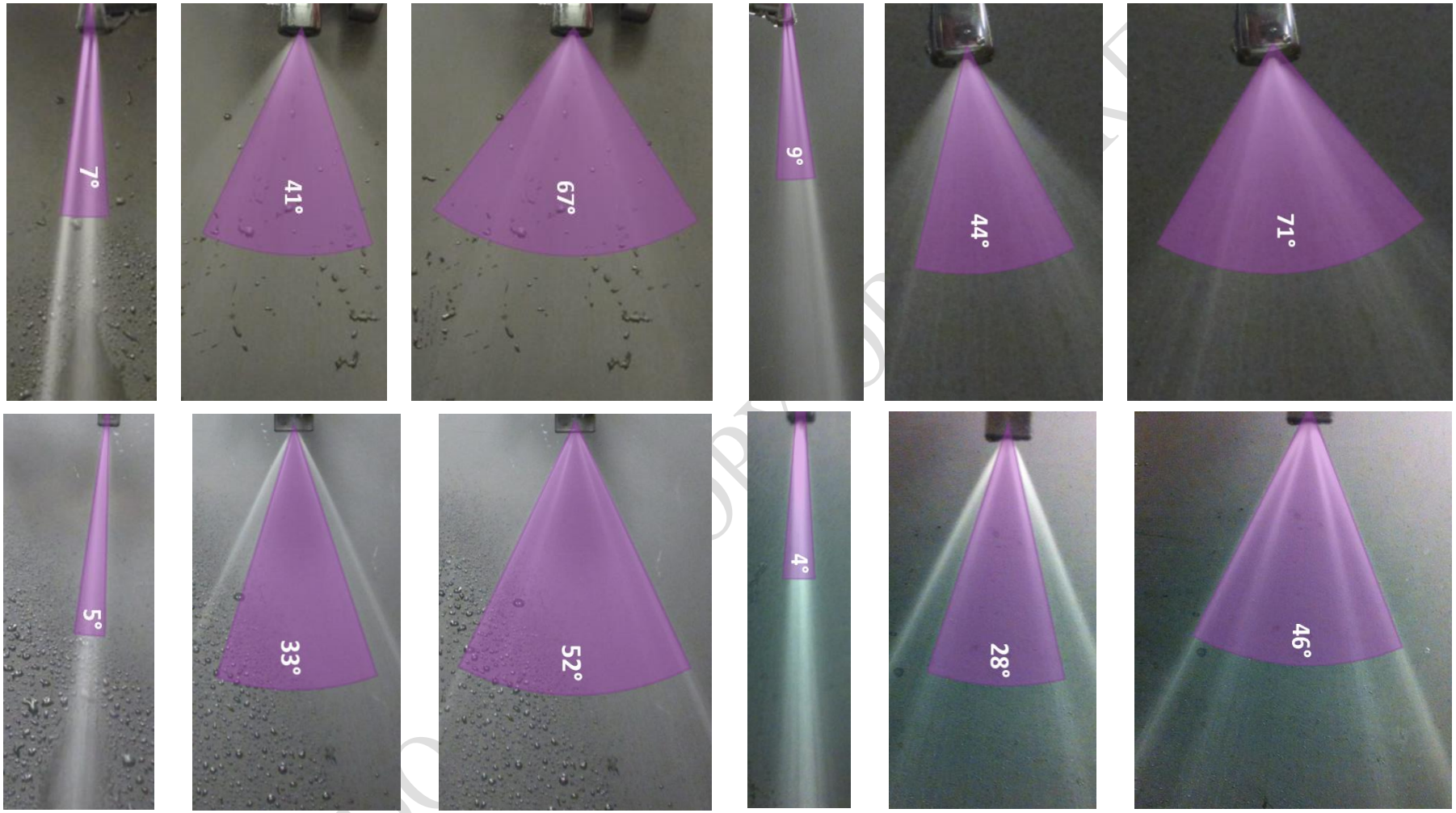

Figure 2-18: Ford Ecosport (top) and Toyota RA4 (bottom) spray angles from the top (left) and side (right) at 2.5 Bar (left)

2.2.2.4. Discussion and Conclusions

The results from Table 2-4 show that the Nissan/Kautex nozzle gives the narrowest spray angle at 35.73° and that the Ford Ecosport gives the overall widest angle at 67.16°. This validates the results from the spray distribution test and proves the hypothesis that wider nozzles will have a wider spray distribution is correct, also shown in Figure 2-15. The reason for the different spray angles for each nozzle is most likely due to the customer preference, the outlet size of the nozzle and the volumetric flow rate for the given pressure, this was further investigated using computational modelling.

Both the Ford and Toyota nozzles give two separate spray streams and angles, an inner and outer one. This is to be expected by the Ford nozzle as there are two outlets in the nozzle body with the two separate fluidic chips supplying each one. It is unusual for a single outlet to give two separate streams however this is likely achieved for the Toyota nozzle due to the unusual, stepped outlet shape (Figure 2-12).

The nozzle giving the tallest spray angle is the Nissan nozzle, this is unexpected as this nozzle has only a single aperture. However, it does have one of the highest volumetric flow rates, meaning that it requires a larger area outlet to accommodate the additional volume (Table 2-3), the taller aperture leads to the likely outcome of a relatively tall spray angle as seen in the spray distribution above. A tall spray angle can be ideal as it ensures that the whole height of the windscreen will receive a cleaning when the washer system is activated. Furthermore, when the vehicle is in motion it will be more likely that some of the water spray will come into contact with the windscreen.

The Ford B-Max nozzle has the shortest spray angle, this is as anticipated as the Ford B-Max nozzle has a low volumetric flow rate (Table 2-3) and a wide spray angle from the top view.

The Ford B-Max spray angle and the inner Ford Ecosport spray angle are the same angle. With the similarity in this test and the spray distribution showing peaks of spray in the same location it is possible to conclude that the Ford B-Max fluidic chip may be the same as one of the chips for the Ecosport.

The increased pressure of 4 Bar in the Toyota nozzle gives smaller spray angles for both top and side views than for 2.5 Bar pressure. This is likely to do with the inner geometry not allowing the fluid to fully attach to the outlet surfaces at the higher internal velocity, leading to an earlier point of separation from the walls of the nozzle. Because the fluid doesn't reach the maximum allowable angle at 4 Bar pressures this leads to the reduced spray angles.

The Nissan nozzle height spray height is smaller for the 4 Bar pressure distribution; this means that the fluid is more concentrated when at 4 Bar pressure giving more force behind the spray. All other aspects of the Toyota nozzle are the same at both pressures.

Additionally, the Ford B-Max nozzle image (Figure 2-16) shows some leakage from the nozzle which does not align with the spray angle meaning that this nozzle is either defective or not a robust design.

Hypothesis 1 predicted that nozzles with thinner apertures would produce a narrower spray angle, by examining Figure 2-15 it shows that within the nozzles studied in this benchmarking this statement was correct. However, to prove that this hypothesis is true unconditionally would require further study as this is a small focus group and two set pressures.

Hypothesis 2 stated that a nozzle with a higher volumetric flow rate would produce a wider spray angle. The graph in Figure 2-19 shows that for the nozzles and pressure tested there was not a clear correlation between the flow rate and the spray angle.

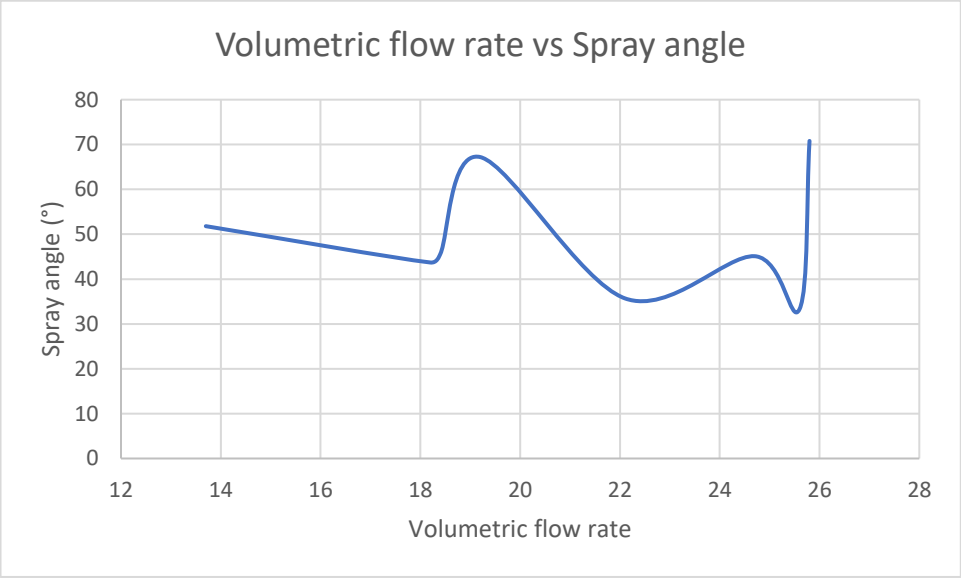

Figure 2-19: Volumetric flow rate vs (outer) spray angle

2.2.3. Oscillatory Frequency and Droplet Size

One of the objects of this experiment was to calculate the frequency at which the output stream oscillates from side to side given by the four different fluidic nozzles. A second aim was to analyse the droplet size given by each nozzle relative to each other. From this data it is possible to compare the four nozzles in the conditions typically experienced when in use in a stationary automobile.

The oscillatory frequency of the water nozzle is important as it will aid in defining the length of time needed for the fluid to be sprayed to achieve full coverage of the pertinent windscreen areas. By having this time duration, it will reduce the amount of fluid and power wasted when in operation as the time impulse for the spray can be set to the minimum time required for an efficient clean.

Droplet size is significant as the size of the water droplets affect the amount of drift that affects the fluid stream when discharging from the nozzle towards the windscreen. Drift is defined as the physical movement of spray particles through the air from the target site to any non- or off-target site at the time of application [46]. As the atmospheric conditions during operation are likely to be dynamic it is important to ensure that the effect of them does not redirect the water, resulting in the spray not reaching the target area.

As the experiment is approached it is valid to create two new hypotheses around the results in these tests. Hypothesis 3 states that it is expected that the nozzles with the narrower spray angles will have a lower frequency due to the less distance to travel from one side to another. Hypothesis 4 predicts also is that the higher the volumetric flow rate a nozzle has the larger the particle size of the water droplets.

A risk assessment was performed to ensure that the experiment was conducted safely. This involved ensuring all electrical cables and the camera were out of ‘splash zones’ and were in good condition with no damage. The nozzle was positioned so that as to minimise the likelihood of water spilling onto the floor causing a slip hazard and if spilt the water was mopped up straight away. The camera was heavy and awkward to position on the tripod therefore this was specified to be a two-person task. In addition to the camera, spotlights were used to achieve suitable lighting conditions. The spotlights became quite hot during prolonged use therefore a period with them turned off was required before handling.

Unfortunately, at the time of testing the Ford B-Max nozzle was not available therefore results are shown only for the Ford Ecosport, Nissan and Toyota RAV4 nozzles as it would not be possible to ensure all variables would be exactly the same for a second round of testing. This issue was resolved for prototype testing.

2.2.3.1. **Method**

A schematic of the apparatus is shown below (Figure 2-20), there is also a list of equipment used:

- Photron Fastcam SA4 and tripod
- Spotlights and stands(x2)
- Laptop
- Ethernet data cable (connecting camera to laptop)
- PFV (Photron Fastcam Viewer) computer program
- Fluidic nozzle (x3)
- Clamp and stand
- Power supply
- Water pump
- Water catchment box/bucket
- Black backdrop

The setup for the nozzle was the same as for the previous spray distribution with the nozzle positioned so the outlet faced downwards, however instead of aiming the nozzle into the water catchment device a simple bucket was used. Similar to the spray angle test, a black back-drop and a bucket to collect the water was used, the back-drop allowed the spray to be more visible and hence easier to measure. The frequency generator was not specified to spray a quantified amount of time, instead allowed to spray for a sufficiently long time period to guarantee precise photographs and video were achieved.

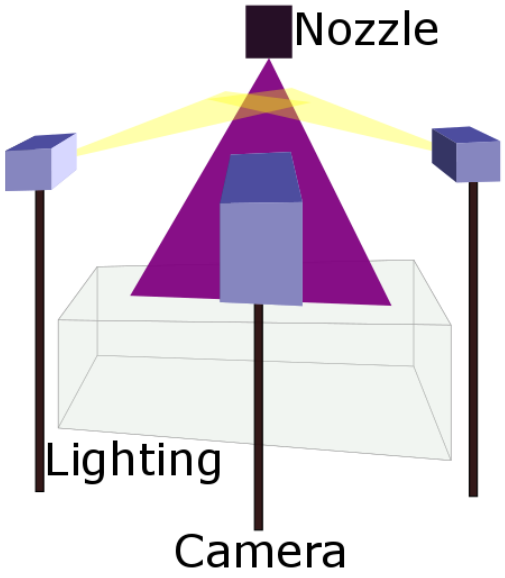

Figure 2-20: High speed testing apparatus

The camera and lighting were set up so that the optimum image was achieved at the nozzle outlet. The camera was connected to the laptop via an Ethernet cable and the interface program PFV. This experiment was conducted with the Nissan/Kautex nozzle in order to verify the past data, and with the Toyota and Ford nozzles.

Initially the camera is set up by altering the camera itself, then the program PFV was used for additional setup to achieve the optimum photos to analyse the flow characteristics. The camera is positioned so that the view shown is directed at the nozzle outlet, the way to do this is to set the camera options in PFV to 'low-light settings' as this increases the brightness in the viewfinder. This mode is then turned off and the spotlights are aimed at the area needing to be photographed. The frame rate and resolution are then chosen, for this experiment the framerate of 20000 fps is chosen which gives the maximum resolution of 512 x 352 pixels.

For each nozzle, two sets of 1000 photos were taken in addition to videos of these photo sets with the videos set at 2 fps. One of the sets of photos was taken with the lighting and settings as normal whilst the other was captured with pseudo-colour layered onto the monochrome image (Figure 2-21). The advantage of taking two sets is that the customer prefers the display to be as expected with normal lighting, and with the pseudo-colours it gives a better ability to see the flow of the water and hence find the oscillation frequency and droplet sizes.

2.2.3.2. **Variables**

The fixed variables in the experiment were the angle of the nozzle relative to the horizontal (kept at 0°), the voltage delivered to the pump (12V), the fluid being used in the nozzle, the camera used to capture the spray angle, the fluid in the system and the lighting used. Additionally, the camera was kept at the same distance from the experiment to ensure that the droplet sizing for the nozzles would be accurate and comparable.

The dependent variable measured was the time taken for the outflow to oscillate from one side to the other.

The independent variables for this experiment were the nozzles and the camera modes. These were the only variable changes, everything else was kept constant in order to provide an accurate measurement.

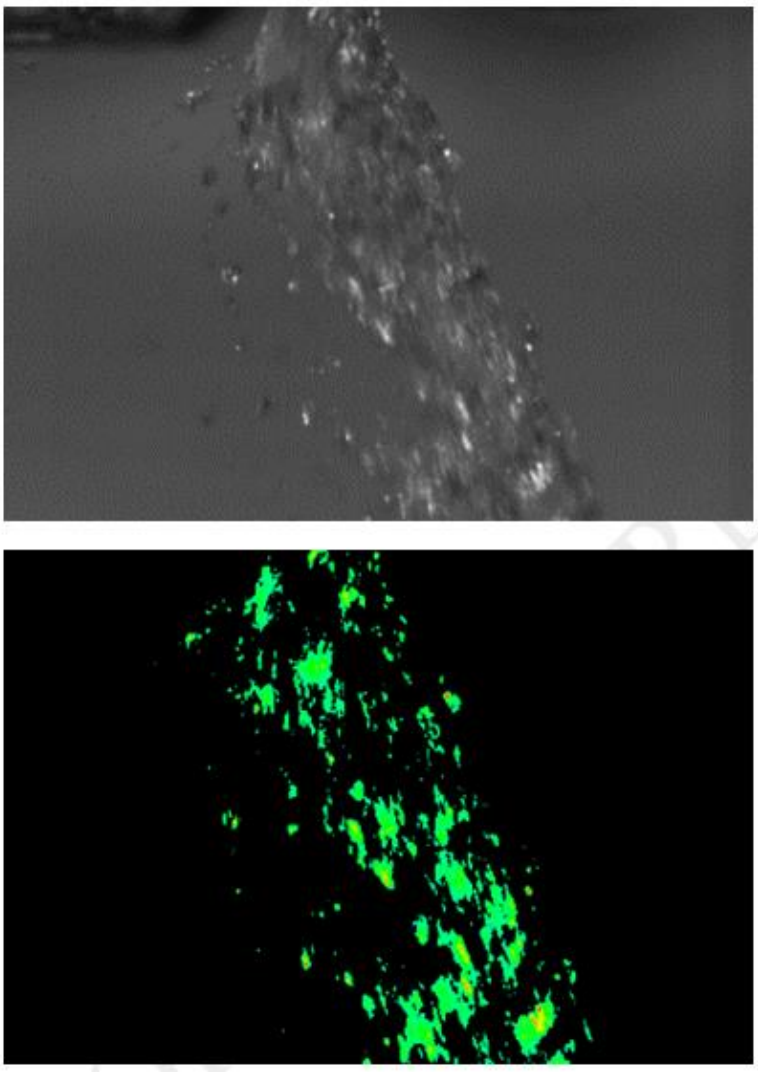

Figure 2-21: Nozzle fluid spray in normal lighting (top) and pseudo-colours (bottom)

2.2.3.3. **Results**

The photographs taken during the experiment were uploaded to a computer and analysed to find the number of frames taken for the spray to move to and from each side. The switching of flow direction was not instantaneous, instead taking a short amount of time to adjust to the new direction of flow. The midpoint frame between where the flow first arrives at an external side and the point when it leaves was used as the frame boundary to calculate the oscillation. This was completed manually for 10 oscillations for all nozzles apart from the Toyota nozzle which did not oscillate 10 times within the amount of footage taken, instead showing 9. These 9 or 10 oscillations were then averaged for each nozzle and multiplied by the number of frames per second to find the time taken and subsequently inversed to find the frequency (Table 2-5).

Table 2-5: Oscillation frequency and Droplet Sizes for Fluidic Nozzles

Characteristic	Ford Ecosport	Nissan	Toyota RAV4
Average frames to return to original side	36.08	62.50	107.83
Average time to return to original side (s)	0.001804	0.003125	0.005392
Average periodic frequency (Hz)	554.3	320.0	185.5
Number of Droplets (all photos)	447	870	792
Average Droplet Area (mm)	1.12	0.60	0.39
Standard Deviation of Droplet Area (mm)	3.41	2.24	1.53
Minimum Droplet Area (mm)	0.013	0.013	0.013
Maximum Droplet Area (mm)	40.37	39.23	21.10

The same program was used to analyse the dimensions of the water droplet particles. Three images from each of the pseudo-colour nozzle selections were chosen, each showing the fluid flow at a quarter, half and three-quarters of the oscillation phase to show the most distinctive difference between images. These image frames were then analysed to find the total amount of droplets, mean, standard deviation, minimum and maximum particle sizes over the three photos (Figure 2-23 - Figure 2-25). For those images with background interference this part of the photo was deselected prior to particle analysis. All images were taken in a single session for the three nozzles to reduce any human error when comparing the image outputs relative to each other, such as lighting changes. The dimensions of the droplets were determined using a

setup device in the PFV software which enabled the calibration of a ruler placed alongside the nozzle at the same distance from the camera lens.

To analyse whether there was any correlation between the volumetric flow rate and other dependent variables examined in these tests were present, a graph displaying the oscillation rate and average droplet size found for the three nozzles tested is shown in Figure 2-22.

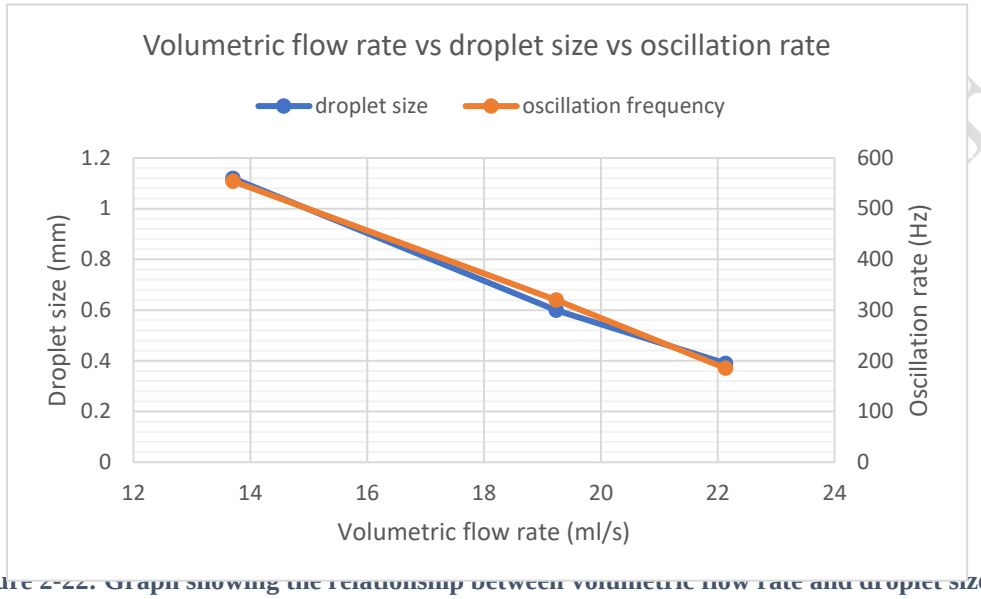

Figure 2-22: Graph showing the relationship between volumetric flow rate and droplet size and oscillation rate

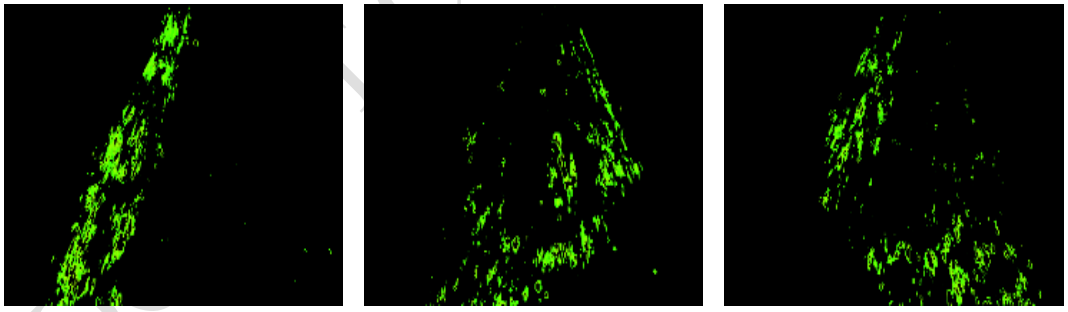

Figure 2-23: Toyota RAV4 Droplet Size Analysis Images

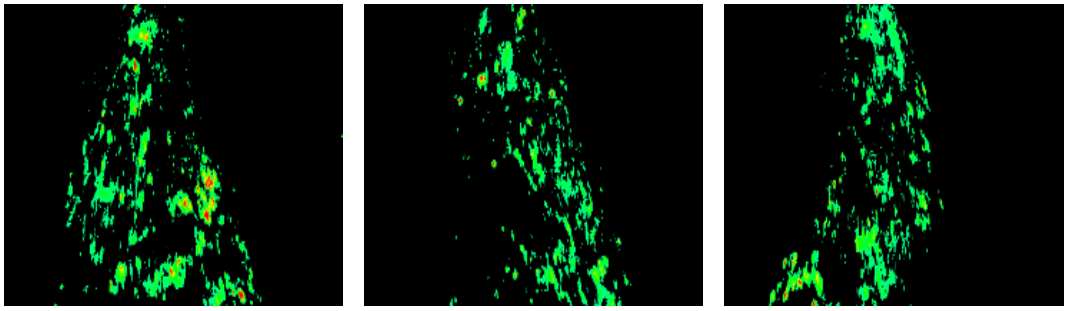

Figure 2-24: Nissan Droplet Size Analysis Images

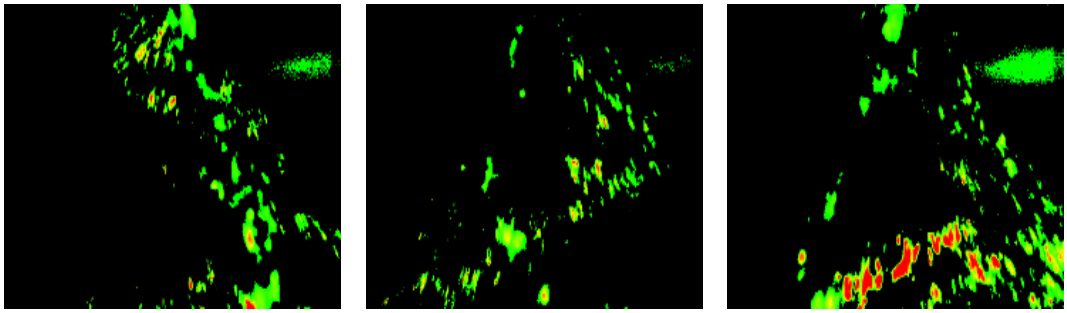

Figure 2-25: Ford Ecosport Droplet Size Analysis Images

2.2.3.4. Discussion and Conclusions

Two hypotheses were predicted regarding the results of this study. Hypothesis 3 predicted that a higher oscillation rate would be seen for the nozzles with a narrower spray angle. Hypothesis 4 stated that a higher volumetric flow rate would lead to larger particle sizes.

As shown in Figure 2-22 there is a negative correlation between the volumetric flow rate and both the oscillation rate and the average droplet size. This means that hypothesis 4 has been proved correct for these cases, however as demonstrated in hypothesis 2 there is no correlation between the volumetric flow rate and spray angle therefore this is incorrect.

2.2.3.4.1. *Oscillation Frequency*

The nozzle with the highest oscillation frequency is the Nissan nozzle and the lowest is the Toyota RAV4 nozzle with the Ford Ecosport nozzle in between the two.

The Nissan nozzle also has the highest volumetric flow rate (Table 2-3) therefore this is the nozzle that needs the least amount of time to fully cover the windscreen with fluid. Hence there will be less power wastage with the Nissan nozzle in comparison to the other two nozzles, however it is unknown whether the distribution of water will be wastefully spent given the much higher volumetric flow rate. Further computational and experimental study was needed to be undertaken to analyse this.

In addition to having the lowest oscillatory frequency the Toyota nozzle also has the lowest volumetric flow rate. This means that there is more likely to be a precise spray pattern for this fluidic nozzle as less water will be wasted with the lower volumetric flow rate. However, the low oscillatory frequency means that there will need to be a fluid impulse for a longer period to achieve the same volume of fluid on the windscreen as the other nozzles therefore there will be more power required to clean the windscreen.

2.2.3.4.2. ***Droplet Size***

The nozzle which gives the most droplets on average is the Nissan nozzle, this is predictable as it has the highest volumetric flow rate. The nozzle with the smallest number of droplets is the Toyota RAV4 which also correlates with the volumetric flow rate (Table 2-3).

The Ford Ecosport nozzle gives the largest size droplets, this means that the droplets from this nozzle are the least likely to be deflected as they are the heaviest. This means that there is a high probability that the fluid from the Ecosport will reach the target area in dynamic conditions. The position of the Ford nozzle is fairly far from the windscreen as it is on the bonnet, therefore this large droplet size will be required as there is more time taken for the fluid to reach the windscreen and hence more time for the fluid to be deflected.

The Toyota RAV4 nozzles discharges the smallest size fluid droplets, this means that a greater amount of drift is likely to occur for this nozzle. However, unlike the other two nozzles tested for water droplet size this nozzle is positioned close to the windscreen on the cowling. With the closer positioning there is a much smaller distance between which the fluid can be deflected meaning that a water droplet size such as this is acceptable and efficient for this vehicle. The Toyota RAV4 nozzle is the nozzle with the shortest aperture out of the four nozzles; therefore, there is a possibility that this is a determining variable in droplet sizing.

The Nissan nozzle mean droplet size is between that of the Ford Ecosport and the Toyota RAV4. The positioning of this nozzle is on the bonnet; therefore, this nozzle is the most likely to be affected by drift. This is compensated by the high volumetric flow rate meaning that there is a greater amount of fluid for this nozzle ensuring at least some of the water will reach the correct position on the windscreen. The Ford Ecosport nozzle is the nozzle has the tallest overall aperture; however, this is constructed from two apertures, this means a certain conclusion about whether the height of the nozzle apertures has a direct correlation on the sizing of droplets and further research is required.

2.3. Benchmarking Conclusions

From the experimental benchmarking of these nozzles a greater understanding and knowledge of how fluidic nozzle basic geometries affect the spray emitted from the nozzles. It has been discovered that:

- a wider fluidic nozzle outlet produces a wider spray angle
- there is no direct correlation between volumetric flow rate and spray angle
- there is a negative correlation between the volumetric flow rate and both average droplet size and oscillation rate
- the spray distribution shape for a single fluidic nozzle is predominantly U-shaped, with two peaks and an area of lower spray volume in the centre
- it is possible to construct a fluidic nozzle with more than two peaks by altering the aperture or by stacking fluidic chips back-to-back
- the angle of the outlet within the fluidic nozzle has more effect on spray angle than the aperture width

To state conclusively that the above conclusions are correct, further research would be necessary with a broader range of nozzles at a wider range of pressures.

3. Computational Fluid Dynamics - Theory

Fluid dynamics is the study of fluid motion, this can be assumed to be the movement of a large number of amalgamated atoms and/or molecules which can be assumed to be modelled as a continuum. This assumption can be made because fluid flow primarily remains within the macroscopic length scale, meaning that the molecular structure and interactions between the microscopic particles can be ignored [47]. There are numerous methods used to calculate and analyse theoretical fluid flow, the one utilised in this project is the Navier-Stokes approach utilising the conservation laws:

- Conservation of mass
- Conservation of momentum
- Conservation of energy

The Lagrangian approach applies the idea that each particle of the continuum is a function of its position (x, y, z) and time (t) [47].

The fluid that will be used in the fluidic nozzle system is water, which is a Newtonian fluid, meaning that it is incompressible. Although washer fluid can be used in automotive washer systems, this is predominantly used only when temperatures drop below zero.

The characteristic of a flow that determines whether it is laminar, turbulent or in transition is the Reynolds number where if $\mathrm{Re} < 2100$ the flow is laminar, $\mathrm{Re} > 4000$ the flow is turbulent in a pipe, otherwise the fluid is in transitional state (Figure 3-1). Disturbances within a flow will dictate how smooth and steady the flow of water is, the fewer and smaller the disturbances, the lower the Reynolds number of the fluid. Once the flow reaches the critical Reynolds number it can start to become unstable and unsteady with randomised flow, this is known as turbulent flow.

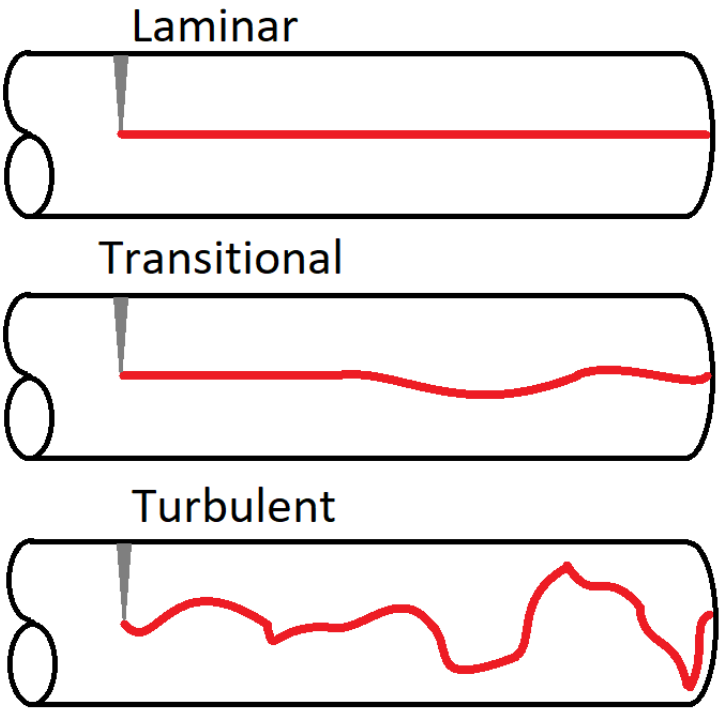

Figure 3-1: Different types of flow in a tube: laminar, transitional and turbulent

The flow can be modelled using an Eulerian Navier-Stokes approach for all regimes, however in turbulent flow of complex geometries an averaged approach may be required in combination with a transport model as shown in the turbulent section in this chapter.

3.1. Laminar Flow

Laminar flow is found in fluids with low Reynolds numbers where fluid travels in a straight path in parallel layers with no interference between the layers.

The Eulerian Navier-Stokes equations are used for steady fluid flows whose control volume is fixed in space, meaning that the displacements of particles are ignored [48]. The Navier-Stokes equations are used to find the pressure and velocity fields of laminar fluids.

3.1.1. Conservation of Mass

The conservation of mass, also known as Euler's continuity equation, is characterised by examining the amount of fluid flow in and out of an infinitesimally small control volume. This is also equal to the change of density of the control volume and can be expressed as shown below (3.1) [47].

$$\frac{\partial \rho}{\partial t} + \nabla(\rho \mathbf{u}) = 0 \qquad (3.1)$$

Where t is time, ρ is density, $\boldsymbol{u}$ is the vector flow velocity (3.2) and ∇ denotes the gradient operator (3.3). The first term represents the rate of density change in the control volume, the second term is the mas flux exiting the control volume and can also be known as the convective term. The continuity equation can be expanded to its divergence form below (3.4) in the Cartesian reference frame.

$$\boldsymbol{u} = \begin{bmatrix} u \\ v \\ w \end{bmatrix} \quad (3.2)$$

$$\nabla = \left[\frac{\partial}{\partial x}, \frac{\partial}{\partial y}, \frac{\partial}{\partial z}\right] \quad (3.3)$$

$$\frac{\partial \rho}{\partial t} + \frac{\partial}{\partial x}(\rho u) + \frac{\partial}{\partial y}(\rho v) + \frac{\partial}{\partial z}(\rho w) = 0 \quad (3.4)$$

For the fluid dynamics calculations in this project, the fluid used is water, which is incompressible, negating the first term of this equation as there is no density flux when the density is a constant value. This reduces the continuity equation to the following
(3.5):

$$\text{div}\, \boldsymbol{u} = \nabla \cdot \boldsymbol{u} = \frac{\partial u}{\partial x} + \frac{\partial v}{\partial y} + \frac{\partial w}{\partial z} = 0 \quad (3.5)$$

The term $\nabla \cdot$ denotes the divergence of a vector.

3.1.2. Conservation of Momentum

Newton's second law of motion is fundamental in momentum conservation, change in momentum is due to the net force acting on an elemental mass. There are two different types of forces that can act on the body: external forces which act on the mass, and surface forces such as pressure and shear. By combining all the contributions of force, the following conservation of momentum equations in *x*- (3.6), *y*- (3.7) and *z*-directions (3.8) can be found [47].

$$\rho \frac{Du}{Dt} = \frac{\partial(-p + \tau_{xx})}{\partial x} + \frac{\partial \tau_{yx}}{\partial y} + \frac{\partial \tau_{zx}}{\partial z} + S_{M_x} \quad (3.6)$$

$$\rho \frac{Dv}{Dt} = \frac{\partial \tau_{xy}}{\partial x} + \frac{\partial(-p + \tau_{yy})}{\partial y} + \frac{\partial \tau_{zy}}{\partial z} + S_{M_y} \quad (3.7)$$

$$\rho \frac{Dw}{Dt} = \frac{\partial \tau_{xz}}{\partial x} + \frac{\partial \tau_{yz}}{\partial y} + \frac{\partial(-p + \tau_{zz})}{\partial z} + S_{M_z} \quad (3.8)$$

Here τ_{ij} and τ_{ii} represent the viscous stress components in respective Cartesian directions (3.9), p is the pressure and S_M is the force contribution from body forces. The first term in the equation represents the momentum rate per unit volume in the control volume. The second term is the tensor representing the rate of momentum lost through convection, this can be expanded (3.10) [47].

$$\tau_{xx} = 2\mu\frac{\partial u}{\partial x} + \lambda(\nabla \cdot \boldsymbol{u}) \qquad \tau_{yy} = 2\mu\frac{\partial v}{\partial y} + \lambda(\nabla \cdot \boldsymbol{u}) \tag{3.9}$$

$$\tau_{zz} = 2\mu\frac{\partial w}{\partial z} + \lambda(\nabla \cdot \boldsymbol{u}) \qquad \tau_{xy} = \tau_{yx} = \mu\left(\frac{\partial u}{\partial y} + \frac{\partial v}{\partial x}\right)$$

$$\tau_{xz} = \tau_{zx} = \mu\left(\frac{\partial u}{\partial z} + \frac{\partial w}{\partial x}\right) \qquad \tau_{yz} = \tau_{zy} = \mu\left(\frac{\partial v}{\partial z} + \frac{\partial w}{\partial y}\right) \tag{3.10}$$

Here there are two different types of viscosity: dynamic viscosity, μ, which relates stresses to linear deformation, and second viscosity, λ, which relates stresses to the volumetric deformation. For liquids $\lambda = 0$ and $\nabla \cdot \boldsymbol{u} = 0$. By substituting the shear stress equations into the conservation of momentum equations the Navier-Stokes equations are formed (3.11 – 3.13) [47].

$$\rho\frac{Du}{Dt} = -\frac{\partial p}{\partial x} + \frac{\partial}{\partial x}\left[2\mu\frac{\partial u}{\partial x}\right] + \frac{\partial}{\partial y}\left[\mu\left(\frac{\partial u}{\partial y} + \frac{\partial v}{\partial x}\right)\right] + \frac{\partial}{\partial z}\left[\mu\left(\frac{\partial u}{\partial z} + \frac{\partial w}{\partial x}\right)\right] + S_{M_x} \tag{3.11}$$

$$\rho\frac{Dv}{Dt} = -\frac{\partial p}{\partial y} + \frac{\partial}{\partial x}\left[\mu\left(\frac{\partial u}{\partial y} + \frac{\partial v}{\partial x}\right)\right] + \frac{\partial}{\partial y}\left[2\mu\frac{\partial v}{\partial y}\right] + \frac{\partial}{\partial z}\left[\mu\left(\frac{\partial v}{\partial z} + \frac{\partial w}{\partial y}\right)\right] + S_{M_y} \tag{3.12}$$

$$\rho\frac{Dw}{Dt} = -\frac{\partial p}{\partial z} + \frac{\partial}{\partial x}\left[\mu\left(\frac{\partial u}{\partial y} + \frac{\partial w}{\partial x}\right)\right] + \frac{\partial}{\partial y}\left[\mu\left(\frac{\partial v}{\partial z} + \frac{\partial w}{\partial y}\right)\right] + \frac{\partial}{\partial z}\left[2\mu\frac{\partial w}{\partial z}\right] + S_{M_z} \tag{3.13}$$

The Navier-Stokes equations can then be rearranged to group the viscous terms. Below is an example of how the *x*-component of the Navier-Stokes equation (3.14) can be presented. The same manipulation can be completed for the *y*- and *z*-components [47].

$$\frac{\partial}{\partial x}\left[2\mu\frac{\partial u}{\partial x}\right]+\frac{\partial}{\partial y}\left[\mu\left(\frac{\partial u}{\partial y}+\frac{\partial v}{\partial x}\right)\right]+\frac{\partial}{\partial z}\left[\mu\left(\frac{\partial u}{\partial z}+\frac{\partial w}{\partial x}\right)\right]$$
$$=\frac{\partial}{\partial x}\left(\mu\frac{\partial u}{\partial x}\right)+\frac{\partial}{\partial y}\left(\mu\frac{\partial u}{\partial y}\right)+\frac{\partial}{\partial z}\left(\mu\frac{\partial u}{\partial z}\right) \quad (3.14)$$
$$+\left[\frac{\partial}{\partial x}\left(\mu\frac{\partial u}{\partial x}\right)+\frac{\partial}{\partial y}\left(\mu\frac{\partial v}{\partial x}\right)+\frac{\partial}{\partial z}\left(\mu\frac{\partial w}{\partial x}\right)\right]=\mu\nabla^2 u+\left[s_{M_x}\right]$$

Here the term ∇^2 is used to represent the Laplacian operator (3.15) [49].

$$\nabla^2 u=\left(\frac{\partial^2}{\partial x^2}+\frac{\partial^2}{\partial y^2}+\frac{\partial^2}{\partial z^2}\right)u \quad (3.15)$$

The momentum equations have been simplified by adding the smaller contributions of momentum into the momentum source component (3.16).

$$S_M=S_M+[s_M] \quad (3.16)$$

The Navier-Stokes equations for directional momentum can now be written more simply as the follows (3.17 - 3.19):

$$\frac{\partial(\rho u)}{\partial t}=-\frac{\partial p}{\partial x}+\mu\nabla^2 u+S_{M_x} \quad (3.17)$$

$$\frac{\partial(\rho v)}{\partial t}=-\frac{\partial p}{\partial y}+\mu\nabla^2 v+S_{M_y} \quad (3.18)$$

$$\frac{\partial(\rho w)}{\partial t}=-\frac{\partial p}{\partial z}+\mu\nabla^2 w+S_{M_z} \quad (3.19)$$

Again, due to the flow being incompressible the momentum equation can be simplified to the following form (3.20):

$$\frac{D\boldsymbol{u}}{Dt}=-\nabla p+\mu\nabla^2\boldsymbol{u} \quad (3.20)$$

3.1.3. Conservation of Energy

The first law of thermodynamics states that the total energy in a system is constant, energy cannot be created or destroyed. This law provides the basis for the equation for energy conservation in relation to a fluid particle (3.21) [47]:

$$\begin{array}{c}\text{Rate of increase}\\ \text{of energy of}\\ \text{fluid particle}\end{array}=\begin{array}{c}\text{Net rate of}\\ \text{heat added to}\\ \text{fluid particle}\end{array}+\begin{array}{c}\text{Net rate of}\\ \text{work done on}\\ \text{fluid particle}\end{array} \quad (3.21)$$

The rate of increase of energy of a fluid particle per unit volume can be stated as:

$$\begin{matrix}\text{Rate of increase}\\ \text{of energy of}\\ \text{fluid particle}\end{matrix} = \rho \frac{DE}{Dt} \quad (3.22)$$

Where the term E is the specific energy of a fluid.

3.1.3.1. Work Done in System

The net rate of work done on a fluid particle is found by combining the force and velocity components on a particle. Shown below are the equations for the work done in each of the Cartesian axes (3.23 – 3.25) and the total rate of work done (3.26) per unit volume [47]. In the below equations W represents the work done in the system.

$$W_x = \left[\frac{\partial\left(u(-p+\tau_{xx})\right)}{\partial x} + \frac{\partial\left(u\tau_{yx}\right)}{\partial y} + \frac{\partial(u\tau_{zx})}{\partial z}\right]\delta x\delta y\delta z \quad (3.23)$$

$$W_y = \left[\frac{\partial\left(v\tau_{xy}\right)}{\partial x} + \frac{\partial\left(v(-p+\tau_{yy})\right)}{\partial y} + \frac{\partial\left(v\tau_{zy}\right)}{\partial z}\right]\delta x\delta y\delta z \quad (3.24)$$

$$W_z = \left[\frac{\partial(w\tau_{xz})}{\partial x} + \frac{\partial\left(w\tau_{yz}\right)}{\partial y} + \frac{\partial\left(w(-p+\tau_{zz})\right)}{\partial z}\right]\delta x\delta y\delta z \quad (3.25)$$

$$\boldsymbol{W} = -\frac{\partial(up)}{\partial x} - \frac{\partial(vp)}{\partial y} - \frac{\partial(wp)}{\partial z} = -\nabla\cdot(p\boldsymbol{u}) \quad (3.26)$$

3.1.3.2. Heat Flux

The net rate of heat added to a fluid particle is found by examining the heat flow in specific Cartesian coordinates through the heat input and loss across the fluid particle. The equations below define the amount of heat flow in each of the Cartesian directions (3.27 - 3.29) and for the total amount in the system divided by the volume (3.30) [47]. Here q represents the heat flux.

$$\left[\left(q_x - \frac{\partial q_x}{\partial x}\frac{1}{2}\delta x\right) - \left(q_x + \frac{\partial q_x}{\partial x}\frac{1}{2}\delta x\right)\right]\delta y\delta z = -\frac{\partial q_x}{\partial x}\delta x\delta y\delta z \quad (3.27)$$

$$\left[\left(q_y - \frac{\partial q_y}{\partial y}\frac{1}{2}\delta y\right) - \left(q_y + \frac{\partial q_y}{\partial y}\frac{1}{2}\delta y\right)\right]\delta x\delta z = -\frac{\partial q_y}{\partial y}\delta x\delta y\delta z \quad (3.28)$$

$$\left[\left(q_z - \frac{\partial q_z}{\partial z}\frac{1}{2}\delta z\right) - \left(q_z + \frac{\partial q_z}{\partial z}\frac{1}{2}\delta z\right)\right]\delta x\delta y = -\frac{\partial q_y}{\partial y}\delta x\delta y\delta z \quad (3.29)$$

$$-\frac{\partial q_x}{\partial x} - \frac{\partial q_y}{\partial y} - \frac{\partial q_z}{\partial z} = -\nabla\cdot\boldsymbol{q} \quad (3.30)$$

The heat flux in the system can be related to Fourier's law of heat conduction (3.31), with k representing the thermal conductivity of the fluid and T the temperature:

$$q_x = -k\frac{\partial T}{\partial x} \qquad q_y = -k\frac{\partial T}{\partial y} \qquad q_z = -k\frac{\partial T}{\partial z} \qquad \boldsymbol{q} = -k\nabla T \tag{3.31}$$

By combining the equations of heat flow (3.30) and heat flux (3.31), it is possible to find the net rate of heat added to the fluid due to conduction (3.32):

$$-\nabla \cdot \boldsymbol{q} = \nabla \cdot (k\nabla T) \tag{3.32}$$

3.1.3.3. Energy Equation

The energy equation is composed of the internal energy and the kinetic energy. A conservation of momentum equation is obtained by accumulating the previous equations for the net rate of work done on a particle (3.26), the net heat flux of a particle (3.32) and any additional heat sources acting on the particle (S_E) and associating the product of this with the change of energy of the fluid particle (3.21). It is easiest to arrange the terms of the equation into the Cartesian components (3.33) [47]:

$$\begin{aligned}\rho\frac{DE}{Dt} = -\nabla\cdot(\rho\boldsymbol{u}) &+ \left[\frac{\partial(u\tau_{xx})}{\partial x} + \frac{\partial(u\tau_{yx})}{\partial y} + \frac{\partial(u\tau_{zx})}{\partial z} + \frac{\partial(v\tau_{xy})}{\partial x} + \frac{\partial(v\tau_{yy})}{\partial y}\right. \\ &\left. + \frac{\partial(v\tau_{zy})}{\partial z} + \frac{\partial(w\tau_{xz})}{\partial x} + \frac{\partial(w\tau_{yz})}{\partial y} + \frac{\partial(w\tau_{zz})}{\partial z}\right] + \nabla \\ &\cdot(k\nabla T) + S_E\end{aligned} \tag{3.33}$$

The energy equation (3.33) can be split up into a kinetic energy equation (3.34) and an internal energy equation (3.35):

$$\begin{aligned}\rho\frac{D\left[\frac{1}{2}(u^2+v^2+w^2)\right]}{Dt} &= -\boldsymbol{u}\nabla p + u\left(\frac{\partial\tau_{xx}}{\partial x} + \frac{\partial\tau_{yx}}{\partial y} + \frac{\partial\tau_{zx}}{\partial z}\right) \\ &+ v\left(\frac{\partial\tau_{xy}}{\partial x} + \frac{\partial\tau_{yy}}{\partial y} + \frac{\partial\tau_{zy}}{\partial z}\right) + w\left(\frac{\partial\tau_{xz}}{\partial x} + \frac{\partial\tau_{yz}}{\partial y} + \frac{\partial\tau_{zz}}{\partial z}\right) \\ &+ \boldsymbol{u}\boldsymbol{S}_M\end{aligned} \tag{3.34}$$

$$\rho c \frac{Di}{Dt} = \nabla \cdot (k \nabla T) + \tau_{xx} \frac{\partial u}{\partial x} + \tau_{yx} \frac{\partial u}{\partial y} + \tau_{zx} \frac{\partial u}{\partial z} + \tau_{xy} \frac{\partial v}{\partial x} + \tau_{yy} \frac{\partial v}{\partial y} + \tau_{zy} \frac{\partial v}{\partial z} + \tau_{xz} \frac{\partial w}{\partial x} + \tau_{yz} \frac{\partial w}{\partial y} + \tau_{zz} \frac{\partial w}{\partial z} + S_i \quad (3.35)$$

Where i denotes the sum of the internal energy, therefore S_i is an energy source related to the internal energy, $S_i = S_E - \boldsymbol{u} \cdot \boldsymbol{S}_M$

3.1.4. Equation of State

Other than the conservation equations an important equation to utilise for Navier-Stokes equations is the equation of state. This equation relates the density and temperature of a fluid to the pressure and internal energy of the fluid system. For a perfect gas the equations are [47]:

$$p = \rho R T \quad (3.36)$$

Where R is the universal gas constant and C_v is the molar specific heat at constant volume.

These equations are used primarily only for compressible flows as there is no density variation for incompressible fluids. This results in only the conservation equations being utilised in this project as water is an incompressible fluid.

3.2. Turbulent Flow

Turbulent flow is the result of unsteady fluid streams, meaning that fluid fluctuates randomly in time and space and is found in flows with sufficiently high Reynolds numbers. Turbulence is generally self-sustaining and once it commences within a flow, it will continue to be turbulent without further outside influences, it will also diffuse to outer flow areas causing wider spread turbulence in an unsteady flow. Although water is irregular the maximum amount of fluctuation is around 10-30 % of the mean velocity, therefore it is possible to predict the mean velocity of a turbulent flow [50].

Within a turbulent flow there can be spatial arrangements of concentration or dispersion of flow known as eddies or vortexes. Vortexes can be a variety of shapes and sizes depending on the fluid characteristics, it is usually possible to find a vortex within another vortex or for two or more vortices to interlock. Vortices are a set of fluid trajectories along which the strain acceleration tensor is indefinite over directions of zero strain [51].

3.2.1. Turbulence Generation

There are three main groups of turbulent flow generators: grid flows, free-shear layers and wall layers [52]. The principal type of turbulence generated in a wall-attachment fluidic oscillator is wall layers in the channels and boundary layers due to the presence of the Coanda effect and the vorticial effects that are attributable to boundary layer separation. Free-shear layer turbulence is present in the fluidic oscillator where the fluid from the feedback channel intersects with the mainstream flow travelling from the inlet to the internal chamber of the oscillator.

Next to a boundary there are three different flow regimes (Figure 3-2): laminar flow, turbulent flow, and freestream flow, all of which can be modelled with RANS (Reynolds Averaged Navier Stokes) equations as discussed in the turbulent portion of this chapter.

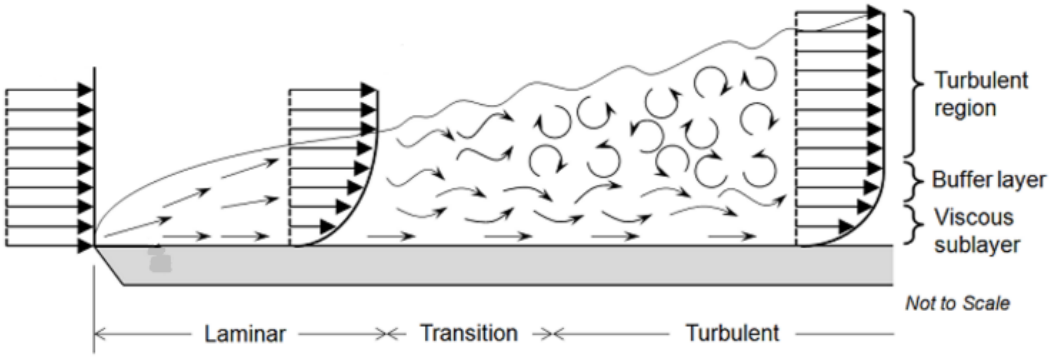

Figure 3-2: Laminar, Buffer and Turbulent Regimes on a Flat Plate [53]

The fluid closest to the wall is the viscous sublayer which is composed mainly of irrotational flow travelling in one direction along the wall or plane, this is what laminar flow is composed of. Turbulent flow and transitional flow are composed of some of the viscous sublayer and additionally the layer known as the turbulent region. The turbulent region is affected by the surface friction of the boundary layer however to a much lesser degree, allowing it some freedom of motion to create vortices and eddies of motion in addition to more complex fluid patterns or phenomena. Finally, the layer furthest from the boundary layer is the freestream flow, this area is not constrained by the boundary layer, allowing the mainstream flow to travel in a direction different to the boundary layer [53] [54].

3.2.2. Reynolds Averaged Navier-Stokes

Although turbulent fluid flow is predominantly of a randomised nature, it is still vital to applications requiring turbulent flow to be able to estimate with good understanding how the fluid will react and behave in its environment. This can be calculated by utilising mean averaged equations which can be incorporated into the traditional Navier-Stokes equations.

For this case a method called Reynolds-averaged Navier-Stokes (RANS) is employed due to the lesser complexity compared to Direct Numerical Simulation (DNS) or Large Eddy Simulation (LES) [55]. RANS is based on the theory that over time the flow field contains small, local oscillations that can be approximated in a time-averaged purpose [55].

In turbulent flows there are fluctuations in the mean properties of the flow, therefore it is necessary to add an additional term for the time fluctuating components to the average mean characteristics. However, it is necessary to first be aware of the commutative rules (3.38) that govern time averaging fluctuating properties [55]:

$$\overline{\phi'} = \overline{\psi'} = 0 \qquad \overline{\Phi} = \Phi \qquad \overline{\frac{\partial \phi}{\partial s}} = \frac{\partial \Phi}{\partial s} \qquad \overline{\int \phi \mathrm{d}s} = \int \Phi \mathrm{d}s$$
$$\overline{\phi + \psi} = \Phi + \Psi \qquad \overline{\phi\psi} = \Phi\Psi = \overline{\phi'\psi'} \qquad \overline{\phi}\Psi = \Phi\Psi \qquad \overline{\phi'}\Psi = 0 \tag{3.37}$$

Here ϕ and ψ represent general scalar variables. The rules from (3.38) can be extended to a fluctuating vector quantity $\boldsymbol{a} = \boldsymbol{A} + \boldsymbol{a}'$ and a fluctuating scalar $\phi = \Phi + \phi'$:

$$\overline{\operatorname{div} \mathbf{a}} = \operatorname{div} \boldsymbol{A} \qquad \overline{\operatorname{div}(\phi \boldsymbol{a})} = \operatorname{div}\overline{(\phi \mathbf{a})} = \operatorname{div}(\Phi \mathbf{A}) + \operatorname{div}\overline{(\phi' \mathbf{a}')}$$
$$\overline{\operatorname{div} \operatorname{grad} \phi} = \operatorname{div} \operatorname{grad} \Phi \tag{3.38}$$

For the RANS method the time varying quantities of velocity and pressure are split up into the respective averaged quantities $\overline{V}_i$, $\overline{p}$, and time fluctuating components $\boldsymbol{v}$, $\mathbf{p}$ (3.40 – 3.41) [55].

$$V_i = \overline{V}_i + v_i \qquad P_i = \overline{P}_i + p_i \tag{3.39}$$

$$\overline{V}_i = \frac{1}{\Delta t}\int_t^{t+\Delta t} V_i \, dt \qquad \overline{P}_i = \frac{1}{\Delta t}\int_t^{t+\Delta t} p_i \, dt \tag{3.40}$$

By substituting the RANS equations into the Navier-Stokes conservation equations we find the Unsteady Reynolds Averaged Navier-Stokes (URANS) equations (3.42 – 3.44) [55].

$$\frac{\partial \rho}{\partial t} + \nabla \cdot (\rho V_j) = 0 \quad (3.41)$$

$$\frac{\partial \rho V_i}{\partial t} + \frac{\partial}{\partial x_j}(\rho V_i V_j) = -\frac{\partial p}{\partial x_i} + \frac{\partial}{\partial x_j}(\tau_{ij} - \rho\overline{v_i v_j}) + S_M \quad (3.42)$$

$$\frac{\partial \rho h_{tot}}{\partial t} - \frac{\partial p}{\partial t} + \frac{\partial}{\partial x_j}(\rho V_j h_{tot}) = \frac{\partial}{\partial x_j}\left(\lambda \frac{\partial T}{\partial x_j} - \rho\overline{v_j h}\right) + \frac{\partial}{\partial x_j}\left[V_i(\tau_{ij} - \rho\overline{v_i v_j})\right] + S_E \quad (3.43)$$

In the URANS momentum conservation equation there is an additional term, the turbulence flux $\rho\overline{u_i h}$, the h being specific static enthalpy. There is an additional term of turbulent kinetic energy k for the enthalpy for turbulent flow as shown in eq. (3.45 – 3.46) [55].

$$h_{tot} = h + \frac{1}{2}U_i U_i + k \quad (3.44)$$

$$k = \frac{1}{2}\overline{u_i^2} \quad (3.45)$$

3.2.3. Menter Shear Stress Transport (SST) Model

Once the URANS equations were formed it is necessary to form a model for the Reynold stress terms, this is where a turbulence model can be used. The model used in this report is the Menter two equation shear stress transport (SST) $k-\omega$ turbulence model, which relates the turbulence viscosity μ_t , turbulence kinetic energy k and turbulent frequency ω by (3.46). The Menter model has advantages over the $k-\varepsilon$ model and $k-\omega$ models as it is able to utilise the precise measurements of the $k-\omega$ near the wall boundaries and fully $k-\varepsilon$ in the freestream. Both the $k-\varepsilon$ model and $k-\omega$ models were considered, but due to the highly complex internal geometry with a large proportion of walls with some areas of relatively large free-space it was determined that the Menter model would be the most robust [55] [53]. This would allow for good accuracy at the fine elements at the wall boundaries and feedback channels in addition to the central portion in the internal mixing chamber.

$$\mu_t = \rho \frac{k}{\omega} \quad (3.46)$$

The starting point for the SST model is the four main equations for the $k-\omega$ and $k-\varepsilon$ models. The Wilcox ($k-\omega$) transport equations shown below are in the form of the k-equation (3.47) and the ω-equation (3.48). The $k-\varepsilon$ transport equations are in the form of the k-equation (3.49) and the ω-equation (3.50) [55]. These are combined to make the Menter SST $k-\omega$ model (3.52).

$$\frac{\partial(\rho k)}{\partial t} + \frac{\partial}{\partial x_j}\left(\rho U_j k\right) = \frac{\partial}{\partial x_j}\left[\left(\mu + \frac{\mu_t}{\sigma_{k1}}\right)\frac{\partial k}{\partial x_j}\right] + P_k - \beta'\rho k\omega \quad (3.47)$$

$$\frac{\partial(\rho\omega)}{\partial t} + \frac{\partial}{\partial x_j}\left(\rho U_j \omega\right) = \frac{\partial}{\partial x_j}\left[\left(\mu + \frac{\mu_t}{\sigma_{\omega 1}}\right)\frac{\partial \omega}{\partial x_j}\right] + \alpha_1 \frac{\omega}{k} P_k - \beta_1 \rho \omega^2 \quad (3.48)$$

$$\frac{\partial(\rho k)}{\partial t} + \frac{\partial}{\partial x_j}\left(\rho U_j k\right) = \frac{\partial}{\partial x_j}\left[\left(\mu + \frac{\mu_t}{\sigma_{k2}}\right)\frac{\partial k}{\partial x_j}\right] + P_k - \beta'\rho k\omega \quad (3.49)$$

$$\begin{aligned}\frac{\partial(\rho k)}{\partial t} + \frac{\partial}{\partial x_j}\left(\rho U_j k\right) &= \frac{\partial}{\partial x_j}\left[\left(\mu + \frac{\mu_t}{\sigma_{\omega 2}}\right)\frac{\partial k}{\partial x_j}\right] + 2\rho\frac{1}{\sigma_{\omega 2}\omega}\frac{\partial k}{\partial x_j}\frac{\partial \omega}{\partial x_j} + \alpha_2 \frac{\omega}{k} P_k \\ &\quad - \beta_2 \rho \omega^2\end{aligned} \quad (3.50)$$

$$\begin{aligned}\frac{\partial(\rho\omega)}{\partial t} + \nabla\cdot(\rho\omega \boldsymbol{U}) &= \nabla\cdot\left[\left(\mu + \frac{\mu_1}{\sigma_{\omega 1}}\right)\nabla(\omega)\right] + \gamma_2\left(2\rho S_{ij}S_{ij} - \frac{2}{3}\rho\omega\frac{\partial U_i}{\partial x_j}\delta_{ij}\right) \\ &\quad - \beta_2\rho\omega^2 + 2\frac{\rho}{\sigma_{\omega 2}\omega}\frac{\partial k}{\partial x_k}\frac{\partial \omega}{\partial x_k}\end{aligned} \quad (3.51)$$

The Menter model is made up by a number of terms which in words can be shown to be (3.53):

$$\begin{array}{ccccccc}\text{Rate of change of } k \text{ or } \omega & + & \text{Transport of } k \text{ or } \omega \text{ by convection} & = & \text{Transport of } k \text{ or } \omega \text{ by turbulent diffusion} & + \text{Rate of production of } k \text{ or } \omega & - \text{Rate of dissipation of } k \text{ or } \omega \\ & & & & & & + \text{cross} - \text{diffusion term}\end{array} \quad (3.52)$$

Here P_k is the turbulence production due to viscous forces and μ_t is the turbulent viscosity. $\alpha_1, \alpha_2, \beta_1, \beta_2, \beta', \sigma_{k_1}, \sigma_{k2}$, $\sigma_{\omega 1}$ and $\sigma_{\omega 2}$ are constants whose values are described below (Table 3-1).

Table 3-1: Constants for SST k-ω Model

Constant	Value
$\boldsymbol{\sigma_k}$	1
$\boldsymbol{\sigma_{\omega 1}}$	2
$\boldsymbol{\sigma_{\omega 2}}$	1.17
$\boldsymbol{\gamma_2}$	0.44
$\boldsymbol{\beta_2}$	0.083
$\boldsymbol{\beta^*}$	0.09

3.2.3.1. Blending of $k-\varepsilon$ and $k-\omega$ equations

As the Menter transport model is composed of two different turbulence models it is vital to understand where one ends and the other finishes and to ensure that there will be no area which is not covered by the transport model. This leads to the need of a blending function to ensure a smooth transition between the two areas. For the blending function the term C_1 is used to model the $k-\omega$ model and C_2 denotes the Menter's transformed $k-\varepsilon$ model (3.54) [55]:

$$C = F_C C_1 + (1 - F_c) C_2 \quad (3.53)$$

Where F_C is a blending function, $F_C = F_C(\ell_1/y\,, Re_y)$, and ℓ is the ratio of turbulence, $\ell_1 = \sqrt{k}/\omega$ with y being the distance to the wall rather than a Cartesian direction for the Reynolds number, $Re_y = y^2\omega/v$ [55].

This blending function allows the $k-\omega$ only to be present at the wall, only Menter $k-\varepsilon$ in the far-field and a smooth transition halfway between [55].

3.2.3.2. Limitations and Limiters

As the SST equations stand there is a tendency to incorrectly predict the onset and amount of flow separation on smooth boundaries. This is due to the equations not considering the shear stress transport in this turbulent region. Therefore, it is necessary to introduce a kinematic viscosity equation as a limiter on the wall boundary layer to ensure that this can be correctly predicted (3.55) [55].

$$\mu_T = \frac{a_1 \rho k}{\max(a_1 \omega, SF_2)} \quad (3.54)$$

Where F_2 is also a blending function, similar to F_1 that limits the equation to be used only at the wall boundary layer. Here S is a measure of the strain rate, $S = \sqrt{2S_{ij}S_{ij}}$.

There is also a problem for the SST model in that there is a predisposition to generate much larger turbulence energy at and around stagnation points than there should be. A limiter on the shear production of turbulence (3.55)) can be added to the original SST equations to ensure the correct values are predicted [55].

$$P_k = \min\left(10\beta^* \rho k\omega, 2\mu_t S_{ij}.S_{ij} - \frac{2}{3}\rho k \frac{\partial U_i}{\partial x_j}\delta_{ij}\right) \quad (3.55)$$

Here P_k denotes the production term which can be found using the Boussinesq approximation (3.57) [55].

$$\tau_{ij} = -\rho\,\overline{u_i' u_j'} = \mu_t\left(\frac{\partial U_i}{\partial x_j} + \frac{\partial U_j}{\partial x_i}\right) - \frac{2}{3}\rho k \delta_{ij} \quad (3.56)$$

3.3. Meshing Method

The equations from the previous sections of this chapter deal with general systems of regular shape, however when solving these equations for a finite volume instead of a single value or small series of values it is necessary to utilise a mesh within the geometry. This involves splitting the geometry up into smaller, simpler parts and completing the equations mentioned earlier on these smaller sections.

There are a number of different ways to split up a complex shape depending on the shape and the type of testing of the shape involved. There are two main methods of splitting up complex geometries: structured curvilinear grid arrangements and unstructured grid arrangements. The most complex geometries utilise unstructured grids, where every mesh cell within the geometry is a different block and less complex shapes can use structured grids [56].

An unstructured grid could be used in this research; however, it gives less control of particular parts of the geometry. If a single block of structured curvilinear mesh is used to mesh the complex shapes in this investigation it will not be sufficiently accurate and would result in a large amount of error.

This project requires a form of the structured curvilinear grid arrangement in the form of a block-structured body-fitted grid. This means that the shape is split up into different parts or regions within which the mesh can be tailored to ensure the best grid of coverage for the fluid flow. Block-structured grids allow some parts of the overall shape to be more finely meshed than others so that the more intricate parts of the shape will have a finer mesh than those that are straightforward. It is also possible to include refined boundary layers to suit each section of the complex geometry saving the requirement to have a fine mesh throughout the whole part which would be very computationally expensive [56].

The meshing will be completed in a computer program as it is not possible to complete by hand for the complex geometry involved in this project.

3.4. Conclusion

Now that the Navier-Stokes equations have been assembled, the Menter SST model chosen and the optimum mesh method found it is possible to take the theoretical equations and adapt them to be used on a large-scale simulation. The software used in the computational fluid dynamics (CFD) modelling for this project is ANSYS ICEM for meshing and ANSYS CFX for the fluid flow calculations.

4. Internal Fluid Dynamics – Computer Simulation

Now that the equations that will be used to analyse the fluid flow have been established it is possible to begin the process of introducing the parts to computational analysis. The computer programs used to analyse the flow in the fluidic chips and at the outlet are ANSYS ICEM and ANSYS CFX [57].

The first step in the computational analysis is to obtain the computer aided design (CAD) for the nominal fluidic nozzle, the production of the CAD in this project is handled by a member of Kautex Textron CVS Ltd. Rather than have the actual nozzle in the CAD file the part that is required is the internal area where the fluid will flow, therefore it is necessary to adjust the CAD that Kautex has in their system to suit computational fluid dynamics (CFD) analysis.

Next the CAD must be meshed; this is performed using ANSYS ICEM. ANSYS software is used as it is very user friendly and this project required a swift learning process in order to produce analyses quickly and regularly from an early stage. ANSYS ICEM has a high standard of meshing capability which is needed to tailor the mesh to the complex shape of a fluidic chip.

Subsequently the mesh is inputted into ANSYS CFX-Pre to set domains and boundaries in addition to setting inlets and outlets in the mesh. The processed mesh is then inputted into the solver manager to calculate the desired fluid characteristics throughout the geometry (and over time in transitional simulations), such as the velocity vectors, pressure, vorticity and shear rates. Finally, once the results are obtained it is possible to utilise ANSYS CFX-Post to visualise the data gathered to verify whether the results are as predicted and that the nozzle is fluidic in nature.

Once the data from the stationary set up of the nozzle has been calculated it is possible to use this as the initial values for a transient simulation. This is completed by going back to ANSYS CFX-Pre and maintaining all values set up but changing the simulation type to transient, additionally informing the pre-processer the total time for the simulation to run and the sizing of the time steps and how many repeat tests were required for accuracy. This is then inputted into the solver manager and then finally the data collected is analysed using ANSYS CFX-Post.

The main reason behind utilising ANSYS CFX rather than Fluent is that it allows more flexibility when inputting a complex 3D mesh and it is very simple to incorporate monitor points into an analysis. Both of these properties of the program work well in this project, as the shape of the chip is complex and later when external flow of the fluidic chip is defined it will be necessary to know the velocity at the outlet of the nozzle throughout time and across the whole area.

4.1. ANSYS ICEM

Meshing is performed to facilitate the discretisation of a continuous volume or element into smaller volumes or elements to make it faster and more accurate to solve problems that would take much longer if solved as a whole. The two main types of discretisation of complex geometries are structured curvilinear grid arrangements and unstructured grid arrangements as discussed in the previous chapter, 3.3 Meshing Method.

In this project the block-structured body-fitted grid is used, a form of structured curvilinear arrangement, as it allows a more precise arrangement of the elements required to suit the complex geometry of the fluidic nozzle. This enables fine tuning of the mesh to ensure that all areas of the geometry have mesh tailored for optimum computation.

4.1.1. Meshing Process

The first step in the meshing process is to import the geometry into ICEM and make certain that all the dimensions and the overall shape of the nozzle water path is correct (Figure 4-1).

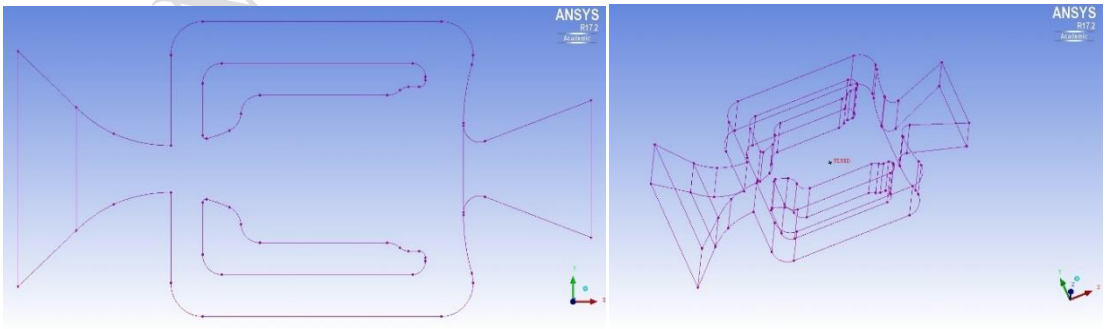

Figure 4-1: Initial Geometry

The next step is then to add additional points to the geometry along the curvature to ensure that sufficient points are applied to give a good meshing strategy and coverage. The curves that the points are on are then split by the points to give a greater amount of smaller sized curves for the mesh to follow. This allows a higher

level of precision in determining how the mesh is articulated around the bends and gaps within the geometry (Figure 4-2).

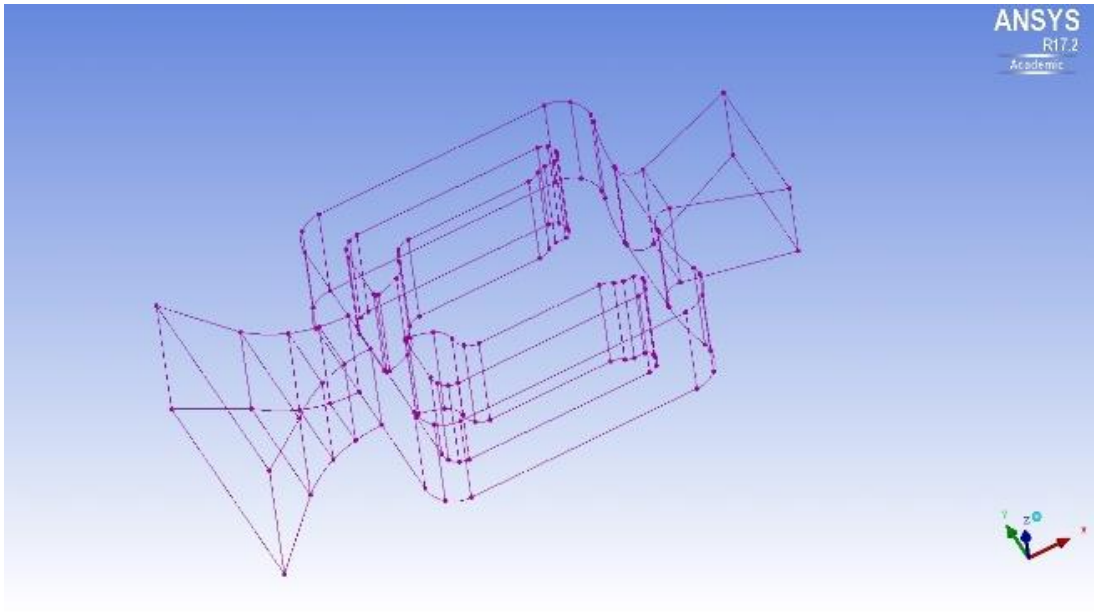

Figure 4-2: Geometry with added points and curves

Once the geometry is ready to be meshed with the added points and curves, an initial blocking is added. This initial block contains the whole of the geometry part and is the base for the mesh which needs adapting to more closely follow the outline of the complex structure (Figure 4-3).

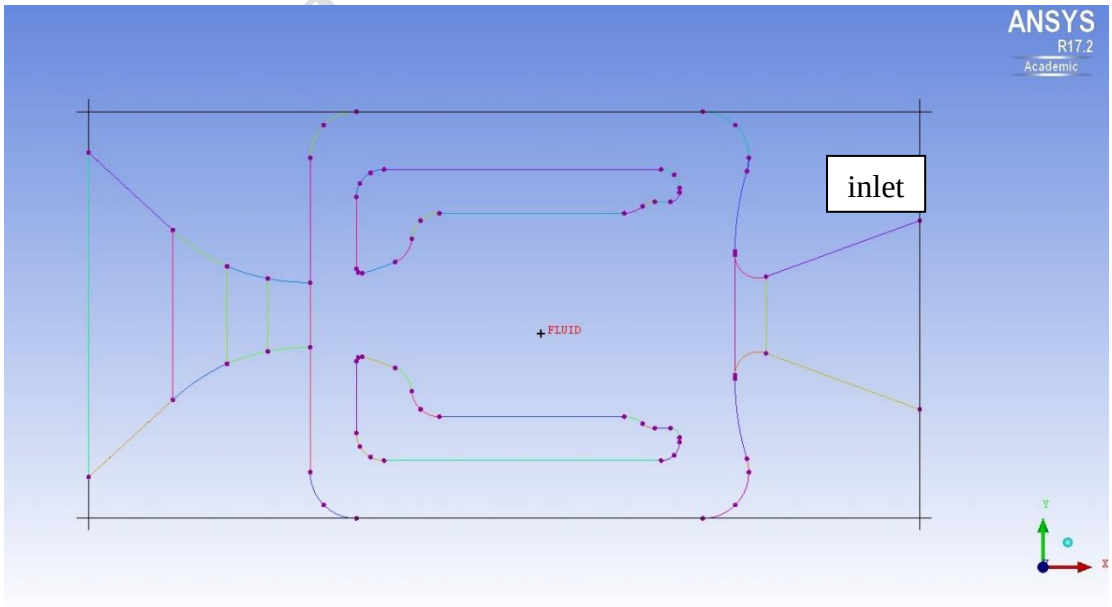

Figure 4-3: Initial Block

This block is subsequently split into several smaller blocks to allow the blocking to more closely follow the geometry of the fluidic path (Figure 4-4).

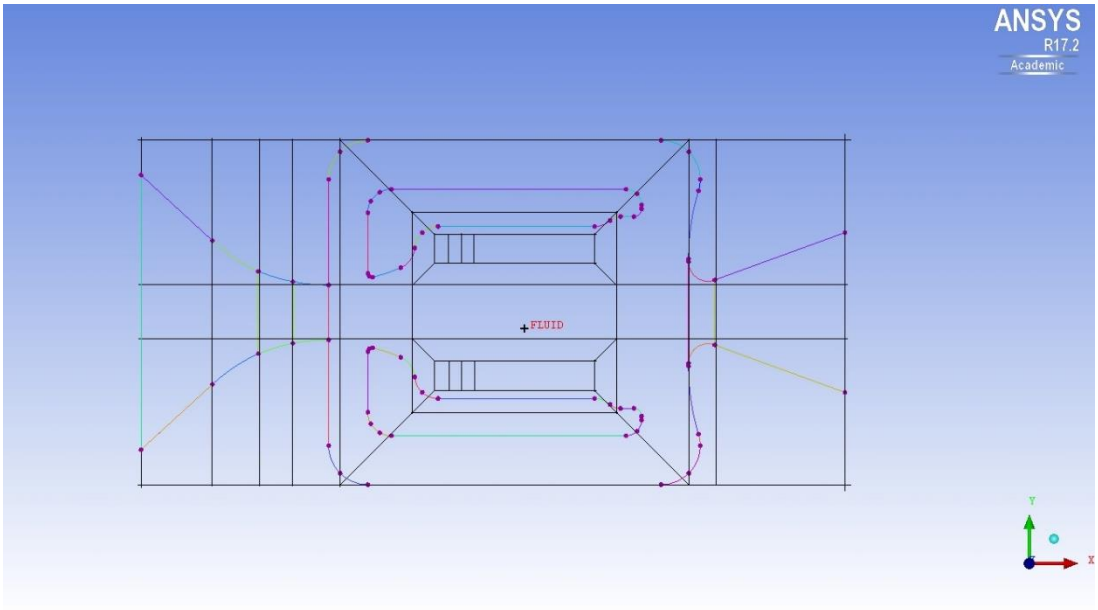

Figure 4-4: Initial Blocking Selections

Finally, the blocks that are not necessary to the geometry mesh are removed from the visual plane to allow easier manipulability of the edges and vertices of the blocks (Figure 4-5).

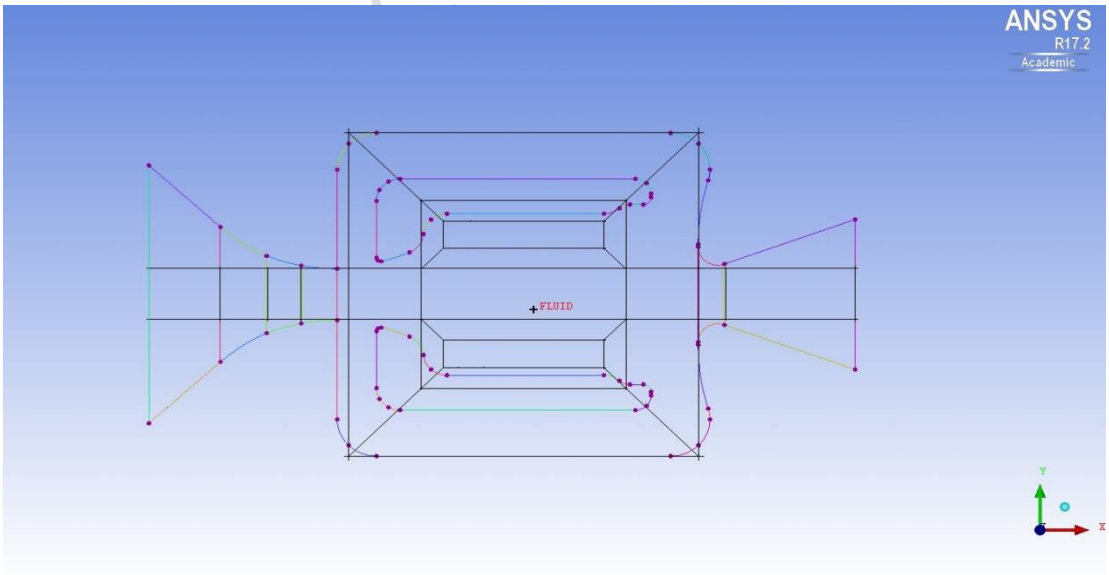

Figure 4-5: Final Blocks

The next part of the meshing process involves setting associations between all block edges to the geometry curves (Figure 4-6) and all block vertices to the points of the geometry.

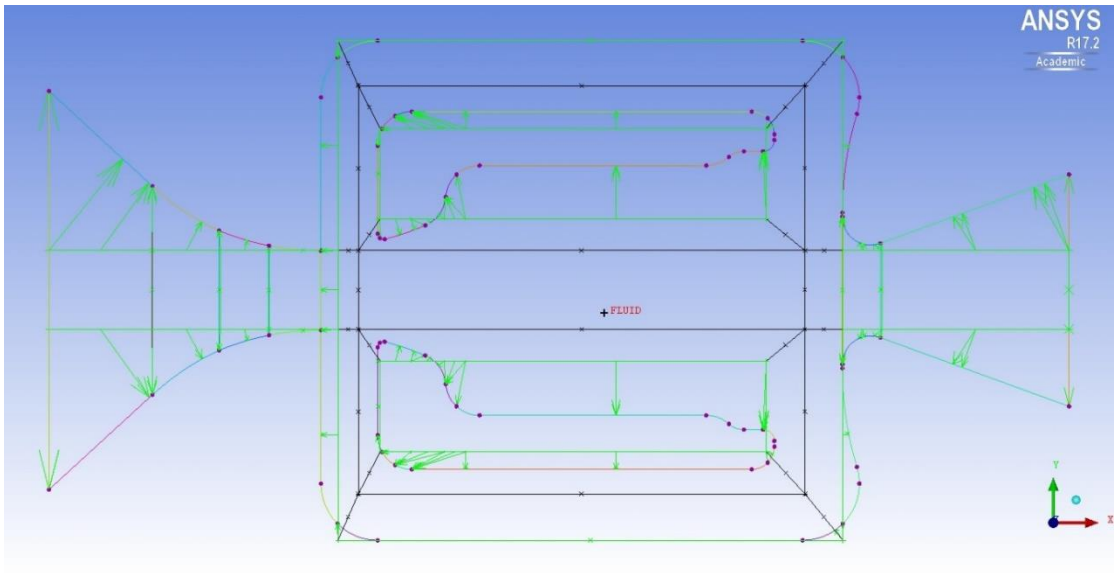

Figure 4-6: Edge and Curve Associations

An additional split is added between the two primary o-grids to aid in the curvature of the mesh in these areas during the vertex association step (Figure 4-7).

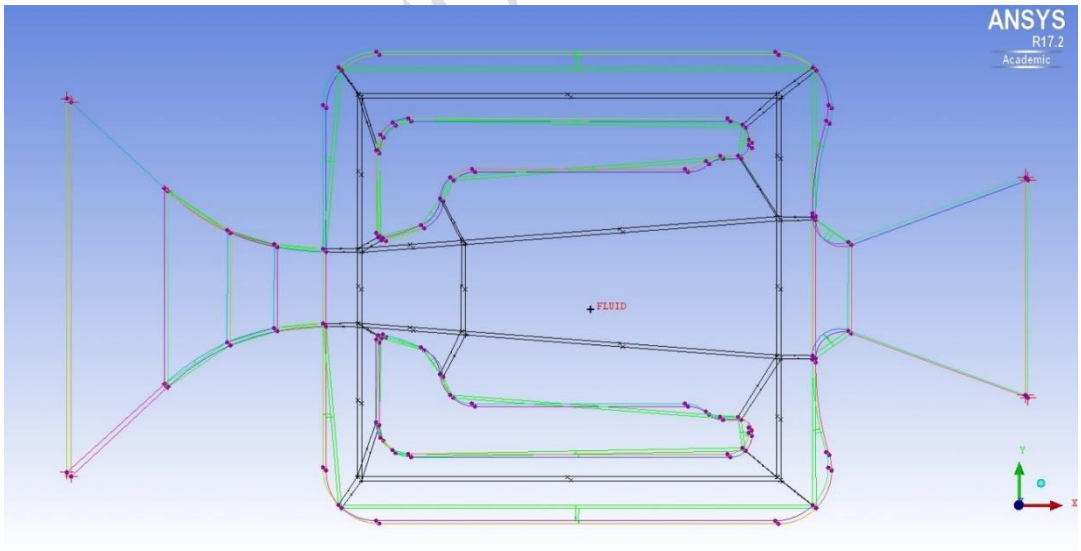

Figure 4-7: Vertex and Point Associations and Additional Split

Once the blocking is complete it is possible to alter the edge parameters for each edge to produce a fine mesh which gave relatively equal sized elements throughout the geometry (Figure 4-8). This is called the pre-mesh.

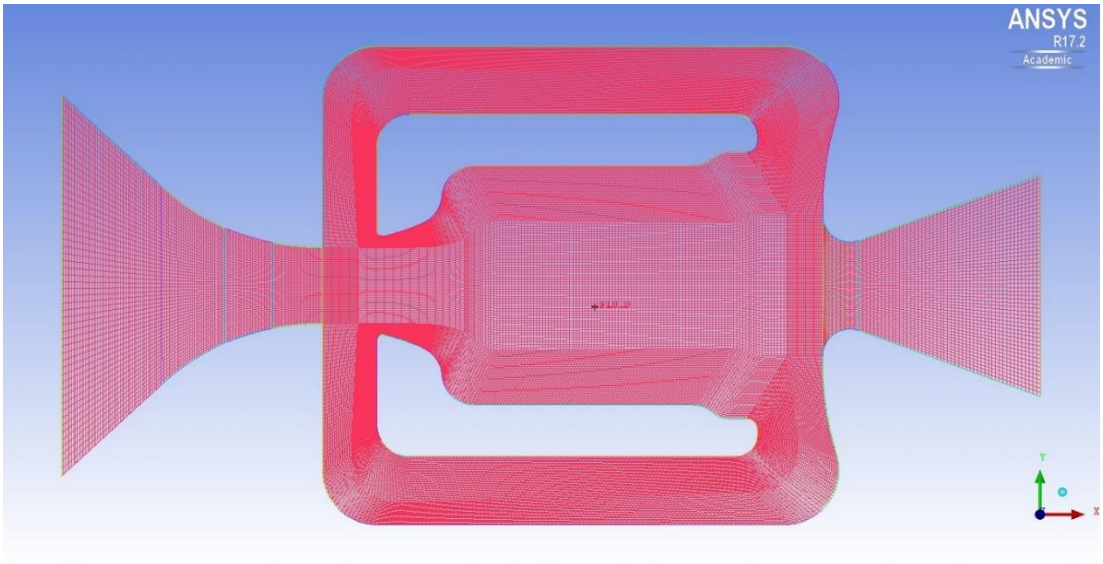

Figure 4-8: Pre-Mesh of Top Wall

Next it is important to add the boundary layers to the walls to ensure accurate calculation of the flow near the stationary walls as this is where the greatest change in velocity will be found (Figure 4-9). The boundary layers must be more refined than the main body of the geometry producing a local Reynolds number, y^+, that ensures accurate near wall results are produced. In this project it was ensured that y^+ at the wall boundaries was always lower than 2. This is a good validation as research suggests that the viscous sublayer should have a value of $y^+ < 5$ [58].

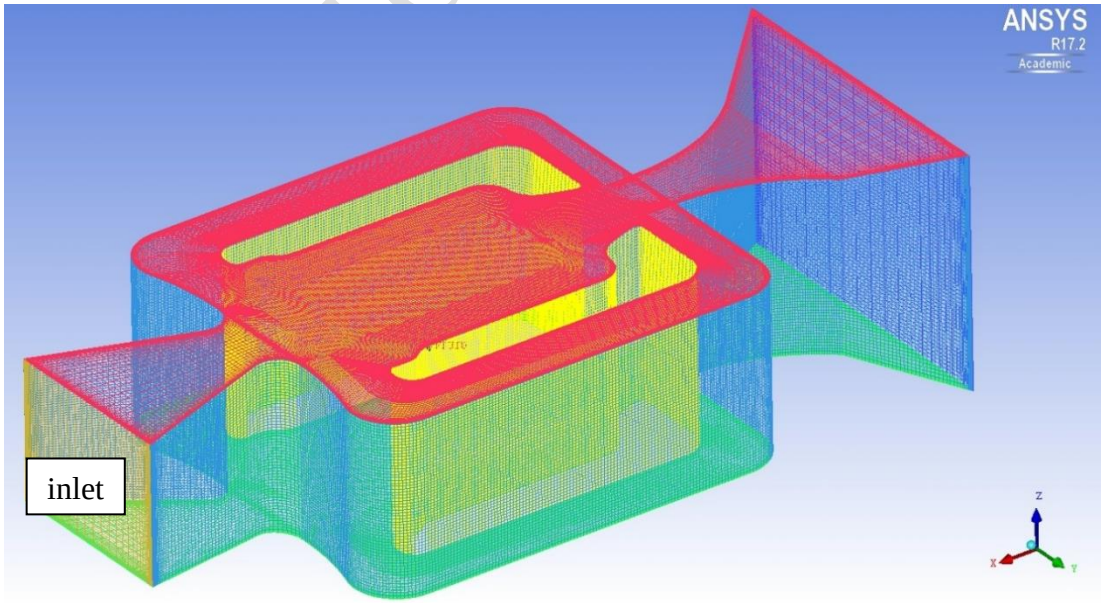

Figure 4-9: Full Mesh of Fluidic Nozzle

This pre-mesh can then be converted into an unstructured mesh, the mesh is checked for any errors and then an output mesh file is created ready to be used in ANSYS CFX-Pre [59].

4.1.2. Mesh Quality

The validity of the mesh was determined by using the ANSYS ICEM inbuilt quality function checker, in addition to a mesh convergence study. The main quality functions in the software used were the cell aspect ratio, the skewness, and the orthogonality.

4.1.2.1. Cell Quality

The cell aspect ratio is the ratio of the longest edge to the shortest edge, the ideal value for the cell aspect ratio is one. In all meshes created it was ensured this was kept to within the limits of 0.95 to 1.05 in the main body of the mesh, the boundary layer was not kept to this constraint as this is expected to have a much higher cell aspect ratio due to the thin layers at the boundary [60].

The skewness of the cells describes how much a cell is diverted from a “perfect” equilaterally shaped cell. The skewness is a value between 0 and 1, where the lower the value of this is the higher the quality [60] [61]. The skewness for the meshes used in this project were all below the value of 0.1.

The orthogonality of a mesh element or cell concerns the angles of the cell between adjacent faces, and how this relates to the ideal angle for the cell topology. This value scales from 0 to 1 where 1 is the ideal end of the scale [60]. Mesh variations were ensured to have an orthogonality of no smaller than 0.85. This value would be higher if the geometry did not comprise of a great number of curved faces.

4.1.2.2. Mesh Convergence

To improve the efficiency and accuracy of the CFD tests, a mesh resolution convergence study was conducted. By performing a mesh converge study it confirmed that a sufficient degree of accuracy could be achieved, and the computational time expense justified for each given design concept.

A series of 5 different meshes were created with different average sized cells, these resulted in the fluidic nozzle geometry being comprised of between 500,000 to 20,000,000 elements. This upper element bound was chosen to balance the accuracy of the test and the time that would be taken for the CFD software to run the solver analysis.

In the convergence analysis three main variables were studied to determine the characteristics and performance of each of the meshes, each at 3 different total pressure values set at the inlet. The values chosen were the velocity, pressure, and oscillation rate. Within these values the maximum, minimum and average pressure and velocity were studied in addition to the variation of the oscillation rate over a 0.01 second time period.

The mesh with 20,000,000 elements did converge to an extent however did not fully converge, however the solver did converge to an extent. The mesh test with this quantity of elements each took approximately 4 days to complete, a study with a greater number of elements was not feasible in this project due to insufficient computing power and time available to complete each of the design concept tests.

Utilising the mesh comprising of 20,000,000 as the standard for each of these variables at the different pressures, the error in each of the meshes was studied and the time taken for each recorded. By balancing these priorities, a mesh sizing of approximately 6,000,000 elements was chosen, this sizing would take approximately 18 hours to complete a 0.015 second analysis with timestep sizing of 0.0001 seconds. Each of the results from the 6,000,000 returned the same results as the 20,000,000 tests within 95%. This was sufficiently accurate and time saving as possible for these cases in this project.

4.2. ANSYS CFX-Pre

4.2.1. Boundary Conditions

From the experimental analysis, it has been possible to find the average volumetric flow rate for each of the nozzles at the pressure of 2.5 Bar. From this value and the dimensions of the nozzles the average velocity at a cross section of the nozzle can be calculated, by dividing the volumetric flow rate, Q, by the cross-sectional area, A (4.1).

The cross-sectional area in addition to the wetted perimeter (WP) and kinematic viscosity of water, ν, can be used in calculating the Reynolds number within the geometry by taking the assumption that the chip can be modelled as several oblong pipes with changing hydraulic radius, R [62] [63]. The hydraulic radius is calculated using the formulas (4.8) – (4.0), where b is the lateral distance between the walls of the chip, H is the height of the chip.

These calculations require the assumption that the flow within the chip is uniform and unidirectional, which is not the case, however it will give a guide which can then be developed with further analysis of the system. The sections that the Reynolds number is calculated for are at the inlet and outlet portions as these areas would experience the more homogeneous flow characteristics.

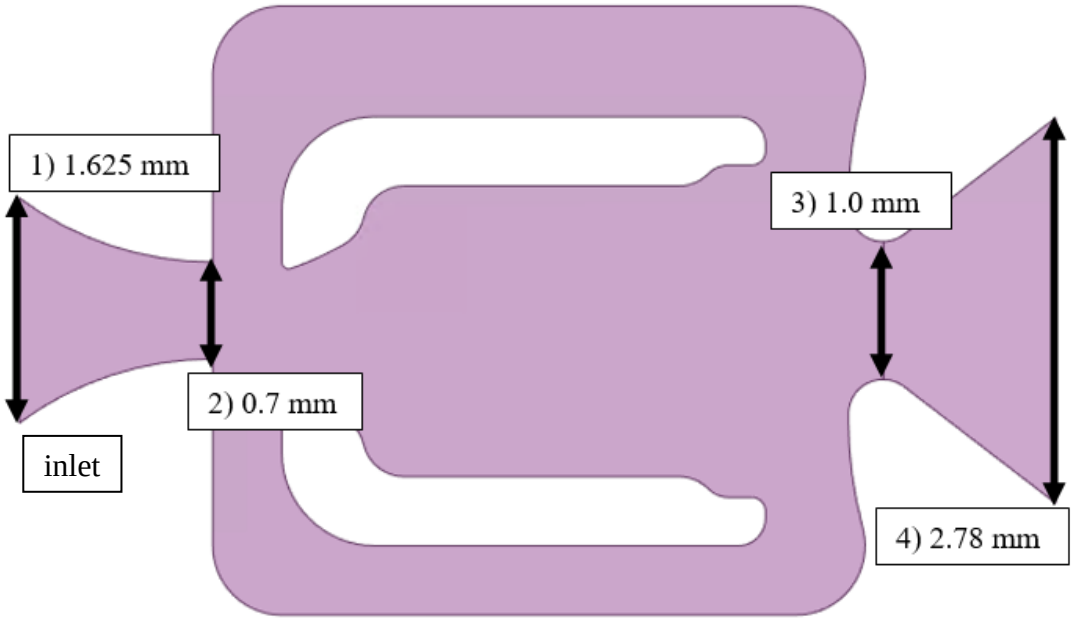

Figure 4-10: Areas of the fluidic chip where lateral width was captioned to find Reynolds

$$v = Q/A \quad (4.1)$$

$$\mathrm{Re} = \frac{v(4R)}{\nu} \quad (4.2)$$

$$R = \frac{A}{WP} \quad (4.8)$$

$$\mathrm{WP} = 2b + 2H \quad (4.9)$$

$$A = bH \quad (4.10)$$

The height of the fluidic chip for all areas but section 4 was 1.566mm, the final section being 1.631mm. Utilising this and the knowledge that the kinematic viscosity of water at 25°C is 0.8927 mm^2/s it is possible to calculate the Reynolds number for each area and determine whether the fluid flow is laminar, transitional or turbulent [63].

An experimental test was conducted to find a volumetric flow rate of 20.2 ml/s or 2.02e-5 m^3/s. As this is a geometry of constant volume and water can be considered to be incompressible it is possible to assume that the volumetric flow rate would be approximately the same at all of the cross-sections examined.

Table 4-1: Reynolds number and regime analysis for fluidic chip sections

Section of nozzle	b (mm)	H (mm)	A (mm^2)	WP (mm)	R (mm)	v (m/s)	Re	Regime
1	1.625	1.566	2.545	6.382	0.399	7.937	3548	transitional
2	0.700	1.566	1.096	4.532	0.242	18.431	4996	turbulent
3	1.000	1.566	1.566	5.132	0.305	12.899	4407	turbulent
4	2.780	1.631	4.534	8.822	0.514	4.455	2565	transitional

The data from Table 4-1 shows that the fluid within the nozzle is on the border between turbulent and transitional. Behaving transitionally at the outlet and inlet planes of the chip and fully turbulent in the more central portion of the nozzle. This means that when utilising the ANSYS CFD program, transitional turbulence must be allowed in the turbulence model.

4.2.2. Pre-Processer

The program utilised in setting the boundaries and the equation sets used for pre-processing in this project is ANSYS CFX-Pre [59].

The domain for the simulation type is set to be fluid, more specifically water at 25°C at a pressure of 1atm. The turbulence model used is fully turbulent SST (shear stress transport) with an automatic wall function, the same model as used in the theoretical analysis.

The inlet velocity is required to find whether the flow inside the nozzle is laminar, transitional or fully turbulent. These values are then inputted as the boundary data for the inlet and outlet of the fluidic nozzle, with all other boundaries set as walls (Figure 4-11).

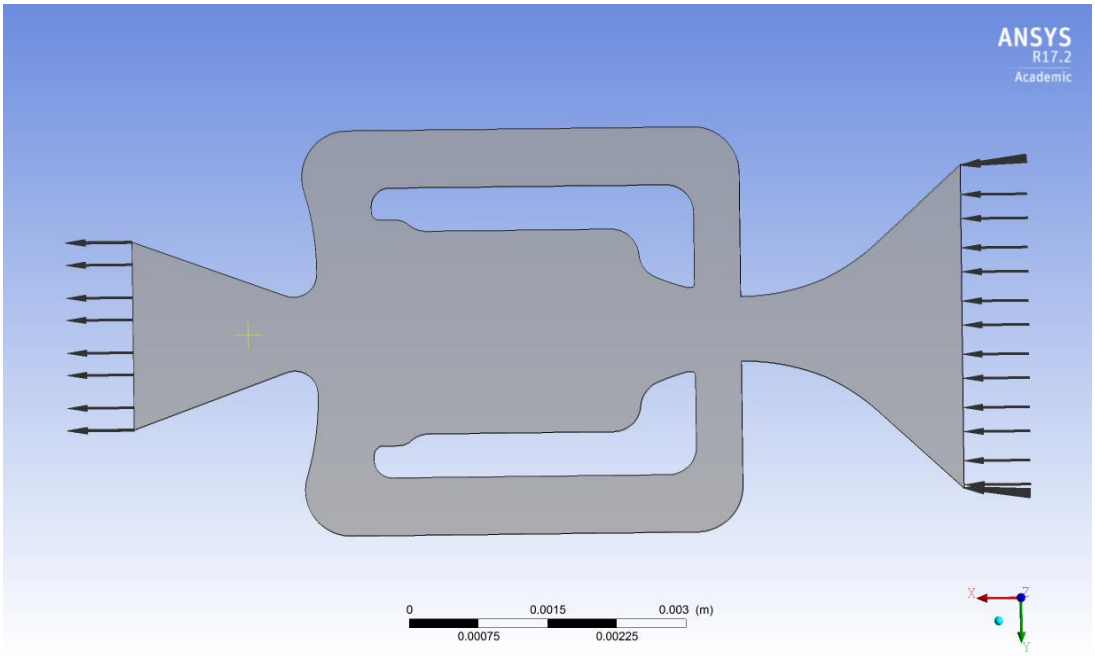

Figure 4-11: Boundary Vectors in ANSYS CFX-Pre

4.2.3. Solver

For both the steady state and the transient simulations, ANSYS CFX-Pre is used to set the parameters of the solver.

4.2.3.1. Steady-State

Although the flow inside the domain is unsteady and turbulent, a steady state solver was used initially. The reason for this was to establish the internal values of the fluidic chip in a single time step point with good accuracy before running the transient case. This meant that it was possible to see a more developed flow in the transient analysis sooner than if the domain was set to be stationary water at the start of transient analysis.

For the steady state solver, the parameters that need to be set in ANSYS CFX-Pre are that the advection scheme is at high resolution, and that there is first order turbulence numerics. The convergence control used has maximum iterations set at 50 loops with an RMS residual at 1.E-4, other finer residual values were evaluated, and it was determined that this would provide accuracy within 98%. The results outputted from the solver are the standard for ANSYS CFX and a backup of results is applied after every 10 loops of convergence, replacing older files to ensure that the computational expense is kept to a minimum and ensuring minimal data losses if errors occur.

4.2.3.2. Transient

The transient analysis requires a time step definition to run, for this simulation a choice of 15ms is chosen for the overall simulation time with time step sizing of

0.1ms. Simulations were conducted with timesteps of much smaller size up to 0.001ms, however this was very computationally expensive, and the results produced in relation to the flow rate, velocity and oscillatory rate had minimal error when utilising this timestep value. This timestep size allows the fluid within the nozzle to oscillate a sufficient number of times to prove oscillation, with a smooth flow pattern to prove no jumping of time steps or oscillations.

The Courant number throughout the solver process was monitored throughout the testing of the transient solution and averaged at around 25. The ideal case is for the Courant number to be as low as possible, in this project it was ensured that the Courant number was always below the value of 30 [64].

Similar to the steady state analysis, a high-resolution advection scheme is used with first order turbulence numerics and the same convergence criteria. Due to the high processing power required for the simulation a second order backward Euler scheme is used with a maximum loop coefficient of 10. The results outputted from the solver are the standard for ANSYS CFX and a backup of results is applied after every 10 loops of convergence, replacing older files to ensure that the computational expense is kept to a minimum and all data kept safe from error losses. A point monitor is added to the centre of the outlet of the nozzle to measure the vector velocity to analyse the change in flow angle at the outlet.

4.3. ANSYS CFX-Post

The post-processing for this project is completed in ANSYS CFX-Post. Two main options are used for post processing the nozzle water path – streamlines and planes. A series of streamlines are used, starting at the inlet of the nozzle to analyse the flow path of individual water particles whereas the plane is used to demonstrate the flow within the nozzle as a whole domain.

4.3.1. Streamline Results

Streamlines are used to show the flow path of an individual particle throughout a geometry at a particular moment of time. For this project a series of 50 individual streamlines originating from the inlet of the nozzle are utilised to show the different flow paths through the geometry (Figure 4-12).

From the image of the streamlines it is possible to see that the Nissan nozzle is in fact a fluidic oscillatory nozzle. This is demonstrated by the majority of the streamlines dominating a slightly arced trajectory towards the outlet with other streamlines

tending to flow through the feedback channels prior to the exit. It can also be established that a vortex forms between the main curvature of the flow path and one side of the internal chamber of flow.

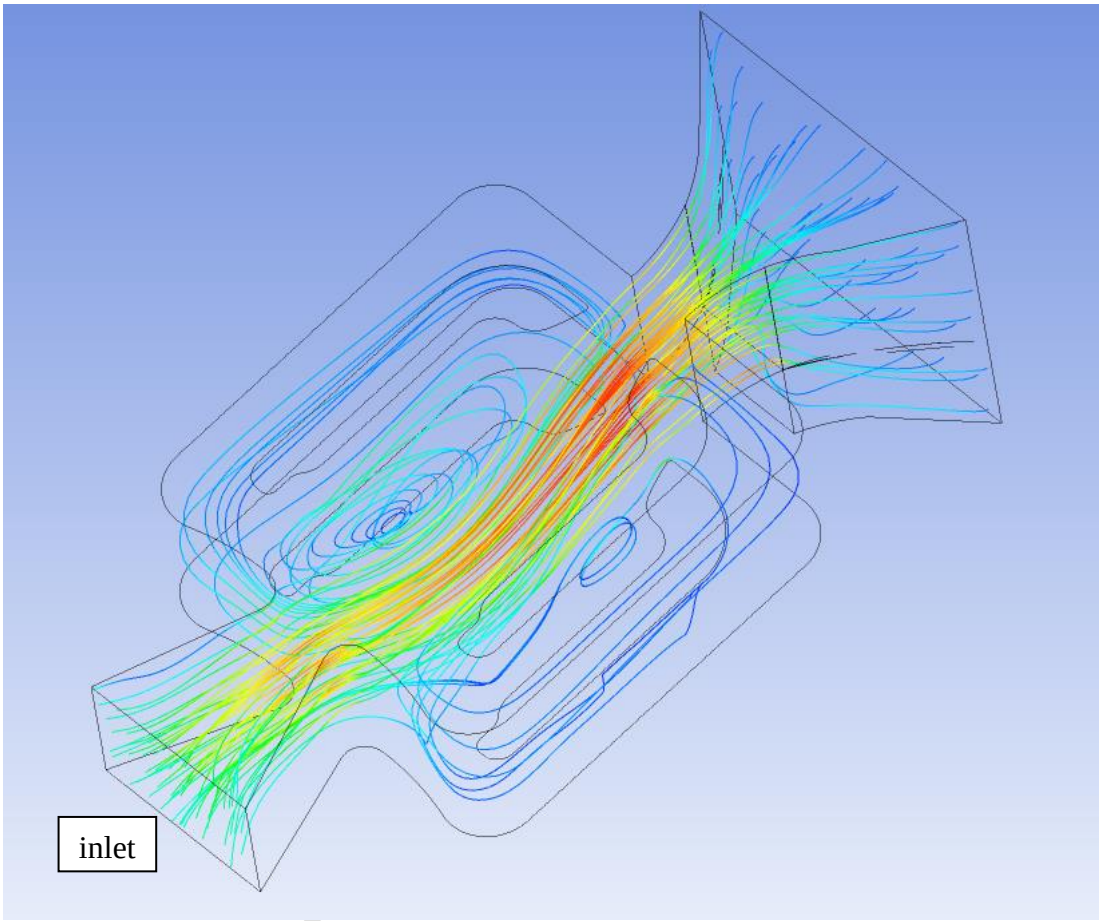

Figure 4-12: Streamlines within the Nissan Nozzle

4.3.2. Velocity Plane Results

A coloured x-y plane within the geometry is added to analyse the velocity patterns within the nozzle geometry at particular time steps. The coloured distribution is set over the global velocity data values to keep the data visualisation as accurate as possible. A series of time steps are used to show how the flow pattern within the Nissan nozzle develops from a straight stream through the internal chamber to that of a flow deflected by a minimal amount of turbulence to finally an oscillatory flow.

In this test the time period for one full oscillation was 57 milliseconds, this is the time taken for the flow at the outlet to transition from one boundary of the outlet wall to the other and then back again. This time period, T_o, was calculated over five different later portions of the animation images to ensure accuracy. The time period was determined by analysing the point when the velocity magnitude in the x-

direction changed from positive to negative and vice versa for the halfway point. The plane results are taken at a later point in the testing to ensure that the fluid flow is fully developed (Figure 4-13).

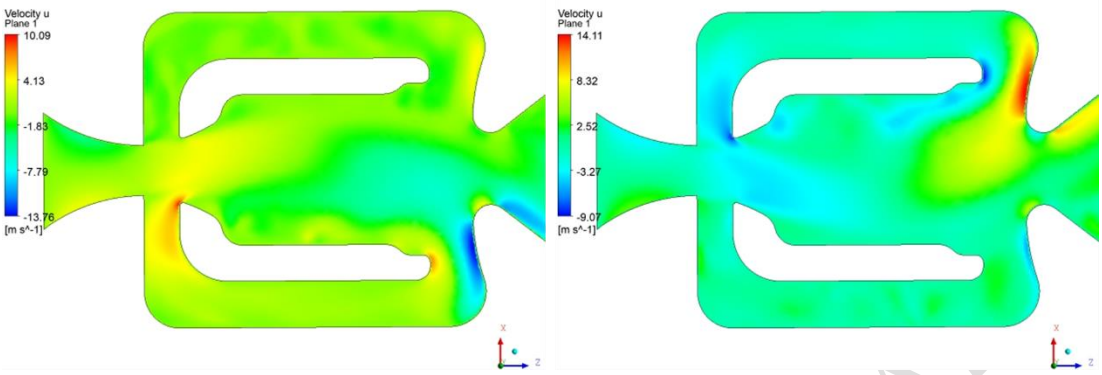

Figure 4-13: Velocity in the x-axis within the fluidic chip at T_o =0 and T_o=0.5

Figure 4-14 shows the first timestep in the oscillatory motion period for the Nissan customer fluidic chip. At this point the mainstream of velocity is exiting the outlet of the nozzle at the lowest x-direction experienced in the oscillation. Here the magnitude of the velocity has the highest negative x-component value, this is the bounding area for the spray angle when the jet is sprayed into the atmosphere.

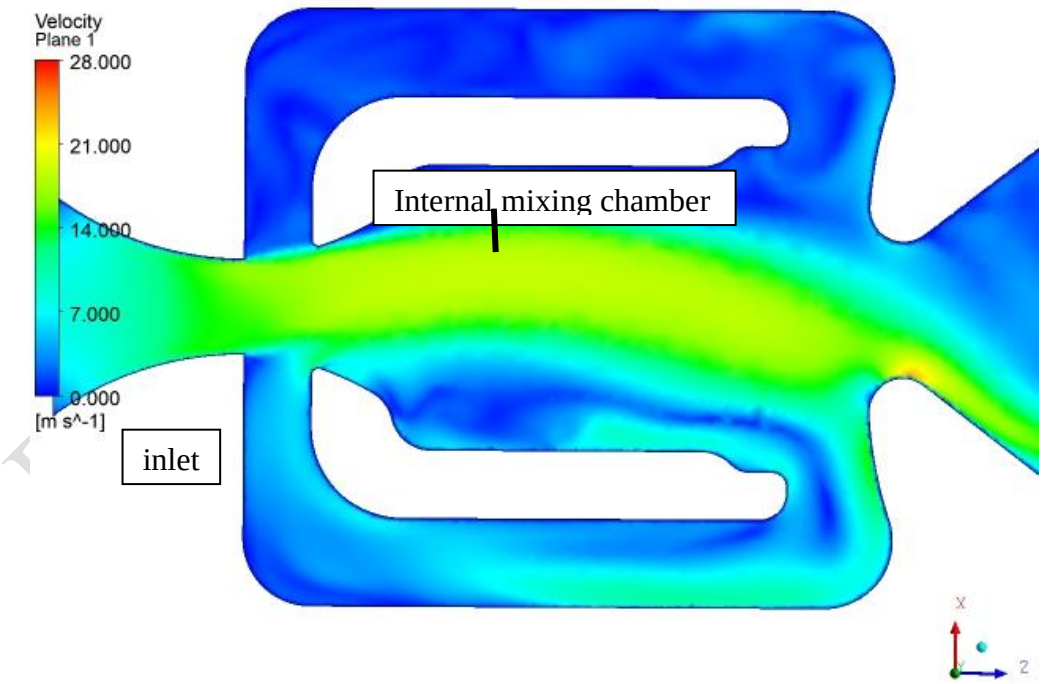

Figure 4-14: Velocity flow path aT_o = 0 t for Nissan fluidic chip

The fluid is travelling over a high portion of the internal mixing chamber in the x-direction with a defined curvature in the flow of the water, initially travelling

attached to the upper wall of the mixing chamber. It is possible to see that the some of the water is returning toward the inlet of the nozzle via the lower feedback channel as there is a defined increase in velocity in this area in comparison to the upper channel.

At $T_o = 0..1$ (Figure 4-15) it is possible to see that where the upper curvature of the main flow has reached the upper portion of the internal mixing chamber where in the previous step this was more centralised. This timestep still experiences a high magnitude in the negative x-direction, however the spray is becoming more widespread as it moves away from the outlet wall. In addition to this it is possible to see that the increased velocity in the feedback channel is spreading closer towards the inlet area to meet back with the main flow.

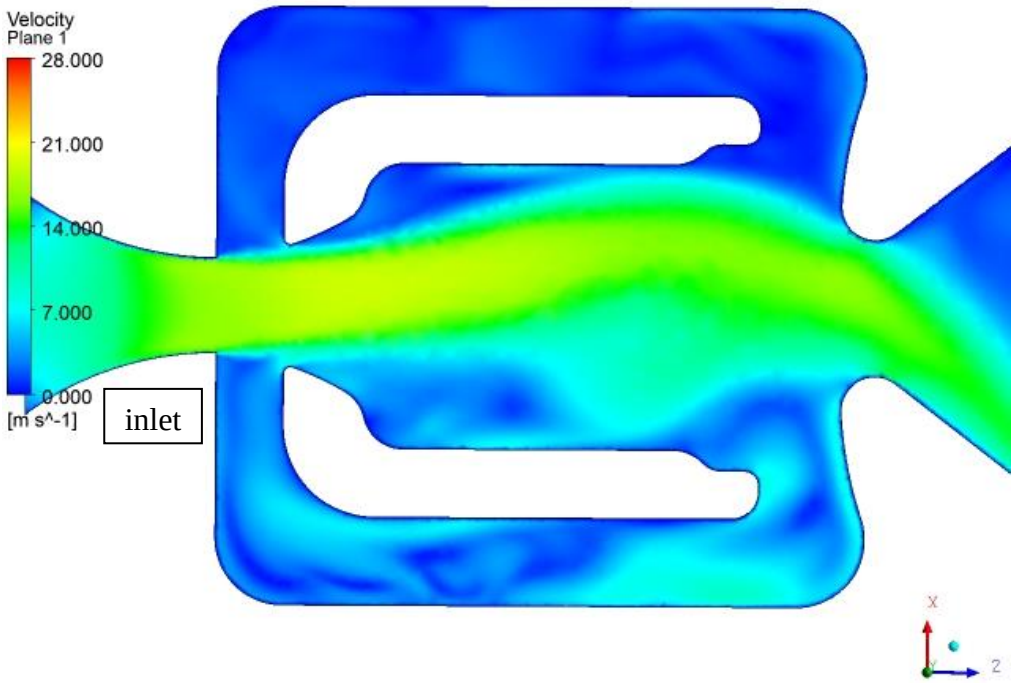

Figure 4-15: Velocity flow path at $T_o = 0.1$ for Nissan fluidic chip

At $T_o = 02$ (Figure 4-16), the bend in the mainstream has changed, now instead of being a full curvature throughout, the initial portion of the mainstream velocity in the mixing chamber is relatively straight. This signalises that a switch in the direction of the flow leading towards the outlet will come in the next phases. There is still a negative x-direction velocity magnitude at the outlet however the main flow of velocity is no longer attached to the wall.

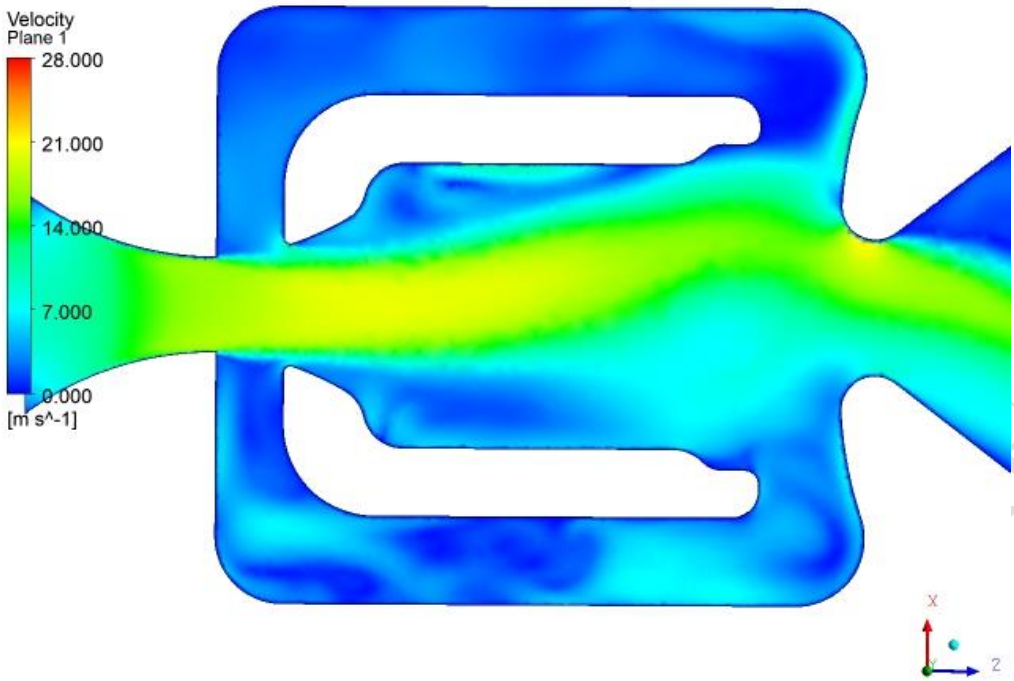

Figure 4-16: Velocity flow path at $T_o = 0.2$ for Nissan fluidic chip

There has been a small change in the velocity distribution within the feedback channels. Where before there was only increased velocity in the lower feedback channel, there is a very small portion of higher velocity water spreading around the corner of the upper feedback channel.

Figure 4-17 shows the velocity plane at $T_o = 0.3$, here the curvature of the main flow in the mixing chamber is starting to change and spread more towards the lower portion in the early section. There remains a small x-directional peak however this has moved closer towards the outlet of the fluidic chip. This has created a velocity profile in the outlet portion which is at a higher position than the previous timesteps.

There is very little increase in velocity in the lower feedback channel, instead the fluid in the upper channel is beginning to develop and spread further back towards the inlet from this portion. This is because the curvature of the mainstream flow is travelling over the curved portion of the outlet channel, allowing some of the water to flow in the direction of the channel.

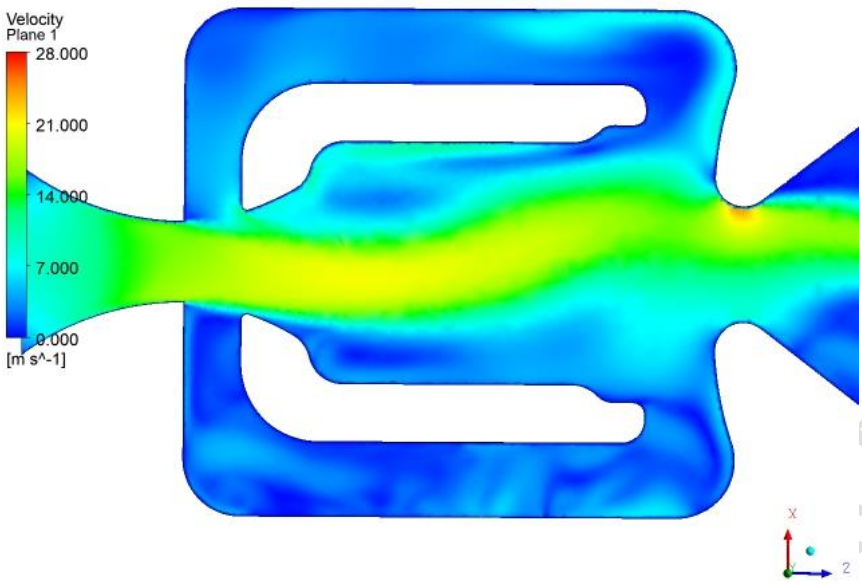

Figure 4-17: Velocity flow path at $T_o = 0.3$ for Nissan fluidic chip

The velocity distribution within the chip at $T_o = 0.4$ (Figure 4-18) is very similar to the previous step, however the details previously found are becoming more noticeable. The downward peak of travel in the mixing chamber is more pronounced and the upper one less obvious. The flow at the outlet has moved further upwards and there is more increase in velocity throughout the upper feedback channel. the internal chamber.

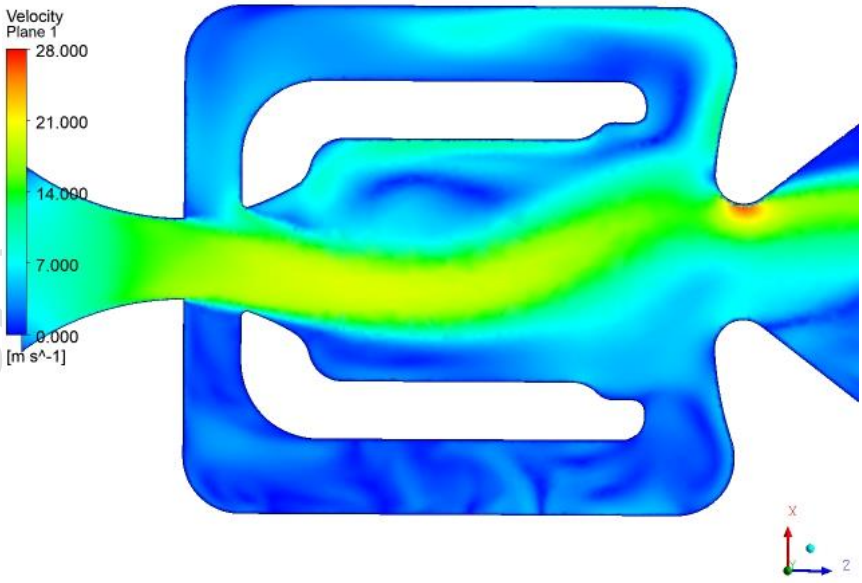

Figure 4-18: Velocity flow path at $T_o = 0.4$ for Nissan fluidic chip

At time step $T_o = 0.5$, (Figure 4-19) the simulation is very similar to the fluid flow at time step 75 except reversed. In this image, it is possible to see that the main flow of

the velocity has a central downwasrds peak in the internal mixing chamber after following the direction of the lower wall of the chamber. The velocity at the outlet is now fully positive in the x-direction, forming the boundary for the spray angle. There is a noticeable increase in the amount of higher velocity flow in the upper feedback channel.

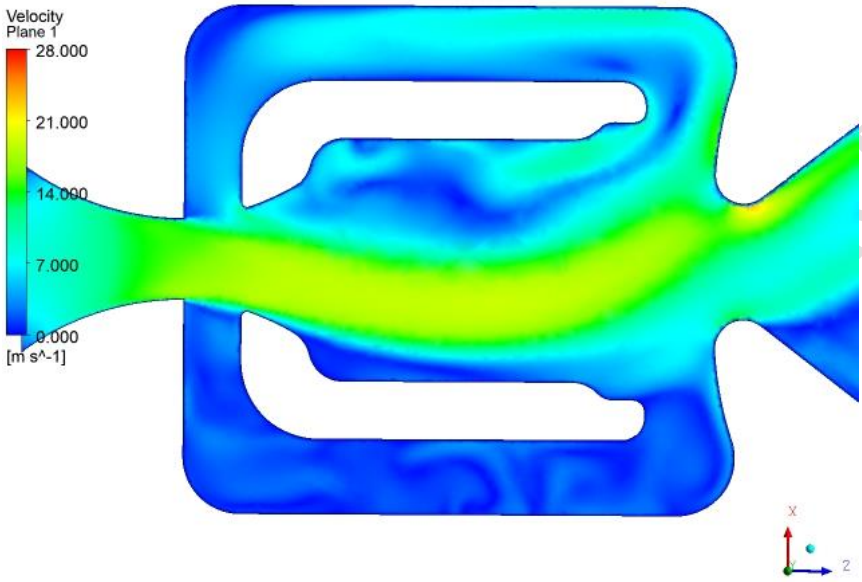

Figure 4-19: Velocity flow path at 9.5 ms for Nissan fluidic chip

The cycle repeats the same as stated in the previous steps but with reversed x-direction as the outlet velocity starts to move back into the peak lowest x-direction.

By completing this visual simulation, it is now possible to view how the fluid flows through the fluidic nozzle for a chip with these dimensions and of this size. The cycle of velocity through the chip has been established as:

1. Fluid enters fluidic chip at the inlet
2. Fluid crosses open area through feedback-channels towards internal mixing chamber
3. Coanda effect attracts the flow to one of the interior chamber walls causing deflection
4. Fluid is deflected against internal chamber wall giving reversed y-direction velocity component
5. Some fluid:
    a. Leaves through the outlet into the atmosphere
    b. Is directed into the feedback channels.

i. This then flows towards the inlet and meets the mainstream of flow.
ii. The addition of the two flows results in a velocity change towards the opposite of the initial Coanda deflection
iii. Repeat step 3-5 until no fluid into inlet

4.3.3. Pressure, Velocity and vorticity Plot

A coloured x-y plane is created within the oscillator to analyse the velocity and pressure variations at several time steps. Three different setups are used in CFX-Post view the fluid properties, these include: a pressure plane analysis, a combined pressure plane and velocity vector plot analysis and a vorticity or vector curl analysis. This permits visualisation of both the individual properties in addition to viewing the interaction.

As in the velocity plane results, the plots shown are from the first half of the time period. This shows how the pressure vortices develop and translate through the internal chamber of the oscillator, influencing the velocity of the fluid. These vortices are the cause of the oscillatory output of the nozzle and are an essential feature of the nozzle.

At the first time step (Figure 4-20) it is possible to see in the velocity plot (c) that the main flow of fluid is tending towards the upper surface of the internal chamber. The pressure plot (b) shows that there is a decrease in pressure in a large circular area near the opposite wall at the end of the internal chamber. There is also a much smaller developing pressure decrease at the upper wall near the inlet to the internal. By looking at the combined velocity and pressure plot (a), it is shown that the pressure decrease coincides with a flow of water that concentrates at the centre of each of the low-pressure zones or vortices.

In the images below (Figure 4-21 - Figure 4-24) it is possible to see that the smaller vortex is stationary at the top wall near the inlet to the internal chamber. The vortex is developing in size, the pressure at the centre of the vortex decreasing and a greater velocity of fluid circulating it. Due to the increased amount of fluid in this area, the main fluid flow is forced to detour around the vortex, causing a shift in the main flow stream to a more central position. The vortex at the lower wall has translated to a position further down the internal chamber, this is causing the jet to deflect to the upper surface of the oscillator after flowing into the central area.

The next part of the fluidic oscillatory cycle is when the main fluid flow stream is deflected towards the other side of the internal chamber wall (Figure 4-23 - Figure 4-25). The pressure distribution diagrams (b) show that the depression moves along the length of the chamber, growing in size. This coincides with the increased velocity around the edges of the vortex (c) causing the fluid flow to deflect further towards the lower wall.

As the vortex reaches the boundary of the feedback channel the pressure begins to diffuse and amalgamate with the surrounding areas. The reason for this is that the fluid flow surrounding the vortex now has been deflected so far that it becomes directed into the feedback channel, balancing the pressure vortex to a pressure similar to the rest of the oscillator.

The main fluid flow in the internal chamber is currently being directed towards the lower internal chamber wall, following the curve of the inlet due to the Coanda effect. However, there is flow separation occurring near the top of the wall as the fluid can't exactly follow the line of the wall, this causes a decrease in pressure where the pressure is not flowing. This decrease in pressure is shown by the darker aspect of the small area near the bottom wall of the internal chamber near the inlet (Figure 4-25). This is the start of the cycle flipping to the opposite side.

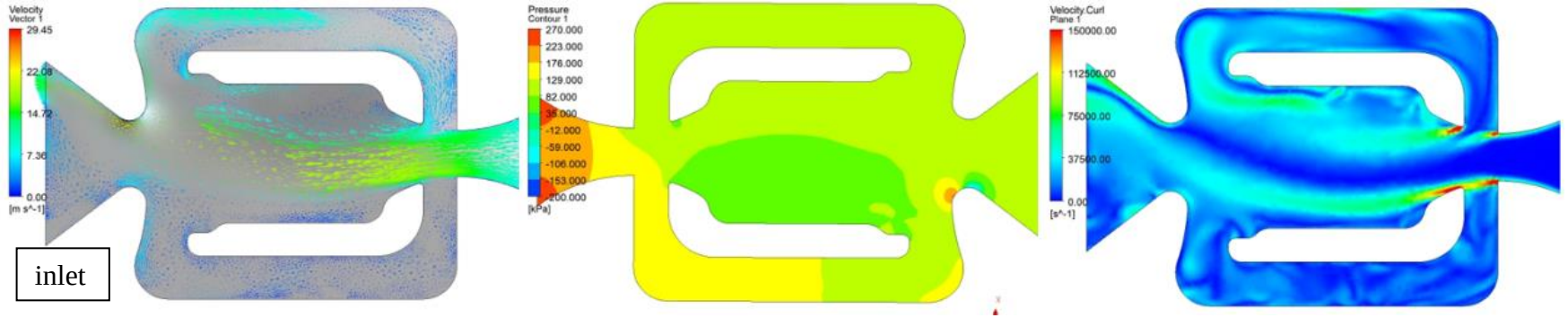

Figure 4-20: Velocity vector and pressure contour plot (left), pressure plot (centre) and vorticity plot (right) at $T_o = 0$

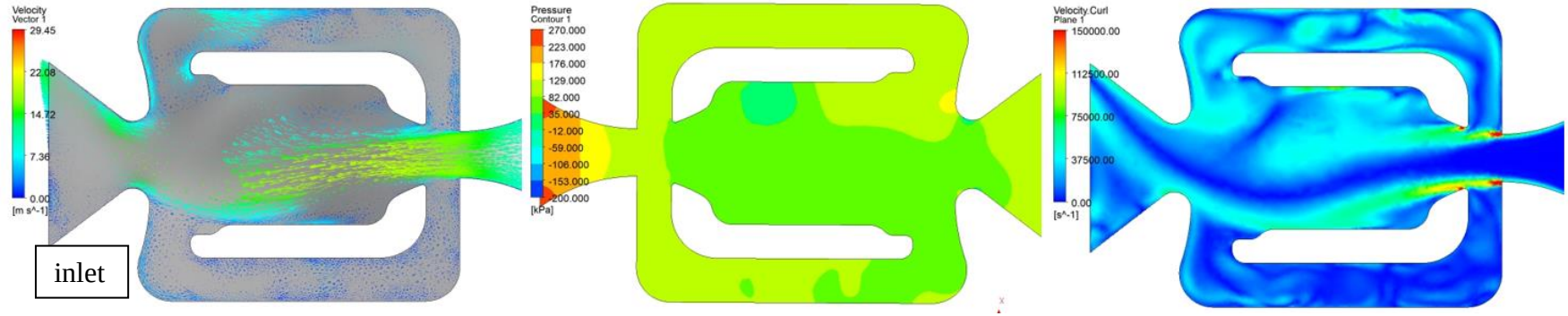

Figure 4-21: Velocity vector and pressure contour plot (left), pressure plot (centre) and vorticity plot (right) at $T_o = 0.1$

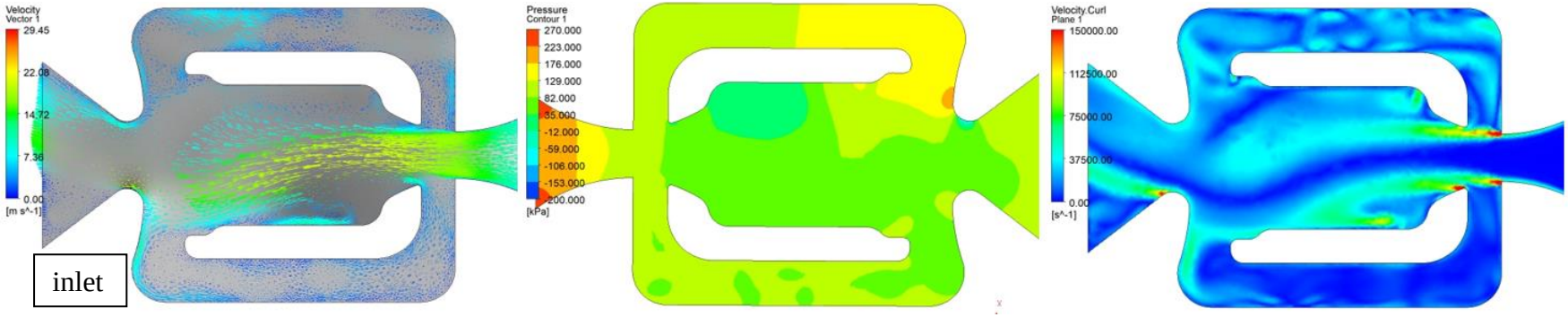

Figure 4-22: Velocity vector and pressure contour plot (left), pressure plot (centre) and vorticity plot (right) at $T_o = 0.2$

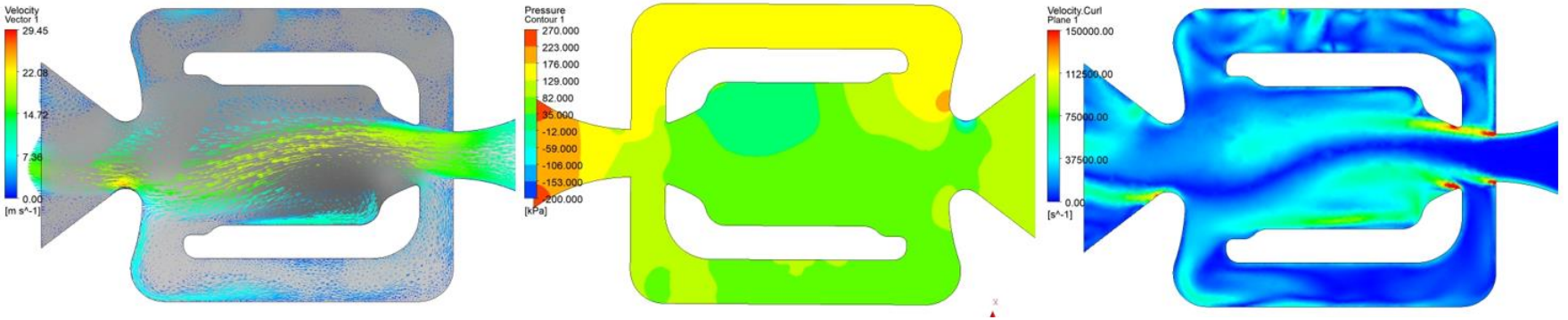

Figure 4-23: Velocity vector and pressure contour plot (left), pressure plot (centre) and vorticity plot (right) at $T_o = 0.3$

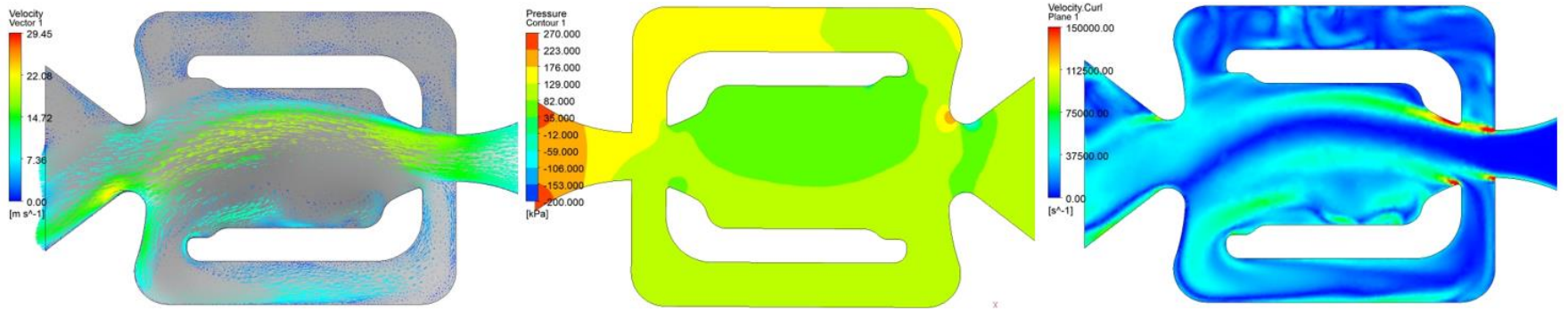

Figure 4-24: Velocity vector and pressure contour plot (left), pressure plot (centre) and vorticity plot (right) at $T_o = 0.4$

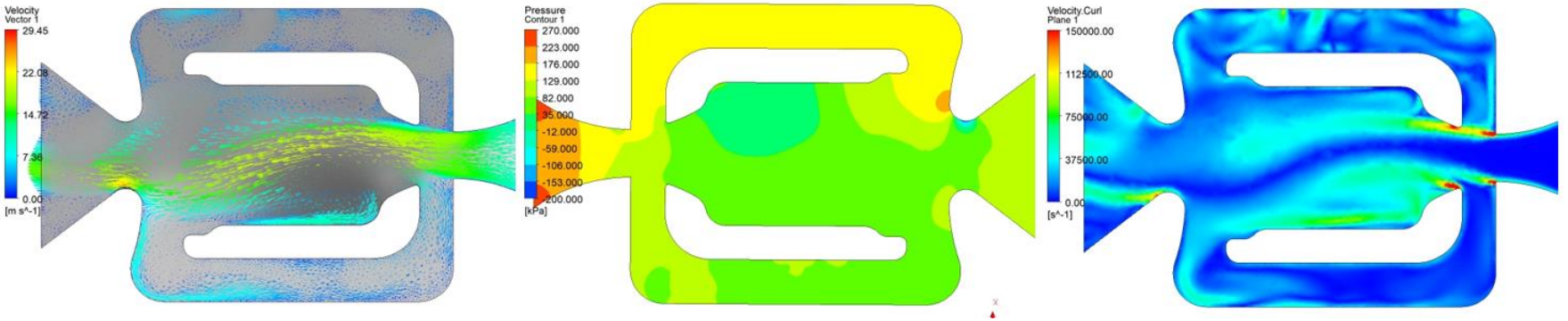

Figure 4-25: Velocity vector and pressure contour plot (left), pressure plot (centre) and vorticity plot (right) at $T_o = 0.5$

The final image (Figure 4-25) shows that the same process of pressure and velocity changes for the opposing side of the oscillator is starting to occur. The pressure builds at the flow separation area, the depression moves along the chamber, building in size. This vortex deflects the main column of water until it dissipates at the feedback channel entrance.

The whole process of switching from side to side through visualisation of pressure and velocity occurs as following: a vortex forms due to the Coanda effect and flow separation. This vortex then travels down the length of the internal chamber and builds in size. The main flow stream of the nozzle is deflected to the opposite side of the chamber by the pressure vortex.

Fluidic oscillators can come in a variety of different shapes and sizes, further research could be conducted to find whether the same process is found in every feedback fluidic oscillator. Additional research could be conducted to investigate a variety of fluids with a variety of Reynolds numbers and at different temperatures to find whether all fluids react similarly to water.

4.4. Conclusion

From the images developed through ANSYS CFX-Post it is possible to see that the nozzle developed for Nissan is a fluidic oscillatory nozzle that works correctly, outputting a velocity that moves from one side to the other and repeating in a cycle. These results align with other research articles involving experimental testing of a fluidic oscillator [38]. It is also established that the time required for a full oscillation for this particular nozzle is approximately 57ms by viewing the peak curvatures of the flow path within the internal chamber.

5. External Fluid Dynamics – Computer Simulation

CFD (computational fluid dynamics) simulations were vital to understand the internal mechanics of fluidic nozzles; however, it was also important to know the spray characteristics once the fluid has been emitted. This could be found experimentally as described in Chapter 2 Experimental Benchmarking Analysis, however this involved manufacturing the nozzle parts which could be expensive and time intensive. There were other detriments to early prototype manufacturing such as inferior manufacturing quality in comparison to the final product, this could result in different conclusions gained from the same CAD (computer-aided design) data due to manufacturing techniques and material choices.

As an alternative to manufacturing a large quantity of different nozzles when in the early design stages, it was possible to utilise computational fluid dynamics to visualise the spray discharged from a nozzle. Unfortunately, this method of utilising the output from the internal CFD simulations in a multi-phase simulation was discovered late in the design process therefore only one nozzle concept was examined. Further studies could eventually be simulated to show how the fluid reacts in dynamic multiphase flows as can be expected when the nozzle is operated on a vehicle travelling at speed. In CFD simulations the process for finding the spray emitted involved finding the velocity of the nozzle at the outlet throughout its internal operation and setting this as the inlet velocity.

Due to the complexity of the velocity in fluidic nozzles it was vital to first simulate the internal mechanics of the nozzle, there was then the high volume of outlet data collected to sort through. This data was then applied to the outlet function as a velocity profile in ANSYS CFX after altering the output data to include timesteps in addition to the location coordinates and velocity magnitudes in x-, y- and z-direction.

As the complexity of multiphase flows had not yet been a part of the project, the progress was slow and was completed in numerous steps to ensure CFD validity. The first step in this process was to run a simulation that had an accompanied tutorial [65] [66] to investigate how multiphase flows worked in ANSYS CFX. The next step was to simulate water coming through a larger inlet such as a fan jet and finally the fluidic nozzle with the time-dependent inlet variables.

5.1. Multiphase External Flow in a Fan Jet

The next progression in the external flow study was to find how to set a constant predefined velocity and direction for a nozzle over a wider area, as would be seen in a fan jet. In order to most accurately model this, an approximation of an internal fan jet outlet area was constructed in CAD to find what the outlet velocity distribution of the nozzle would be, this was then set as the inlet for the multiphase simulation.

5.1.1. Internal Simulation

A fan jet was constructed in ANSYS design modeller and meshed in ANSYS ICEM with similar dimensions to those for the outlet of the fluidic nozzles studied in this report as shown below in Figure 5-1.

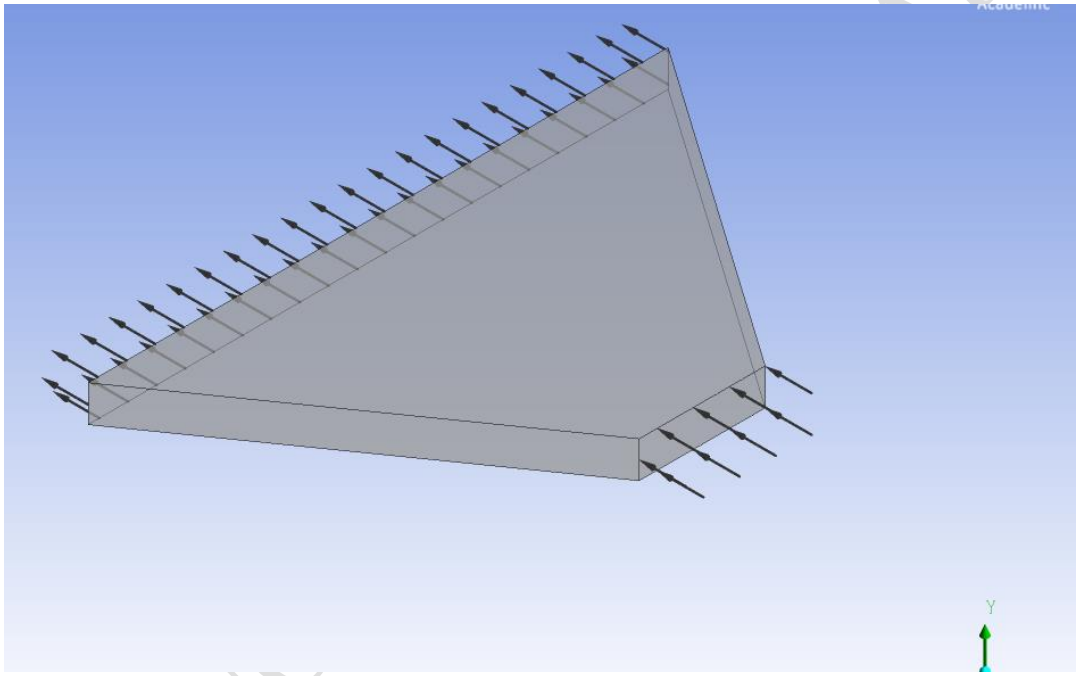

Figure 5-1: Fan jet outlet in CFX-Pre

Water was used as a continuous fluid in the test with a constant mass flow rate of 2 gs^{-1} added to the inlet and an average static pressure of 1 atmosphere was set for the outlet to simulate exit into air. All other geometrical boundaries were set as smooth walls. The simulation for the nozzle was steady state as there is assumed to be no change in velocity or direction over time, with no heat transfer and automatic turbulence set on the shear stress transport turbulence model.

5.1.1.1. Fan jet with a straight velocity flow path

For the initial simulation the mass flow rate was set to be perpendicular to the inlet surface. However, in a further test to approximate how the fluidic nozzle would

appear in oscillation, the velocity was simulated to enter the inlet at an angle of 60° to the inlet surface.

The results for the simulation with the mass flow rate perpendicular to the inlet are shown below in Figure 5-2 as a contour velocity plane plot in ANSYS and in Figure 5-3 as an excel plot of the velocity distribution along the plane of the outlet of the fan nozzle.

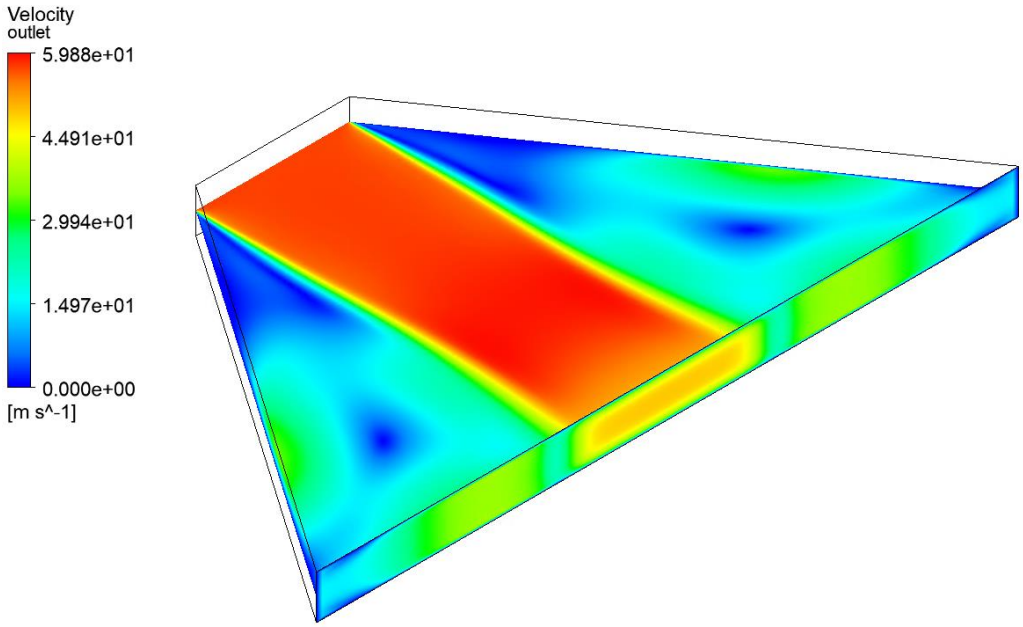

Figure 5-2: Internal velocity distribution of fan nozzle

The velocity distribution of the fluid in the fan nozzle had three peaks, as shown in Figure 5-3, the highest in the centre with two peaks of fluid found surrounding the central highest velocity spike. The majority of the fluid in the fan nozzle flowed straight out through the nozzle forming the peak of flow shown in Figure 5-3. Both Figure 5-2 and Figure 5-3 show that some of the fluid is projected laterally which allows the formation of water to occur throughout the whole length of the fan nozzle outlet. There is a drop in velocity between the peaks, this is seen as a drop in velocity along the whole length of flow shown in Figure 5-2 and is likely due to the surface friction and compression of the fluid at the inlet and the formation of a boundary layer around the fast moving fluid.

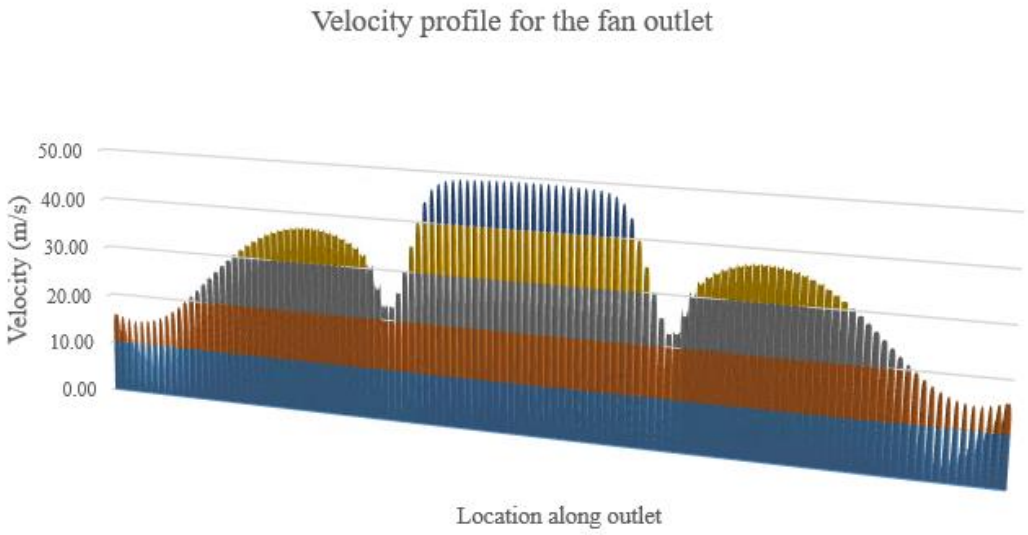

Figure 5-3: Velocity distribution for fan nozzle

5.1.1.2. Fan jet with an incined velocity flow path

In addition to the normal fan jet internal simulation, a second CFD experiment was undertaken with the velocity set at an angle of 30° away from the normal orientation of the outlet. The purpose of this simulation test was to aid in the prediction of how the flow at the outlet and entering the atmosphere would be for a fluidic nozzle at the maximum deflection point.

Below is the result for the simulation with the mass flow rate 30° from the normal to the inlet, these results are displayed as a geometric outlet velocity plot in Figure 5-4.

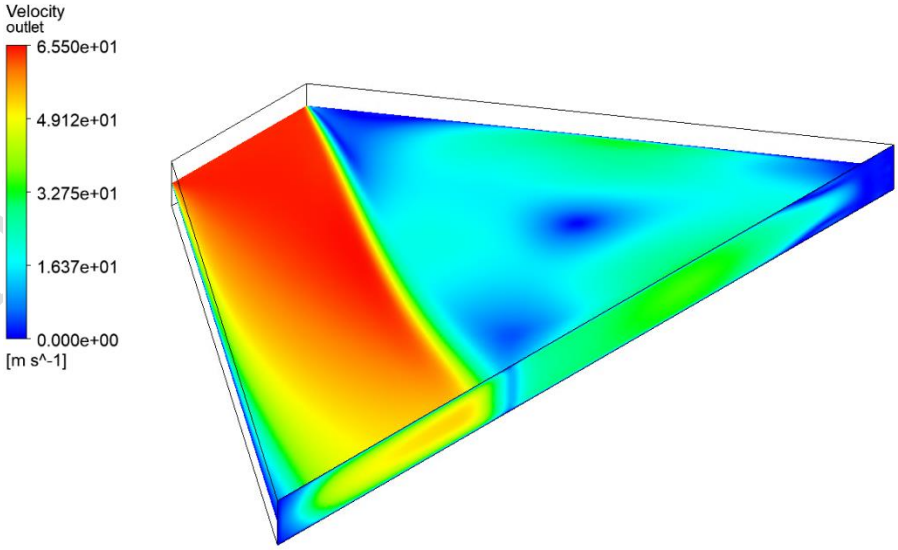

Figure 5-4: Internal velocity profile for fan nozzle with velocity set at 30° to inlet

Below in Figure 5-5 is a 3D graph of the velocity at the outlet to the nozzle. The majority of the fluid velocity within the fan nozzle with the angled inlet velocity is found on the side of the outlet where the fluid is aimed, this is as would be expected from a nozzle with the water aimed along the wall of the outlet.

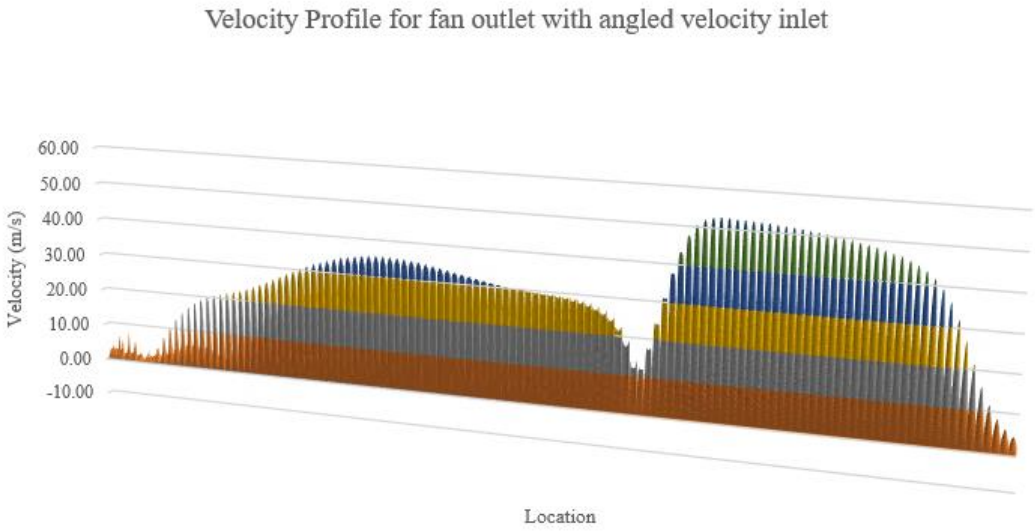

Figure 5-5: Velocity distribution at outlet of fan nozzle with velocity set at 30° to inlet

There is also a small velocity peak on the opposite side of the outlet as seen in Figure 5-5, this is likely due to the Coanda effect taking place, with the inclined opposite wall becoming a low-pressure zone and allowing fluid to flow easily along the boundary layer of the wall. The maximum velocity reached with the angled flow was approximately 50% more than that for the original normal flow for the fan nozzle. This was due to the water flowing through a more concentrated area within the outlet geometry, but at the same mass flow rate.

Once the velocity profiles for the fan outlet were produced it was possible to use the data at the outlet as an inlet for multiphase simulations.

5.1.2. External Multiphase Simulation

The next stage of the investigation into the fluid characteristics and distribution of fluid flow in atmospheric conditions was to create a box geometry of air into which the fluid could be sprayed. To ensure that the process would work correctly with data inputted from a separate simulation a small sized domain was used initially.

A simulation utilising the data from the fan nozzle with the straight fluid flow direction utilising the CAD for the small box shown above. This involved meshing

the box in such a way that there were refinement areas near the inlet of water and increasingly large element sizes in areas that were not expected to see fluid flow.

CFX-Pre was setup as a transient solution to enable the visualisation of the progress of the water as it encounters the air. The air in the box was set as a continuous fluid whereas the water was inputted as a particle transport fluid to allow a more accurate dispersal of water droplets. The volume fraction at the start of the simulation is completely air in the box with only water at the inlet. By utilising the internal velocity profile results as an inlet, it meant that the velocity profile was not uniform, it instead allowed for a variation of the velocity speed and direction throughout the inlet area to the new simulation.

The results for the smaller atmospheric box are shown below in Figure 5-6 as a volume rendering with velocity as the coloured legend. The plot displays the water dispersion velocities at 0.0001 seconds after being released from the nozzle outlet.

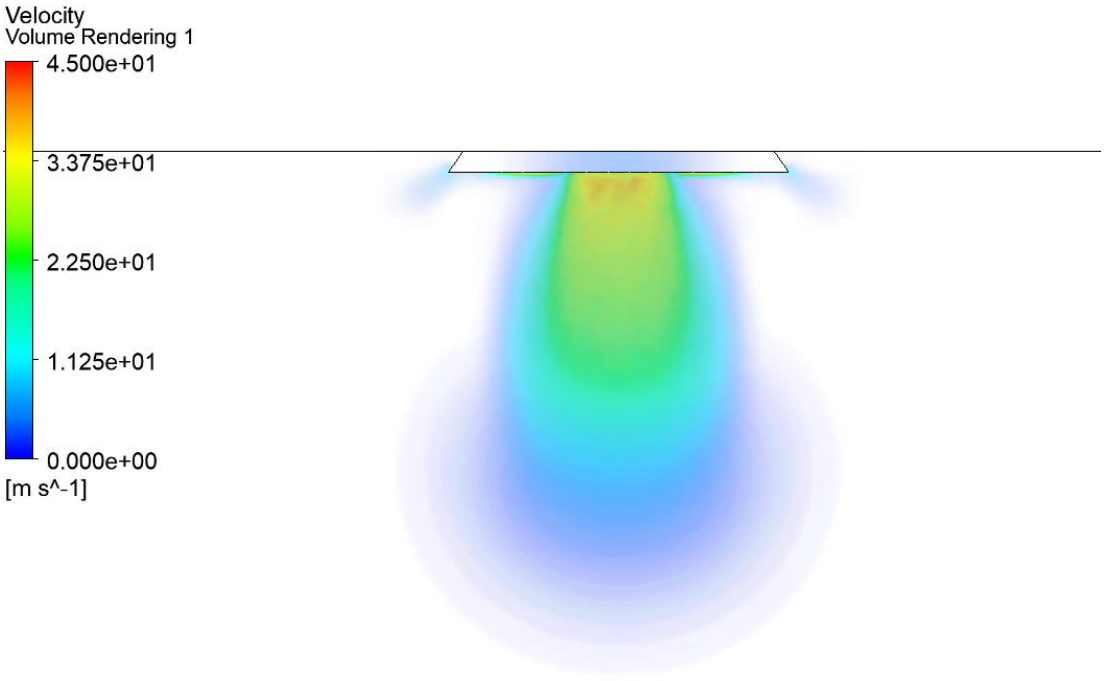

Figure 5-6: Interaction between air and water from fan nozzle in small air box

The particle distribution plot in Figure 5-6 clearly showed that the interaction of the water particles with the atmosphere was linked to the internal geometry simulation velocity profile. In the internal simulation velocity profile (Figure 5-3) there is a central area where the main concentration of high velocity fluid was present, this is represented by the fluid particles spreading further in Figure 5-6.

The plot showed that the further the water was from the inlet the slower it became, as would be expected due to the transfer of kinetic energy into movement. It was useful to see that the water did not simply constrain itself to the width of the outlet upon reaching the air, instead it dispersed and flowed through a larger volume of space. At this point it was too soon to say whether the spray angle of the water would reach 70°, the geometric outlet angle of the fan nozzle (Figure 5-1).

5.1.2.1. Large atmospheric domain with straight fluid flow fan jet

The results from the external flow interaction in the small atmospheric box allowed sufficient confidence for an atmospheric box with an increased size to be constructed. Again, the box was meshed using ANSYS ICEM and the input velocity in ANSYS CFX-Pre was set from the previous simulation of the internal fluid dynamics of the fan jet.

The first image captured, Figure 5-7, was taken from the simulation at 0.000025 seconds where the water was just beginning to enter the atmosphere inside the domain.

The fluid dispersed in an approximately circular pattern along the length of the outlet, with a higher concentration of particles around the centre and near the outlet of the spray jet. The peak velocity area aligned with the distribution of velocity from Figure 5-2, it was possible to see a very small peak in velocity around the circular water concentration, this was due to the smaller peaks in velocity of the distribution from Figure 5-3. As the fluid moves further from the outlet it is rapidly decreasing in velocity from around $56 \mathrm{ms}^{-1}$ to $12 \mathrm{ms}^{-1}$ in the particle rich areas.

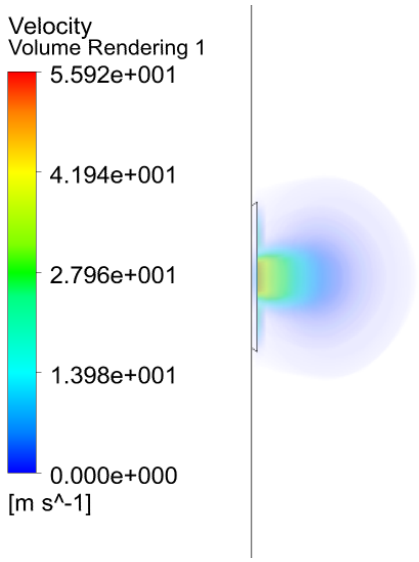

Figure 5-7: Fan nozzle water and atmospheric reaction at 0.00025 seconds

The next image, Figure 5-8, was taken from when the fluid was in the atmospheric domain at the time of 0.00075 seconds after initial water emission.

In Figure 5-8 the water had dispersed a lot further from the outlet of the nozzle, so the image was scaled to encompass the entire interaction region. The water distribution was densest along the axis perpendicular to the centre of the nozzle outlet, with faster velocities found closest to the nozzle.

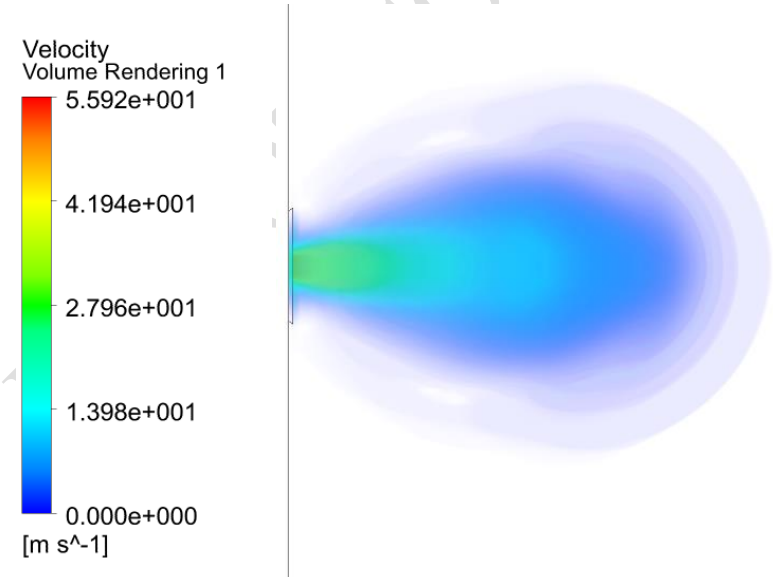

Figure 5-8: Fan nozzle water and atmospheric reaction at 0.00075 seconds

By closely examining the surrounding water flow it was possible to see that there was a concentration around two spots, one where the water speed reduces from around $3\ ms^{-1}$ and one where it decreases to approximately $1\ ms^{-1}$. The result of these concentration points was that the gradual reducing amount of water particles formed an outer 8-figure rather than a circular distribution. The water particles were interfering with each other and collecting at areas of decreased velocity as the potential energy from the nozzle pressure was utilised as kinetic energy with larger particles slowing down faster than the smaller due to gravitational effects.

The next image in the series showed the distribution of the water in the atmosphere at $0.00175\ ms^{-1}$. Again, the image was scaled to allow for an accurate representation of the whole water dispersion in the atmospheric domain. Here it was possible to see that the water is much more dispersed through the atmosphere, there was a concentration along the axis perpendicular to the nozzle as shown in Figure 5-9, however the water was no longer a figure of 8 distribution along the outside, with more of a teardrop shape instead.

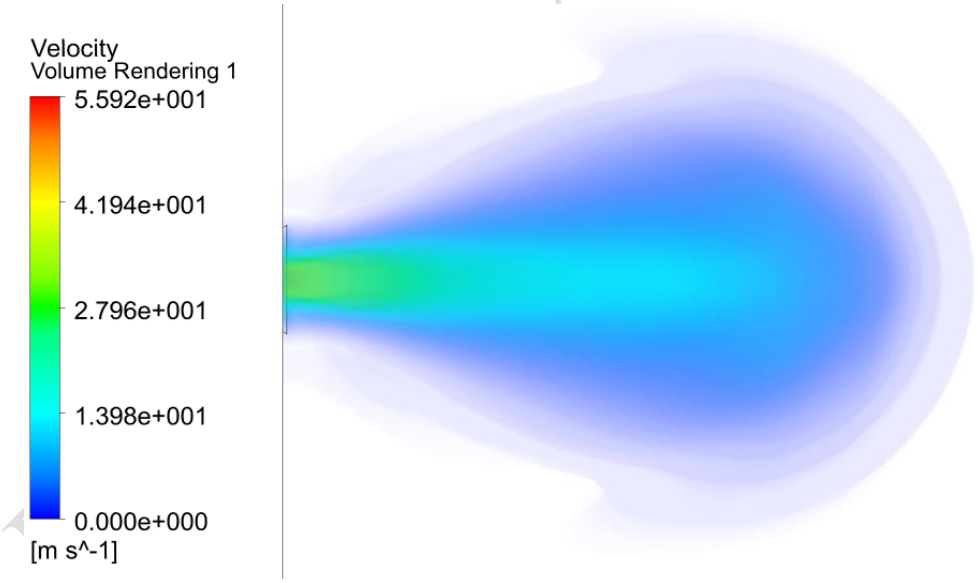

Figure 5-9: Fan nozzle water and atmospheric reaction at 0.00175 seconds

The concentration of water remained along the axis with a more diffuse water concentration along the edges of the teardrop distribution shape. The water was reaching a much further distance from the outlet than for the previous image with the velocity remaining at a higher speed for longer, this was due to the momentum effect as there was water already travelling that path which is moving out of the way of the following particles to make moving into the next zone easier.

The final image in this simulation series shows that the distribution of the water expanded even further as the time step increases, as seen by the water population in Figure 5-10. Additionally, the water spray was a lot wider in the later images and had a smooth outer spray dispersal, this allowed the water to be delivered to an area with a greater width than that of the original nozzle outlet geometry width.

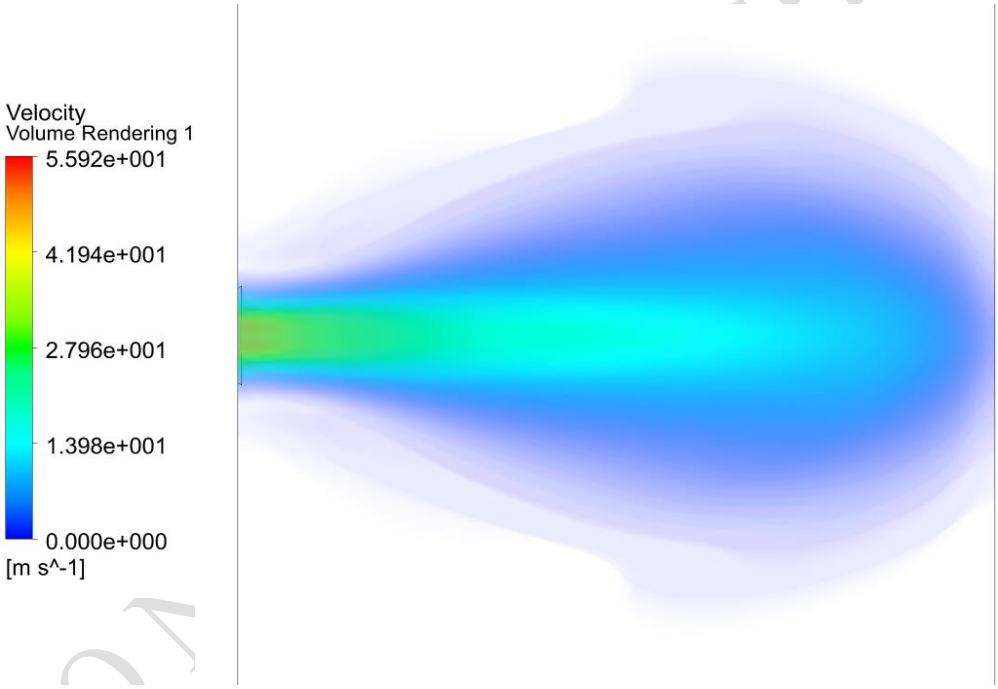

Figure 5-10: Fan nozzle water and atmospheric reaction at 0.0025 seconds

5.1.2.2. Large atmospheric domain with angled fluid flow fan jet

The same setup and domain geometry were utilised for the external flow simulation involving the inclined fluid flow with the fan jet. The only difference in this simulation setup in comparison to the previous, was the velocity profile set at the inlet was taken from the second simulation of the internal fan jet (Figure 5-5).

The purpose of this simulation was to discover how a fluid flow reacts when the flow from an inlet into a multiphase simulation is not perpendicular to the outlet, but at an inclined plane. This was intended to give insight into how the fluidic nozzle would react when tested with an external simulation.

Below in Figure 5-11 the fluid flow from the angled fan jet at 0.00025 seconds, in the image it is possible to see a similar distribution of fluid to that found resulting from the normal fan jet at the same time step. The water is mainly discharged in the direction of the internal jet flow, however there is some dispersal and widening of the spray. There is additional diffusion of water particles around the tip of the flow discharge, where the particles have more freedom to travel and are unrestricted by the momentum within the mainstream.

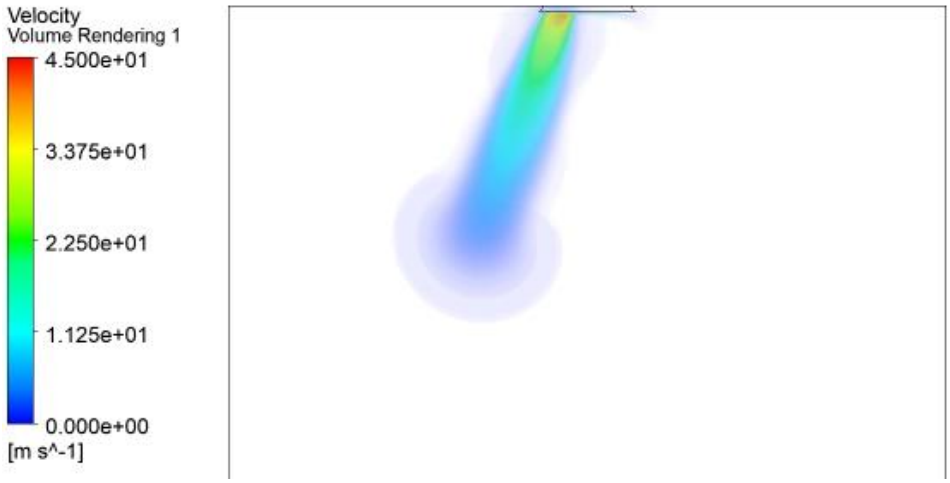

Figure 5-11: Angled fan nozzle water and atmospheric reaction at 0.00025 seconds

inclined fan jet was from 0.001 seconds (Figure 5-12). In this second image the fluid spread more diffusively into the atmosphere, particularly around the end portion of flow and where the innermost spray decelerates from approximately 22.5 ms^{-1} to a lower velocity.

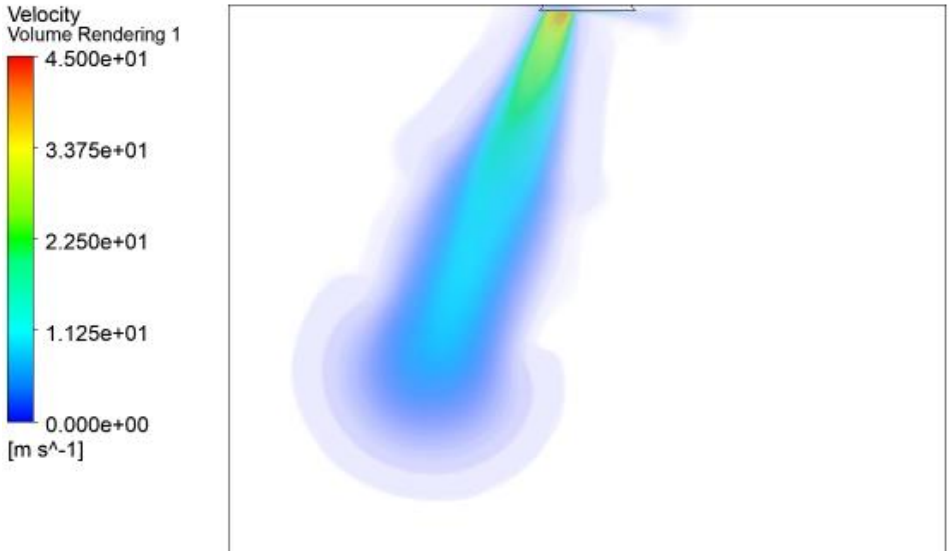

Figure 5-12: Angled fan nozzle water and atmospheric reaction at 0.001 seconds

Unlike the results from the previous fan simulation, the spread of water outwards from the central flow is reduced. The fluid in these results has a maximum velocity of 45 ms^{-1} which is 75% of the maximum velocity for the straight fan velocity, this could explain why there is less spread. There is less momentum in the flow and therefore less energy within the water molecules, allowing for a greater restriction in where the particles can rebound from the main path to.

The final image in the series for the angled fluid flow interaction between the air and the inclined fan jet was taken at 0.0025 seconds into the CFD simulation (Figure 5-13). In this final image, the flow from the nozzle was much more developed, now travelling the entire length of the atmospheric domain box and spreading out of one side.

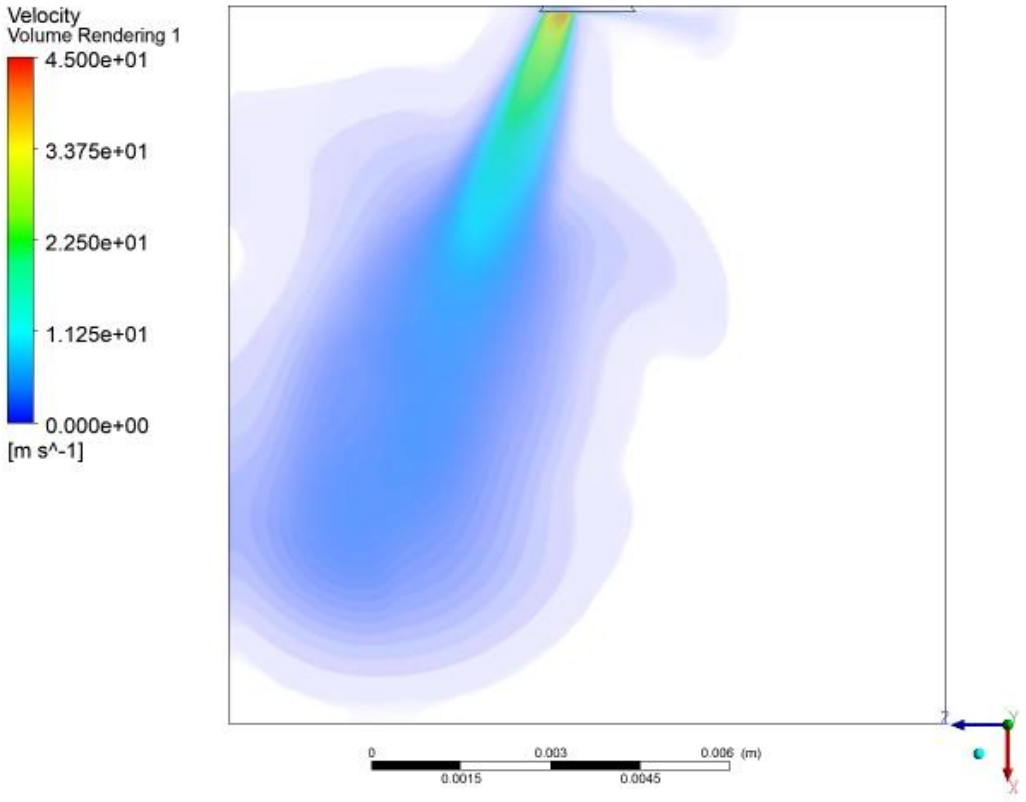

Figure 5-13: Angled fan nozzle water and atmospheric reaction at 0.0025 seconds

The dispersal of the fluid increased as the time increased and the flow of water began to widen and elongate. The main area that there is widespread dispersal occurs after the flow velocity decelerates from approximately 20 ms^{-1}, this is the same as in the previous timestep. However, the outward area of dispersal is more oval-shaped rather than being two separate pieces at the middle and end of the fluid flow.

5.1.3. Conclusions

Through conducting the examination of the two fan jet simulations, it was established that it was possible to take the outlet from one CFD solution to input into a second problem involving multiphysics and generate a realistic visualisation of water spray entering the atmosphere. Therefore, the next step was to involve an input with a time-variable input such as with the fluidic nozzle.

5.2. Multiphase External Flow in Fluidic Nozzles

The final goal in the external simulation of flow project section was to be able to apply this to a fluidic nozzle from this project. The nozzle chosen to simulate in a CFD study is the original 70° outlet angle fluidic nozzle designed for Honda. Now that a simulation a tutorial simulation and a steady inlet multiphysics simulation had been completed the next stage was to add time varying inlet properties.

The inlet boundary conditions were produced by placing an array of monitor points at the outlet of a fluidic nozzle and setting the points to record the coordinates and velocity values of the water throughout a standard transient simulation (Figure 5-14). These velocity values were found by exporting the transient solver results in ANSYS Solver Manager into a .csv file with the co-ordinate points recorded from the monitor points. This file was then copied into excel and adjusted to suit inputting into ANSYS CFX-PRE as transient boundary profile data.

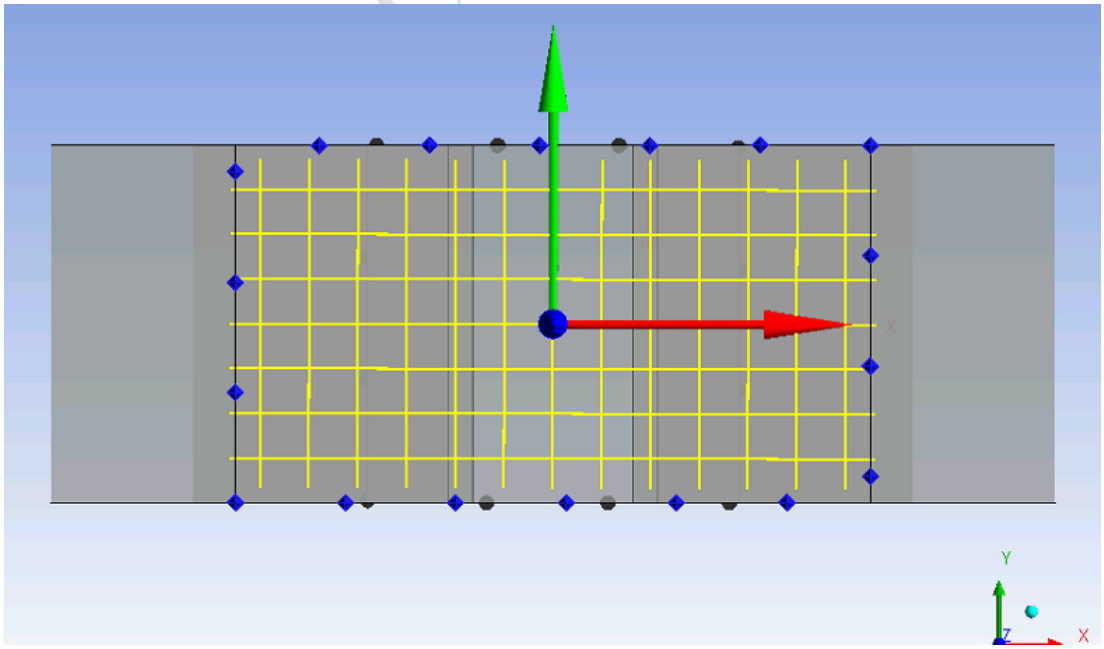

Figure 5-14: Array of monitor points used to measure transient velocity

Again, it was necessary to construct in CAD a secondary box to form the atmosphere into which the flow of water was ejected into. As the fluid is expected to discharge at an angle, the corners of the box were removed (Figure 5-15), the box was split into two portions with additional mesh refinement around the nozzle outlet area.

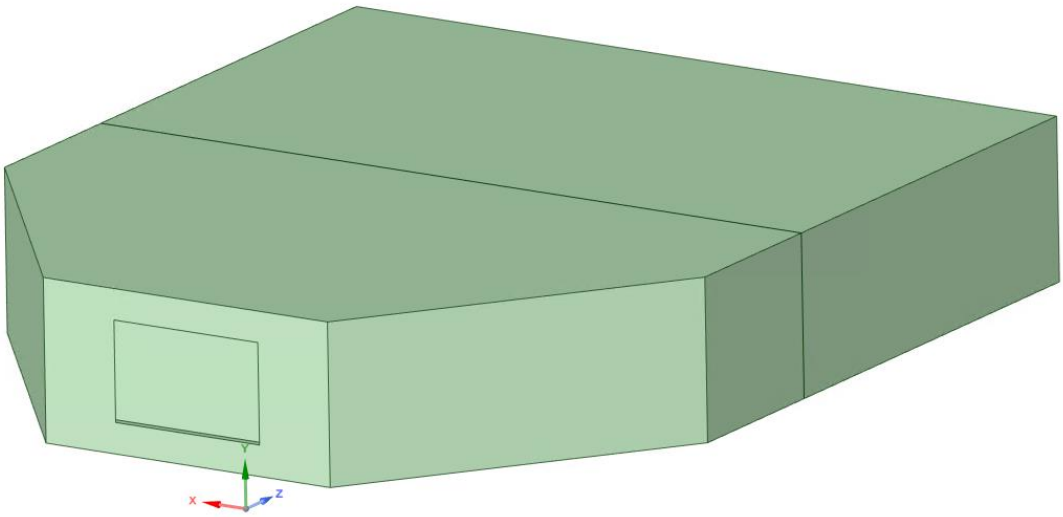

Figure 5-15: CAD for external multiphase flow emitted from fluidic nozzle

It is then possible to begin defining the simulation properties in CFX-Pre for the transient simulation of oscillating water flow into air. The set up in CFX-Pre was the same as for the steady inlet flow apart from the velocity profile for the inlet was imported from the excel file of the transient results from the internal flow oscillating simulation. The air in the box was set as a continuous fluid whereas the water was inputted as a particle transport fluid to allow a more accurate dispersal of water droplets. The volume fraction at the start of the simulation is completely air in the box with only water at the inlet.

The results for this external simulation are shown beside the corresponding image displaying the internal flow of the fluidic nozzle. The images are not sized to be accurate, instead with an enlarged external domain. This was displayed in this way to more clearly visualise how the internal mechanics of the fluidic nozzle affect the external flow direction and intensity. A dashed line is added to the images at the area of greatest velocity, this was done manually to give an approximation of the flow direction and is not a fully accurate representation of the actual flow path.

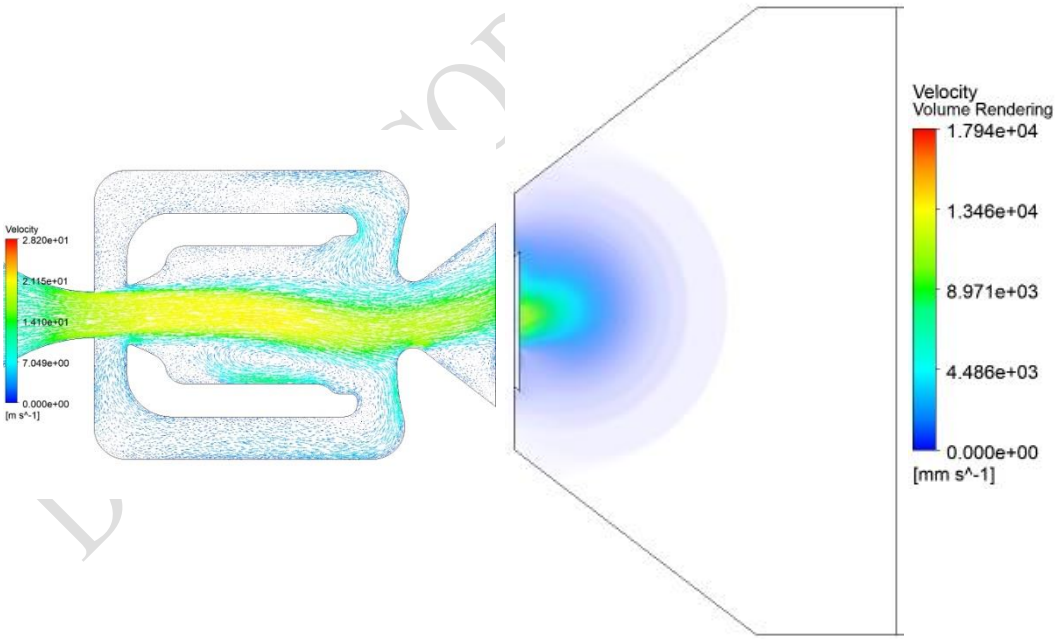

Figure 5-16: Fluidic nozzle internal and external flow at 0.001 seconds

At 0.001 seconds (Figure 5-16), the flow from the internal fluidic nozzle flow was trending toward the upper part of the outlet, this was reflected in the external fluid distribution. The centre of the external flow of water was marginally above the central point of the outlet and there was a slight angle in the upward direction

correlating to the internal flow. The spray angle was fairly narrow and tended toward the upper side of the outlet of the nozzle, then as the flow reached further from the outlet it dispersed into a wider area. The main concentration of flow remained at the same angle as it travelled away from the nozzle outlet.

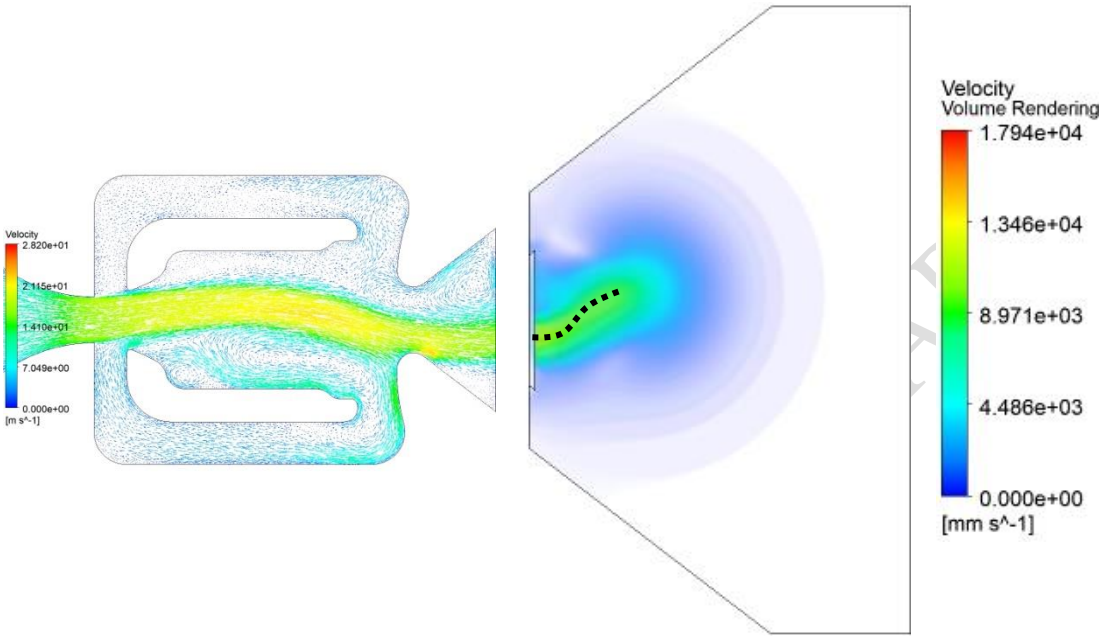

Figure 5-17: Fluidic nozzle internal and external flow path at 0.004 seconds

In Figure 5-17 at 0.004 seconds, the flow of water is no longer at the same angle as the previous time step image, instead the internal simulation shows that the water is now angled downwards. This is reflected by the water in the external simulation image, where the spray closest to the outlet starts at a point lower on the outlet image.

The flow from the previous timestep remains at the same positioning in relation to the outlet however this fluid is positioned slightly further afield as it has had more time to distance itself from the nozzle outlet. This results in a curved fluid flow image result in the external flow diagram with the initial fluid positioned higher than the current timestep. The fluid released in earlier timesteps has diffused whereas the new influx of water from this timestep is more concentrated. This is the same phenomenon as experienced with the fan nozzles, however in this case as the water oscillates from one side of the fluidic chip to the other the area containing the most spread particles should change.

The next image shows the fluid distribution at 0.008 seconds. In this image, the internal flow of the fluidic chip has reached the extreme bottom edge of the nozzle

outlet and the most upward portion in the internal chamber. In the external flow diagram, it is still possible to see where the past positioning of the fluid flow was as there is a further diffused spray in the positions shown from Figure 5-17. Additionally, there is the beginning of spray from the outlet of the nozzle which is aimed at the same angle as the outlet shape for the internal simulation.

The fluid at the central portion of the most recent flow in the multiphase diagram is at a greater velocity than for the previous timesteps. This could be a result of the maximum internal deflection inside the fluidic chip, resulting in there being a greater distance for the fluid flow to accelerate through and reach a higher terminal velocity prior to being discharged into the atmosphere. Alternatively, this could be caused by the small amount of decreasing width of high velocity flow inside the internal fluidic chip outlet, causing a higher concentration of water to be present, increasing the momentum and velocity of the water particles.

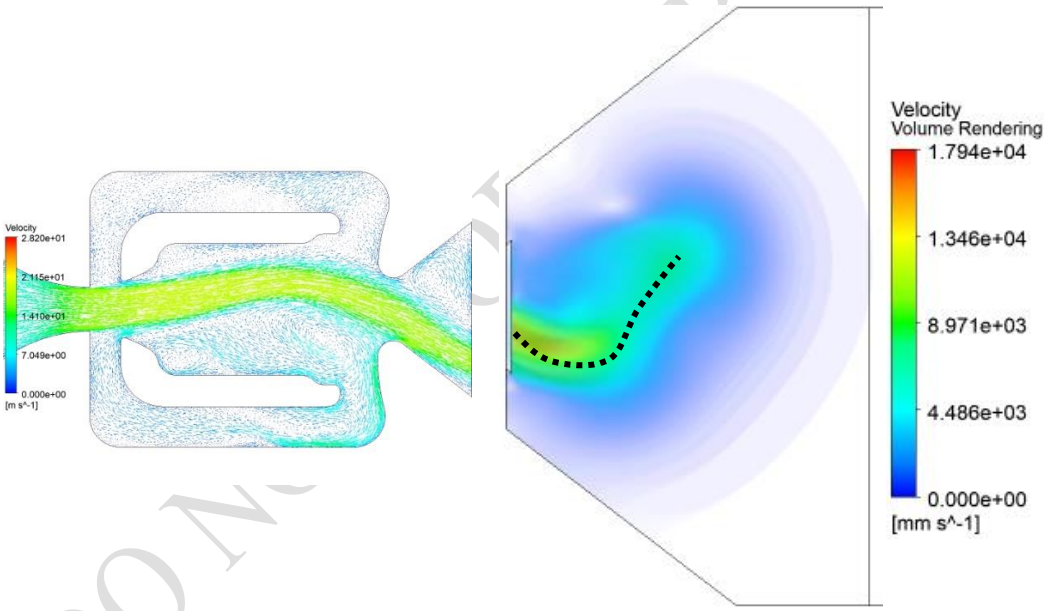

Figure 5-18: Fluidic nozzle internal and external flow path at 0.008 seconds

The next series of images are taken as the fluidic nozzle switches from a downwards exiting motion to the upward portion of the cycle (Figure 5-19 - Figure 5-20). The distribution of water particles in the atmospheric domain box is unique for a fluidic oscillator, where it is possible to see a pattern emerging showing where the fluidic chip began in the oscillatory cycle and in which direction the fluid has been at the greatest velocity concentration subsequently.

The images show that the fluid began at or near the top portion of the oscillatory cycle and a distinct path of increased velocity distribution shows the presence of the previous timesteps. It is possible to see that when the nozzle generated the flow at the most downwards position of the cycle the angle of main portion of flow was parallel to the nozzle outlet chamber wall. This can be used to establish whether a fluidic nozzle is operating at the maximum spray angle it can for a given nozzle outlet width. As often when there is a pressure generated which is too high a nozzle spray angle will begin to narrow and become more concentrated, this is the phenomenon used in multiple other applications [67].

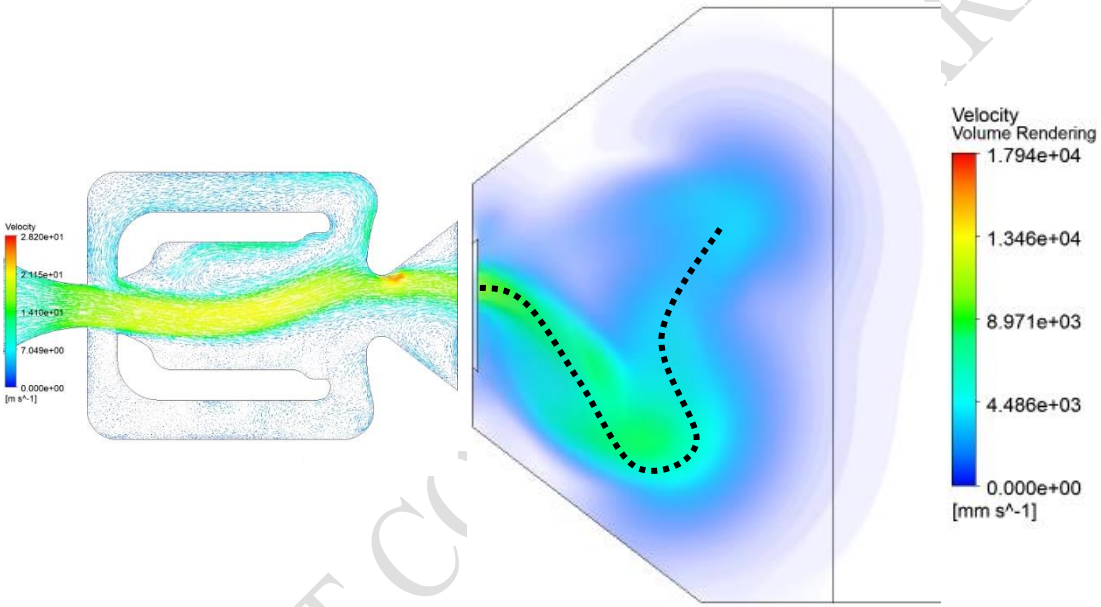

Figure 5-19: Fluidic nozzle internal and external flow path at 0.015 seconds

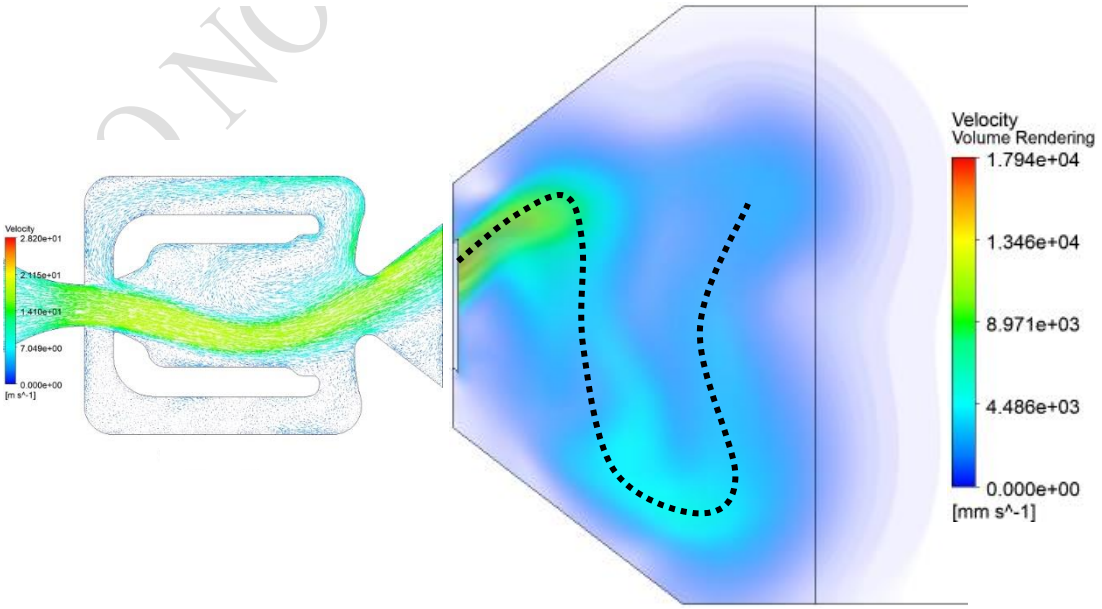

Figure 5-20: Fluidic nozzle internal and external flow path at 0.021 seconds

As the images progress through the timesteps (Figure 5-21 - Figure 5-23) the cycle repeats with the particles from the previous timesteps spreading further throughout the atmospheric domain. In the images for 0.042 seconds and 0.056 seconds it remains possible to interpret the flow and visualise the path that the water from the outlet has taken. When at the time of 0.100 seconds into the simulation the flow becomes more overlapped and harder to interpret, however it is remains possible to see where the most recent flow of water added to the domain is and the direction in which it is travelling (Figure 5-23).

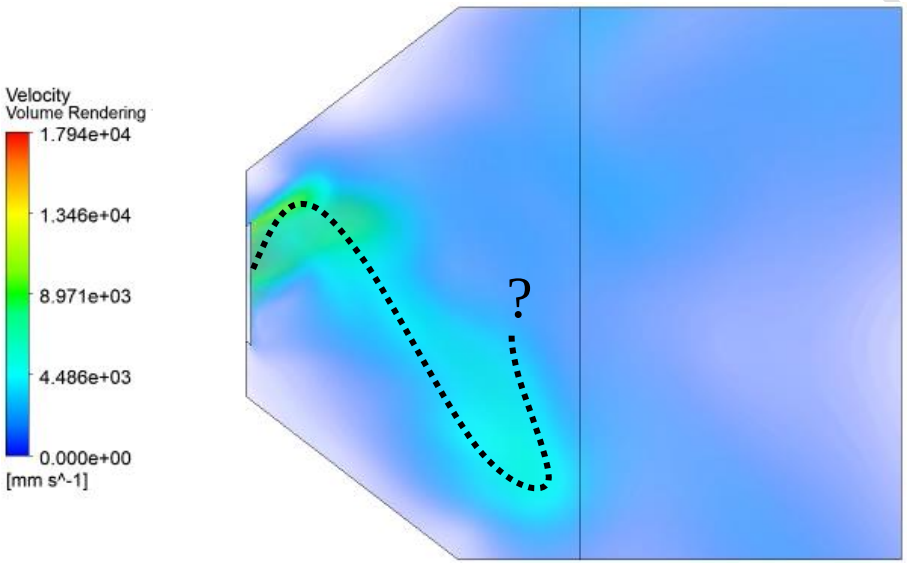

Figure 5-21: Fluidic nozzle external flow path at 0.042 seconds

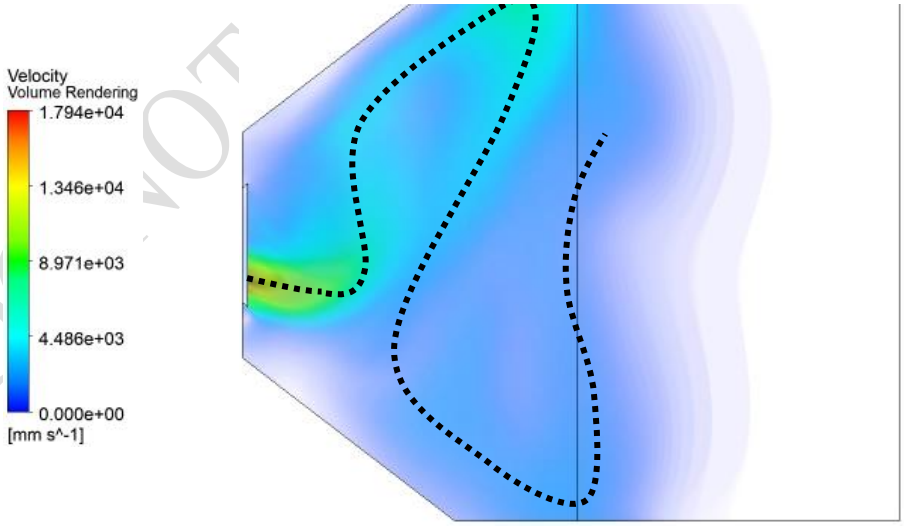

Figure 5-22: Fluidic nozzle external flow path at 0.056 seconds

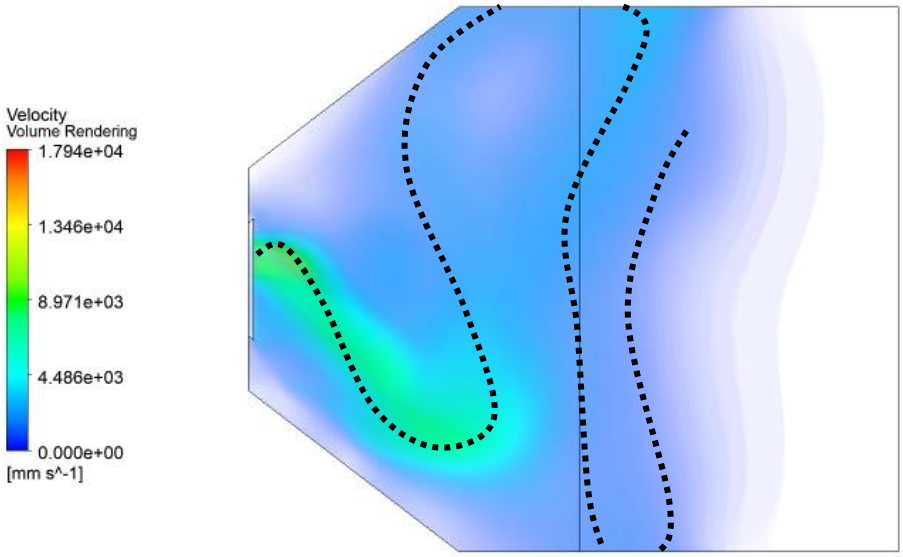

Figure 5-23: Fluidic nozzle external flow path at 0.100 seconds

A close examination of the fluid path at 0.042 seconds, Figure 5-24, with an image analysis shows that the resultant spray angle of the most concentrated flow areas was approximately 74°. When compared to the spray angle from the experimental testing of this nozzle in the next chapter (Figure 6-15), this computationally calculated value is only 1° more than the experimental value achieved in the spray angle test. This proves that the computational model would work well in replacing an experimental spray angle test for this fluidic nozzle.

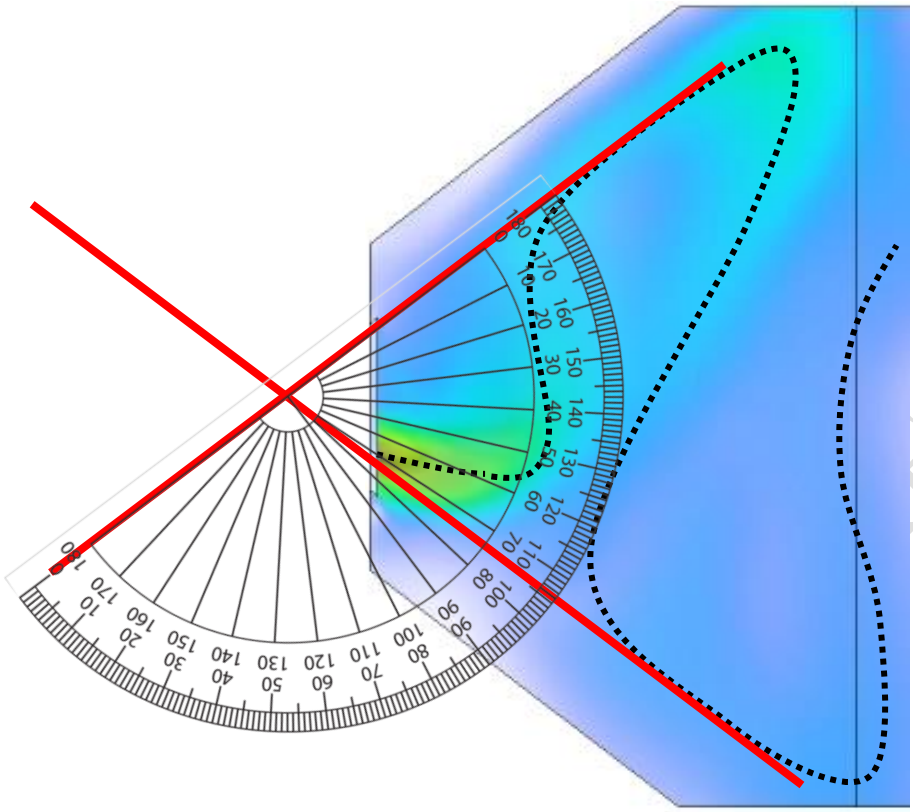

Figure 5-24: Spray angle for fluidic nozzle external simulation

5.3. Conclusions

To conclude this section, the external computational research was successful in predicting the spray angle for a specified fluidic nozzle. Although only one nozzle is tested in this research in this way, it seems feasible that CFD simulations of fluidic nozzles with very similar geometry would produce results correlating to experimental data. The reason that no further nozzles were experimentally tested in this research as the process for producing the external multiphase flow was developed late into the research period. The complexity of transferring the outlet file to a time-dependent inlet file was time consuming and the computational expense required for the simulation was too high with the current processor power on the electronics utilised.

It has been possible through these simulations to visualise the key differences between the flow of a fan jet and a fluidic nozzle. The main differences between these nozzles shown in this chapter, were that the fluidic nozzle was able to produce a much wider spray angle than the fan jet. Secondly, the velocity distribution in the fluidic nozzle differs from the fan jet in the way that the highest velocity of fluid

flow away from the nozzle outlet was at the external edges of the spray distribution in the fluidic simulation and more central in the fan experiment. Finally, the amount of water required to cover an area near the jet outlet can be much more diffuse for the fluidic nozzle as the water particles are deposited in layers rather than all as one spry.

In the fan jet simulations, the fluid emitted from the nozzle primarily remained central to the point of maximum velocity with spread in outward directions the further from the nozzle outlet the water travelled. However, due to the oscillatory motion of the fluidic nozzle, the highest point of velocity in the outlet is constantly moving from one side of the outlet to the other, this results in a much wider spray angle. For the same outlet size and angle.

The water particles from the fluidic nozzle are discharged in an oscillatory motion , this creates layers of fluid rather than a main central column. This results in there being less water required to cover the width of the spray as there are gaps between the layers of fluid.

These differences result in the knowledge that a smaller quantity of water would be required to cover an area of equal size when using a fluidic nozzle over a fan jet. Also, the geometry for the fluidic nozzle could include a tighter nozzle outlet profile in comparison to the fan jet, meaning that a wider spray angle could be achieved using the same internal nozzle space for the design.

6. Nozzle Development

The main aim of this project is to develop three different fluidic nozzles for three vehicle manufacturers. These nozzles are then to be mass produced and rolled out to be used on vehicles in the automotive sector globally.

Kautex Textron CVS Ltd already owned the designs for a fluidic nozzle from previous research with Swansea University, the goal is to adapt this nozzle to suit the different applications and specifications given by the new customers. This involves checking tolerances, altering spray angles and changing other characteristics by altering the geometry of the current fluidic chip using existing theory and experimentation through physical and computational testing.

6.1. Nissan Nozzle

6.1.1. Specification

The first nozzle in this project to be investigated and redesigned is the fluidic nozzle for Nissan vehicles. The specification given to Kautex Textron CVS Ltd included that the nozzle should meet a spray angle of [redacted] from the top, and [redacted] from the side, and should have a mass flow rate of [redacted] (Figure 6-1 - Figure 6-2). These figures and images were given by the customer.

Figure 6-1: Nissan specification for spray angle

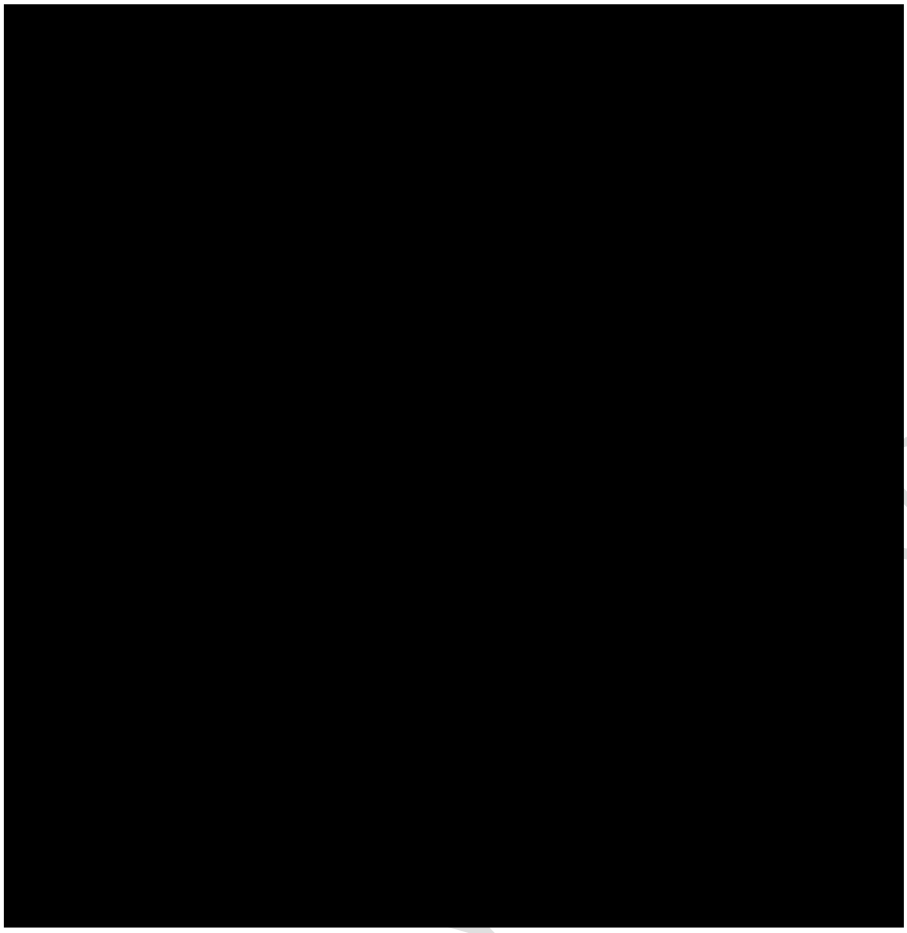

Figure 6-2: Nissan specification for spray distribution

This nozzle is thoroughly tested both experimentally and computationally to ensure that it satisfied the specification. Experimental testing includes the testing of spray distribution, angle, mass flow rate, oscillation frequency and droplet sizing (9.3 Appendix C - 9.5 Appendix E). Computational testing involves modelling the internal flow of the fluidic chip to examine the predicted spray angle and to assess the oscillation rate of the spray. The computational results are utilised in comparison and validation to ensure that the experimental results are not due to any defects that can be found within the fluidic chip.

The nozzles for Nissan vehicles are mounted under the bonnet, the estimated number of nozzles per vehicle is three, this number was assumed due to the width of the vehicle and the coverage provided by the current nozzles (Table 2-1). Attributable to the larger quantity of nozzles mounted on the vehicles there is an allowance for a narrower jet of water through the outlet of the nozzle of [redacted] in width and [redacted] in height.

The fluid distribution in the specification is predominantly concentrated at the two peaks on the far ends of the spray laterally. This gives a good approximation to what

would be found if two pencil jets were used rather than one fluidic however there is additional fluid in between the two peaks. This distribution is useful as the fluid is more densely projected at both sides of each C-zone and in the centre when all three nozzles are utilised, one for the driver and the other for the passenger with an additional central nozzle, this ensures maximum coverage and a more consistent clean over the windscreen.

6.1.2. Development and Defect Analysis

Upon joining this project, Kautex Textron CVS Ltd had developed a nozzle that they believed to be suitable for the Nissan vehicle specification. This nozzle had been developed by the company alongside Swansea University and had been through numerous development loops to design a basic nozzle that could be altered slightly to improve reliability and quality. This nozzle was able to provide a lateral spray angle of [redacted] and a vertical spray angle of [redacted] (Table 2-4).

The existing Kautex nozzle spray distribution is shown below in Figure 6-4, unfortunately the spray is asymmetric and unevenly distributed between the two peaks, resulting in a higher peak on one side than the other. This is a peculiar phenomenon as the computer aided design (CAD) fluidic chip is symmetric and therefore should not produce an asymmetrical spray distribution result (Figure 6-3).

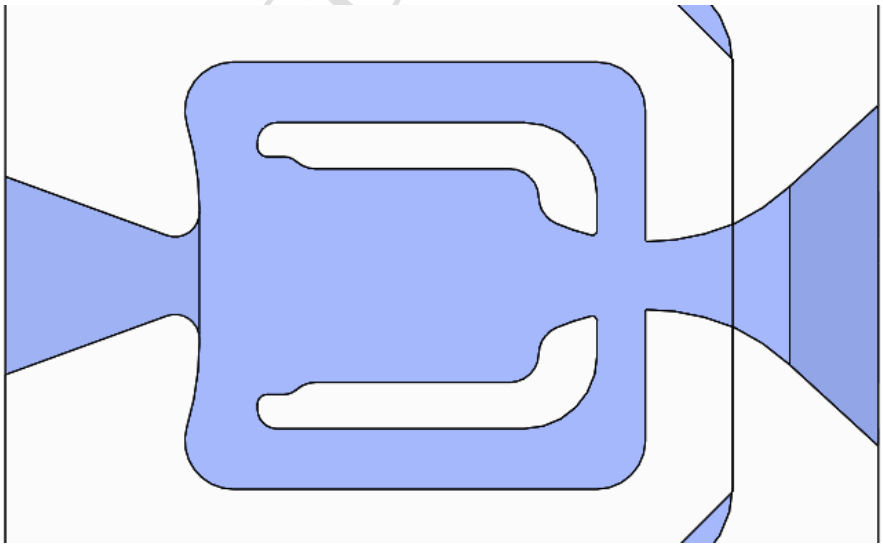

Figure 6-3: CAD for Kautex/Nissan nozzle

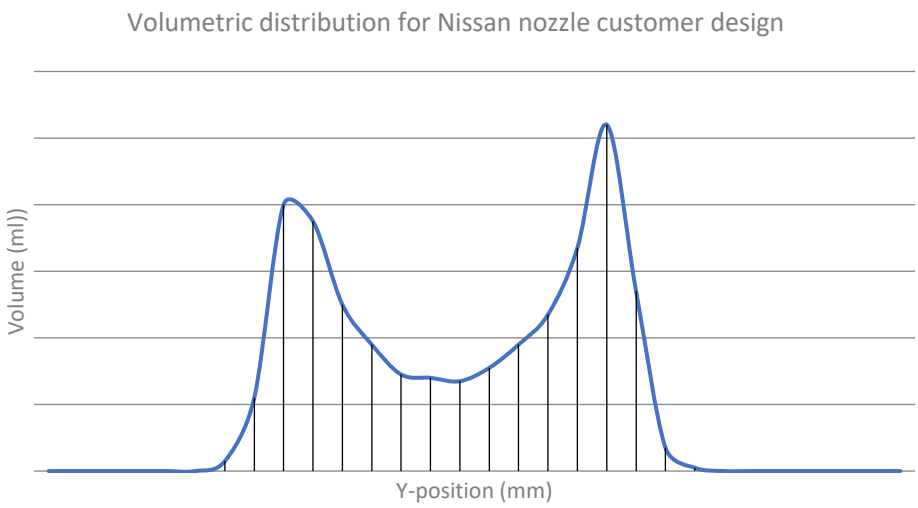

Figure 6-4: Asymmetrical spray distribution produced by Nissan nozzle design

An investigation into the physical prototype fluidic chips utilising an imaging microscope, discovered that there were defects within the chips which caused asymmetrical geometries. One of these defects included the fact that the internal walls of the chip to be misaligned with the outlet and the inlet of the chip (Figure 6-5). Additionally, the height of the chip was not equal throughout allowing water to flow over the internal walls and effectively skip one of the feedback loops and shorten the time required to switch from one side to the other (Figure 6-6).

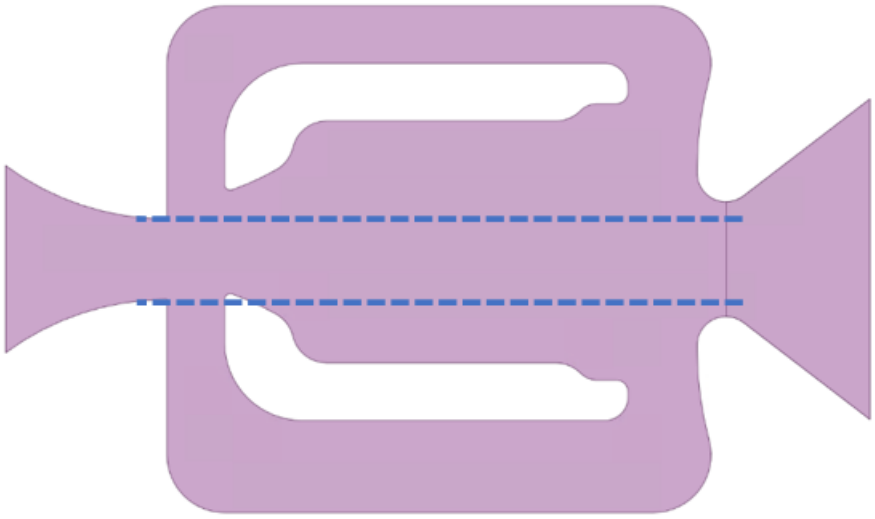

Figure 6-5: Fluidic nozzle with misaligned walls

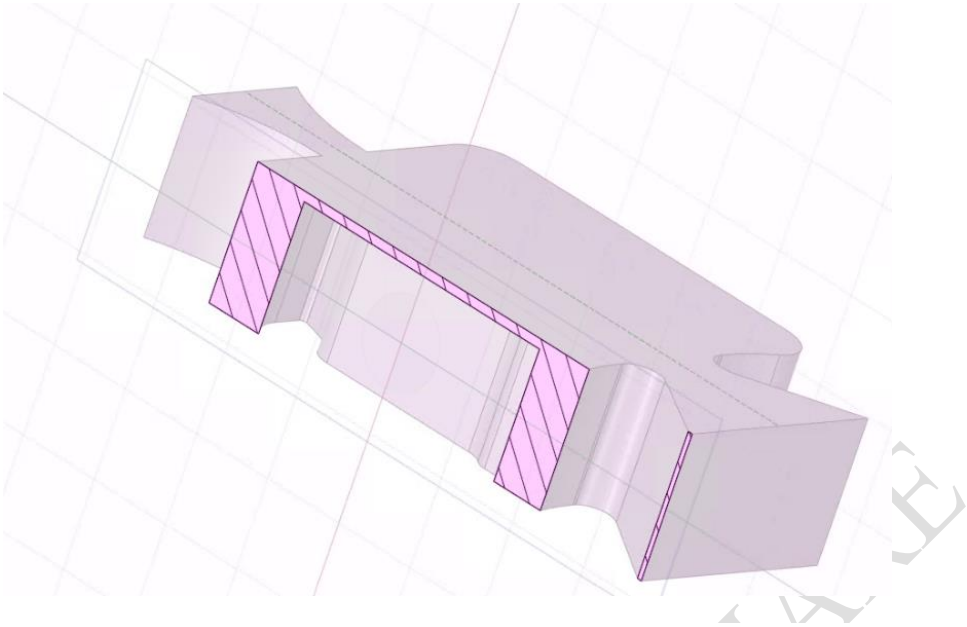

Figure 6-6: Fluidic chip with shorter inner walls

The misalignment of the walls was causing excess water to flow back into the side with the narrower feedback channel, reducing the outlet flow and changing the spray angle (Figure 6-7). A secondary issue was that due to the added width in the opposite feedback channel, it allowed space for the flow to distort and form vortices further disrupting the flow within the fluidic chip.

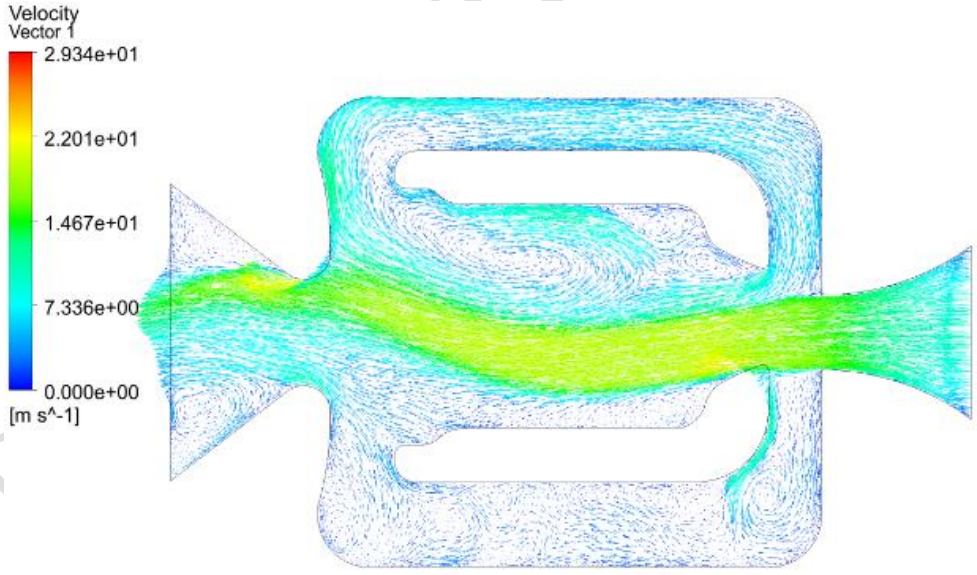

Figure 6-7: Resultant flow with misaligned walls

The misalignment issue was consistent throughout all the fluidic chips therefore an investigation into the CAD drawing of the chip was completed rather than a redesign of the chip. Unfortunately, in the CAD drawing there was not a driving geometry that the chip should be symmetric with the outlet, inlet and gap between the walls to be aligned. This issue was resolved by changing the driving geometry for the plastic injection moulds used to those which were completely symmetrical.

Below in Figure 6-8 the resultant flow for the lower height internal walls is shown. Unlike the previous defect where there it is visible that the fluidic nature of the chip is still active, this is not present in this distortion of the chip. Much of the high velocity water flow remains central in a straight stream from the inlet to the outlet. The remaining water is predominantly found towards the outlet side of the nozzle rather than recirculating through the feedback channels. It is possible to see that there is turbulence in the area above the feedback channels, this is likely due to this higher portion of the water flow interacting with the lower part where the internal walls are present.

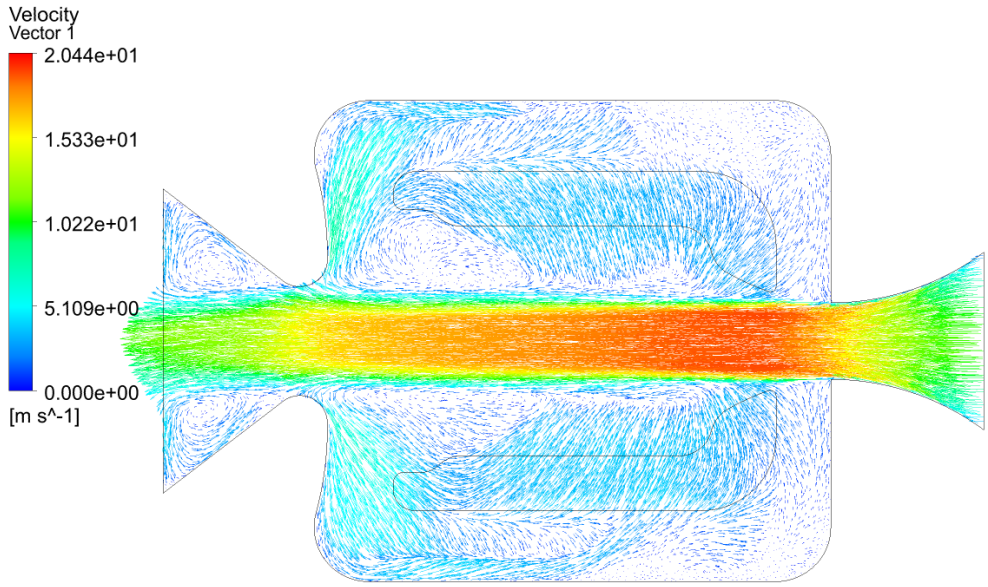

Figure 6-8: Resulting flow from lower internal walls

The height of the walls within the fluidic chip in the CAD drawings and the mould utilised was equal for both the internal and external walls. Therefore, the issue within the chip allowing to uneven fluid cycles was resolved by increasing the height of the internal walls so that they would be taller than that of the external walls of the fluidic chip. This would involve utilising an interference fit when the fluidic chip was inserted into the nozzle eyeball, however it would negate the issue experienced with the uneven flow and therefore it was necessary.

In addition to the defects present in these fluidic chips, it is possible to get numerous other defects due to geometry tolerances and distortions due to manufacture. Therefore, a computational investigation into how different defects can affect the flow of water was conducted to determine which tolerances required tightening in order to ensure correct throughflow of the water in the chip as shown in chapter 4.

Once the tolerances for the Nissan nozzle had been increased it was possible to guarantee that all manufactured parts had the same internal dimensions and therefore the correct outlet flow. The defect investigation for the Nissan nozzle was beneficial for the project as it allowed additional knowledge to be gained about how changing different part dimensions in the fluidic chip affects the outflow of the nozzle.

6.1.3. Conclusion

The final Nissan nozzle design had a lateral spray angle of [redacted], a vertical spray angle of approximately [redacted] with the majority of the spray within [redacted], and a mass flow rate of [redacted]. This did not meet the exact initial specification that was given to Kautex Textron CVS Ltd as that had included that the nozzle should meet a spray angle of [redacted] from the top, and [redacted] from the side, and should have a mass flow rate of [redacted] (Figure 6-9).

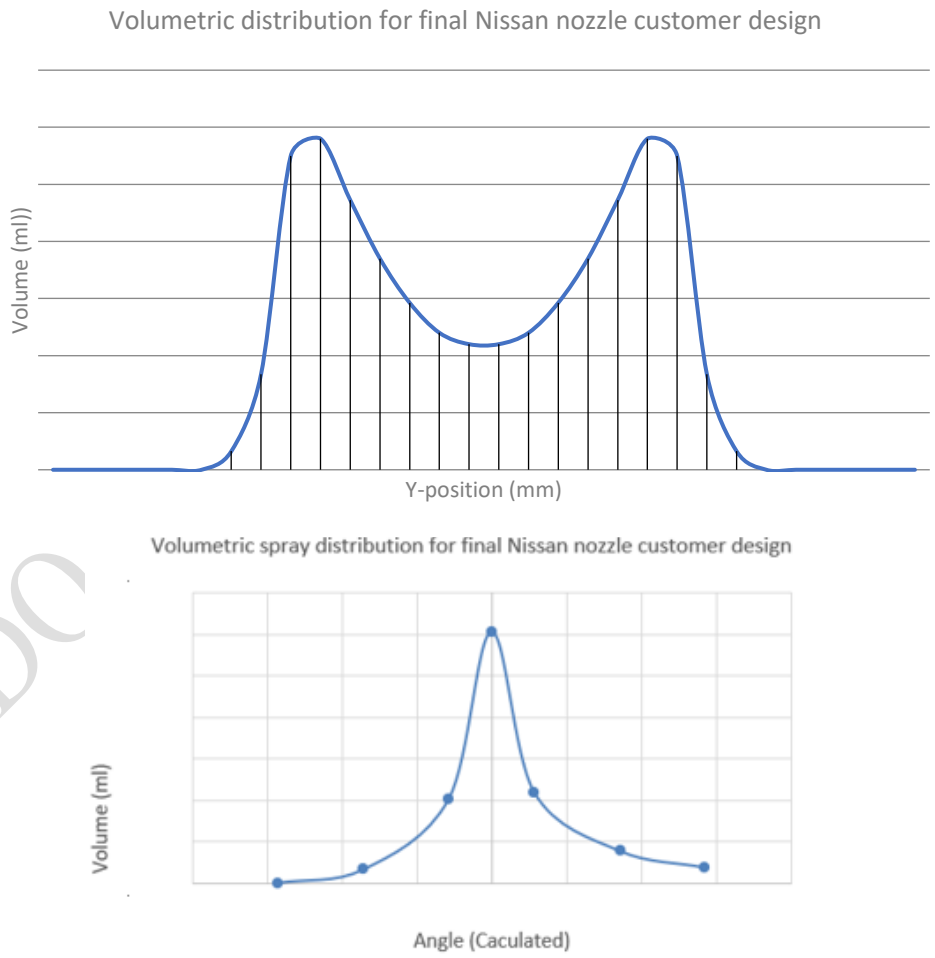

Figure 6-9: Nissan final design volumetric spray distribution from front angle (top) and side angle (bottom)

Through constant contact and feedback of designs with the customer it was found that an increased mass flow rate than initially stated would improve cleaning performance. A nozzle with the lower mass flow rate in-line with the specification was produced early in the development process but better results were seen with an increased amount of water.

The side spray angle did not meet the initial specification brief, however due to most of the spray being concentrated within the angle specified the customer approved the nozzle design.

This nozzle is now being mass produced by Kautex Textron CVS Ltd for Nissan vehicles.

6.2. Honda Nozzle Project

6.2.1. Specification

The second nozzle designed and developed in this project is the fluidic nozzle for Honda vehicles. At the start of this project collaboration, Honda was unclear about what spray angle would be most suitable for their vehicles therefore the company asked for a range of nozzles to be designed with spray angles from [redacted] to [redacted] and the same mass flow rate as their current nozzle of 15ml/s. From these designs the company would be able to select the nozzle most suited to their vehicles. There was no specification on oscillation speed or for the height of the peaks for this nozzle.

The designs for these nozzles were modified from the Nissan fluidic chip part established previously with this project. By expanding on the tolerance study results for the Nissan nozzle (9.8 Tolerance Defects), key features within the nozzle were chosen to be altered to produce the larger spray angles at low mass flow rates (Figure 6-10).

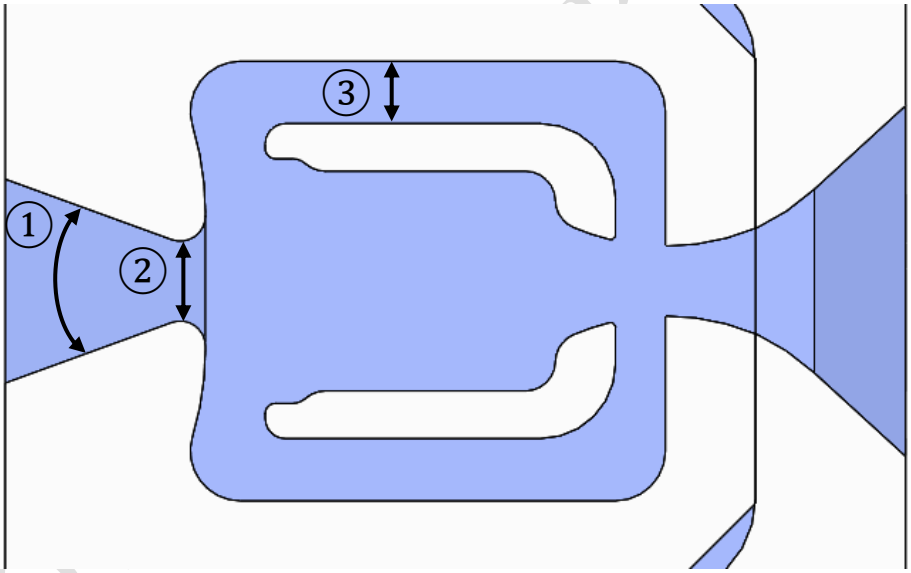

Figure 6-10: Key features for nozzle development

The initial designs were constructed using a 3D printing machine new to Kautex, to build a series of prototype nozzles as a batch process on site. This allowed the nozzles to be tested quickly to validate which key features would need to be changed and by how much. Simultaneous computational fluid dynamics (CFD) simulations of several nozzles was also completed to see whether the manufacturing of the nozzles corresponded to the CFD.

Unfortunately, due to material choice there were some errors in the manufactured nozzles that did not line up with the computer simulations, the nozzles were

dimensionally incorrect when looked at through a microscope. Therefore, a new manufacturer was used which resolved the issues and the project could move forward.

A few months after the finalised design was sent to Honda, feedback was received that there were a couple of additional issues with the fluidic nozzle that had been supplied. Although the nozzle met the specification given initially, additional parameters were included with the new design request. The requirements included having a smaller distance of dropdown when travelling at speed, an increased concentration of fluid at the sides of the distribution and an increased mass flow rate.

The two development loops are documented in separate sections within this chapter to easily see the focuses of each study, one of which was to change the spray angle and secondly to address the issues subsequent to the delivery of the nozzle to the customer.

6.2.2. Spray Angle and Flow Rate Development

This section covers the initial development aim for the Honda nozzle which includes geometry changes to increase the spray angle and mass flow rate of the nozzle. Honda did not include a conclusive specification regarding spray angle therefore the experimental and computational testing results were utilised to gain an understanding on which angle to use. Additionally, dynamic testing was completed at this stage to determine the dropdown of the spray when travelling at speed. This testing was conducted in the same way as in the dynamic testing from the experimental chapter.

6.2.2.1. Initial Prototype Testing

A series of prototype designs to change the spray angle were considered based off the tolerance testing from the Nissan project. It was found that the best dimensional control for the spray angle could be found by altering the angle of the outlet, this aligns with past experimental research [68].

The mass flow rate of the nozzle is governed by the conservation of mass equation (6.1) [69]. This means that the mass flow rate can be changed by changing the density (ρ) or the velocity ($\boldsymbol{V}$) of the fluid over a period of time (t). Water is incompressible, meaning that $\frac{\partial \rho}{\partial t} = 0$, therefore the property that needs to be changed is the velocity of the water coming into the nozzle. Therefore, it is necessary to alter the domain size to change the mass flow rate, by reducing the volume size it will be possible to increase the velocity of the water and therefore the mass flow rate.

$$\frac{\partial \rho}{\partial t} + \nabla \cdot (\rho \mathbf{V}) = 0 \quad \textbf{(6.1)}$$

Through experience with altering internal dimensions in this project, it has been found that it is very complicated to reduce the lateral dimension sizing of the nozzle without compromising the outlet spray properties therefore instead of altering the intricate interior dimensions, the depth into which the water path is in fluidic chip was reduced. This caused there to be a decreased volume for the water to flow through which resulted in a higher velocity of water within the system. This system of changing the height worked well in the Nissan fluidic chip design and therefore was utilised throughout the chip designs which required a decrease in mass flow rate.

To attempt to change the spray angle, the width of the outlet choke, and the feedback channel were extended; the connection between the spray angle and these features was taken from the Nissan tolerance testing (9.8 Tolerance Defects). The tolerance study outcome found that by increasing the width of the outlet choke or the nozzle inlet, there would be an increase in the spray angle. Additionally, a short study into changing the internal chamber width was completed as with the increased deflection angle experienced by this situation in the study it was hypothesised that this would be a conceivable design.

The new investigation involved changing the outlet choke or inlet width by 10%, both investigations were completed separately to examine the resulting difference with a change to each geometry. Through this study it was discovered that there are limits to the amount the dimensions can be extended, beyond these limits the nozzle ceases to operate as a fluidic nozzle (Figure 6-11). Instead of the flow recirculating into the feedback channels there was an increased chance that the water would flow with a minor deflection towards the outlet only.

Through the investigation, it was discovered that the width of the outlet choke could not extend further than 1.0mm in this fluidic chip else the water would not have sufficient space for part of it to be deflected back into the feedback channels, reducing the possibility of the water emitted being oscillatory.

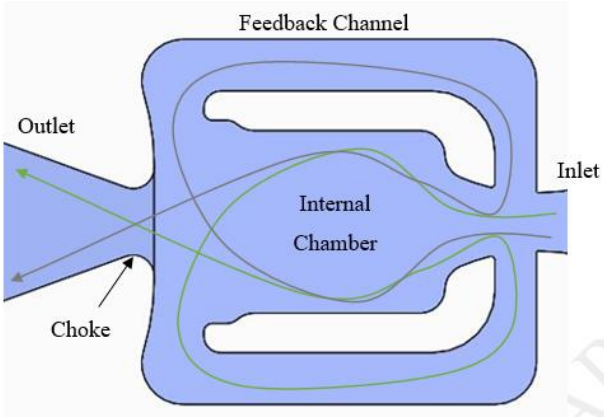

Figure 6-11: Normal flow circuit

Similarly, if the internal chamber of the nozzle is too wide, the influence of the Coanda effect lessens resulting a smaller deflection in the fluid, again reducing the possibility of feedback flow (Figure 6-12). There was minimal difference found in spray angle when the inlet width was changed therefore this was not the approach utilised in further investigations.

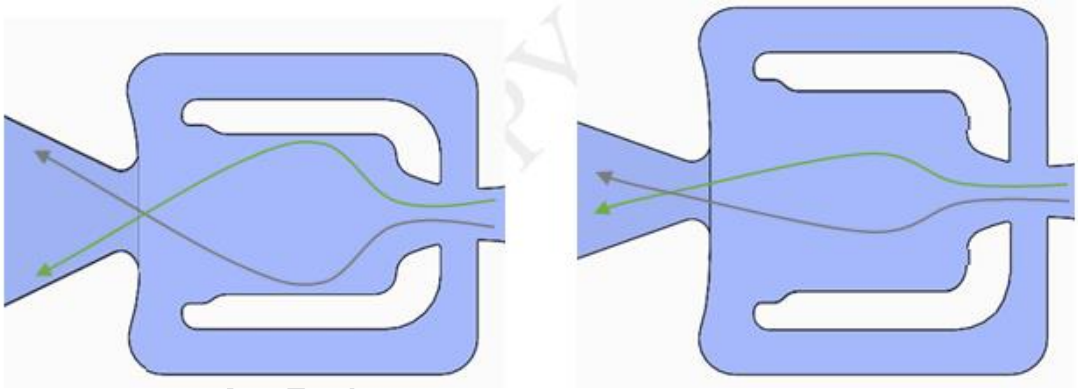

Figure 6-12: Abnormal flow circuits due to increased outlet choke width (left) and increased internal chamber width (right)

Subsequent to the investigations utilising the tolerance study as a base of ideas, a secondary experiment was conducted which involved simply changing the outlet angle of the fluidic chip. The original Nissan nozzle fluidic chip outlet angle was 40° and the spray angle for that nozzle was 40° therefore it was pertinent to the study to investigate how the spray would be affected if the outlet angle were to be increased.

It was found that increasing the outlet angle of the nozzle but keeping all other parameters the same would be suitable for the change in spray angle up to a point. If the angle were to become too large it was possible that the internal deflection of the water leading to the spray angle would not be sufficient to cover the whole of the outlet width. Therefore, with this design change at the forefront of the development process, four

different fluidic chips were tested experimentally and computationally to examine the bounds of the spray angle and to discover the best feasible design for the customer.

A series of designs were tested at different angles, but it was determined that a wider spray angle would be most desirable in this project therefore these designs were streamlined into four main concepts between 60° and 75°. Results from the testing showed that the 70° outlet angle fluidic chips had a decreased mass flow rate which would be suitable to the specification given by Honda. However, the 75°, 60° and 65° outlet angle chips had a mass flow rate which was greater than desired, therefore the methodology of decreasing the height of the chip to decrease the mass flow rate was utilised causing the mass flow rate to decrease to within the desired parameters.

Experimental and computational testing was performed on each of the nozzles to find the mass flow rates and spray angles (Figure 6-13 - Figure 6-20); this allowed Honda to greater understand the benefits and drawbacks of each nozzle. High speed video was taken of each of the nozzles to ensure that the resulting flow was consistent and contained no abnormalities.

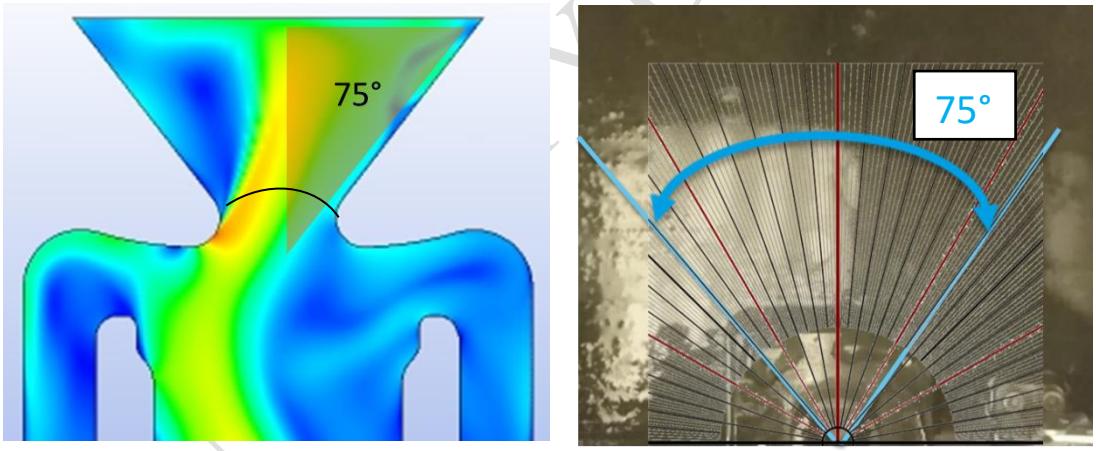

Figure 6-13: Spray angle results for 75° Honda nozzle from CFD (left) and experimental (right)

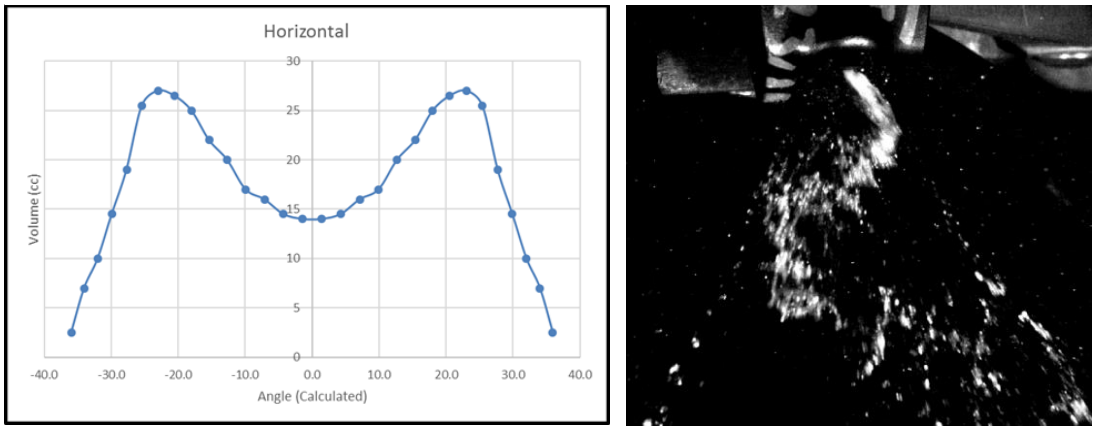

Figure 6-14: Spray distribution (left) and high speed image (right) for 75° Honda nozzle from experimental testing

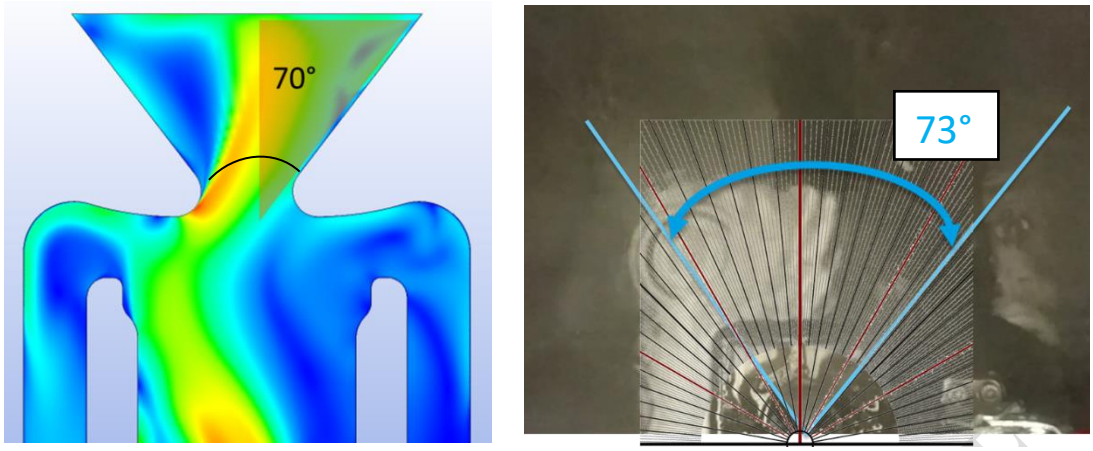

Figure 6-15: Spray angle results for 70° Honda nozzle from CFD (left) and experimental (right)

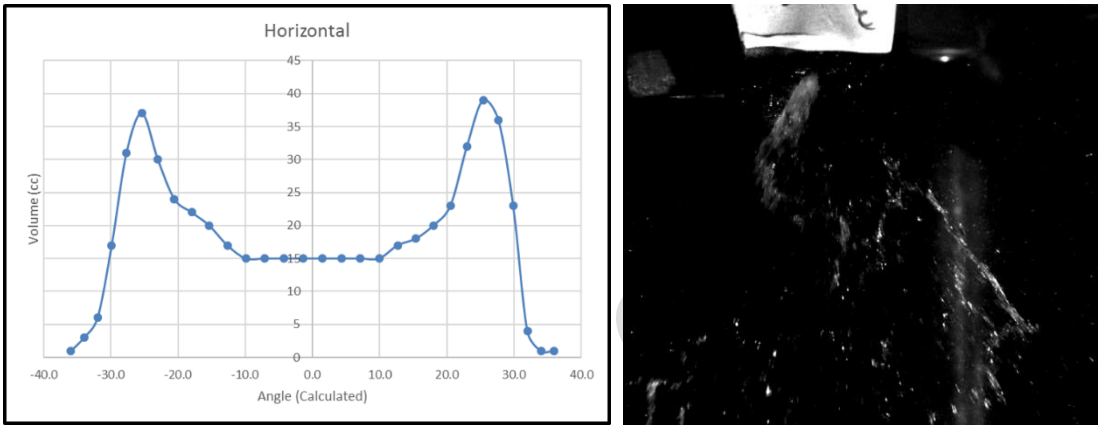

Figure 6-16: Spray distribution (left) and high speed image (right) for 70° Honda nozzle from experimental testing

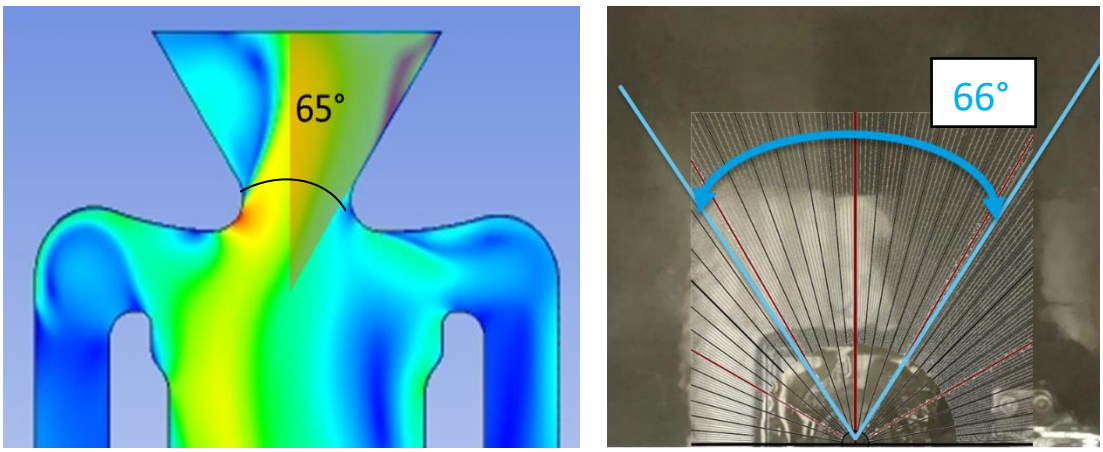

Figure 6-17: Spray angle results for 65° Honda nozzle from CFD (left) and experimental (right)

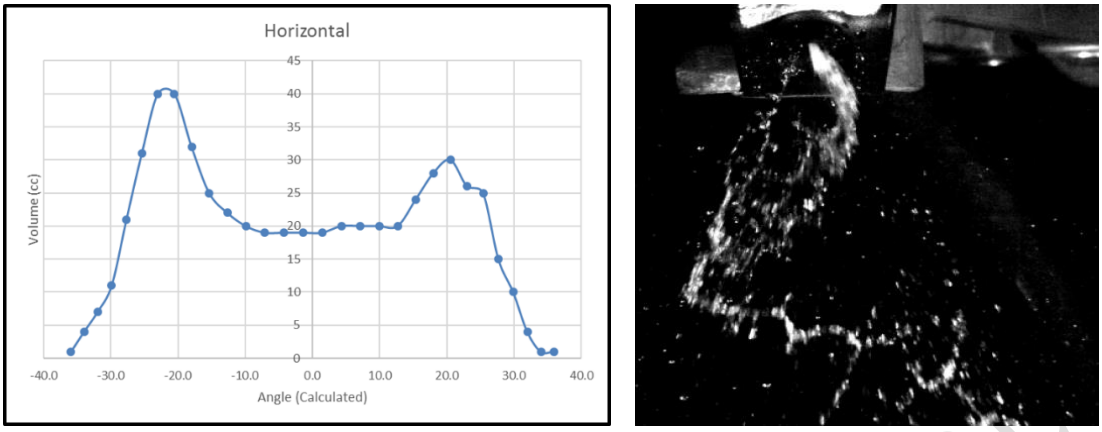

Figure 6-18: Spray distribution (left) and high speed image (right) for 65° Honda nozzle from experimental testing

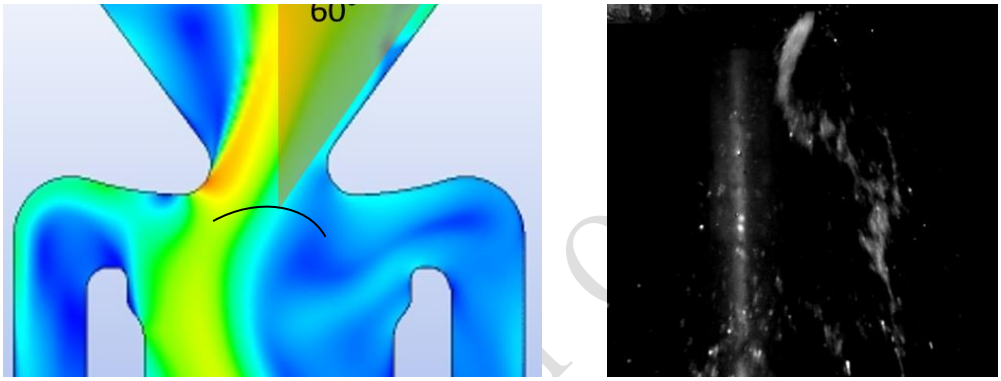

Figure 6-19: Spray distribution (left) and high speed image (right) for 60° Honda nozzle from experimental testing

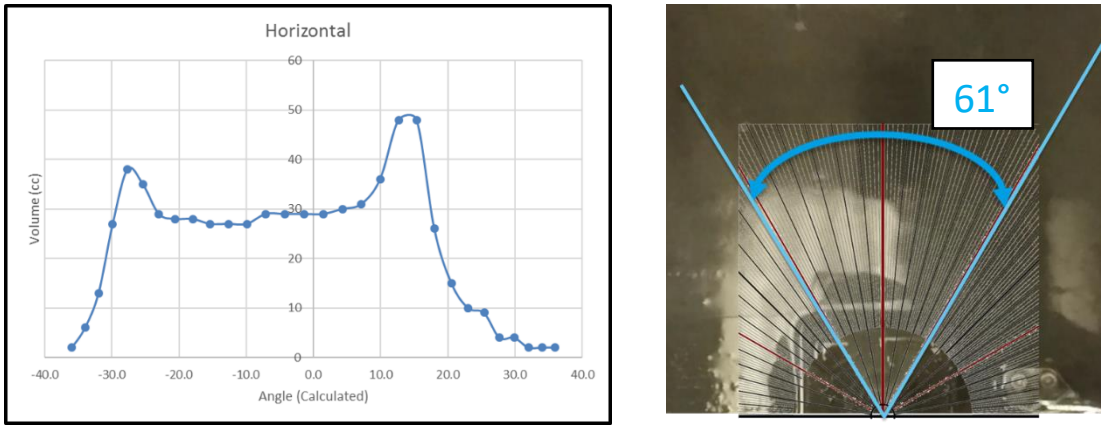

Figure 6-20: Spray angle results for 60° Honda nozzle from CFD (left) and experimental (right)

The final designs for the range of nozzles with different spray angles and mass flow rates designed for Honda are shown in the table below (Table 6-1). The Nissan nozzle is shown in the table to show the differences between the fluidic chips developed for Honda and the original previous design. The numbers within the table represent the key feature points shown in Table 6-1, where ① is the outlet angle, ② is the outlet width and ③ is the feedback chamber width.

The spray angles and mass flow rates data were given to Honda and subsequent discussion resulted in proceeding with nozzle 1 with the spray angle of [redacted] and mass flow rate [redacted]. These measurements were taken through the same process as when the competitor nozzles were benchmarked in 2. Experimental Benchmarking Analysis.

Table 6-1: Final Honda nozzle design dimensions

Design	① (°)	② (mm)	③ (mm)	Angle achieved (°)	Mass Flow Rate (ml/s)
0 (Nissan nozzle)	40	[redacted]	[redacted]	[redacted]	[redacted]
1	75	[redacted]	[redacted]	[redacted]	[redacted]
2	70	[redacted]	[redacted]	[redacted]	[redacted]
3	65	[redacted]	[redacted]	[redacted]	[redacted]
4	60	[redacted]	[redacted]	[redacted]	[redacted]

6.2.2.2. Dynamic Spray Distribution Testing

In addition to the testing conducted for the spray angle and mass flow rate analysis, the Honda nozzle also underwent dynamic testing. Dynamic testing is similar to spray distribution analysis however with the nozzle attached to a vehicle travelling at speed and when stationary. The object of the experiment is to show where the water encounters a vehicle windscreen at a series of velocities to examine the amount of dropdown experienced and ensure that the spray always hits within the C-Zone (Figure 6-21). From this data it is possible to know whether the nozzle is suitable for operation.

Figure 6-21: C-Zones on Vehicle Windscreen

Knowledge of where the water encounters the windscreen is vital as the windscreen must be fully clean, and secondly the windscreen wipers will react poorly to dry-wipe areas. Through real world experimentation it was possible to see with clarity whether the nozzle designed was fit for purpose. It also gave a chance to calculate the appropriate angle for the nozzle eyeball to be mounted to ensure the spray hit within the C-zone at speed and when stationary, achieving the target specified by the manufacturer.

It was expected that when the vehicle was travelling at increased velocities the spray distribution would not travel as far up the windscreen of the vehicle. This was hypothesised because with the increased velocity of the vehicle, the fluid would reach the windscreen more rapidly, decreasing the amount of time allowed for the spray to be projected in the vertical axis. The top of the distribution would likely alter more greatly than the bottom due to the angle of the nozzle as at the top of the distribution the spray angle from the nozzle would be much greater and would be more greatly affected by the time reduction of the impact to the windscreen.

6.2.2.2.1. *Method*

Two images below show the setup of the apparatus used in the experiment to test the spray impact and dropdown dynamic testing (Figure 6-22 - Figure 6-23). The apparatus used in the experiment is listed below:

- Vehicle with nozzle attached to test jig
- 12V car socket connector
- Tank and pump
- Timer switch

- Multi-meter
- Hose assembly
- Circular stickers on vehicle windscreen to mark area of interest
- Camera

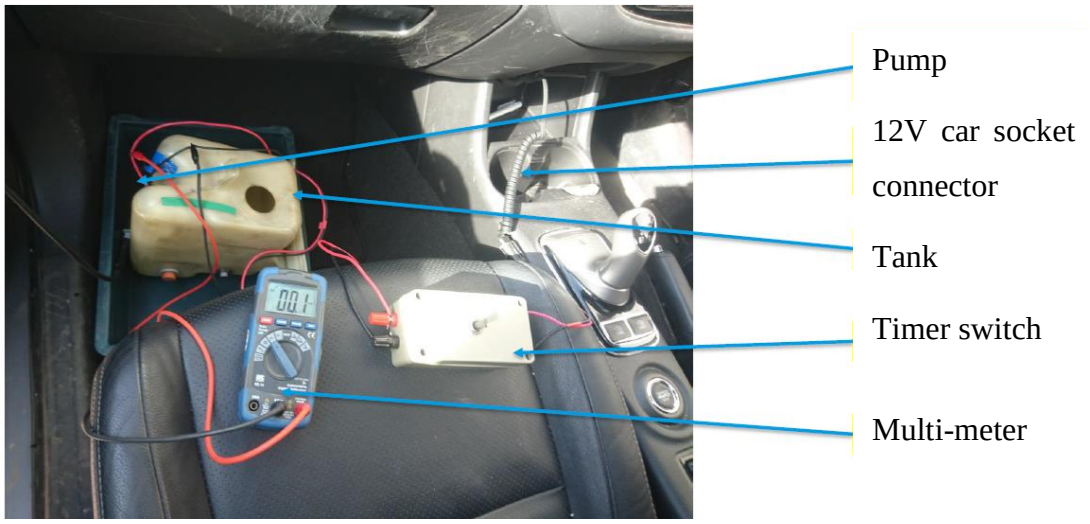

Figure 6-22: Interior apparatus assembly

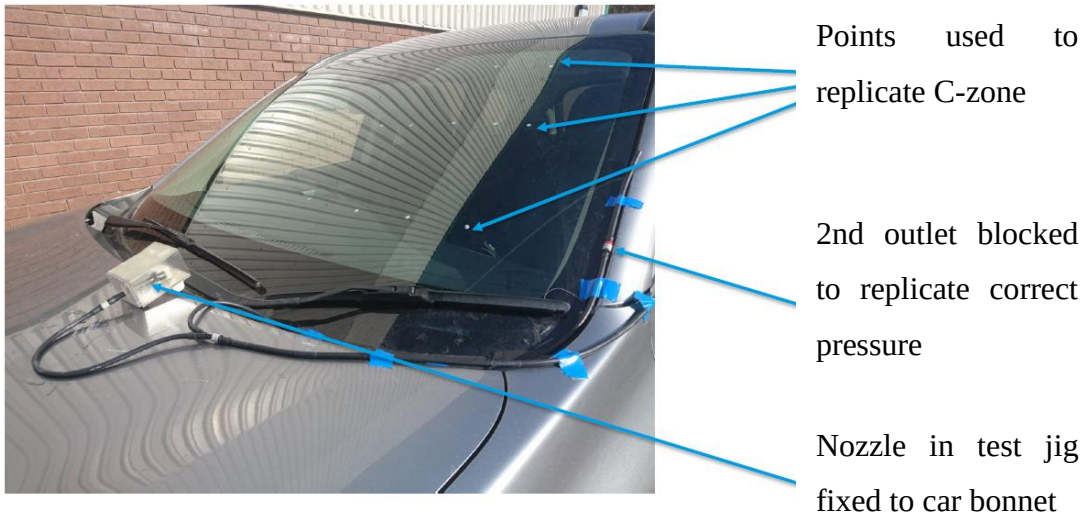

Figure 6-23: Exterior apparatus assembly for dynamic testing

The experiment setup was designed by Kautex Textron CVS Ltd specifically to measure the areas that the spray from a nozzle covers. The nozzle is positioned in a test jig mounted on the bonnet of the car and the chip is pointed to a specific position on the windscreen determined to be preferential for real-life use, the positioning of the nozzle is taken from a CAD study performed by Kautex.

The power for the pump and other apparatus was supplied by a 12V, the voltage at the pump was measured by the multi-meter to be 12.4V. The pressure for the nozzle

in operation was 290kPa, the ambient temperature was between 15-20°C. The timer switch was used to operate the nozzle at the various velocities required for testing, the velocities the spray was analysed at are 0kph, 80kph, 100kph and 120kph.

Small white circles were added to the vehicle windscreen to better enable the visualisation of where the water reached and the dry areas of the surface where the water didn't encounter. Photographs were taken of the spray to record the distribution of the water on the windscreen. The perimeter of the sprayed area on the windscreen was outlined in various colours corresponding to the velocities tested at on a CAD version of the windscreen to easily visualise the comparative differences in the distribution with the change in velocity.

6.2.2.2.2. *Variables*

The fixed variables in this experiment were the vehicle, the positioning of the nozzle relative to the vehicle, the voltage delivered to the pump, the pressure at the nozzle, the fluid being used and the amount of time that the water was sprayed onto the windscreen.

The independent variables were the velocities the nozzle was tested at and the angle at which the nozzle was positioned.

The dependent variable was the spray distribution achieved.

The only variable that could not be controlled was the atmospheric temperature however it did not alter greatly throughout the testing as the tests were performed all on the same day in the same location, there was a maximum temperature change of 1°C.

6.2.2.2.3. *Results*

The spray distribution found was illustrated and superimposed onto the windscreen with coloured zones for the desired distribution, the range of velocities are shown in one image (Figure 6-24). This allowed comparison of the upper and lower limits of the spray to show how much it differed with greater speeds and ensure it remained within the target zones. Six main points of the spray distribution were chosen to describe the distribution of water, this enabled accurate calculation of how much the spray changed with velocity (Table 6-2).

Table 6-2: Spray distribution change with velocity change

	Bottom of Spray (mm)			Top of Spray (mm)		
Speed (kph)	Left	Centre	Right	Left	Centre	Right
80	[redacted]					
100	[redacted]					
120	[redacted]					

Table 6-3: Key for Figure 6-24 and Figure 6-25

Pink	Purple	Blue	Yellow	Red	Green	Blue	Black
0kph	80kph	100kph	120kph	Driver side target	Overall target (Zone C)	Maximum spray zone	Wiper coverage

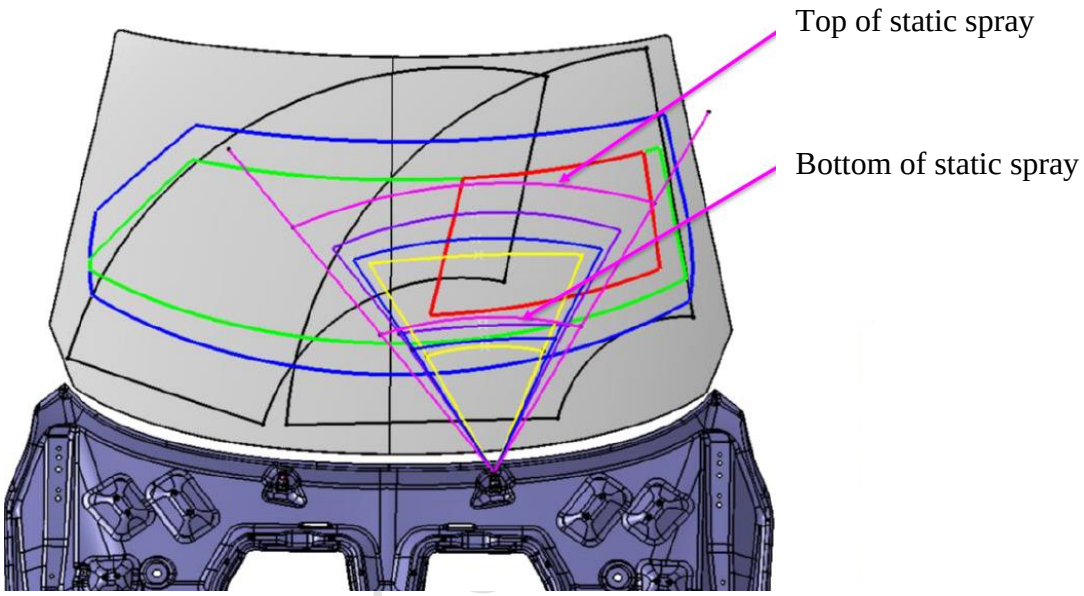

Figure 6-24: Spray distribution on windscreen at multiple vehicle velocities

The initial angle for attack for the testing was determined by past research and experience from designers in the Kautex Textron CVS Ltd development team. However, through the experimental testing it was discovered that the ideal angle of attack for the nozzle is at nominal – straight forward towards the windscreen (Figure 6-25). The reason for additional testing at [redacted] from nominal was that this was the preferential angle in the CAD analysis produced by Kautex Textron CVS Ltd. By changing to this new angle there was an elimination of overspray in static conditions in addition to a reduction in the dropdown, the rate that the spray distribution descends at higher velocities.

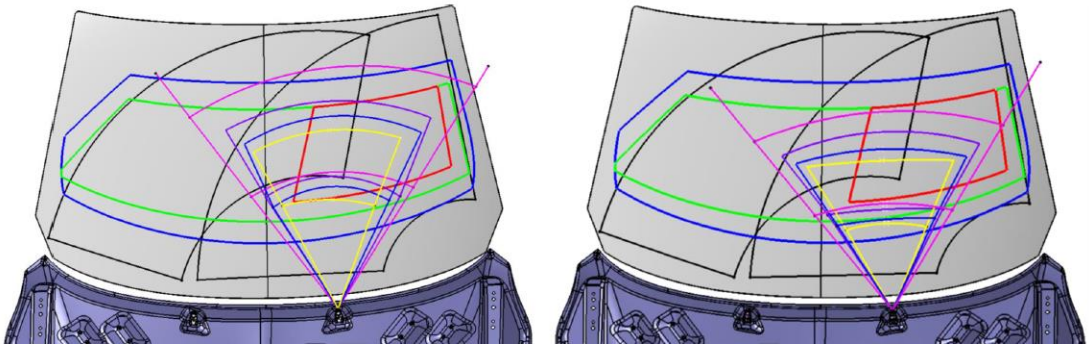

Figure 6-25: Attack angle 16.5° from nominal (left) and 0° from nominal (right)

From the data collected it was possible to see that the water spray distribution descended through the windscreen area with increased vehicle velocity and the angle of spray was compressed with higher velocity (Table 6-4). This is due to the reduced amount of time allowed for the spray to reach the windscreen surface, giving the water droplets less time to spread out from the nozzle. A second possible reason for the less widespread deposition of water is that the velocity from the surrounding air influences the boundaries of the spray so that they travel at an angle closer to parallel to the vehicle velocity.

Table 6-4: Spray angle at multiple velocities

Speed (kph)	Spray Angle (°)
0	[redacted]
80	[redacted]
100	[redacted]
120	[redacted]

6.2.2.2.4. *Discussion and Conclusions*

It was proven in the experiment conducted that the greater the velocity of the vehicle, the lower the positioning of the distribution of spray on the vehicle. However, by angling the nozzle at a more perpendicular angle to the nozzle body it is possible to decrease the original angle of attack and therefore the rate that the spray distribution moves by with increased speed.

It was shown that with the increase of velocity there is a spray angle reduction, this is due to the reduced amount of time allowed for the water to spread in the air before deposition on the windscreen. Further study would be required to determine whether the velocity of the surrounding air has an effect on the longitudinal boundaries of the spray.

The majority of the spray for this nozzle fell within Zone C (Table 6-3) which is ideal for the specification given by the manufacturer. It was not possible to eliminate the deposition of water outside Zone C, as evidenced by Figure 6-25 showing the static spray distribution being slightly below the zone, however it is within the maximum spray

zone. It was not possible to eliminate dry-wipe areas for this nozzle; however, the new angle positioning of the nozzle greatly minimised the area of windscreen which does not receive a deposition of fluid.

6.2.3. Nozzle Selection for Design Loop One

Utilising the data from the initial prototype testing and the dynamic spray distribution testing it was possible to recommend and supply Honda a nozzle that was suitable for their specification. The prototype testing had ensured that a fluidic chip with the optimum properties to suit the spray angle and mass flow rate targets given by the customer were met. The dynamic testing of the nozzle ensured that the nozzle would be appropriate when the vehicle was both travelling at speed and when static.

The nozzle was then sent to Honda for the company to conduct their own test situations and to compare to the existing nozzle being utilised by the company. After thorough testing from Honda there was feedback that the nozzle sent to them by Kautex Textron CVS Ltd had fallen short in testing when compared to the competitor nozzle supplied by a competing automotive washer system supplier. There was a change to the specification given by Honda, therefore it was necessary to create a second design loop to process and develop the nozzle to suit the new requirements.

6.2.4. Spray Concentration and Drop-Down Development

When Honda put the nozzle through their testing it was found that the nozzle was generating too small a mass flow rate for their new desired output, the edges of the fluidic nozzle did not contain as high a percentage of spray as was anticipated and that there was too large a change in spray positioning for static and dynamic testing. Therefore, there was a requirement to adjust the nozzle to ensure that the Honda client was happy.

Below Figure 6-26, shows the comparison between the competitor nozzle and the nozzle submitted by Kautex Textron CVS Ltd. Here it shows that the Kautex nozzle spray did not hit the windscreen at the predetermined height of the C-Zone when the vehicle was travelling at 120 kmh^{-1}, whereas the Bowles nozzle did meet the revised specification. The testing by Honda showed that the dropdown experienced by the competitor nozzle was half of that which was experienced by the Kautex nozzle, therefore there was a requirement to reduce this amount to be more in line with the specification.

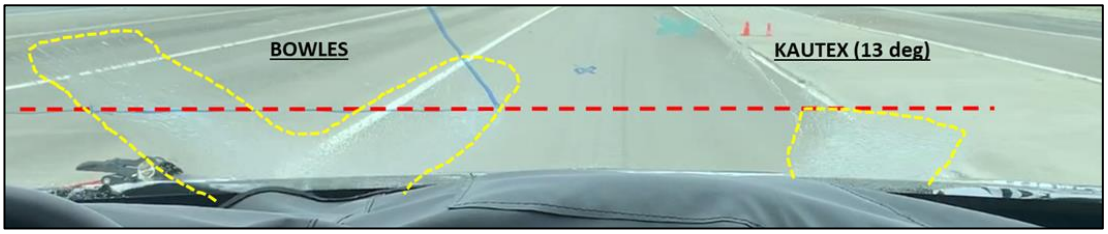

Figure 6-26: Comparison of Kautex (right) and Bowles (left) spray distribution at 120 kmh^{-1}

A minor issue experienced by the testers at Honda was that one in every batch of 6 nozzles supplied was faulty, with a spray distribution which was not in-line with the developed nozzle. With this abnormal nozzle a consistently narrowed spray was experienced (Figure 6-27), meaning that there was a major fault in the design of one of the mass production cavities. An exhaustive analysis of the production process was required to find the fault in the system, which was a defective cavity in the mould for the fluidic chip components. This was resolved by tightening the tolerances on the mould cavities in line with the key features found in the previous tolerance study to produce the spray shown in Figure 6-28 and Figure 6-29.

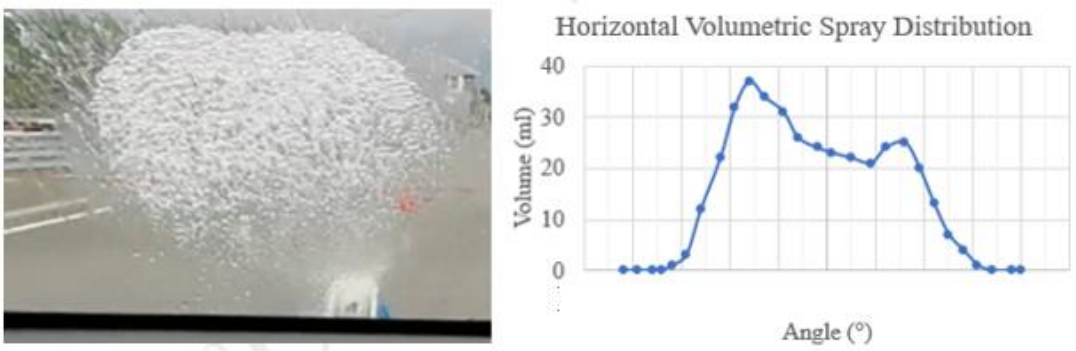

Figure 6-27: Abnormal Honda nozzle spray distribution at speed (left) and graphically (right)

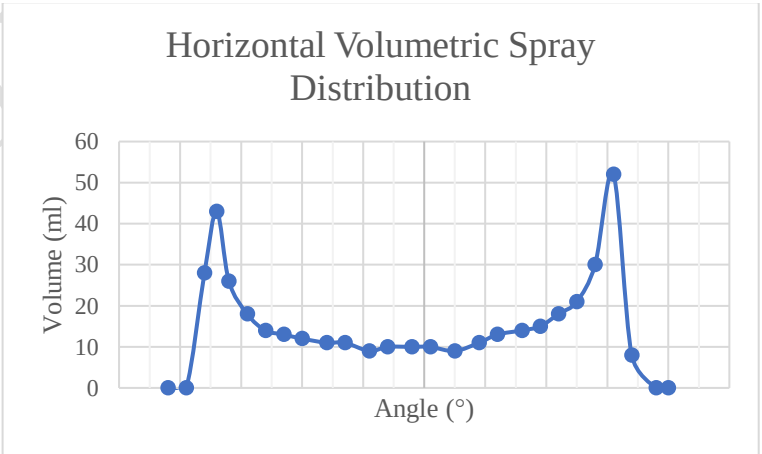

Figure 6-28: Spray distribution of Honda fluidic chip with tightened tolerance limits

Figure 6-29: Spray distribution at speed for Honda fluidic chip with tightened tolerance limits

Below is an image showing the spray of a Kautex nozzle and a competitor nozzle when travelling at 120 kmh^{-1} (Figure 6-30). There is a much greater concentration of water at either end of the spray for the competitor nozzle than the Kautex nozzle, where there is visually more water between the two concentration points. This twin-peaked distribution of spray was a high priority for Honda therefore research was needed to find a method to facilitate this requirement.

The next section detail how these issues were resolved to improve the nozzle so that it would meet the revised specification from Honda.

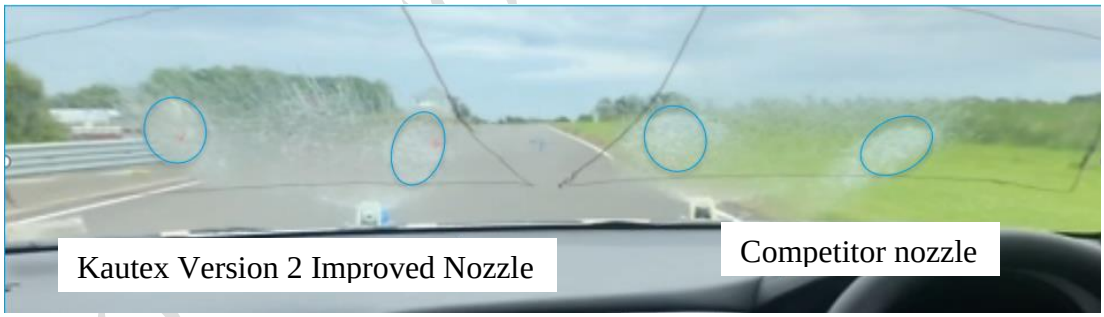

Figure 6-30: Spray concentration on windscreen for Kautex nozzle (left) and competitor nozzle (right) at 120 kmh^{-1}

6.2.4.1. Mass Flow Rate

Rather than change the internal geometry of the fluidic chip which could be detrimental to the other properties of the spray, in this situation it was possible to alter the nozzle body to alter the mass flow rate through the nozzle. The body geometry was altered to be more streamlined so that the water would travel more linearly causing minimal turbulence and increasing the mass flow rate into the fluidic chip (Figure 6-31).

The modifications to the nozzle body included moving the spring mechanism to the rear of the nozzle body, adding flow guides and reducing the length of the nozzle leg. The purpose of these design changes was to reduce the possibilities of eddies of flow occurring which could cause turbulence, increasing the linearity of the flow and therefore the velocity and mass flow rate into the nozzle.

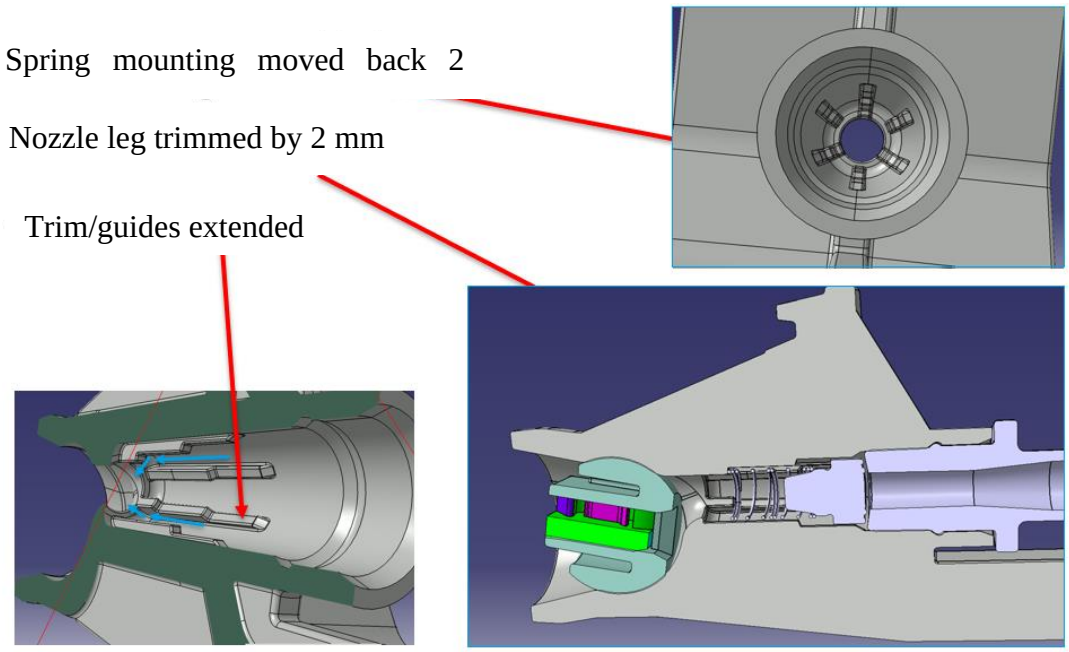

Figure 6-31: Honda nozzle body modifications

These modifications were completed by the internal development team at Kautex Textron CVS Ltd who have vast experience in the feasibility and efficacy of changing components within the nozzle bodies. Through these design changes a sufficient increase in mass flow rate was experienced to satisfy the specification by Honda.

In addition to changing the mass flow rate of the fluidic chip, these design changes also changed the pressure at which the nozzle the fluidic chip operated. This resulted in an increase in the Reynolds number of the fluid within the nozzle, subsequently decreasing the size of the droplets formed by the fluid as evidenced by past research into spray characterisation by Semião et al. [70].

With a reduction in size of droplets there is a reduced dropdown experienced by particles emitted from a nozzle [71]. This means that by increasing the mass flow rate of the nozzle by altering the nozzle body geometry the issue of dropdown was reduced sufficiently to be able to produce a spray which consistently hit the windscreen within the C-Zone.

6.2.4.2. Spray Concentration

Very little research on how to change the concentration of the different parts of the spray distribution from a fluidic nozzle. Therefore, some exploration and experimentation of the nozzle geometry was required to satisfy Honda's requirement for a heavier ended spray.

Through close inspection of the fluid from the past experiments in the research utilising the Photron Fastcam high speed camera and the CFD studies it was possible to see that the distribution of water is influenced by the time spent at each end of the spray angle cone. Through manipulation of the oscillation rate it was possible to change the distribution of the water spray emitted from the nozzle.

It was theorised that by increasing the amount of time for the water to change from side to side the flow would remain at one side for an increased period of time, resulting in a higher concentration of spray at each end. Secondly, as the current nozzle was producing a moderately heavy ended spray with the current oscillation rate, it was possible that simply increasing the oscillation rate would solve the issue as there would be a higher proportion of time spent at each end overall.

Past research by others shows that one of the key factors relating to the oscillation rate is the mass flow rate [72] [73] and therefore the speed at which the separation bubble within the internal chamber grows [68]. Unfortunately for this occasion the changes made to alter the mass flow rate have not sufficiently altered the spray distribution to change the spray distribution to concentrate the spray at the edges of the spray. Therefore, it is necessary to find a different way to change the oscillation properties.

The oscillation frequency in a microfluidic oscillator is comprised of transmission time and switching time. The switching time, τ_s, is the time it takes for the fluid to move from one side of the nozzle to the other and the transmission time, τ_t, is the period of time at which the nozzle remains at one of the sides. This results in the following equation to express the oscillation time period, T, for a microfluidic oscillator [74]:

$$T = 2(\tau_t + \tau_s) \tag{6.2}$$

The current frequency for the Honda microfluidic oscillator nozzle was [redacted], with a 1:2 ratio of switching time to transmission time.

To increase the concentration at the edges of the distribution it is necessary to increase the transmission time or decrease the switching time. The transmission time is determined by the time it takes for a separation bubble to form and grow sufficiently large for the fluid flow to become deflected and start to switch. Therefore, one method that can be utilised to increase the transmission time is to increase the amount of time for required for the fluid to travel through the feedback channels. This can be accomplished by increasing the length of the feedback channels or by decreasing the velocity of the fluid in the feedback channels [75].

Due to the restriction of the size of the fluidic chip the decision was made to investigate how to decrease the velocity of the fluid. Due to the complex geometry within the fluidic chip several designs were produced, but the key features remained the same to ensure that no detrimental effects would occur due to the changes in geometry.

The first geometry change was to decrease the length of the fluidic oscillator within the chip. This geometry alteration was driven by the theory that with a decrease in the length of the chip there would be a decrease in time allowed for the velocity to accelerate in the internal chamber.

A second study was conducted which involved reducing the volume of the overall oscillator by either decreasing the height of the fluidic chip or by scaling down the whole fluidic chip.

Below is the geometry and the velocity vector distribution within the fluidic nozzle with the decreased length of fluidic oscillator (Figure 6-32 - Figure 6-33). Unfortunately for this case although there was fluid flowing through the feedback channels, there was not sufficient space for the water in the fluidic chip to sufficiently deflect to cause oscillatory motion, instead the water flowed relatively straight from the inlet to the outlet.

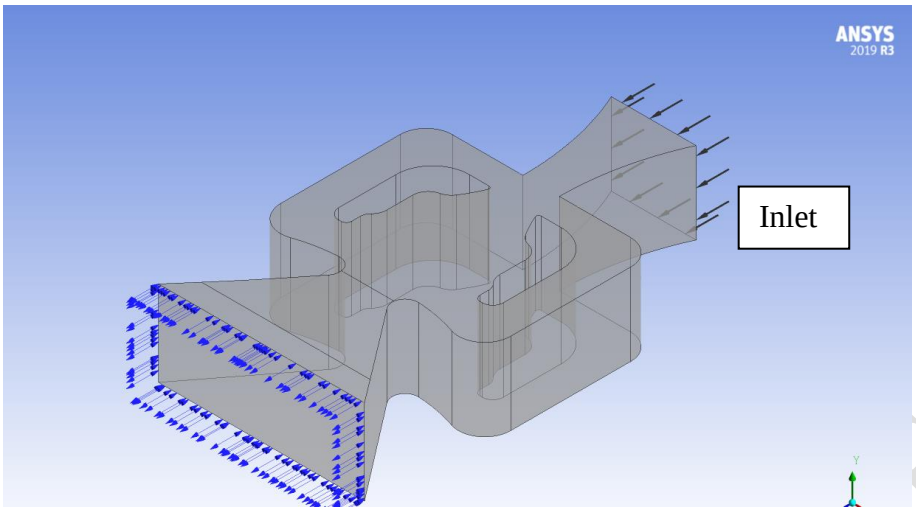

Figure 6-32: Decreased length Honda concept geometry

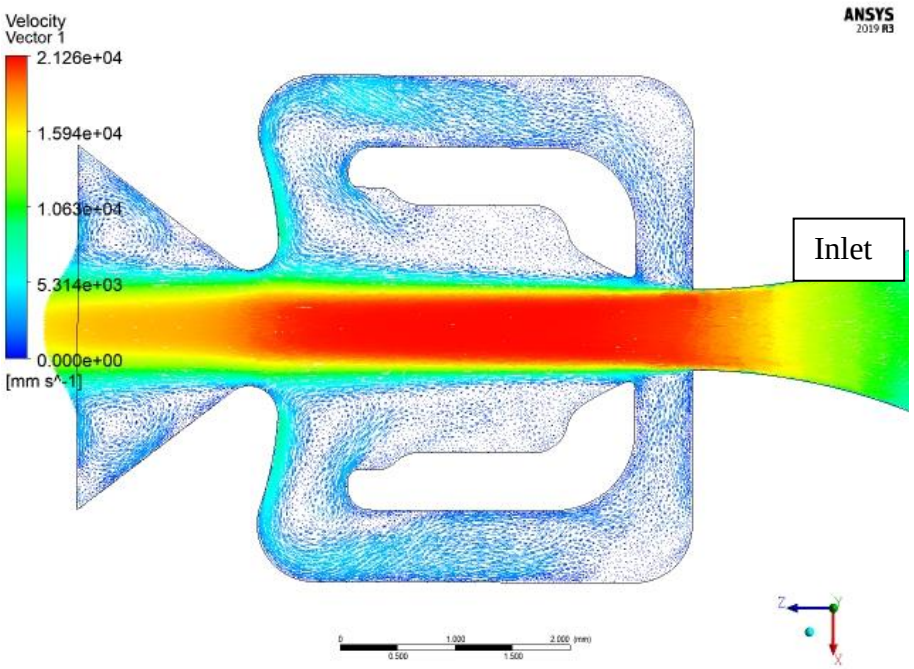

The short concept design for the fluidic nozzle no longer functioned as a fluidic nozzle. The fluid flowed straight from the inlet to the outlet without any diversion, this was because the fluid did not have enough space to develop and interact with vortices in the internal chamber.

Due to the shortened length concept not functioning correctly, a second design with a decreased length mid-way between the original design and the above concept was developed. The geometry of this chip included a length which was shortened by half the amount that the earlier short concept included (Figure 6-34). The fluid flow results from the CFD study are shown below (Figure 6-35).

Initially there was some deflection of the fluid to create an angled flow at the outlet in the mid-length concept design, however as more time elapsed the fluid became more linear (Figure 6-35).

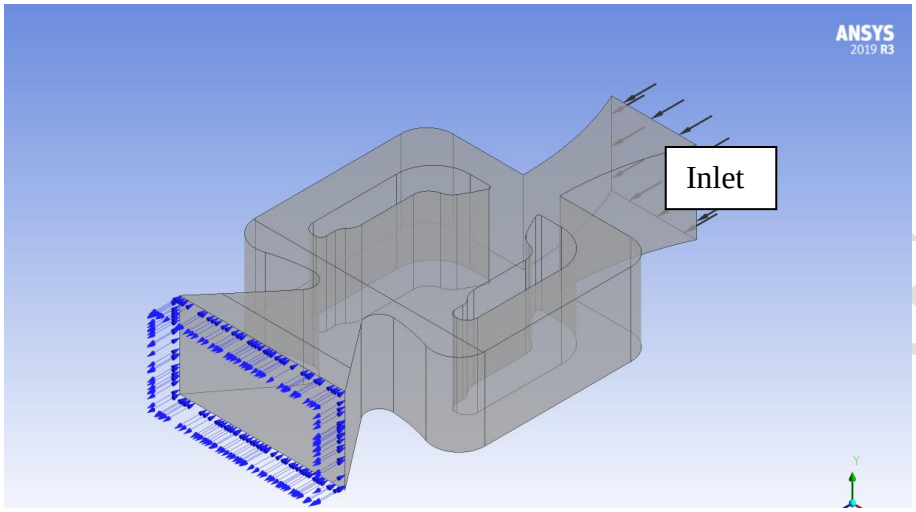

Figure 6-34: Mid-length Honda concept geometry

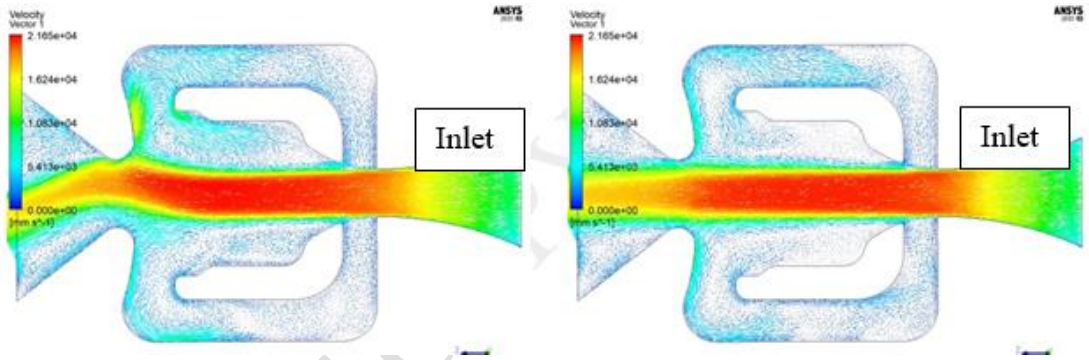

Figure 6-35: Mid-length Honda concept fluid-flow (left) and resulting fluid flow (right)

to amend the design to decrease the likelihood of the linear flow of the water and to increase the chance of the Coanda effect occurrence. A design with the same length as the above design but with a narrowed oscillation chamber was created (Figure 6-36). The CFD fluid flow results for this design are shown in Figure 6-37.

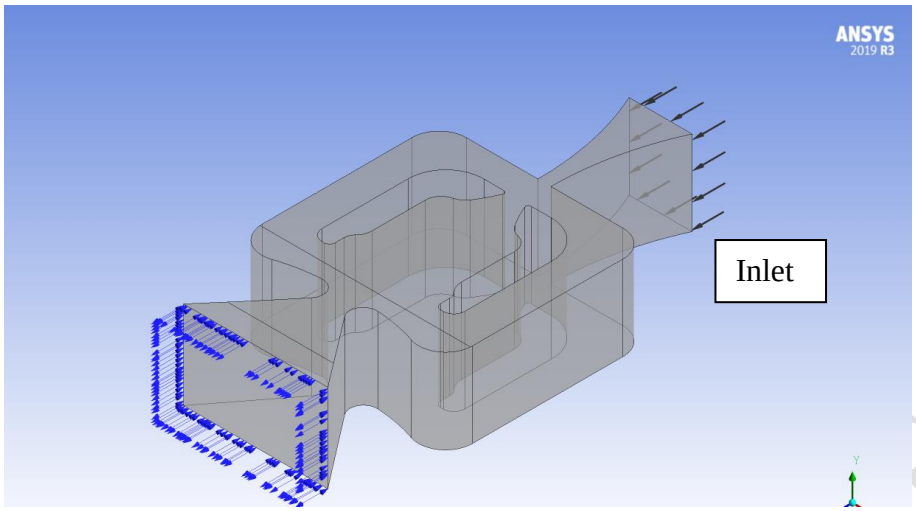

Figure 6-36: Narrow mid-length Honda concept geometry

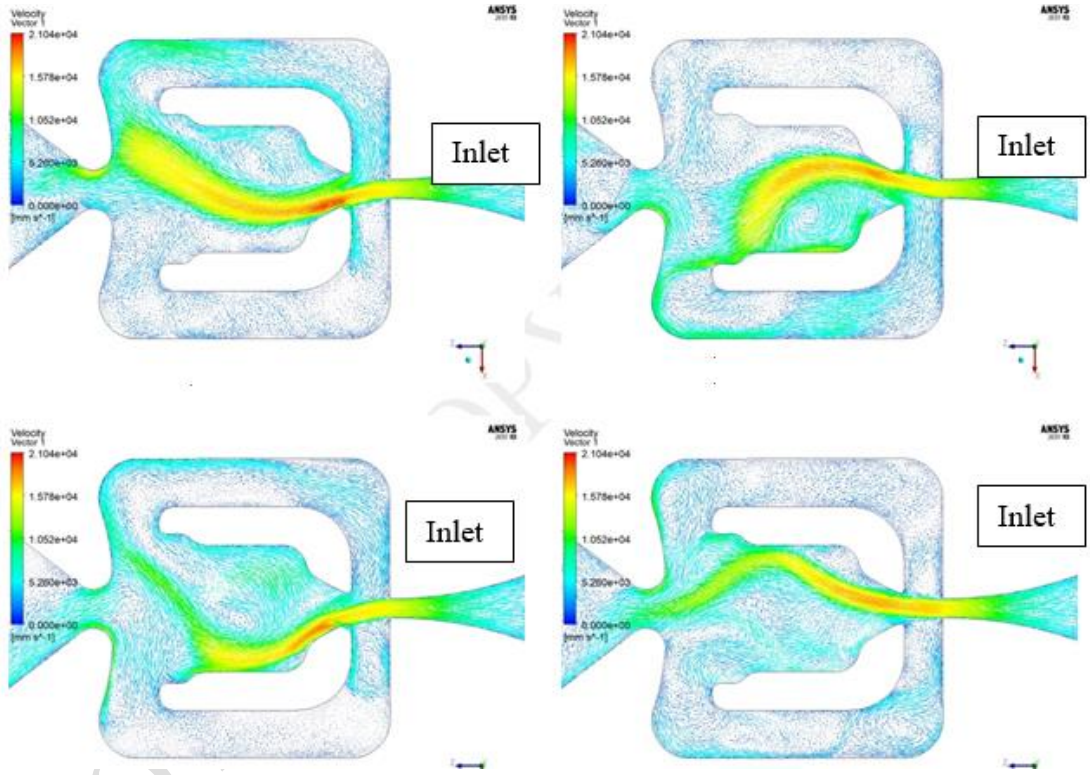

Figure 6-37: Fluid flow images within narrow mid-length Honda concept abnormal flow

oscillatory flow which was much faster than the original design. However, the oscillatory motion within the nozzle was unusually unsteady resulting in the flow not consistently switching from one side to the other and instead causing the flow to begin flowing toward one side and then reverting back to the original side without touching the opposite side. This phenomenon occurred because there was a very small outlet width, resulting in more fluid flow into the feedback channels and distorting the internal motion usually expected in a fluidic nozzle. This made this concept and other narrow design fluidic chips unfeasible.

The next concept considered was a design where instead of changing a particular aspect of the fluidic chip geometry, the fluidic chip was simply scaled down to 80% of the original design size (Figure 6-38). By scaling down the geometry but keeping the inlet pressure constant it was hoped that the overall velocity within the fluidic chip would increase, therefore decreasing the switching time.

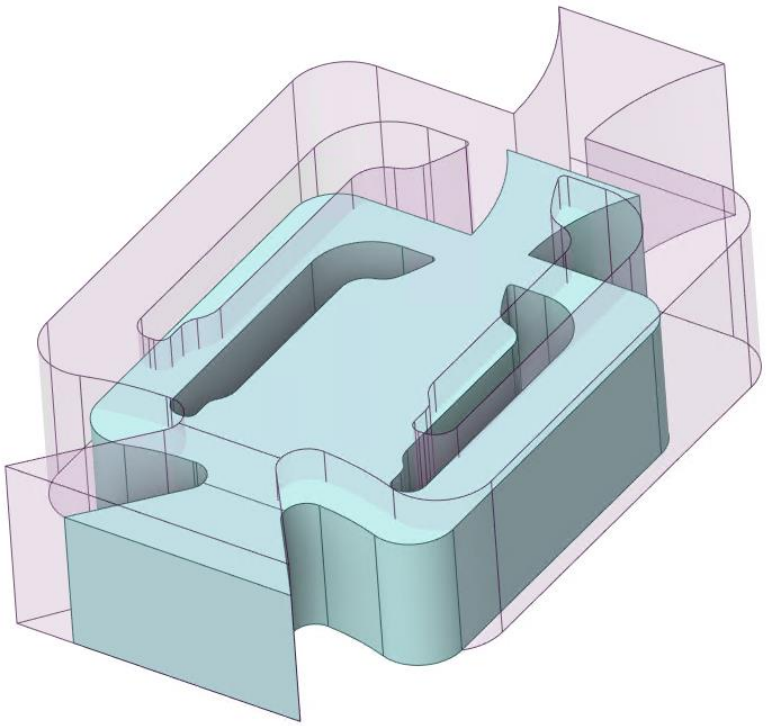

Figure 6-38: Geometry comparison between original design (purple) and 80% scale (blue)

The resultant flow from the scaled fluidic chip created an oscillatory flow which was consistent and predictable (Figure 6-39). The oscillation frequency in this concept was increased from the original design of [redacted] to [redacted], however unfortunately the ratio of switching time to transmission time increased to 5:8.

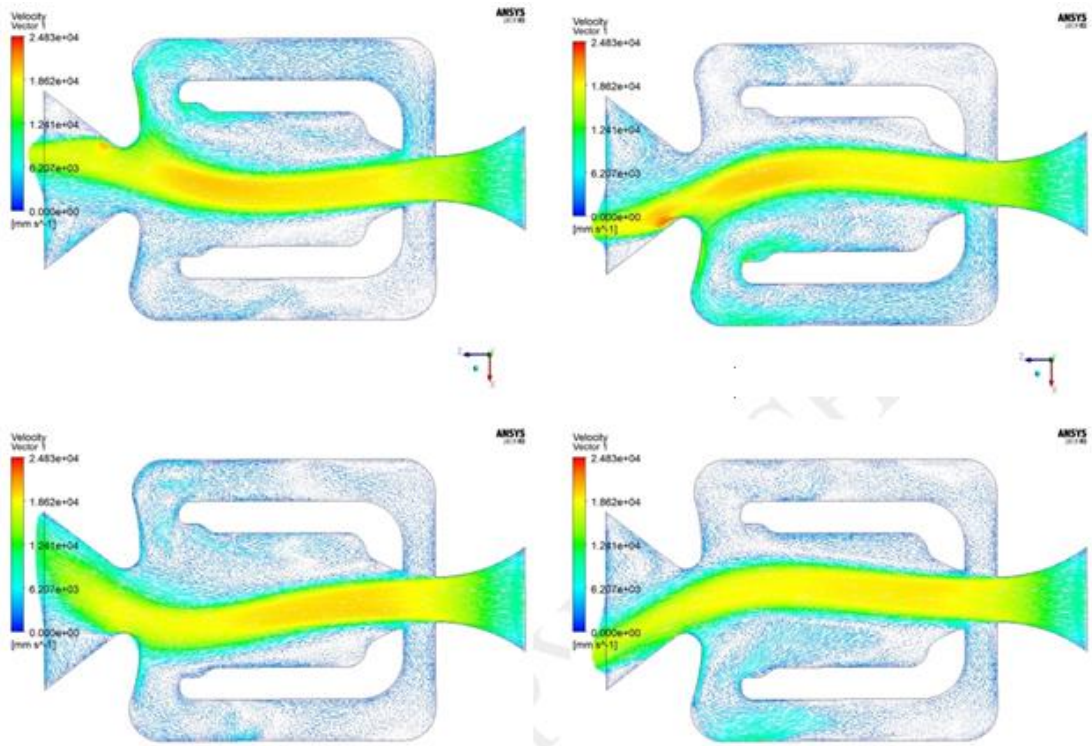

Figure 6-39: Fluid flow images within scaled 80% Honda concept fluidic chip

A secondary side effect of decreasing the scale of the nozzle was that the spray angle achieved in this design was decreased at points in the flow cycle. The image series shows maximum internal deflection of the fluidic chip but an inconsistent spray angle at the outlet portion of the chip.

Deteriorating results are consistent with past results into aspect ratio within fluidic oscillators [76]. Where a change in aspect ratio changes the boundary layers sufficiently so that the fluid is only minimally affected by the viscous sublayer, therefore becoming more laminar in flow distribution and no longer oscillating at large aspect ratios.

The final design modification undertaken involved a more drastic change to the geometry whilst still maintaining the geometrical dimensions to fit within the nozzle chip design (Figure 6-40). This design instead of taking a change in velocity approach to altering the oscillation rate altered the length of the feedback channels. This will increase the switching time as there will be a greater distance for the

recirculating flow to travel before interacting with the main flow from the inlet, resulting in a greater time for the separation bubble to increase in size.

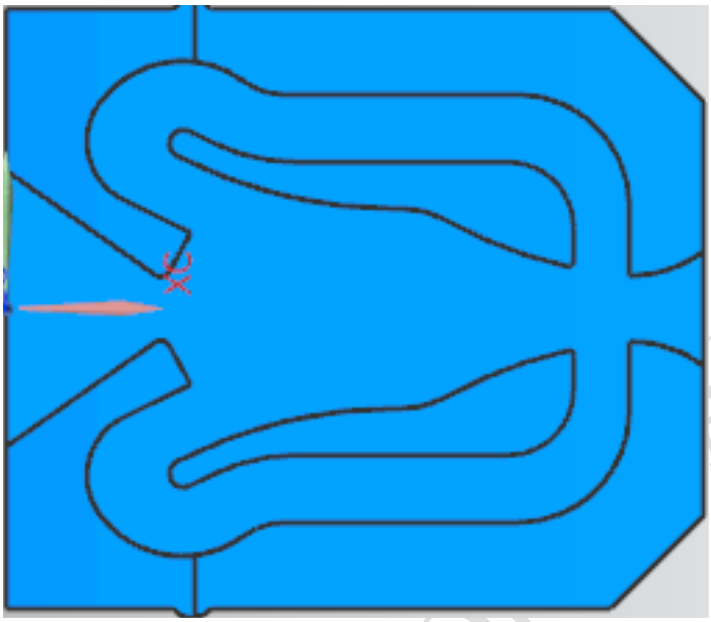

Figure 6-40: Fluidic chip geometry with extended feedback channels

Unfortunately, at the time that this concept was created, access to ANSYS CFD software was unavailable therefore there are no simulation results. Therefore, testing of this chip design experimentally was necessary.

Initially a photograph was taken of the spray emitted from the nozzle to examine the visible distribution of spray, this is shown in Figure 6-41. The spray distribution results from the spray angle photograph were positive, the spray consisted of dense peaks of spray seen at either end combined with a much lighter central spray.

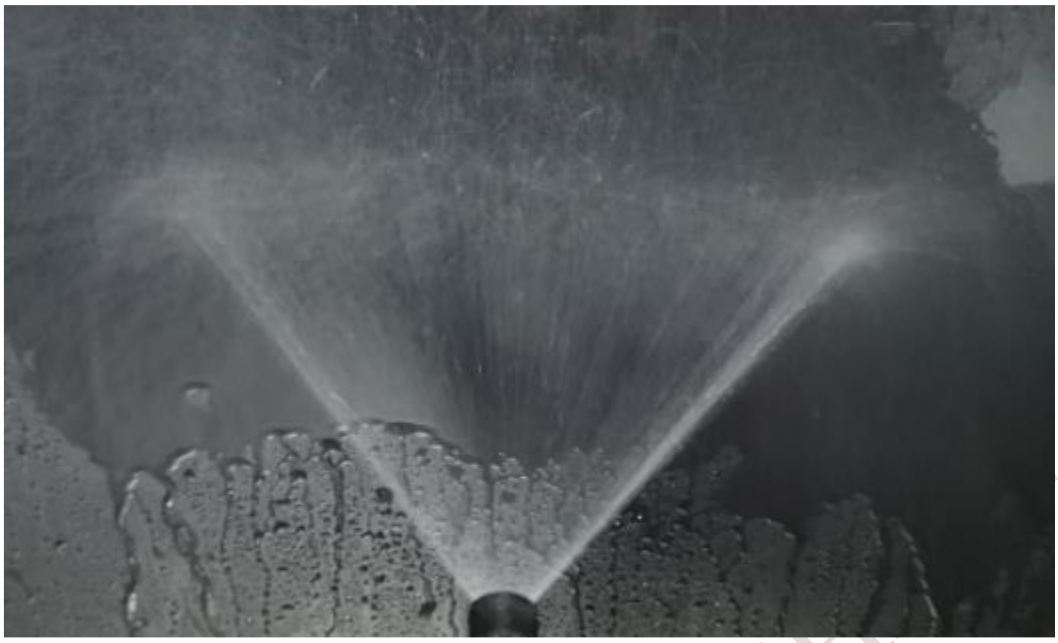

Figure 6-41: Image capture of spray from Honda concept with elongated feedback channels

The success of the image capture of the spray when in use, meant that next the spray distribution testing was used to examine the spray distribution (Figure 6-42). Unlike past spray distribution graphs, this volumetric diagram shows the volume discharged by the nozzle at each degree angle from the nozzle. This graph type was used instead of the traditional volumetric spray vs distance as it gives a more accurate visualisation of the water being produced by the nozzle and whether there are peaks in concentration at the appropriate parts of the distribution.

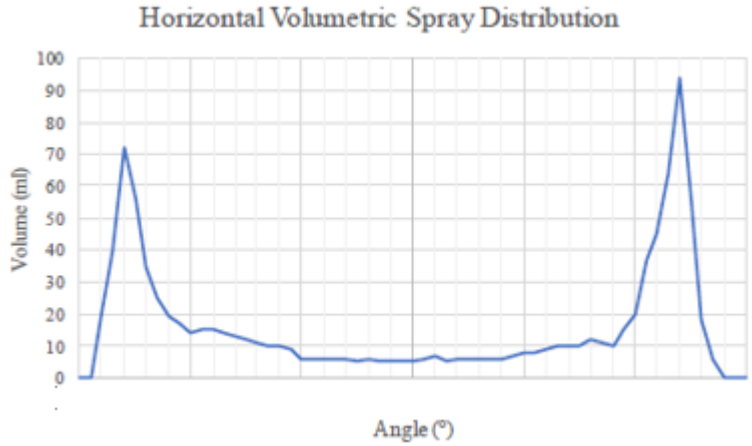

Figure 6-42: Spray distribution for Honda concept with elongated feedback channels

6.2.5. Conclusion

Through the design and development of the Honda fluidic chip a great deal of knowledge was acquired concerning how internal features and geometries can alter the flow of water for this nozzle. The main driving force behind the spray

distribution and concentration of the fluid was the oscillation rate and the ratio of transmission time to switching time. By altering a part of the feedback channel, it was possible to completely change the oscillation rate and therefore how the nozzle discharged the water to create a spray output matching the one desired by the customer.

If the part is not used after testing by Honda, this project remains an achievement as a great deal was learnt about the behaviour of fluidic nozzles and utilising specific changes in geometry to influence the spray output. This will aid in future designs of fluidic chips at Kautex Textron CVS Ltd.

6.3. Toyota Nozzle Project

The final nozzle designed and developed through this project was for the car manufacturer Toyota. This project initially ran concurrently with the Honda project; however, this was pushed back as the Honda deadline was brought forward.

The following design developments occurred between the finalisation of the original Honda concept and the secondary developments in-line with the new Honda specification. Unfortunately, it was not possible to create a final design for this nozzle due to the refocus on Honda to meet the customer deadline. Despite this, valuable actions were performed in the design stages to aid in future design enhancement by Kautex Textron CVS Ltd.

6.3.1. Specification

The nozzle specification for this nozzle differed from the previous two designed in that Toyota specified a nozzle with a 4-peak spray distribution (Figure 6-43). This presented a complex challenge as this design concept had not been seen before by Swansea University or Kautex Textron CVS Ltd. According to the legal department at Kautex Textron, the current methods of achieving this output have been patented, therefore a completely new concept for producing twice the normal number of peaks was required.

This meant that it would not be possible to utilise a stepped outlet as seen in the Toyota nozzle previously benchmarked (Figure 2-4) or a double type outlet as seen with the Ford Eco Sport nozzle (Figure 2-3). Instead, a new way of producing a distribution with four peaks of water concentration needed to be investigated.

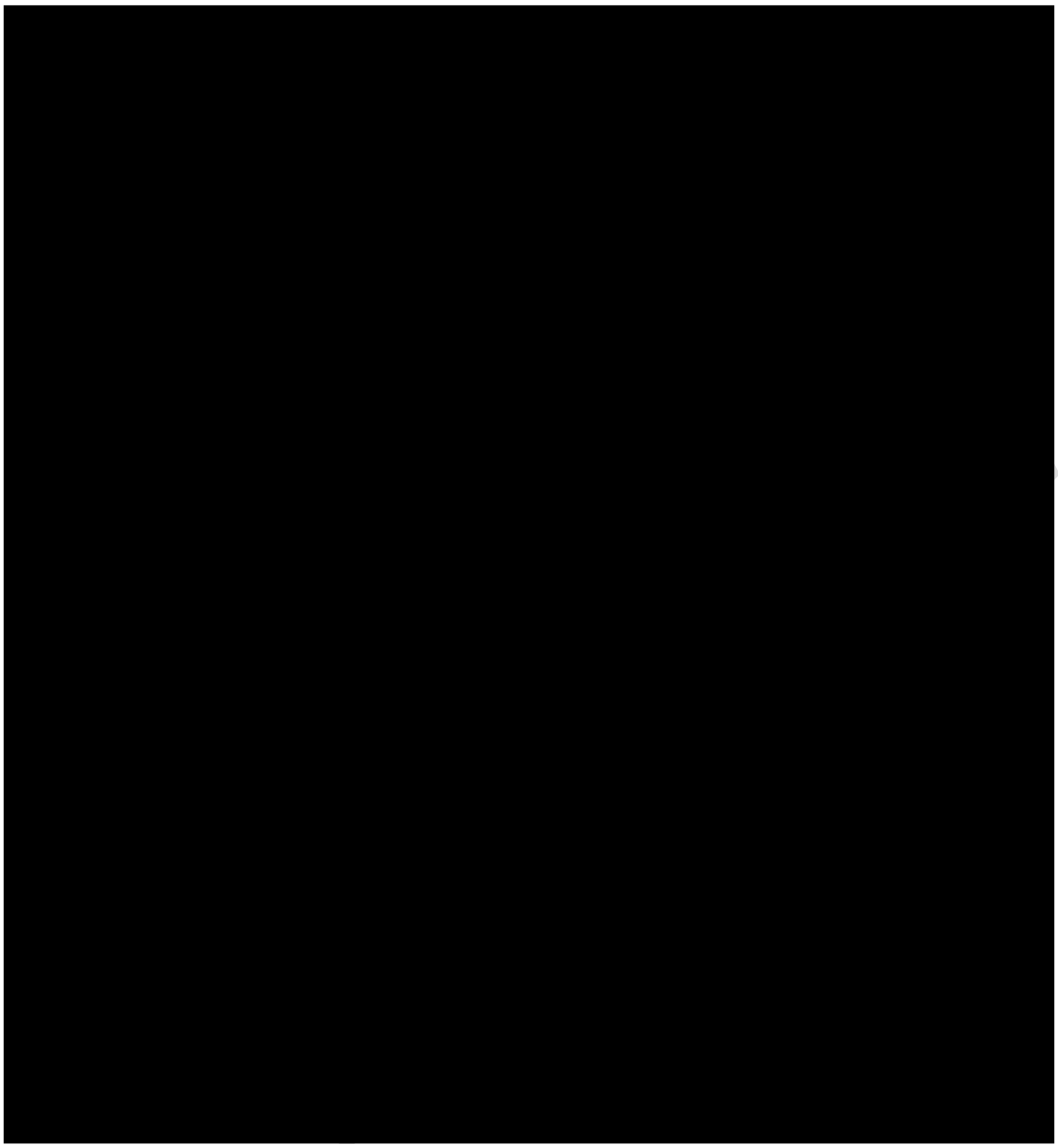

Figure 6-43: Specification given by Toyota for front windscreen wash nozzle

The specification from Toyota shows that the desired peaks of water have spray angles of [redacted] and [redacted], and that all peaks in spray distribution are of equal concentration. These angles were achievable by current Kautex nozzles separately by altering the current designs in line with the modifications completed for the Honda nozzle adaption. The difficulty was in producing the two sets of spray angles concurrently in one nozzle.

6.3.2. Design Development

The design development for the Toyota nozzle drew on inspiration from the original Toyota nozzle benchmarked with the stepped outlet and fluidic logic arrangements [77]. However rather than stepping the outlet at the edges as with the Toyota design, obstructions to the flow were introduced at the central portion from the fluidic logic parts.

Despite there being a lot of research about fluid logic components, very few parts included the spray distribution information. This meant that it would be necessary to complete a thorough investigation into what type of obstruction to use in the fluidic chip that would create the desired effect of splitting the main bodies of water flow into four separate equal parts.

There were four main questions in terms of the design of the instruction, these were each investigated individually and collectively. These questions were:

- Should the obstruction be at full or partial height in relation to the fluidic chip?
- Should there be one obstruction at the outlet or multiple?
- Should the obstruction be at a constant height throughout or increase in height gradually?
- What angle should the obstruction have in relation to the outlet exterior walls?

The drive behind utilising obstructions or 'fins' in the fluidic chips was that it would split the water into two paths and that the water would, through surface friction or the Coanda effect, attach to the surfaces of the fins and the walls of the outlets to create 4 peaks of spray distribution. From this concept it would be possible to alter the geometry to tailor how much water would be delivered to each distribution peak, unfortunately however, this concept did not work with either one or two fins used in the designs.

Three main concept designs were created, one with a central triangular obstruction at the outlet, and two concepts where two separate triangles with an angle similar to that desired by the internal spray concentration points. The first of the concepts with two triangles involved an edge perpendicular to the outlet, whereas the second concept had a more acute angle at the inner portion of the triangle.

These three main concepts were tested at full-height, half-height and with a gradual incline to full height to examine the difference experience with height change. This variable height design was inspired by the Toyota nozzle benchmarked in 2.1 Competitor Nozzle Descriptions.

6.3.2.1. Half-Height Obstruction Concepts

The first concept design was based off the original Toyota chip, however where the Toyota chip has an outlet with an upside-down ‘T’ shape, a ‘U’ shape is utilised to avoid copying the patents in place. Three designs are tested with a half-height obstruction, the first including a single fin, and the two subsequent designs comprising of two fins but with differing fin geometry.

Below in Figure 6-44 is the first fluidic chip design tested with an obstacle included intended to deflect the flow from the outlet to create a spray distribution with four peaks. It comprises of a design with a single triangular obstacle at the outlet with an angle designed to create a [redacted] inner spray concentration and [redacted] outer spray concentration.

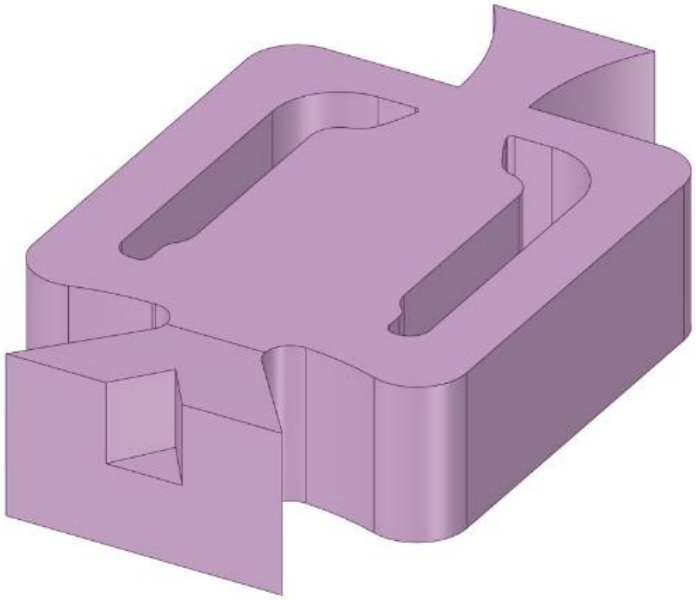

Figure 6-44: Honda concept geometry with half-height triangle triangular obstacle

The design was initially tested using CFD to determine the flow within the nozzle and investigate whether the design was feasible. This test was used to determine whether it would be a practical design to produce and experimentally test. The CFD results are shown below in Figure 6-45 - Figure 6-46. The images on the left are the velocity profiles at the outlet of the fluidic nozzle and are examined to determine the locations of the outlet at which the spray is most concentrated. The right-side images show a view of the internal flow distribution within the fluidic chip.

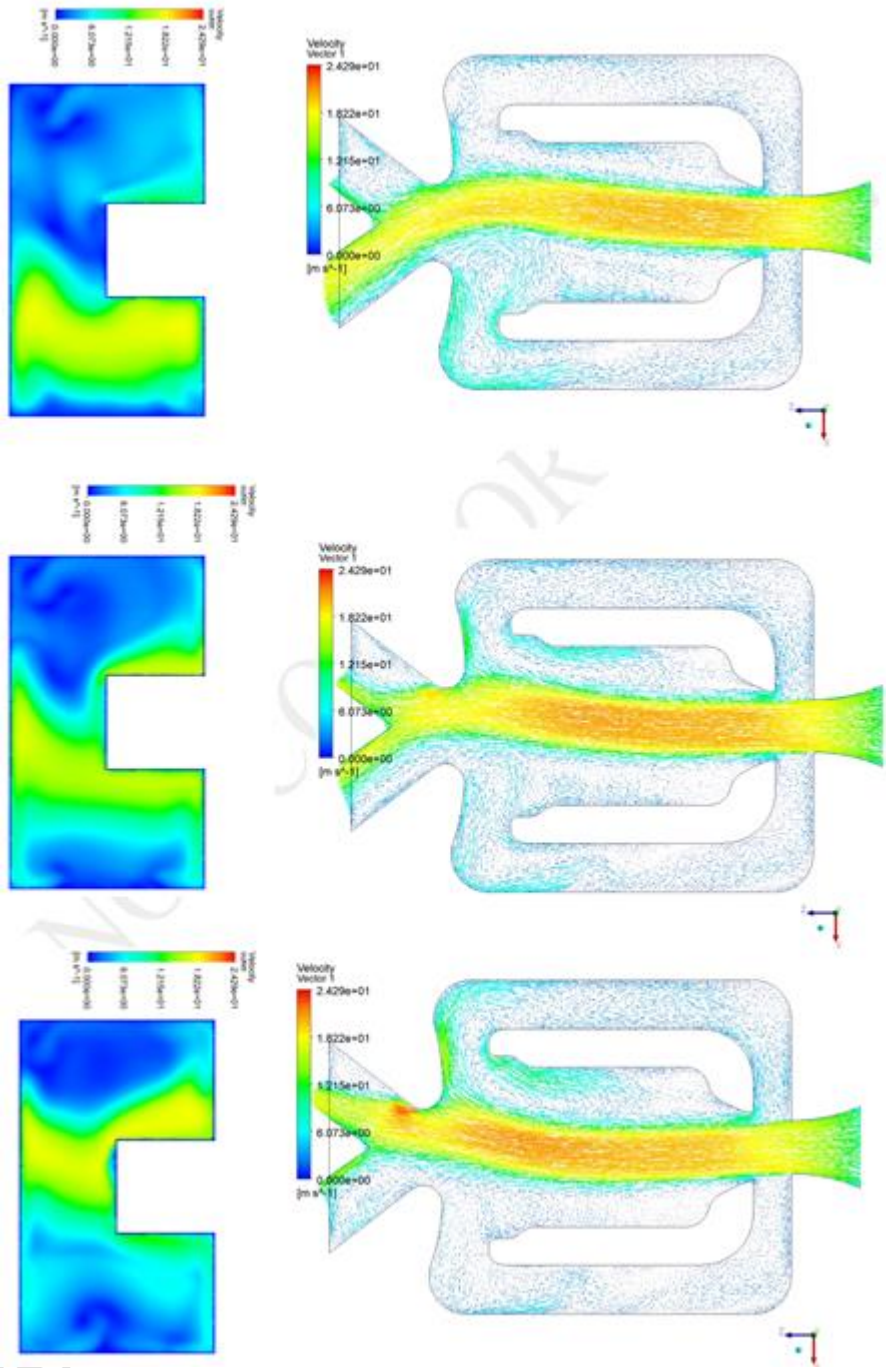

Figure 6-45: Outlet velocity profile (left) and internal fluid flow (right) image series of Toyota concept with single half-height fin

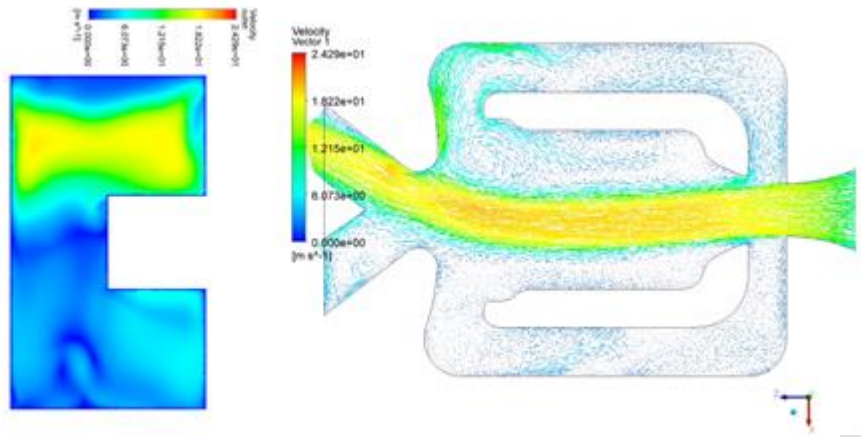

Figure 6-46: Outlet velocity profile (left) and internal fluid flow (right) image series of Toyota concept with single half-height fin

The image series above shows the flow of water when the fluid is predominantly concentrated at both external edges and when the fluid is in motion between the two oscillatory extremes. The fluid flow diagram shows the top view only where the fin is positioned as the bottom portion without the obstacle resulted in the same flow as the original design.

From the image series it is not possible to definitively say whether the current design worked in the way desired. However, the outlet velocity plots did show how there was a difference between the bottom unobstructed flow and the upper fluid with the triangular fin. With the involvement of the fin, a portion of the water begins to flow and attach to an internal surface whilst the remainder of the fluid remains in the opposite outlet channel.

This nozzle concept was tested experimentally to examine the fluid flow with an obstacle partially obstructing the outlet. The spray distribution is shown below in Figure 6-47. The spray distribution displayed equal peaks of distribution of fluid, however three peaks of concentrated fluid were present rather than two. The likely cause of the central peak is that the fluid is attaching to the inner outlet walls and guiding the water into a peak. This combined with the ordinary fluid flow from the lower portion of the fluidic chip resulted in a peak of spray concentration.

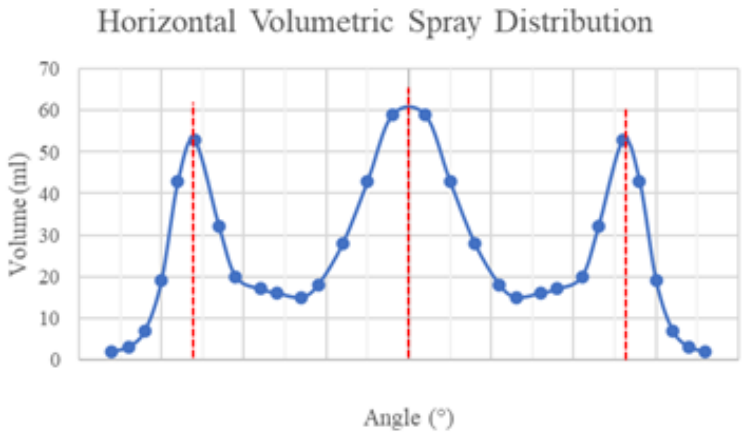

Figure 6-47: Volumetric spray distribution for Honda concept with single half-height fin

In an effort to decrease the likelihood of a central peak of concentration the width of the obstacle was increased. The depth into the outlet that the obstacle was placed was ideal for the single triangular obstacle as it allowed the fluidic chip to oscillate correctly, this meant that this property could not change. Additionally, the angle needed to be set to a degree at which a [redacted] inner spray would result.

A decision was made to split the triangle into two separate fins or to create a flat obstruction parallel to outlet exit. It was decided to split the fin into two fins as it was theorised that if there were a flat obstruction the water would reflect into the internal chamber, causing a disruption to the oscillatory flow.

Two concepts involving two fins were created (Figure 6-48), one in which the inner portion of the triangles formed a right angle, and a second design with a more obtuse angle. An acute angle was not utilised as it was theorised that this would simply result in the same spray distribution as that which was experienced with the single obstacle. The fluid flow and outlet velocity profile data for both concepts are shown in Figure 6-49 - Figure 6-50 respectively.

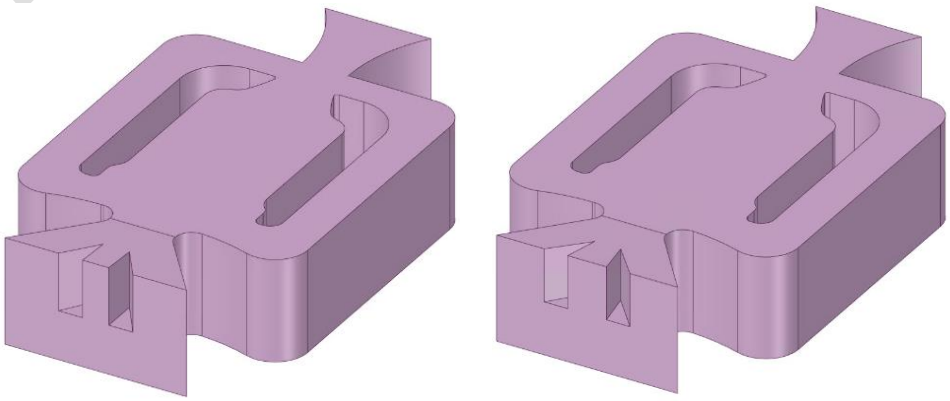

Figure 6-48: Honda concept with half-height fins with inner right angle (left) and obtuse angle (right)

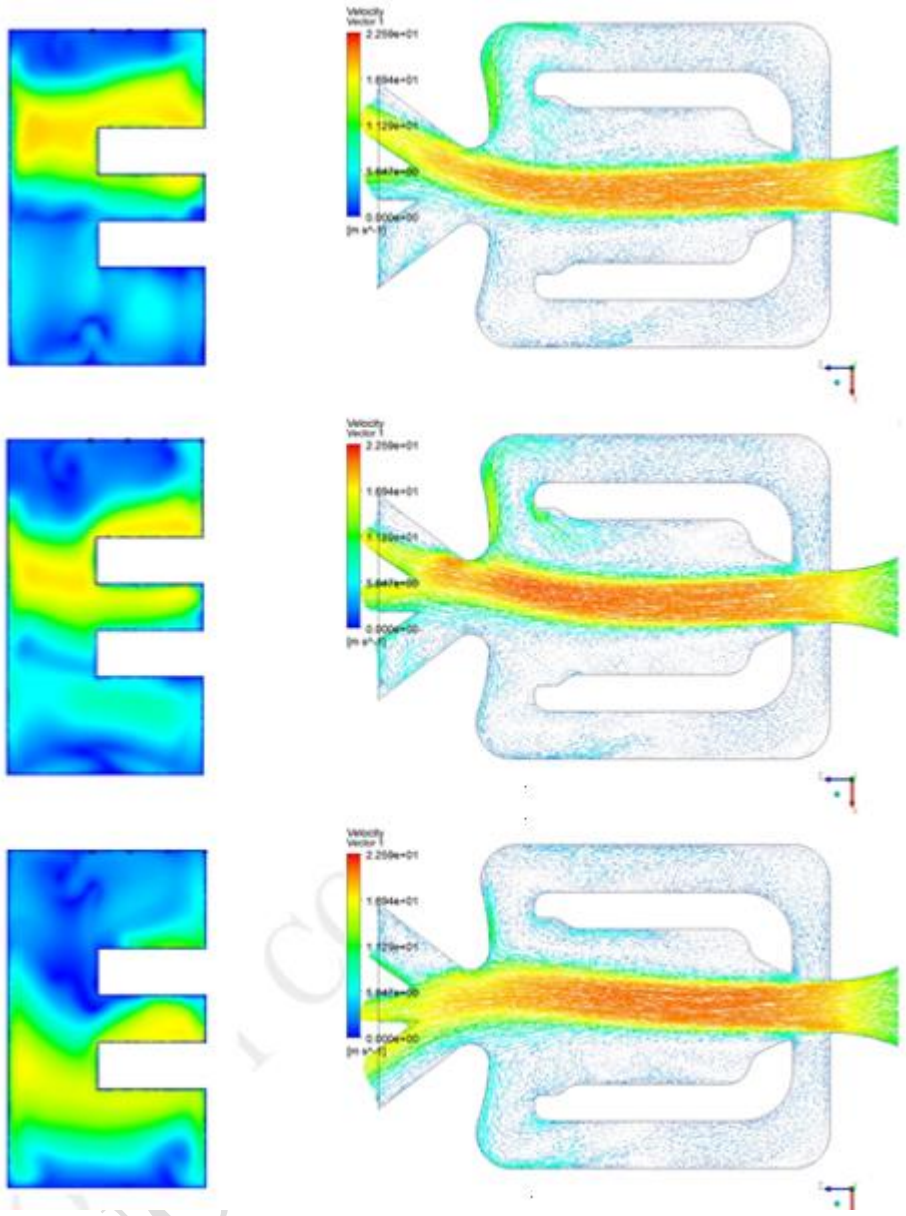

Figure 6-49: Outlet velocity profile (left) and internal fluid flow (right) image series of Toyota concept with two half-height fins with right angle

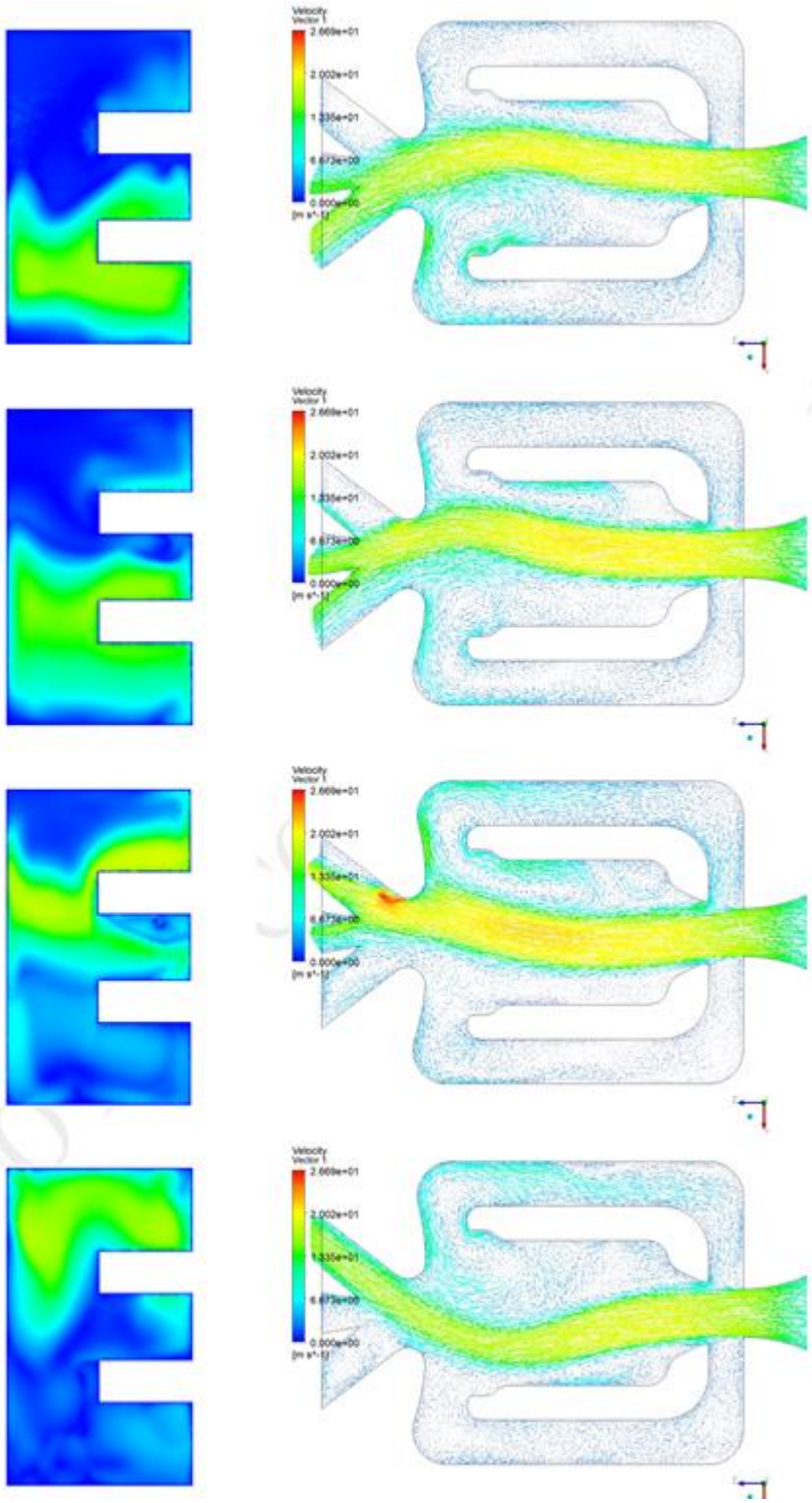

Figure 6-50: Outlet velocity profile (left) and internal fluid flow (right) image series of Toyota concept with two half-height fins with obtuse angle

The fluid flow and outlet velocity profiles for both the concepts with two outlet obstructions were very similar to each other. The main difference between these designs and the concept with one triangular obstruction was that the water

experienced further separation into separate portions, and the point at which the flow separates was earlier in the oscillatory cycle.

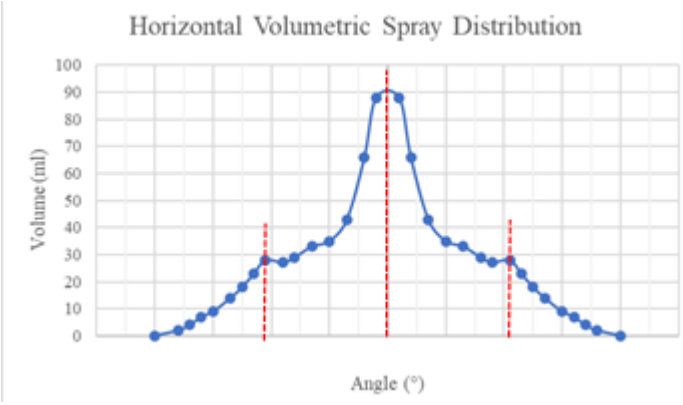

Figure 6-51: Spray distribution of Toyota concept with two half-height fins with right angle

The fluidic chip model with the right-angled twin fins had less spread of high concentration velocity in the outlet velocity profile than the design with an obtuse angle. This design was better as it would likely lead to an increase in spray concentration points, therefore this fluidic chip was tested experimentally to find the spray distribution (Figure 6-51).

This design did show an increase in concentration in some portions of the distribution and a decrease in others, however the changes were the inverse to those desired. The spray was mainly concentrated in a central peak, although the external peaks are visible there is only a minor indication of these points outlying from a bell-shaped curve.

The concepts involving obstructions or fins with a half-height design were considered to be non-functional in this specified task of forming four equal peaks. The next series of tests with a full height obstruction began after these result failures.

6.3.2.2. Full-Height Obstruction Concepts

The second set of fluidic chip models were based off a full-height obstruction model. By utilising a full-height obstruction there was a decreased possibility of the fluid forming a central concentrated peak as there was no longer a lower portion of the fluid flow influencing the direction of the water spray velocity. These fluidic chips would be the simplest fluidic chip to manufacture would have minimal tolerance requirements added to the original design if the concepts proved successful.

Below in Figure 6-52 is the geometry for the design concept with a single triangular obstruction and the resulting velocity profile and fluid flow image series is shown in Figure 6-53 - Figure 6-54.

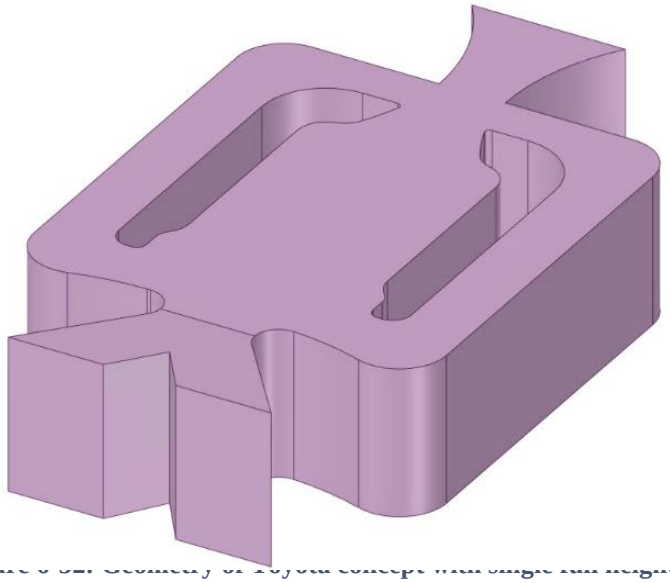

Figure 6-52: Geometry of Toyota concept with single full-height fin

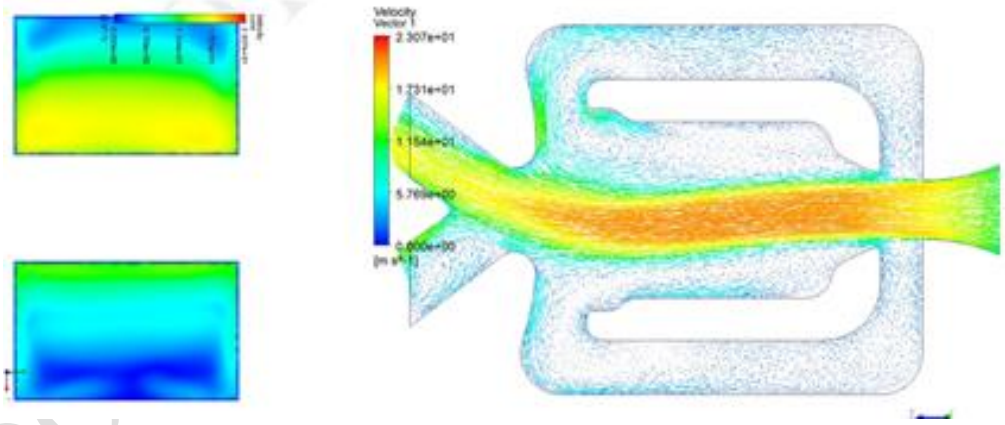

Figure 6-53: Outlet velocity profile (left) and internal fluid flow (right) image series of Toyota concept with singular full-height obstruction

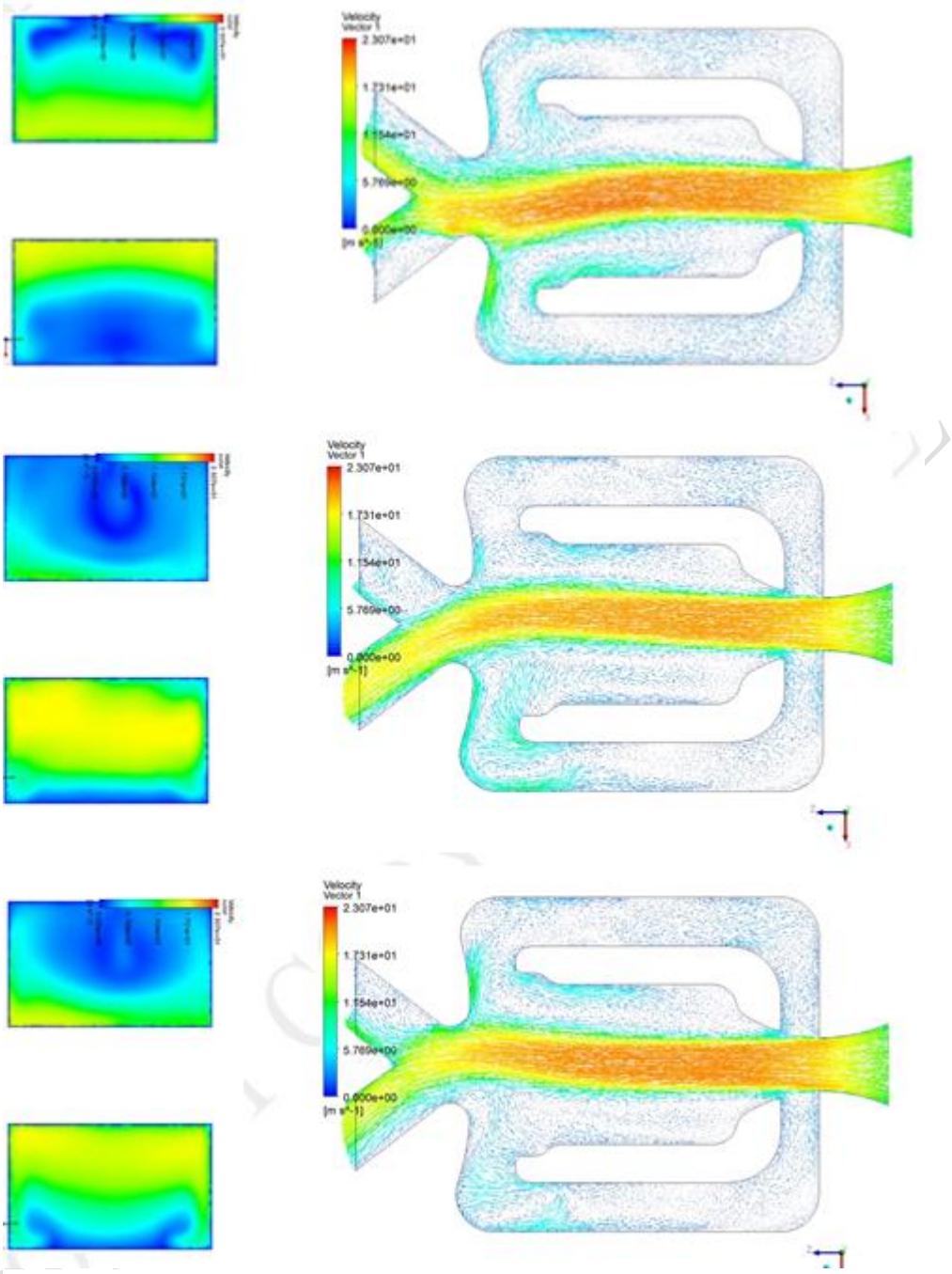

Figure 6-54: Outlet velocity profile (left) and internal fluid flow (right) image series of Toyota concept with singular full-height obstruction

The top view CFD fluid flow distribution in the image series shows that the velocity of the fluid behaves very similarly to the original design without the fin geometry. The velocity profile at the outlet of the nozzle shows that the main concentration of water travels with the oscillation of the fluid. Due to these properties and the fact that the oscillation characteristics are unchanged with the obstacle at the outlet; it was highly likely that with the high transmission time and lower switching time there would be little change to the overall spray distribution.

As it was possible that this could be a good design for either this or other specifications an experimental spray distribution test was conducted. The results for the test are shown below in Figure 6-55. As hypothesised in the above paragraph, the spray distribution showed little change in comparison to the original excluding there being a greater difference in volume in the peaks to the central area.

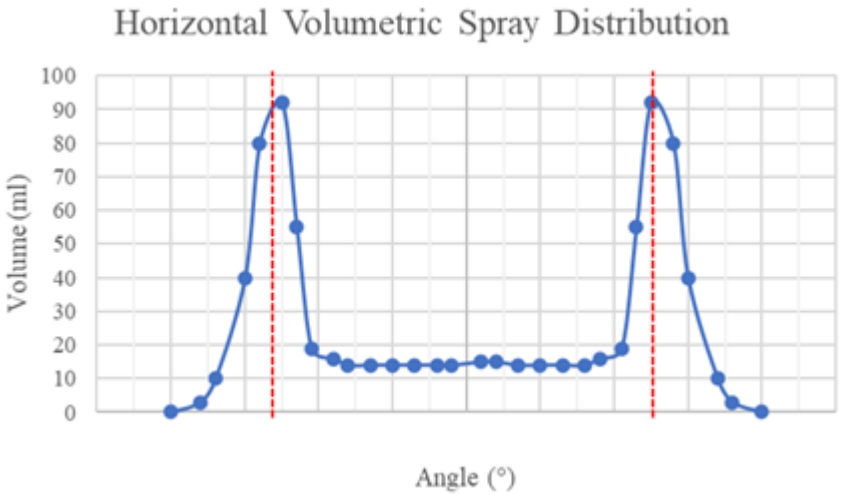

Figure 6-55: Spray distribution for Toyota concept with single obstruction

Although the spray angle for the outer peaks in this spray distribution are correct and equal the above concept was considered unsuccessful for this specification. It was unsatisfactory as only two peaks of concentrated water were formed rather than the intended four.

The second and third concepts with a full height obstruction at the outlet consisted of two separate fins or obstacles (Figure 6-56). The first concept involved the inner angle of the triangular fins being a right angle whereas the second involved a more obtuse angle. It was intended with this design to increase the deflection of the flow to reduce the amount of fluid flowing into areas which required less coverage and increase the areas receiving an increased volume of water.

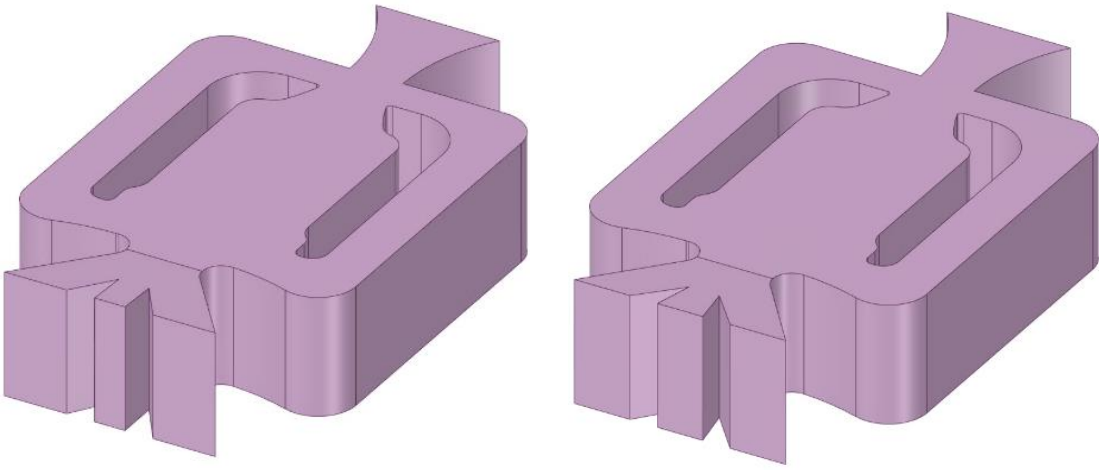

Figure 6-56: Geometries of Toyota concepts with two full height fins

Below are the image series for each of the concepts with two obstacles placed at the outlet (Figure 6-57 - Figure 6-58).

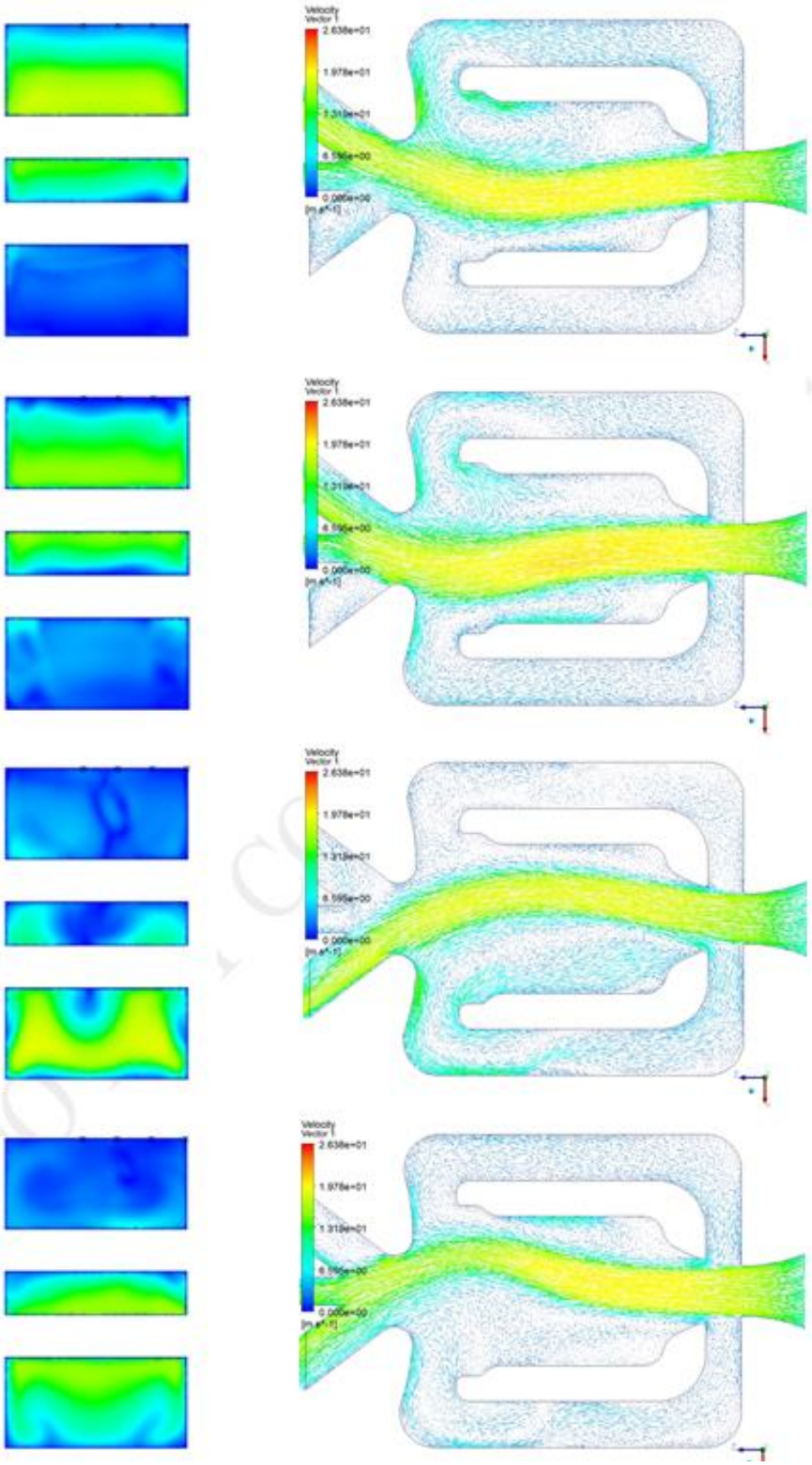

Figure 6-57: Outlet velocity profile (left) and internal fluid flow (right) image series of Toyota concept with two full-height fins with right angle

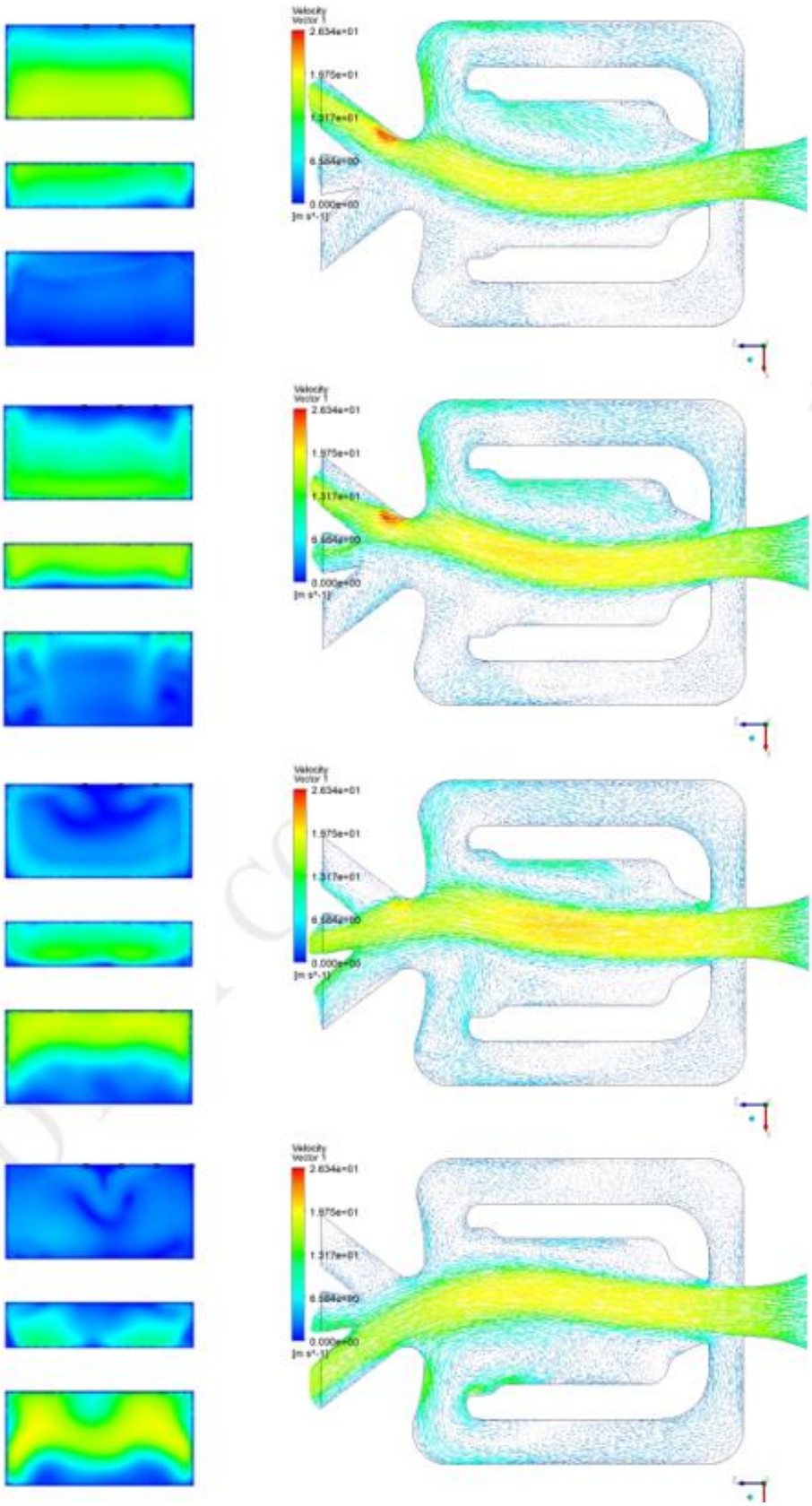

Figure 6-58: Outlet velocity profile (left) and internal fluid flow (right) image series of Toyota concept with two full-height fins with obtuse angle

The results for of the outlet velocity profile and the fluid flow diagram were again very similar as was seen in the test with half-height obstructions. These results showed a consistently linear concentrated area of high velocity at the outlet with a relatively large area of high velocity flow.

Due to the widespread high velocity flow, it was predicted that the spray distribution would not contain singular points of high concentration. The spray distribution for the nozzles were calculated experimentally and are show below in Figure 6-59 - Figure 6-60. The spray distributions do show four peaks; however, they are unequal in height with the outer peaks being much higher than the inner peaks and there remained a high proportion of water in the central portion of the spray distribution rather than four singular peaks.

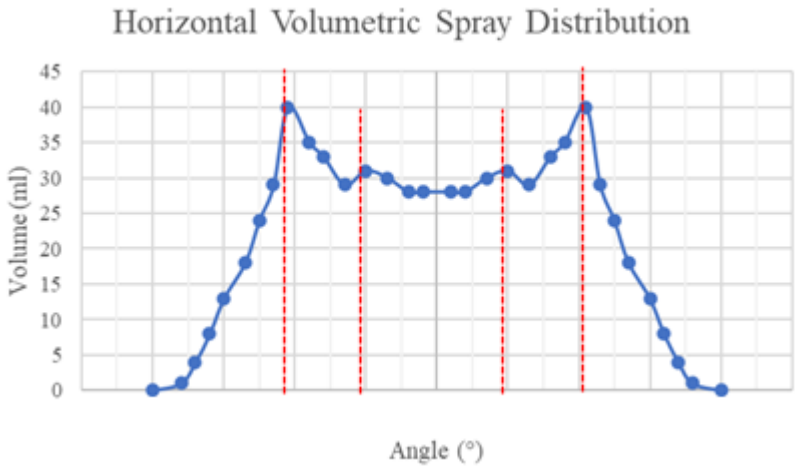

Figure 6-59: Spray distribution for Toyota concept with two full height fins with right angle

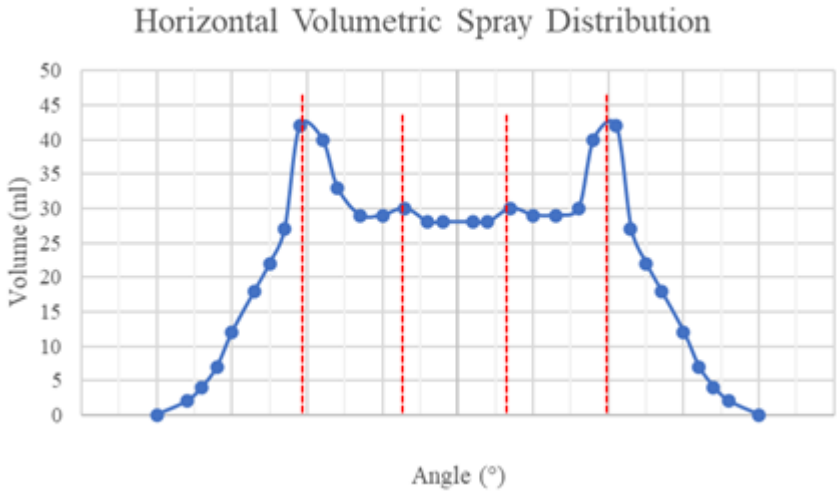

Figure 6-60: Spray distribution for Toyota concept with two full height fins with right angle

As a lot of issues involving a high concentration of flow in the central portion of the spray distribution were experienced with these designs, therefore a design concept containing an outlet with three obstacles was considered. This design was created with the intention of blocking the flow to the central portion of the outlet and creating the four-peak spray distribution design required. The geometry of the three-peak fin fluidic chip is shown below in Figure 6-61.

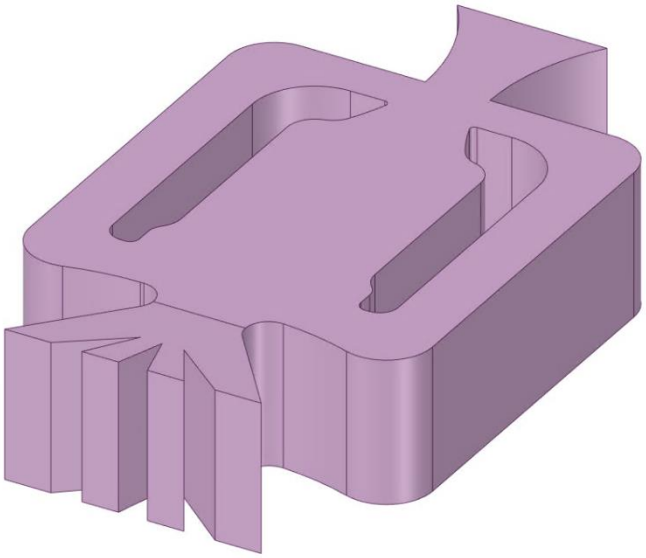

Figure 6-61: Geometries of Toyota concepts with two full height fins

The angle for the outer triangles was set wider than that utilised with the two fin designs, this was due to the inner spray concentration areas shown in the spray distribution being narrow. By increasing the angle of the inner obstacle deflection, it was predicted that a spray concentration point closer to the desired 30° inner spray angle would be achieved.

The results from the CFD simulation is shown below for the concept with three full-height obstacles placed at the outlet (Figure 6-62).

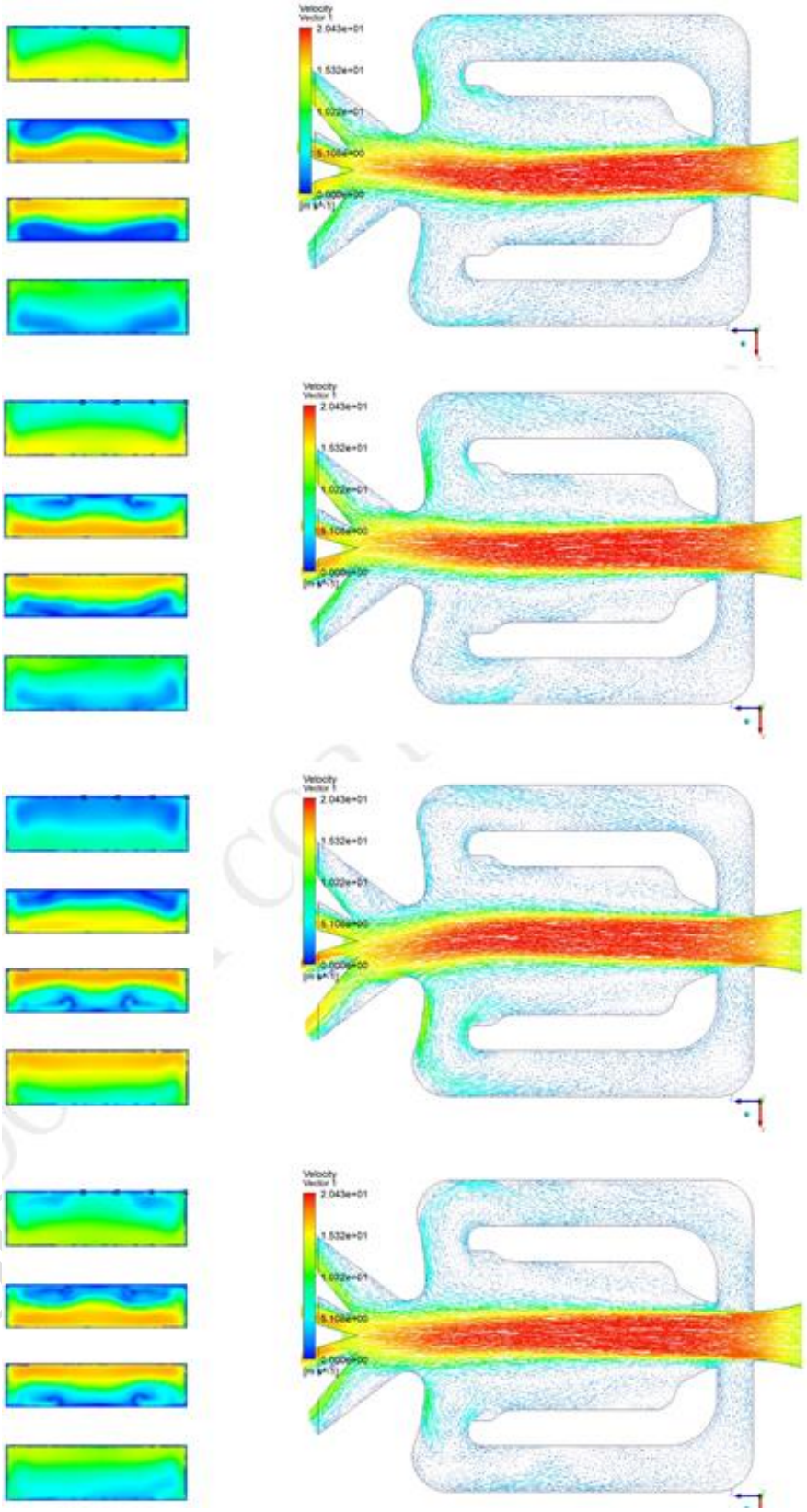

Figure 6-62: Outlet velocity profile (left) and internal fluid flow (right) image series of Toyota concept with three full-height fins

The flow of high velocity in this concept is split into more sections than the previous designs, producing a narrower concentration of spray. It was hoped that this would cause a distribution more closely aligned to the design specification. This nozzle was tested experimentally to find the difference better understand the fluid distribution. The results for the spray distribution test are shown below in (Figure 6-63).

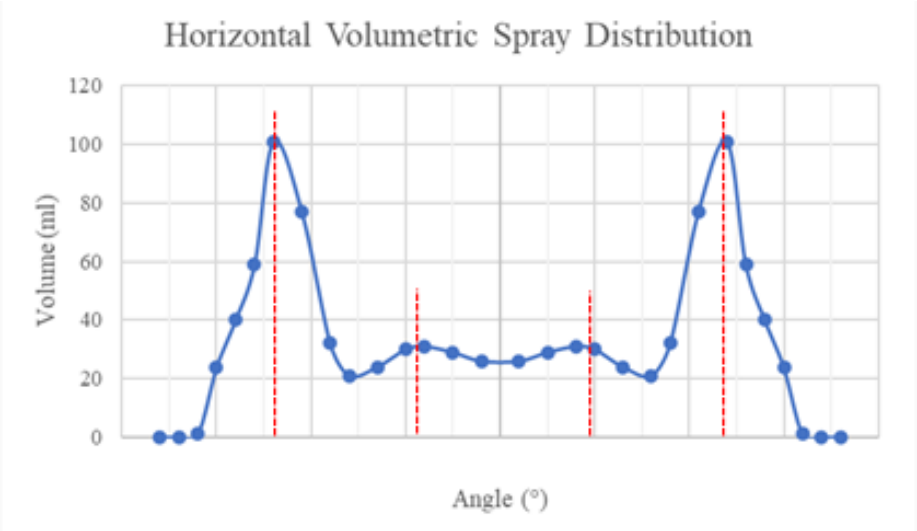

Figure 6-63: Spray distribution for Toyota concept with two full height fins with right angle

The fluid discharge for this nozzle concept with three obstructions at the outlet created the best spray distribution out of the current concepts with obstacles. There are four peaks of concentrated fluid volume, although the outer concentration peaks are much higher than the inner peaks, they remain visible and there is a much smaller percentage of fluid volume in the central portion of the spray.

With this spray distribution the outer peaks occurred at a point that equated to a 46° spray angle and the inner peaks were at a [redacted] spray angle. These values did not match the specification values of [redacted] outer peaks and [redacted] inner peaks, therefore further research into this design concept was necessary.

6.3.2.3. Inclined Height Obstruction

Concept involving inclined heights for the obstruction were considered, however the manufacturing team at Kautex Textron CVS Ltd stated that these designs would not be possible to manufacture. Therefore, the results from the computational testing of these designs were not included in this research.

6.3.3. Toyota design development conclusion

Unfortunately, the Honda post-development issues occurred partway through the Toyota project and with the Honda project deadline being much closer that project

was a priority. Therefore, the Toyota project was not completed and instead was referred to an innovation department at a different location within Kautex Textron CVS Ltd.

The design concept that was sent to the new team involved in the project was the fluidic chip with three fins at the outlet as this was the most closely sufficient design out of those which were tested and were feasible.

7. Conclusions

The main goals for this project were stated in the introduction portion of this thesis, they were:

- To develop an understanding of a range of nozzle types that can be used for automotive applications, focusing primarily on fluidic nozzles
- To redesign and optimise the performance of three fluidic nozzles for screen wash cleaning applications
- To ensure that the fluidic nozzles can be used when stationary and at high velocities
- To compare the performance of fluidic nozzles to more conventional straight and fan nozzles

One of the goals of the project was to further the understanding of fluidic nozzles and how the geometry can affect the performance of the nozzle. This was established in the form of multiple hypothesis resulting in the following statements for the nozzles studies within this project:

- There is a positive correlation between nozzle outlet width and spray angle
- There is no proven correlation between volumetric flow rate and spray angle
- There is a negative correlation between volumetric flow rate and both average droplet sizing and oscillatory rate

The second goal of this research was to develop three fluidic nozzles to be utilised by three different customers of Kautex Textron. This design and development were to be completed utilising both experimental and computational testing methods to provide accurate results. Although the goal of completing three final design fluidic nozzles was not completed, a wide range of fluidic nozzle designs were created, two of which were delivered successfully to Kautex Textron CVS Ltd customers.

Through an issue with the Honda nozzle, testing of the performance of a fluidic nozzle on a vehicle moving at a high velocity was further investigated. It was found that provided a sufficient pressure and precise geometry were applied to the fluidic chip, there would be minimal change in the positioning of the spray deposition on the windscreen between when the vehicle was stationary and at high velocity.

Although fan nozzles were only studied in the introduction and as a by-product of the external computational fluid dynamics (CFD), it was shown that it is possible to distribute water particles over a much wider area with a fluidic nozzle in comparison to the fan nozzle. Also, the mass flow rate to cover a given area utilising a fluidic nozzle would be lower than that required for a fan nozzle.

Despite not all the goals of the project being explicitly met, through this development process a new knowledge resource on how different properties within fluidic nozzles affect the spray from a nozzle. This research will help Kautex Textron to develop more fluidic nozzles in the future to meet further customer specifications. The computational study on how parts of this size can contain defects and how this influences the flow inside a fluidic chip will help to ensure that they function effectively with correct tolerances and defects. The correlation between the external CFD simulation and the spray angle results for the Honda nozzle show that it is possible to create design and predict accurate resulting spray angles amongst other properties.

In addition to the knowledge gained throughout the project and the fluidic chip designs created for customer manufacture, the way in which Kautex Textron CVS Ltd. as a company approaches nozzle design and development has changed. The company now employs a full-time CFD engineer to undertake fluid analysis of all new nozzle designs, this includes fluidic jets, fan jet and pencil jets. These are analyses are used to pinpoint inefficiencies within the nozzles and possible problem areas, in addition to predicting the spray angle and hit points on automotive surfaces that require a cleaning system.

8. Future Work

To improve upon this project several steps could be performed to improve the reliability, scope of the results produced and validity.

As shown in the conclusion chapter and the experimental chapter, some hypotheses were made regarding the results from the experimental testing. These analyses were performed on a very small batch size; therefore, it would be recommended to investigate whether the confirmed hypotheses hold true for other fluidic nozzles. All the hypotheses apart from hypothesis 4 regarding the oscillatory rate could also be tested with fan nozzles.

Further research and analyses into the vorticity values in the fluidic nozzle and the interaction between the main flow and the viscous sublayers at the boundaries should be performed. This would enhance the understanding of whether the Coanda effect is in fact present in these fluidic nozzles. It would be worthwhile to utilise a PIV (particle image velocimetry) experiment to validate the internal simulation results in addition to the external result validation seen in this project.

Further research should be conducted into the external simulation of the fluidic nozzle, as in this project only the case where the nozzle is in a stationary position is examined. To further develop this the test could be run with a domain of moving velocity streams to simulate the vehicle movement, the spray angle could then be validated utilising the dynamic testing detailed in the project or through wind tunnel testing.

It would be a worthwhile endeavour to investigate the properties of the fluidic flow as it impacts a surface in the cleaning system. This could be enabled by the customer providing a CAD surface of a portion of the vehicle with the C-zone highlighted. This in turn could then be investigated in conjunction with the above point to simulate close to real world conditions in a CFD analysis.

9. Appendices

9.1. Appendix A

Table 9-1: 2014 Benchmarking Summary by Kautex Textron CVS Ltd.

Total Manufacturers Surveyed	Total Nozzles Surveyed	Fluidic Spray	Fan Spray	Pencil Jet Spray	End User Adjustability	Heating Option	Under Bonnet Location
19	143	72 (50%)	13 (9%)	57 (40%)	44 (31%)	47 (33%)	87 (60%)

9.2. Appendix B

9.2.1. Ford B-Max Nozzle Spray Distribution Tests

9.2.1.1. 2.5 Bar Pressure

Table 9-2: Ford B-Max Nozzle Test 1

Set-Up Details:							
	Fan		Fluidic	Y	Part No/Cust	Ford B-Max	Flow (ml/sec)	22.01
	Spray Height (mm)	400			Cycle Time	30	Pressure (Bar)	2.52

NOTE: INPUT VOLUME = CC

VIEW FROM ABOVE

0	0	0	0	0	0	0	0	0	0	0	0	0	0	0	0	0	0	0	0	0	0	0	0	0	0	0	0	0	0
0	0	0	0	0	0	0	0	0	0	0	0	0	0	0	0	0	0	0	0	0	0	0	0	0	0	0	0	0	0
0	0	0	0	1	1	2	4	4	3	3	2	2	2	4	2	2	2	3	3	4	5	6	4	2	1	0	0	0	0
0	0	0	0	1	2	6	57	17	7	5	4	3	2	2	2	3	4	5	7	8	17	70	21	2	1	0	0	0	0
0	0	0	1	2	2	5	75	24	8	5	4	3	2	1	1	2	3	3	4	5	12	32	10	3	1	0	0	0	0
0	0	0	0	0	0	0	1	3	4	2	2	1	0	0	0	0	1	1	2	2	2	2	0	0	0	0	0	0	0
0	0	0	0	0	0	0	0	0	0	0	0	0	0	0	0	0	0	0	0	0	0	0	0	0	0	0	0	0	0

Table 9-3: Ford B-Max Nozzle Test 2

Set-Up Details:	**Fan**		**Fluidic**	**Y**	**Part No/Cust**	Ford B-Max	**Flow (ml/sec)**	24.33
	Spray Height (mm)	400	**Cycle Time**	30			**Pressure (Bar)**	2.48

NOTE: INPUT VOLUME = CC *VIEW FROM ABOVE*

0	0	0	0	0	0	0	0	0	0	0	0	0	0	0	0	0	0	0	0	0	0	0	0	0	0	0	0	0	0
0	0	0	0	0	0	0	0	0	0	0	0	0	0	0	0	0	0	0	0	0	0	0	0	0	0	0	0	0	0
0	0	0	1	1	2	2	4	4	3	3	2	2	2	4	2	2	3	3	4	5	6	4	2	2	2	1	1	0	0
0	0	1	1	1	2	9	68	18	8	6	5	4	3	3	2	3	4	5	6	10	19	72	13	4	2	1	1	0	0
0	0	0	0	1	1	6	66	20	8	4	3	2	2	2	2	3	4	5	6	8	13	36	3	2	1	1	0	0	0
0	0	0	0	0	0	1	3	3	2	1	1	1	0	0	0	0	1	1	1	2	3	3	1	1	0	0	0	0	0
0	0	0	0	0	0	0	0	0	0	0	0	0	0	0	0	0	0	0	0	0	0	0	0	0	0	0	0	0	0

Table 9-4: Ford B-Max Nozzle Test 3

Set-Up Details:																															
Fan		**Fluidic**	**Y**	**Part No/Cust**	Ford B-Max																					**Flow (ml/sec)**	21.90				
Spray Height (mm)	400			**Cycle Time**	30																					**Pressure (Bar)**	2.5				

NOTE: INPUT VOLUME = CC *VIEW FROM ABOVE*

0	0	0	0	0	0	0	0	0	0	0	0	0	0	0	0	0	0	0	0	0	0	0	0	0	0	0	0	0	0	0	0
0	0	0	0	0	0	0	0	0	0	0	0	0	0	0	0	0	0	0	0	0	0	0	0	0	0	0	0	0	0	0	0
0	0	0	0	0	0	2	4	4	3	3	2	1	2	3	1	1	2	2	4	4	10	11	4	1	0	0	0	0	0	0	0
0	0	0	0	1	2	8	77	18	7	5	4	3	2	2	1	2	3	4	5	8	18	70	14	2	2	1	0	0	0	0	0
0	0	0	0	1	2	5	59	17	7	5	4	3	2	2	2	2	3	4	5	6	13	33	8	2	1	1	0	0	0	0	0
0	0	0	0	1	1	2	3	2	1	1	0	0	0	0	0	0	0	0	0	1	2	2	2	1	1	0	0	0	0	0	0
0	0	0	0	0	0	0	0	0	0	0	0	0	0	0	0	0	0	0	0	0	0	0	0	0	0	0	0	0	0	0	0

Table 9-5: Ford B-Max Nozzle Average

Set-Up Details:																															
Fan		**Fluidic**	**Y**	**Part No/Cust**	Ford B-Max																					**Flow (ml/sec)**	27.23				
Spray Height (mm)	400			**Cycle Time**	30 seconds																					**Pressure (Bar)**	2.5				

NOTE: INPUT VOLUME = CC *VIEW FROM ABOVE*

0	0	0	0	0	0	0	0	0	0	0	0	0	0	0	0	0	0	0	0	0	0	0	0	0	0	0	0	0	0	0	0
0	0	0	0	0	0	0	0	0	0	0	0	0	0	0	0	0	0	0	0	0	0	0	0	0	0	0	0	0	0	0	0
0	0	0	0	1	2	3	4	4	3	2	2	2	2	3	2	2	2	3	4	4	7	7	3	2	1	0	0	0	0	0	0

0	0	0	0	1	2	8	67	18	7	5	4	3	2	2	2	3	4	5	6	9	18	71	16	3	2	1	0	0	0
0	0	0	0	1	2	5	67	20	8	5	4	3	2	2	2	2	3	4	5	6	13	34	7	2	1	1	0	0	0
0	0	0	0	0	0	1	2	3	2	1	1	1	0	0	0	0	1	1	1	2	2	2	1	1	0	0	0	0	0
0	0	0	0	0	0	0	0	0	0	0	0	0	0	0	0	0	0	0	0	0	0	0	0	0	0	0	0	0	0

Table 9-6: Ford B-Max Nozzle Average (symmetrical)

Set-Up Details:

Fan	

Fluidic	**Y**

Part No/Cust	Ford B-Max

Flow (ml/sec)	18

Spray Height (mm)	400

Cycle Time	30 seconds

Pressure (Bar)	2.5

NOTE: INPUT VOLUME = CC

VIEW FROM ABOVE

0	0	0	0	0	0	0	0	0	0	0	0	0	0	0	0	0	0	0	0	0	0	0	0	0	0	0	0	0
0	0	0	0	0	0	0	0	0	0	0	0	0	0	0	0	0	0	0	0	0	0	0	0	0	0	0	0	0
0	0	0	0	1	2	3	5	5	4	3	2	2	2	3	3	2	2	2	3	4	5	5	3	2	1	0	0	0
0	0	0	1	1	2	12	69	18	8	6	5	4	3	2	2	3	4	5	6	8	18	69	12	2	1	1	0	0
0	0	0	1	1	2	6	50	17	7	5	4	3	2	2	2	2	3	4	5	7	17	50	6	2	1	1	0	0
0	0	0	0	0	1	1	2	3	2	1	1	1	0	0	0	0	1	1	1	2	3	2	1	1	0	0	0	0
0	0	0	0	0	0	0	0	0	0	0	0	0	0	0	0	0	0	0	0	0	0	0	0	0	0	0	0	0

9.2.1.1.1. ***2.5 Bar Pressure***

9.2.2. Ford Ecosport Nozzle Spray Distribution Tests

9.2.2.1. 2.5 Bar Pressure

Table 9-7: Ford Ecosport Nozzle Test 1

Set-Up Details:	**Fan**		**Fluidic**	**Y**	**Part No/Cust**	Ford Ecosport	**Flow (ml/sec)**	19.13
	Spray Height (mm)	400			**Cycle Time**	30	**Pressure (Bar)**	2.47

NOTE: INPUT VOLUME = CC *VIEW FROM ABOVE*

0	0	0	0	0	0	0	0	0	0	0	0	0	0	0	0	0	0	0	0	0	0	0	0	0	0	0	0	0
0	0	0	0	0	0	0	0	0	0	0	0	0	0	0	0	0	0	0	0	0	0	0	0	0	0	0	0	0
0	0	0	0	0	0	1	5	24	25	21	17	14	13	11	11	12	13	15	19	22	24	11	1	0	0	0	0	0
1	6	9	9	8	8	9	9	8	7	6	5	5	4	4	5	4	5	5	6	7	8	9	9	10	10	11	11	8	1
1	4	5	5	6	6	6	5	5	4	3	2	2	2	2	2	2	2	2	2	3	4	5	6	6	6	5	4	1	0
0	0	0	0	0	0	0	0	0	0	0	0	0	0	0	0	0	0	0	0	0	0	0	0	0	0	0	0	0	0
0	0	0	0	0	0	0	0	0	0	0	0	0	0	0	0	0	0	0	0	0	0	0	0	0	0	0	0	0	0

Table 9-8: Ford Ecosport Nozzle Test 2

Set-Up Details:	Fan		Fluidic	Y	Part No/Cust	Ford Ecosport	Flow (ml/sec)	19.00
	Spray Height (mm)	400			Cycle Time	30	Pressure (Bar)	2.4

NOTE: INPUT VOLUME = CC *VIEW FROM ABOVE*

0	0	0	0	0	0	0	0	0	0	0	0	0	0	0	0	0	0	0	0	0	0	0	0	0	0	0	0	0
0	0	0	0	0	0	0	0	0	0	0	0	0	0	0	0	0	0	0	0	0	0	0	0	0	0	0	0	0
0	0	0	0	0	1	3	12	27	23	18	13	13	12	11	11	12	13	15	20	22	20	4	1	1	1	0	0	0	0
0	8	8	8	8	9	9	8	7	6	5	4	4	4	5	5	5	5	5	6	7	8	8	9	8	9	10	8	4	0
0	4	5	5	7	7	6	5	5	4	3	3	3	2	2	2	2	2	3	3	3	5	7	8	8	8	7	5	3	0
0	0	0	0	0	0	0	0	0	0	0	0	0	0	0	0	0	0	0	0	0	0	0	0	0	0	0	0	0	0
0	0	0	0	0	0	0	0	0	0	0	0	0	0	0	0	0	0	0	0	0	0	0	0	0	0	0	0	0	0

Table 9-9: Ford Ecosport Nozzle Test 3

Set-Up Details:	Fan		Fluidic	Y	Part No/Cust	Ford Ecosport	Flow (ml/sec)	19.57
	Spray Height (mm)	400			Cycle Time	30	Pressure (Bar)	2.52

NOTE: INPUT VOLUME = CC *VIEW FROM ABOVE*

0	0	0	0	0	0	0	0	0	0	0	0	0	0	0	0	0	0	0	0	0	0	0	0	0	0	0	0	0
0	0	0	0	0	0	0	0	0	0	0	0	0	0	0	0	0	0	0	0	0	0	0	0	0	0	0	0	0
0	0	0	0	0	0	1	9	27	24	21	17	14	13	11	11	12	13	15	20	23	24	9	2	0	0	0	0	0	0

2	6	8	8	8	8	8	8	8	7	6	5	5	5	5	5	5	5	5	6	6	8	9	9	10	10	12	11	7	2
1	5	7	7	6	6	6	5	4	3	2	2	2	2	2	3	2	2	2	3	3	4	5	6	6	6	5	4	2	1
0	0	0	0	0	0	0	0	0	0	0	0	0	0	0	0	0	0	0	0	0	0	0	0	0	0	0	0	0	0
0	0	0	0	0	0	0	0	0	0	0	0	0	0	0	0	0	0	0	0	0	0	0	0	0	0	0	0	0	0

Table 9-10: Ford Ecosport Nozzle Average

Set-Up Details:

Fan	

Fluidic	**Y**

Part No/Cust	Ford Ecosport

Flow (ml/sec)	19.23

Spray Height (mm)	400

Cycle Time	30 seconds

Pressure (Bar)	2.46

NOTE: INPUT VOLUME = CC

VIEW FROM ABOVE

0	0	0	0	0	0	0	0	0	0	0	0	0	0	0	0	0	0	0	0	0	0	0	0	0	0	0	0	0	0
0	0	0	0	0	0	0	0	0	0	0	0	0	0	0	0	0	0	0	0	0	0	0	0	0	0	0	0	0	0
0	0	0	0	0	0	2	9	26	24	20	16	14	13	11	11	12	13	15	20	22	23	8	1	0	0	0	0	0	0
1	7	8	8	8	8	9	8	8	7	6	5	5	4	5	5	5	5	5	6	7	8	9	9	9	10	11	10	6	1
1	4	6	6	6	6	6	5	5	4	3	2	2	2	2	2	2	2	2	3	3	4	6	7	7	7	6	4	2	0
0	0	0	0	0	0	0	0	0	0	0	0	0	0	0	0	0	0	0	0	0	0	0	0	0	0	0	0	0	0
0	0	0	0	0	0	0	0	0	0	0	0	0	0	0	0	0	0	0	0	0	0	0	0	0	0	0	0	0	0

Table 9-11: Ford Ecosport Nozzle Average (symmetrical)

Set-Up Details:	Fan		Fluidic	Y	Part No/Cust	Ford Ecosport	Flow (ml/sec)	19.23
	Spray Height (mm)	400			Cycle Time	30 seconds	Pressure (Bar)	2.5

NOTE: INPUT VOLUME = CC *VIEW FROM ABOVE*

0	0	0	0	0	0	0	0	0	0	0	0	0	0	0	0	0	0	0	0	0	0	0	0	0	0	0	0	0	0
0	0	0	0	0	0	0	0	0	0	0	0	0	0	0	0	0	0	0	0	0	0	0	0	0	0	0	0	0	0
0	0	0	0	0	0	2	8	24	23	20	15	13	12	11	11	12	13	15	20	23	24	8	2	0	0	0	0	0	0
1	7	9	10	9	9	9	9	8	7	6	5	5	5	5	5	5	5	5	6	7	8	9	9	9	9	10	9	7	1
1	3	5	6	7	7	6	5	5	3	3	2	2	2	2	2	2	2	2	3	3	5	5	6	7	7	6	5	3	1
0	0	0	0	0	0	0	0	0	0	0	0	0	0	0	0	0	0	0	0	0	0	0	0	0	0	0	0	0	0
0	0	0	0	0	0	0	0	0	0	0	0	0	0	0	0	0	0	0	0	0	0	0	0	0	0	0	0	0	0

9.2.2.2. 4 Bar Pressure

Table 9-12: Ford Ecosport Nozzle Test 1

Set-Up Details:	Fan		Fluidic	Y	Part No/Cust	Ford Ecosport	Flow (ml/sec)	27.23
	Spray Height (mm)	345			Cycle Time	30	Pressure (Bar)	3.99

NOTE: INPUT VOLUME = CC *VIEW FROM ABOVE*

0	0	0	0	0	0	0	0	0	0	0	0	0	0	0	0	0	0	0	0	0	0	0	0	0	0	0	0	0	0
0	0	0	0	0	0	0	0	0	0	0	0	0	0	0	0	0	0	0	0	0	0	0	0	0	0	0	0	0	0
0	0	0	1	1	1	1	2	3	5	5	5	5	4	4	3	4	4	6	6	5	2	1	1	1	0	0	0	0	0
1	1	3	5	6	5	6	8	20	30	29	24	20	17	16	17	21	24	29	34	32	13	7	6	6	5	4	2	2	0

0	1	5	11	15	15	15	14	12	9	7	6	5	5	5	5	5	6	6	7	12	13	14	15	15	14	7	3	1	0
0	1	2	2	3	3	4	5	5	4	3	3	3	3	3	3	3	3	4	4	5	4	4	3	2	2	1	1	1	0
0	0	0	0	1	1	1	1	1	1	1	1	1	1	1	1	1	1	1	1	1	1	1	1	1	1	0	0	0	0

Table 9-13: Ford Ecosport Nozzle Test 2

Set-Up Details:	**Fan**		**Fluidic**	**Y**	**Part No/Cust**	Ford Ecosport	**Flow (ml/sec)**	24.30
	Spray Height (mm)	345	**Cycle Time**	30			**Pressure (Bar)**	4.05

NOTE: INPUT VOLUME = CC *VIEW FROM ABOVE*

0	0	0	0	0	0	0	0	0	0	0	0	0	0	0	0	0	0	0	0	0	0	0	0	0	0	0	0	0	0
0	0	0	0	0	0	0	0	0	0	0	0	0	0	0	0	0	0	0	0	0	0	1	1	0	0	0	0	0	0
0	0	0	0	0	0	0	0	0	0	1	1	0	0	0	0	0	0	0	0	0	1	1	0	0	0	0	0	0	0
0	0	0	0	0	0	1	2	5	23	28	23	18	16	13	12	14	15	18	23	27	22	5	2	2	2	1	1	0	0
0	2	7	12	14	13	13	13	13	12	10	10	9	8	8	9	10	11	12	13	13	15	17	15	12	8	4	0	0	0
0	0	2	4	5	6	7	7	6	5	4	4	4	4	4	5	4	4	5	6	8	9	9	8	8	7	4	1	0	0
0	0	0	0	0	0	0	0	1	1	1	1	0	0	1	1	2	2	2	3	3	3	2	2	1	1	0	0	0	0

Table 9-14: Ford Ecosport Nozzle Test 3

Set-Up Details:	**Fan**		**Fluidic**	**Y**	**Part No/Cust**	Ford Ecosport	**Flow (ml/sec)**	25.70

Spray Height (mm)	345

Cycle Time	30

Pressure (Bar)	3.93

NOTE: INPUT VOLUME = CC

VIEW FROM ABOVE

0	0	0	0	0	0	0	0	0	0	0	0	0	0	0	0	0	0	0	0	0	0	0	0	0	0	0	0	0
0	0	0	0	0	0	0	0	0	0	0	0	0	0	0	0	0	0	0	0	0	0	0	0	0	0	0	0	0
0	0	0	0	0	0	0	0	1	1	1	1	1	1	1	1	1	1	1	1	1	1	1	0	0	0	0	0	0
0	0	0	1	2	2	3	4	8	25	29	25	19	16	14	13	13	15	18	23	27	18	3	1	0	0	0	0	0
0	1	3	8	15	16	15	15	14	13	12	10	10	10	9	9	10	11	12	12	13	17	18	16	10	8	4	1	0
0	1	2	3	5	5	6	6	5	4	3	3	3	3	4	4	4	4	5	7	9	10	11	12	12	8	4	1	0
0	0	0	1	1	2	2	2	2	2	2	2	2	2	2	2	2	2	2	2	3	2	2	1	1	0	0	0	0

Table 9-15: Ford Ecosport Nozzle Average

Set-Up Details:

Fan	

Fluidic	Y

Part No/Cust	Ford Ecosport

Flow (ml/sec)	24.82

Spray Height (mm)	345

Cycle Time	30 seconds

Pressure (Bar)	3.99

NOTE: INPUT VOLUME = CC

VIEW FROM ABOVE

0	0	0	0	0	0	0	0	0	0	0	0	0	0	0	0	0	0	0	0	0	0	0	0	0	0	0	0	0
0	0	0	0	0	0	0	0	0	0	0	0	0	0	0	0	0	0	0	0	0	0	0	0	0	0	0	0	0
0	0	0	0	0	0	1	1	1	2	2	2	2	2	2	1	2	2	2	2	2	1	1	0	0	0	0	0	0

0	0	1	2	3	2	3	5	11	26	29	24	19	16	14	14	16	18	22	27	29	18	5	3	3	2	2	1	1	0
0	1	5	10	15	15	14	14	13	11	10	9	8	8	7	8	8	9	10	11	13	15	16	15	12	10	5	1	0	0
0	1	2	3	4	5	6	6	5	4	3	3	3	3	4	4	4	4	5	6	7	8	8	8	7	6	3	1	0	0
0	0	0	0	1	1	1	1	1	1	1	1	1	1	1	1	2	2	2	2	2	2	2	1	1	1	0	0	0	0

Table 9-16: Ford Ecosport Nozzle Average (symmetrical)

Set-Up Details:	**Fan**		**Fluidic**	**Y**	**Part No/Cust**	Ford Ecosport	**Flow (ml/sec)**	24.82
	Spray Height (mm)	345	**Cycle Time**	30 seconds			**Pressure (Bar)**	4.0

NOTE: INPUT VOLUME = CC *VIEW FROM ABOVE*

0	0	0	0	0	0	0	0	0	0	0	0	0	0	0	0	0	0	0	0	0	0	0	0	0	0	0	0	0	0
0	0	0	0	0	0	0	0	0	0	0	0	0	0	0	0	0	0	0	0	0	0	0	0	0	0	0	0	0	0
0	0	0	0	0	0	1	1	1	2	2	2	2	2	2	2	2	2	2	2	2	1	1	1	0	0	0	0	0	0
0	1	1	1	2	2	3	4	8	22	29	25	20	17	15	15	17	20	25	29	22	8	4	3	2	2	1	1	1	0
0	1	3	5	10	12	13	15	15	13	11	10	9	9	8	8	9	9	10	11	13	15	15	13	12	10	5	3	1	0
0	1	2	2	4	5	7	7	7	6	5	5	4	4	4	4	4	4	5	5	6	7	7	7	5	4	2	2	1	0
0	0	0	0	0	1	1	1	2	2	2	2	1	1	2	2	1	1	2	2	2	2	1	1	1	0	0	0	0	0

9.2.3. Nissan Nozzle Spray Distribution Tests

9.2.3.1. 2.5 Bar Pressure

Table 9-17: Nissan/Kautex Textron CVS Ltd Nozzle Test 1

Set-Up Details:	Fan		Fluidic	Y	Part No/Cust	Nissan/Kautex	Flow (ml/sec)	20.77
	Spray Height (mm)	400			Cycle Time	30	Pressure (Bar)	2.55

NOTE: INPUT VOLUME = CC *VIEW FROM ABOVE*

0	0	0	0	0	0	0	0	0	0	0	0	0	0	0	0	0	0	0	0	0	0	0	0	0	0	0	0	0
0	0	0	0	0	0	0	0	0	0	0	0	0	0	0	0	0	0	0	0	0	0	0	0	0	0	0	0	0
0	0	0	0	0	0	0	1	11	12	7	5	3	2	2	2	3	5	6	4	2	0	0	0	0	0	0	0	0
0	0	0	0	0	0	1	7	38	36	20	15	10	7	8	9	15	23	34	51	5	1	0	1	0	0	0	0	0
0	0	0	0	0	0	0	3	16	26	20	14	12	12	12	13	14	15	19	31	17	3	2	0	0	0	0	0	0
0	0	0	0	0	0	0	0	0	1	1	2	3	3	4	4	3	3	3	2	2	1	1	0	0	0	0	0	0
0	0	0	0	0	0	0	0	0	0	0	0	0	0	0	0	0	0	0	0	0	0	0	0	0	0	0	0	0

Table 9-18: Nissan/Kautex Textron CVS Ltd Nozzle Test 2

Set-Up Details:	Fan		Fluidic	Y	Part No/Cust	Nissan/Kautex	Flow (ml/sec)	23.37
	Spray Height (mm)	400			Cycle Time	30	Pressure (Bar)	2.52

NOTE: INPUT VOLUME = CC *VIEW FROM ABOVE*

0	0	0	0	0	0	0	0	0	0	0	0	0	0	0	0	0	0	0	0	0	0	0	0	0	0	0	0	0
0	0	0	0	0	0	0	0	0	0	0	0	0	0	0	0	0	0	0	0	0	0	0	0	0	0	0	0	0
0	0	0	0	0	0	1	5	12	12	7	6	3	2	2	3	3	4	6	6	4	1	0	0	0	0	0	0	0
0	0	0	0	0	0	1	12	48	37	22	15	10	9	8	11	17	24	38	63	37	4	0	0	0	0	0	0	0

0	0	0	0	0	0	1	5	20	25	19	14	13	13	13	14	15	16	21	33	13	2	1	0	0	0	0	0	0	0
0	0	0	0	0	0	0	0	0	1	2	3	3	4	4	3	3	3	2	2	0	0	0	0	0	0	0	0	0	0
0	0	0	0	0	0	0	0	0	0	0	0	0	0	0	0	0	0	0	0	0	0	0	0	0	0	0	0	0	0

Table 9-19: Nissan/Kautex Textron CVS Ltd Nozzle Test 3

Set-Up Details:						
Fan		**Fluidic**	**Y**	**Part No/Cust**	Nissan/Kautex	**Flow (ml/sec)**	22.77
Spray Height (mm)	400	**Cycle Time**	30			**Pressure (Bar)**	2.48

NOTE: INPUT VOLUME = CC *VIEW FROM ABOVE*

0	0	0	0	0	0	0	0	0	0	0	0	0	0	0	0	0	0	0	0	0	0	0	0	0	0	0	0	0	0
0	0	0	0	0	0	0	0	0	0	0	0	0	0	0	0	0	0	0	0	0	0	0	0	0	0	0	0	0	0
0	0	0	0	0	0	1	4	11	12	7	6	3	2	2	2	3	4	5	6	4	2	0	0	0	0	0	0	0	0
0	0	0	0	0	0	0	1	10	42	37	22	16	8	8	10	16	24	40	64	4	1	0	0	0	0	0	0	0	0
0	0	0	0	0	0	0	2	5	23	29	23	15	14	13	14	15	18	26	36	18	5	2	0	0	0	0	0	0	0
0	0	0	0	0	0	0	1	2	2	2	3	4	4	5	5	5	4	3	3	2	2	1	0	0	0	0	0	0	0
0	0	0	0	0	0	0	0	0	0	0	0	0	0	0	0	0	0	0	0	0	0	0	0	0	0	0	0	0	0

Table 9-20: Nissan/Kautex Textron CVS Ltd Nozzle Average

Set-Up Details:						
Fan		**Fluidic**	**Y**	**Part No/Cust**	Nissan/Kautex	**Flow (ml/sec)**	22.13
Spray Height (mm)	400	**Cycle Time**	30 seconds			**Pressure (Bar)**	2.52

NOTE: INPUT VOLUME = CC *VIEW FROM ABOVE*

0	0	0	0	0	0	0	0	0	0	0	0	0	0	0	0	0	0	0	0	0	0	0	0	0	0	0	0	0
0	0	0	0	0	0	0	0	0	0	0	0	0	0	0	0	0	0	0	0	0	0	0	0	0	0	0	0	0
0	0	0	0	0	0	1	3	11	12	7	6	3	2	2	2	3	4	6	5	3	1	0	0	0	0	0	0	0
0	0	0	0	0	0	1	7	32	38	26	17	12	8	8	10	16	24	37	59	15	2	0	0	0	0	0	0	0
0	0	0	0	0	0	0	3	14	25	23	17	13	13	13	14	15	16	22	33	16	3	2	0	0	0	0	0	0
0	0	0	0	0	0	0	0	1	1	2	3	3	4	4	4	4	3	3	2	1	1	1	0	0	0	0	0	0
0	0	0	0	0	0	0	0	0	0	0	0	0	0	0	0	0	0	0	0	0	0	0	0	0	0	0	0	0

Table 9-21: Nissan/Kautex Textron CVS Ltd Nozzle Average (symmetrical)

Set-Up Details:

Fan	

Fluidic	**Y**

Part No/Cust	Nissan/Kautex

Flow (ml/sec)	22.13

Spray Height (mm)	400

Cycle Time	30 seconds

Pressure (Bar)	2.5

NOTE: INPUT VOLUME = CC

VIEW FROM ABOVE

0	0	0	0	0	0	0	0	0	0	0	0	0	0	0	0	0	0	0	0	0	0	0	0	0	0	0	0	0
0	0	0	0	0	0	0	0	0	0	0	0	0	0	0	0	0	0	0	0	0	0	0	0	0	0	0	0	0
0	0	0	0	0	0	0	2	6	8	6	6	4	3	2	2	3	4	6	6	8	6	2	0	0	0	0	0	0
0	0	0	0	0	0	1	3	17	27	43	27	18	12	9	9	12	18	27	43	27	17	3	1	0	0	0	0	0
0	0	0	0	0	0	0	3	9	20	28	20	15	14	13	13	14	15	20	28	20	9	3	0	0	0	0	0	0
0	0	0	0	0	0	0	1	1	1	2	3	3	4	4	4	4	3	3	2	1	1	1	0	0	0	0	0	0
0	0	0	0	0	0	0	0	0	0	0	0	0	0	0	0	0	0	0	0	0	0	0	0	0	0	0	0	0

9.2.3.2. 4 Bar Pressure

Table 9-22: Nissan/Kautex Textron CVS Ltd Nozzle Test 1

Set-Up Details:	Fan		Fluidic	Y	Part No/Cust	Nissan/Kautex	Flow (ml/sec)	25.00
	Spray Height (mm)	400			Cycle Time	30	Pressure (Bar)	4.0

NOTE: INPUT VOLUME = CC *VIEW FROM ABOVE*

0	0	0	0	0	0	0	0	0	0	0	0	0	0	0	0	0	0	0	0	0	0	0	0	0	0	0	0	0	0
0	0	0	0	0	0	2	4	3	0	0	0	0	0	0	0	0	0	0	1	2	1	0	0	0	0	0	0	0	0
0	0	0	0	0	0	8	21	22	12	8	7	5	4	4	4	5	5	8	14	9	3	1	0	0	0	0	0	0	0
0	0	0	0	0	0	9	37	42	28	23	19	15	12	13	17	23	29	41	70	37	6	1	0	0	0	0	0	0	0
0	0	0	0	0	0	0	4	7	9	9	9	10	10	11	11	13	17	26	33	13	2	0	0	0	0	0	0	0	0
0	0	0	0	0	0	0	0	0	0	0	0	0	0	3	3	2	0	0	0	0	0	0	0	0	0	0	0	0	0
0	0	0	0	0	0	0	0	0	0	0	0	0	0	0	0	0	0	0	0	0	0	0	0	0	0	0	0	0	0

Table 9-23: Nissan/Kautex Textron CVS Ltd Nozzle Average (symmetrical)

Set-Up Details:	Fan		Fluidic	Y	Part No/Cust	Nissan/Kautex	Flow (ml/sec)	25.57
	Spray Height (mm)	400			Cycle Time	30 seconds	Pressure (Bar)	4.0

NOTE: INPUT VOLUME = CC *VIEW FROM ABOVE*

0	0	0	0	0	0	0	0	0	0	0	0	0	0	0	0	0	0	0	0	0	0	0	0	0	0	0	0	0	0
0	0	0	0	0	0	1	2	2	1	1	1	0	0	0	0	0	0	1	1	1	2	2	1	0	0	0	0	0	0
0	0	0	0	0	0	4	11	13	11	11	8	5	5	4	4	5	5	8	11	11	13	11	4	0	0	0	0	0	0

0	0	0	0	0	0	5	19	24	33	47	30	22	18	15	15	18	22	30	47	33	24	19	5	0	0	0	0	0	0
0	0	0	0	0	0	0	2	5	11	21	18	14	12	11	11	12	14	18	21	11	5	2	0	0	0	0	0	0	0
0	0	0	0	0	0	0	0	0	0	0	0	0	1	3	3	1	0	0	0	0	0	0	0	0	0	0	0	0	0
0	0	0	0	0	0	0	0	0	0	0	0	0	0	0	0	0	0	0	0	0	0	0	0	0	0	0	0	0	0

9.2.4. Toyota RAV4 Nozzle Spray Distribution

9.2.4.1. 2.5 Bar Pressure

Table 9-24: Toyota RAV4 Nozzle Test 1

Set-Up Details:							
	Fan		**Fluidic**	**Y**	**Part No/Cust**	Toyota RAV4	**Flow (ml/sec)**	14.37
	Spray Height (mm)	400	**Cycle Time**	30			**Pressure (Bar)**	2.49

NOTE: INPUT VOLUME = CC *VIEW FROM ABOVE*

0	0	0	0	0	0	0	0	0	0	0	0	0	0	0	0	0	0	0	0	0	0	0	0	0	0	0	0	0	0
0	0	0	0	0	0	0	0	0	0	0	0	0	0	0	0	0	0	0	0	0	0	0	0	0	0	0	0	0	0
0	0	0	0	2	17	12	5	5	4	3	1	1	1	1	2	2	2	2	3	3	4	4	6	4	1	1	0	0	0
0	0	0	0	1	34	24	9	24	15	8	3	2	2	2	2	3	3	4	10	20	21	10	37	36	2	1	0	0	0
0	0	0	0	0	1	2	3	4	5	4	3	2	2	2	2	2	3	4	5	7	6	5	5	4	1	0	0	0	0
0	0	0	0	0	0	0	0	0	0	0	0	0	0	0	0	0	0	0	0	0	0	0	0	0	0	0	0	0	0
0	0	0	0	0	0	0	0	0	0	0	0	0	0	0	0	0	0	0	0	0	0	0	0	0	0	0	0	0	0

Table 9-25: Toyota RAV4 Nozzle Test 2

Set-Up Details:							
	Fan		**Fluidic**	**Y**	**Part No/Cust**	Toyota RAV4	**Flow (ml/sec)**	13.33
	Spray Height (mm)	400	**Cycle Time**	30			**Pressure (Bar)**	2.49

NOTE: INPUT VOLUME = CC *VIEW FROM ABOVE*

0	0	0	0	0	0	0	0	0	0	0	0	0	0	0	0	0	0	0	0	0	0	0	0	0	0	0	0	0	0
0	0	0	0	0	0	0	0	0	0	0	0	0	0	0	0	0	0	0	0	0	0	0	0	0	0	0	0	0	0
0	0	0	0	1	1	11	10	5	4	2	2	1	0	0	0	0	0	1	2	2	2	3	4	2	0	0	0	0	0
0	0	0	0	3	39	21	10	24	15	8	3	2	1	2	1	1	2	4	9	18	21	10	34	40	1	0	0	0	0
0	0	0	0	2	2	3	3	5	6	4	2	2	1	1	1	1	2	4	5	9	8	5	6	5	1	0	0	0	0
0	0	0	0	0	0	0	0	0	0	0	0	0	0	0	0	0	0	0	0	0	0	0	0	0	0	0	0	0	0
0	0	0	0	0	0	0	0	0	0	0	0	0	0	0	0	0	0	0	0	0	0	0	0	0	0	0	0	0	0

Table 9-26: Toyota RAV4 Nozzle Test 3

Set-Up Details:						
Fan		**Fluidic**	**Y**	**Part No/Cust**	Toyota RAV4	**Flow (ml/sec)**	13.40
Spray Height (mm)	400			**Cycle Time**	30	**Pressure (Bar)**	2.5

NOTE: INPUT VOLUME = CC *VIEW FROM ABOVE*

0	0	0	0	0	0	0	0	0	0	0	0	0	0	0	0	0	0	0	0	0	0	0	0	0	0	0	0	0	0
0	0	0	0	0	0	0	0	0	0	0	0	0	0	0	0	0	0	0	0	0	0	0	0	0	0	0	0	0	0
0	0	0	0	0	11	13	5	5	3	2	1	0	0	0	0	1	1	2	2	3	3	4	3	0	0	0	0	0	0
0	0	0	0	1	28	26	10	23	13	9	3	2	1	1	1	2	2	4	8	17	23	10	26	47	3	1	0	0	0
0	0	0	1	2	4	4	5	5	5	3	2	1	1	1	1	2	3	6	10	7	5	6	7	1	0	0	0	0	0
0	0	0	0	0	0	0	0	0	0	0	0	0	0	0	0	0	0	0	0	0	0	0	0	0	0	0	0	0	0
0	0	0	0	0	0	0	0	0	0	0	0	0	0	0	0	0	0	0	0	0	0	0	0	0	0	0	0	0	0

Table 9-27: Toyota RAV4 Nozzle Average

Set-Up Details:	Fan		Fluidic	Y	Part No/Cust	Toyota RAV4	Flow (ml/sec)	13.70
	Spray Height (mm)	400			Cycle Time	30 seconds	Pressure (Bar)	2.49

NOTE: INPUT VOLUME = CC *VIEW FROM ABOVE*

0	0	0	0	0	0	0	0	0	0	0	0	0	0	0	0	0	0	0	0	0	0	0	0	0	0	0	0	0
0	0	0	0	0	0	0	0	0	0	0	0	0	0	0	0	0	0	0	0	0	0	0	0	0	0	0	0	0
0	0	0	0	1	10	12	7	5	4	2	1	1	0	0	1	1	1	2	2	3	3	4	4	2	0	0	0	0
0	0	0	0	2	34	24	10	24	14	8	3	2	1	2	1	2	2	4	9	18	22	10	32	41	2	1	0	0
0	0	0	0	1	2	3	4	5	5	4	2	2	1	1	1	2	3	5	7	8	6	5	6	3	1	0	0	0
0	0	0	0	0	0	0	0	0	0	0	0	0	0	0	0	0	0	0	0	0	0	0	0	0	0	0	0	0
0	0	0	0	0	0	0	0	0	0	0	0	0	0	0	0	0	0	0	0	0	0	0	0	0	0	0	0	0

Table 9-28: Toyota RAV4 Nozzle Average (symmetrical)

Set-Up Details:	Fan		Fluidic	Y	Part No/Cust	Toyota RAV4	Flow (ml/sec)	13.70
	Spray Height (mm)	400			Cycle Time	30 seconds	Pressure (Bar)	2.5

NOTE: INPUT VOLUME = CC *VIEW FROM ABOVE*

0	0	0	0	0	0	0	0	0	0	0	0	0	0	0	0	0	0	0	0	0	0	0	0	0	0	0	0	0
0	0	0	0	0	0	0	0	0	0	0	0	0	0	0	0	0	0	0	0	0	0	0	0	0	0	0	0	0
0	0	0	0	1	6	8	5	4	3	2	2	1	1	1	1	1	1	2	2	3	4	5	8	6	1	0	0	0
0	0	0	0	2	37	28	10	23	16	9	4	2	2	2	2	2	2	4	9	16	23	10	28	37	2	0	0	0

0	0	0	0	1	3	5	5	6	7	5	4	2	2	1	1	2	2	4	5	7	6	5	5	3	1	0	0	0	0
0	0	0	0	0	0	0	0	0	0	0	0	0	0	0	0	0	0	0	0	0	0	0	0	0	0	0	0	0	0
0	0	0	0	0	0	0	0	0	0	0	0	0	0	0	0	0	0	0	0	0	0	0	0	0	0	0	0	0	0

9.2.4.2. 4 Bar Pressure

Table 9-29: Toyota RAV4 Nozzle Test 1

Set-Up Details:							
Fan		**Fluidic**	**Y**	**Part No/Cust**	Toyota RAV4	**Flow (ml/sec)**	18.00
Spray Height (mm)	400	**Cycle Time**	30			**Pressure (Bar)**	3.98

NOTE: INPUT VOLUME = CC *VIEW FROM ABOVE*

0	0	0	0	0	0	0	0	0	0	0	0	0	0	0	0	0	0	0	0	0	0	0	0	0	0	0	0	0	0
0	0	0	0	0	0	1	1	1	2	3	3	2	1	1	1	1	2	2	3	2	1	2	1	0	0	0	0	0	0
0	0	0	0	0	3	18	7	6	20	27	9	4	2	2	2	3	4	6	17	23	7	5	6	5	2	1	1	1	0
0	0	0	0	0	6	63	18	8	21	12	5	4	4	3	3	3	4	6	11	18	10	10	48	31	2	1	1	0	0
0	0	0	0	0	0	2	3	2	2	2	1	1	1	1	0	0	0	2	2	2	3	4	6	5	2	0	0	0	0
0	0	0	0	0	0	0	0	0	0	0	0	0	0	0	0	0	0	0	0	0	0	0	0	0	0	0	0	0	0
0	0	0	0	0	0	0	0	0	0	0	0	0	0	0	0	0	0	0	0	0	0	0	0	0	0	0	0	0	0

Table 9-30: Toyota RAV4 Nozzle Test 2

Set-Up Details:							
Fan		**Fluidic**	**Y**	**Part No/Cust**	Toyota RAV4	**Flow (ml/sec)**	18.13
Spray Height (mm)	400	**Cycle Time**	30			**Pressure (Bar)**	4.05

NOTE: INPUT VOLUME = CC *VIEW FROM ABOVE*

0	0	0	0	0	0	0	0	0	0	0	0	0	0	0	0	0	0	0	0	0	0	0	0	0	0	0	0	0	0
0	0	0	0	1	1	1	1	1	1	1	1	1	1	1	1	1	1	1	1	1	1	1	1	0	0	0	0	0	0
0	0	0	0	1	1	4	4	4	7	10	5	3	2	2	2	2	2	3	4	3	3	2	1	1	0	0	0	0	0
0	0	0	0	1	5	67	20	9	25	29	9	4	3	2	2	3	3	6	17	31	10	6	43	18	10	0	0	0	0
0	0	0	0	0	2	8	8	5	5	5	3	2	0	1	0	1	2	3	5	8	7	7	22	20	11	0	0	0	0
0	0	0	0	0	0	0	0	0	0	0	0	0	0	0	0	0	0	0	1	1	1	2	3	2	0	0	0	0	0
0	0	0	0	0	0	0	0	0	0	0	0	0	0	0	0	0	0	0	0	0	0	0	0	0	0	0	0	0	0

Table 9-31: Toyota RAV4 Nozzle Test 3

Set-Up Details:	**Fan**		**Fluidic**	**Y**	**Part No/Cust**	Toyota RAV4	**Flow (ml/sec)**	18.97
	Spray Height (mm)	400	**Cycle Time**	30			**Pressure (Bar)**	3.99

NOTE: INPUT VOLUME = CC *VIEW FROM ABOVE*

0	0	0	0	0	0	0	0	0	0	0	0	0	0	0	0	0	0	0	0	0	0	0	0	0	0	0	0	0	0
0	0	0	0	1	2	4	4	4	6	8	5	3	3	2	2	2	3	3	4	3	3	2	2	1	1	1	0	0	0
0	0	0	1	1	6	65	20	10	28	31	10	2	4	3	3	4	5	7	19	30	10	6	8	9	2	1	1	0	0
0	0	0	0	0	2	12	10	6	6	2	4	2	2	2	2	2	3	4	6	11	9	8	51	28	4	1	1	0	0
0	0	0	0	0	0	0	1	1	0	0	0	0	0	0	0	0	0	1	1	1	2	3	4	4	1	0	0	0	0
0	0	0	0	0	0	0	0	0	0	0	0	0	0	0	0	0	0	1	1	1	2	3	4	4	1	0	0	0	0
0	0	0	0	0	0	0	0	0	0	0	0	0	0	0	0	0	0	0	0	0	0	0	0	0	0	0	0	0	0

Table 9-32: Toyota RAV4 Nozzle Average

Set-Up Details:	Fan		Fluidic	Y	Part No/Cust	Toyota RAV4	Flow (ml/sec)	18.41
	Spray Height (mm)	400			Cycle Time	30 seconds	Pressure (Bar)	4.01

NOTE: INPUT VOLUME = CC *VIEW FROM ABOVE*

0	0	0	0	0	0	0	0	0	0	0	0	0	0	0	0	0	0	0	0	0	0	0	0	0	0	0	0	0	0
0	0	0	0	1	1	2	2	2	3	4	3	2	2	1	1	1	2	2	3	2	2	2	1	0	0	0	0	0	0
0	0	0	0	1	3	29	10	7	18	23	8	3	3	2	2	3	4	5	13	19	7	4	5	5	1	1	1	0	0
0	0	0	0	0	4	47	16	8	17	14	6	3	3	2	2	3	3	5	11	20	10	8	47	26	5	1	1	0	0
0	0	0	0	0	1	3	4	3	2	2	1	1	0	1	0	0	1	2	3	4	4	5	11	10	5	0	0	0	0
0	0	0	0	0	0	0	0	0	0	0	0	0	0	0	0	0	0	0	1	1	1	2	2	2	0	0	0	0	0
0	0	0	0	0	0	0	0	0	0	0	0	0	0	0	0	0	0	0	0	0	0	0	0	0	0	0	0	0	0

Table 9-33: Toyota RAV4 Nozzle Average (symmetrical)

Set-Up Details:	Fan		Fluidic	Y	Part No/Cust	Toyota RAV4	Flow (ml/sec)	18.41
	Spray Height (mm)	400			Cycle Time	30 seconds	Pressure (Bar)	4.0

NOTE: INPUT VOLUME = CC *VIEW FROM ABOVE*

0	0	0	0	0	0	0	0	0	0	0	0	0	0	0	0	0	0	0	0	0	0	0	0	0	0	0	0	0	0
0	0	0	0	0	1	1	1	1	2	2	2	1	1	1	1	1	1	2	2	2	1	1	1	1	0	0	0	0	0
0	0	0	0	0	2	15	5	3	9	11	4	2	1	1	1	1	2	4	11	9	3	5	15	2	0	0	0	0	0

0	0	0	0	0	2	24	8	4	9	7	3	2	2	1	1	2	2	3	7	9	4	8	24	2	0	0	0	0	0
0	0	0	0	0	0	2	2	1	1	1	1	1	0	0	0	0	1	1	1	1	1	2	2	0	0	0	0	0	0
0	0	0	0	0	0	0	0	0	0	0	0	0	0	0	0	0	0	0	0	0	0	0	0	0	0	0	0	0	0
0	0	0	0	0	0	0	0	0	0	0	0	0	0	0	0	0	0	0	0	0	0	0	0	0	0	0	0	0	0

9.3. Appendix C

9.3.1. Nissan Nozzle Spray Angle

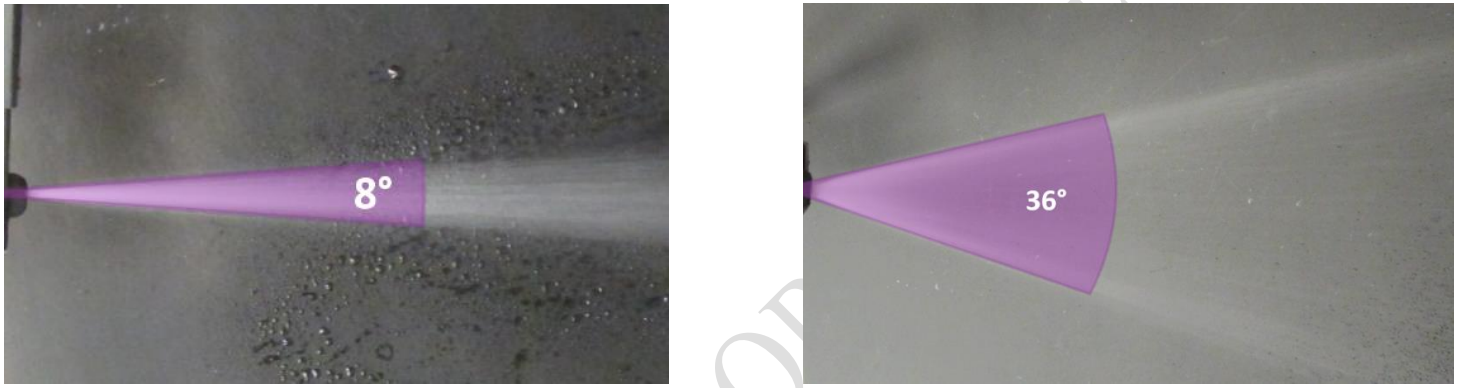

Figure 9-1: Nissan Nozzle Spray Angle Height (Left) and Width (Right)

9.3.2. Nissan Nozzle Spray Distribution and Mass Flow Rate

Set-Up Details:

Fan	0	**Fluidic**	Y	**Part No/Customer**	Sample	**Flow (cc/sec)**	19.00
Spray Height (mm)	400			**Cycle Time (s)**	60	**Pressure (Bar)**	2.50

NOTE: INPUT VOLUME = CC

VIEW FROM ABOVE

FRONT

0	0	0	0	0	0	0	0	0	0	0	0	0	0	0	0	0	0	0	0	0	0	0	0	0	0	0	0	0
0	0	0	0	0	0	0	1	1	2	2	1	1	1	1	1	1	1	1	2	2	1	1	0	0	0	0	0	0	0
0	0	0	0	0	0	0	1	3	7	9	6	6	7	7	7	7	6	6	9	7	3	1	0	0	0	0	0	0	0
0	0	0	0	0	0	0	4	50	68	48	33	25	25	21	21	25	25	33	48	68	50	4	0	0	0	0	0	0	0
0	0	0	0	0	0	1	3	27	61	38	25	16	12	10	10	12	16	25	38	61	27	3	1	0	0	0	0	0	0
0	0	0	0	0	0	0	0	1	2	3	4	3	3	2	2	3	3	4	3	2	1	0	0	0	0	0	0	0	0

0	0	0	0	0	0	0	0	0	0	0	0	0	0	0	0	0	0	0	0	0	0	0	0	0	0	0	0	0	0

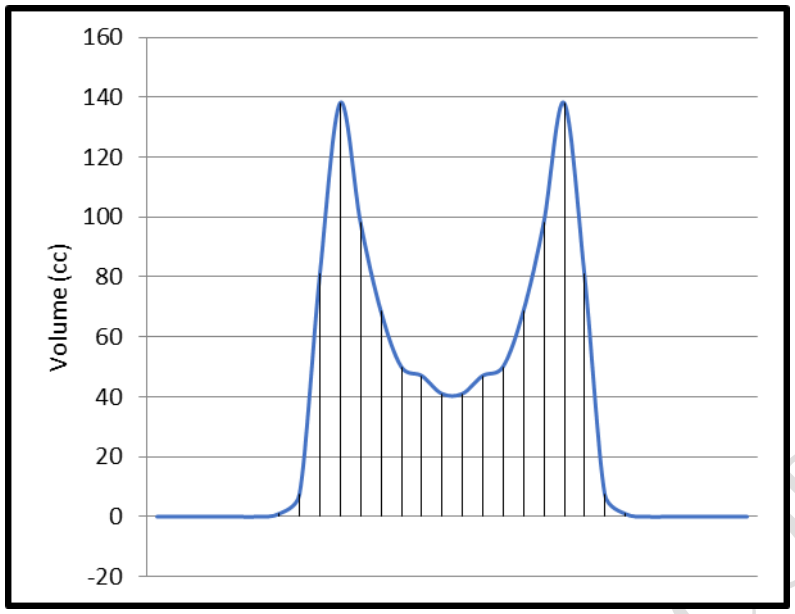

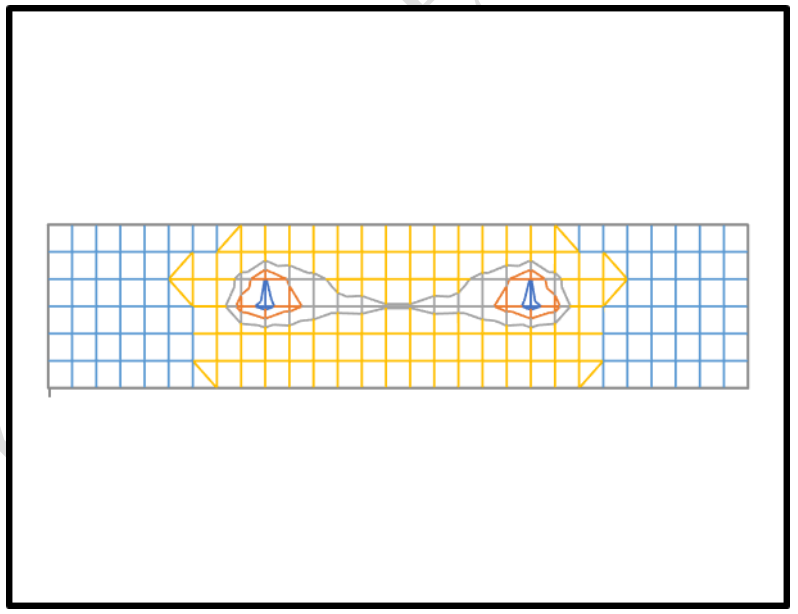

9.3.3. Nissan Nozzle High Speed Imaging

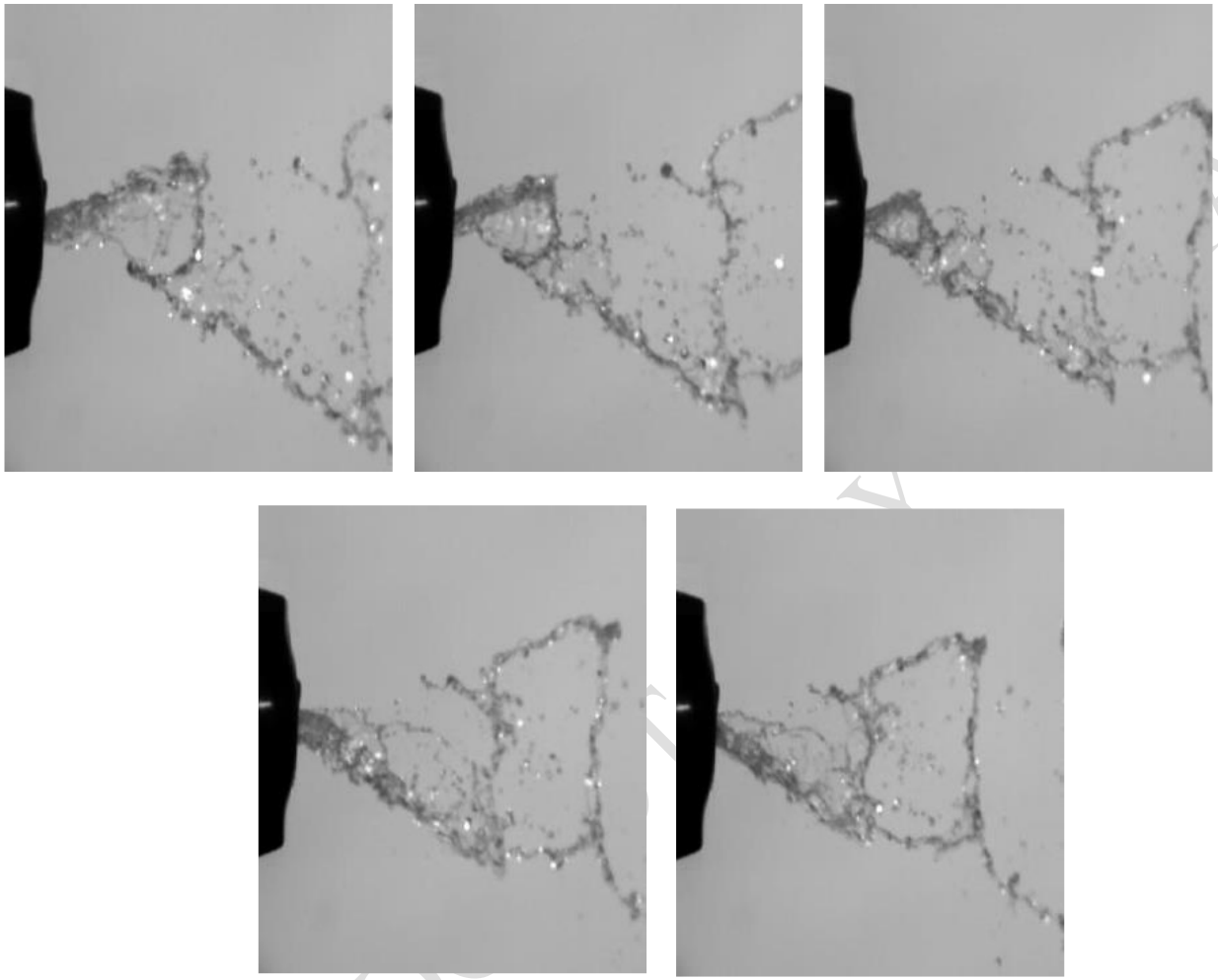

9.4. Appendix D

9.4.1. Spray Angles at 2.5 Bar

Table 9-34: Spray Angles for All Nozzles at 2.5 Bar Pressure

	Photo number	Outer	Inner	Side
Ford B-Max	1	42.774	N/A	3.949
	2	43.88	N/A	4.557
	3	44.295	N/A	4.108
	average	43.64967	N/A	4.204667
Ford Ecosport	1	67.582	40.394	7.706
	2	66.793	40.833	6.899
	3	67.091	40.77	7.638
	average	67.15533	40.66567	7.414333
Nissan	1	35.377	N/A	7.681
	2	35.223	N/A	7.508
	3	36.589	N/A	7.603
	average	35.72967	N/A	7.597333
Toyota	1	51.008	32.989	4.363
	2	51.937	34.886	5.524
	3	52.403	32.41	4.909
	average	51.78267	33.42833	4.932

9.4.2. Spray Angles at 4 Bar

Table 9-35: Spray Angles for All Nozzles at 4 Bar Pressure

	Photo number	Outer	Inner	Side
Ford B-Max	1	N/A	N/A	N/A
	2	N/A	N/A	N/A
	3	N/A	N/A	N/A
	average	N/A	N/A	N/A
Ford Ecosport	1	70.299	43.314	N/A
	2	70.969	44.62	N/A
	3	71.128	43.121	N/A
	average	70.79867	43.685	N/A
Nissan	1	33.334	N/A	5.721
	2	N/A	N/A	N/A
	3	N/A	N/A	N/A
	average	33.334	N/A	5.721
Toyota	1	45.64	28.49	3.898
	2	N/A	N/A	N/A
	3	N/A	N/A	N/A
	average	45.64	28.49	3.898

9.4.3. Spray Angle Summary

Table 9-36: Spray Angles for All Nozzles

Nozzle	2.5 Bar			4 Bar		
	Outer	Inner	Side	Outer	Inner	Side
Ford B-Max	43.65	N/A	4.2	N/A	N/A	N/A
Ford Eco-Sport	67.16	40.67	7.41	70.8	43.69	N/A
Nissan	35.73	N/A	7.6	33.33	N/A	5.72
Toyota	51.78	33.43	4.93	45.64	28.49	3.9

9.5. Appendix E

Table 9-37: High Speed Camera Data

	Ford Ecosport Nozzle				Nissan Nozzle				Toyota RAV4 Nozzle			
Position	Arrive	Leave	Middle	Frames Between	Arrive	Leave	Middle	Frames Between	Arrive	Leave	Middle	Frames Between
1	[redacted]											
2	[redacted]											
1	[redacted]											
2	[redacted]											
1	[redacted]											
2	[redacted]											
1	[redacted]											
2	[redacted]											
1	[redacted]											
2	[redacted]											

1														
2														
1														
2														
1														
2														
1														
2														
1														
2														

Average Frames Between:				
Frames Per Second:				
Time between each side (seconds):				
Time to return to same side (seconds):				
Periodic frequency (Hz):				

9.6. Appendix F: Published papers

9.7. Defects

Polymer materials have increasingly been used in the manufacture of micro-fluidic systems and devices over the past century. This is due to the development of systems requiring the elasticity and heat sensitivity of a polymer for very small parts. These advances in technology necessitated an improvement in manufacturing method for small parts, to ensure that optimum accuracy is achieved. The main type of forming process for polymer micro-fluidic devices is micro-injection moulding.

The manufacturing method used to mass produce the fluidic chips for the nozzles for the vehicles is injection moulding with 8 nozzles on one plate produced at a time. These fluidic chips are produced using micro-injection moulding, this involves the same three main mechanisms as conventional injection moulding: injection, compression and ejection. However, the process and tooling are altered slightly to compensate for the smaller size of the parts being manufactured [78].

Micro-injection moulding characteristically comprises of the following four steps shown in Figure 9-2: a) mould closing, b) injection and holding, c) cooling and plastication and finally d) mould opening and part ejection. The main difference to conventional injection moulding is that some of the stages have been merged for the micro-scale moulding: injection and holding, and cooling and holding. This is due to the substantially smaller parts requiring a shorter time for plastication to occur in the

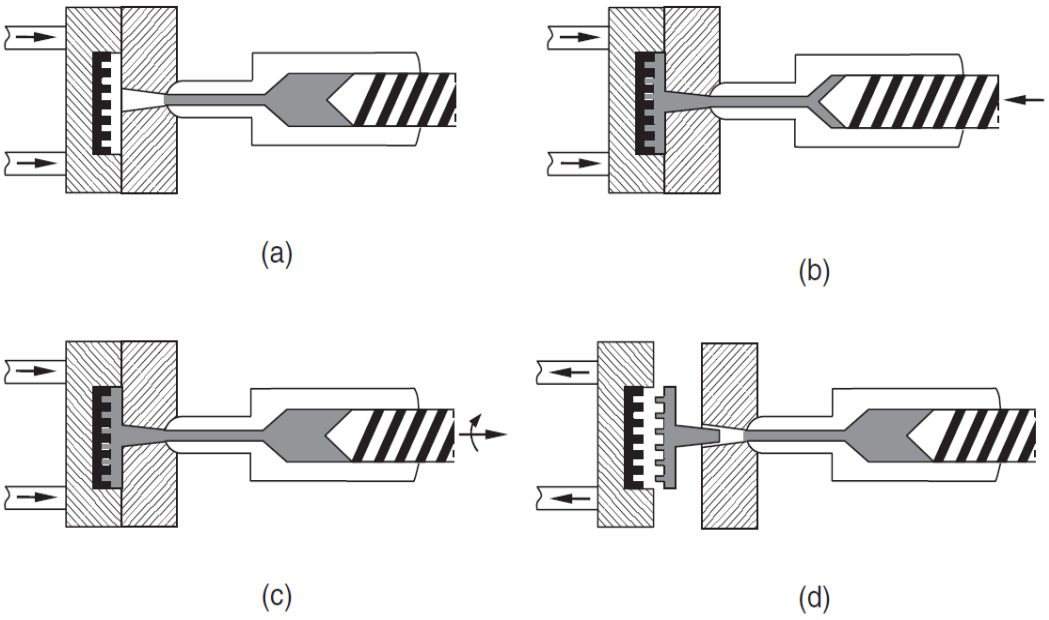

Figure 9-2: Micro-injection moulding stages: a) mould closing, b) injection and holding, c) cooling and plastication and finally d) mould opening and part ejection [79]

mould as there is a large proportion of surface area to volume [79].

There are four main types of micro-structures that can be produced through micro-injection moulding: surface micro-structures, shell micro-structures, continuous micro-profiles and discrete micro-parts (Figure 9-3). The fluidic chips in this project are created as discrete micro-parts, meaning that they have weigh less than a gram and have a 3D shape rather than being a continuous section. Discrete micro-parts can be manufactured through micro-injection moulding or hot embossing, however the injection moulding method is more effective at producing quality parts easily as some modifications would be required in hot embossing [78].

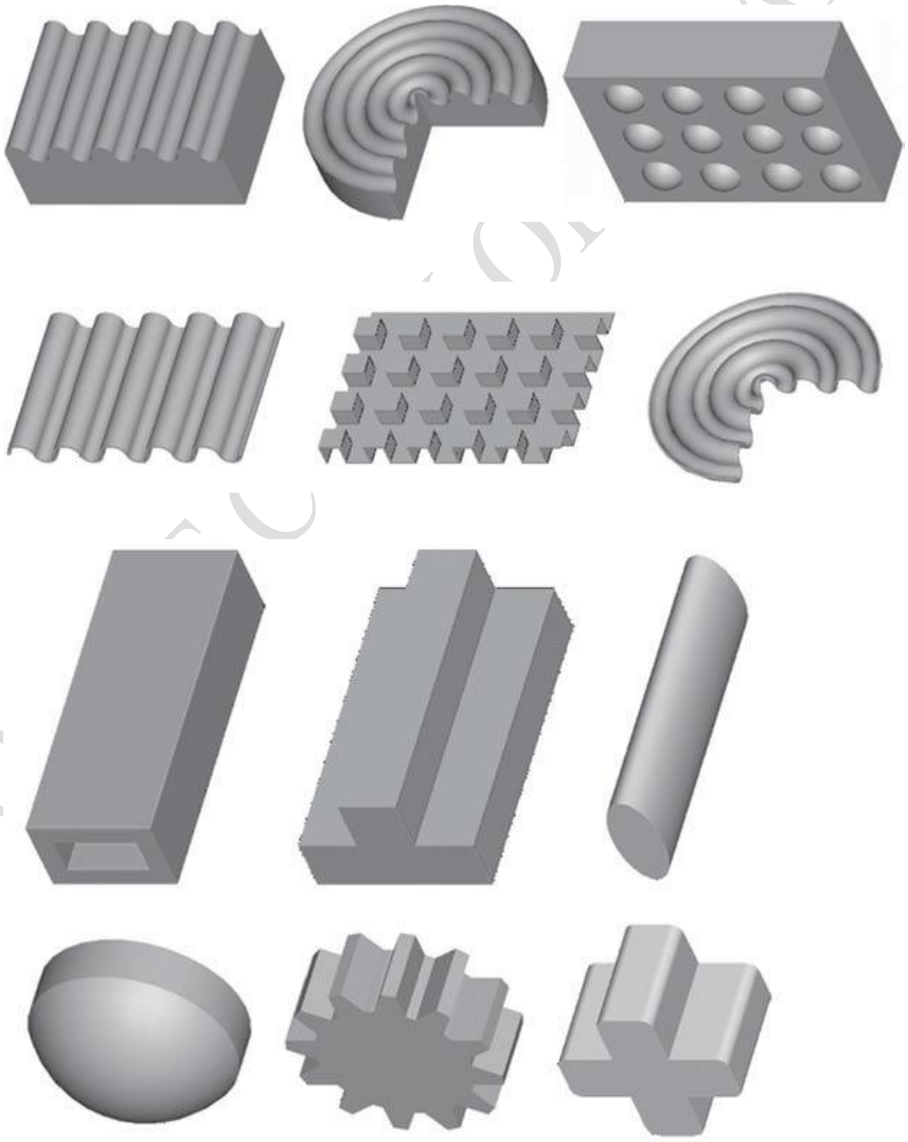

Figure 9-3: Surface microstructure examples (top row), shell micro-structure examples (second row), continuous micro-profile examples (third row) and discrete micro-part examples (bottom row) [78]

Unfortunately, with this production method and such small and intricate parts there can be a number of defects which affect the quality of the finished product. Due to the highly decreased size in comparison to conventional injection moulding the precision must be greatly increased to prevent over- or under-filling moulds, in addition the time taken for the polymer to cool will be increased due to the high surface area to volume ratio. A further issue is the ejection of the part from the mould, there needs to be a method to ensure that there is no distortion of the part when the pins come into contact with it as the part is very small and any alteration of the part could be detrimental to the quality of the part [78].

This was experienced when producing the nozzles for Nissan vehicles, therefore there is a requirement to investigate the different defects that can occur during manufacture and why they are present. This led to some computational experimentation to find how defects within a fluidic chip can affect the fluid flow and further investigation into a simplified straight channel such as those found as a part of the feedback channels in the chip.

9.8. Tolerance Defects

The first step in the defect analysis is to assess the parts of the nozzle which were deemed most vital in terms of how they would affect the flow of the fluid through the nozzle. These parts of the nozzle were then adjusted to either the minimum, maximum or both tolerance values and then assessed using computational fluid dynamics to find the difference between the defected nozzles and the nominal nozzle.

The parts of the nozzle determined as most vital are the following: nozzle outlet width ①, nozzle inlet width ②, inner chamber inlet width ③, inner chamber width ④ and feedback channel width ⑤ (Figure 9-4).

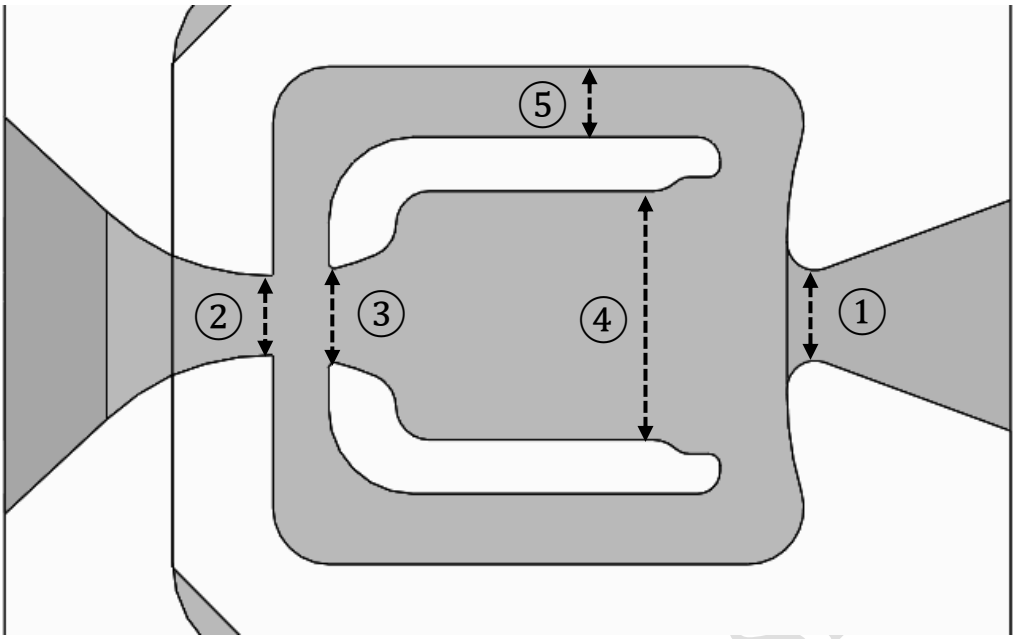

Figure 9-4: Vital Measurements within the Nozzle

The investigation found that by altering the dimensions of the outlet of the nozzle (①), the width of the spray angle could be changed. With a wider outlet, the spray angle increases, and a narrower outlet results in the spray angle decreasing. This is due to the increased amount of water allowed through the outlet and the area of least resistance was at the exterior of the already occurring spray angle. The oscillation speed and velocity are not affected with a wider outlet due to the difference in dimension being at a late point in the system. The oscillation speed however is lower with the narrower outlet, this is due to a differing amount of water being allowed to flow through the feedback channels.

Changing the width of the nozzle inlet (②) or the inner chamber nozzle inlet (③) alters the flow so that the velocity throughout the nozzle is increased with a narrower inlet width and decreased with a wider inlet width. The increased velocity of the water with a narrower inlet is due to the constant mass flow rate used in the simulation and there is a constant volume of water within the nozzle as water is an incompressible fluid. There is a larger spray angle due to the increased velocity, giving to a need for a greater amount of water to flow out of the outlet at any time in a more diffusive method. The higher velocity is additionally the reason for the

greater oscillation rate as the fluid is flowing through the nozzle at a faster rate, feeding back faster and influencing the flow in the internal chamber more often.

There is not a large amount of difference of the fluid flow with a change in dimension for the internal chamber width (④). There is a very small increase in oscillation rate however not enough to deteriorate the effect of the original rate, this is due to the increase in distance required for the flow to travel. With a wider internal chamber, the flow is able to flow further before being deformed by the vortices formed within the internal chamber.

Narrower feedback channel width (⑤) equates to a wider spray angle of fluid emitted from the nozzle, additionally there is a very small decrease in maximum velocity. The spray angle is wider due to the feedback flow velocity being faster to cope with the narrowed area through which it can flow. The faster flow in the feedback channel is able to deflect the main part of the fluid flow in the internal chamber more greatly which guides the flow out of the outlet in a wider area out of the nozzle.

9.9. Manufacturing Defects

It is important to work out what defects can occur and how detrimental they can be to the design and how to solve any problems caused. An investigation into a variety of possible defects that could occur during the injection moulding process so that any problems that occurred could be resolved [80]. Due to the complex geometry of the nozzle part a small section is studied rather than the part as a whole, the section considered is a singular feedback channel.

A series of computational micro-channels with a variety of the most common defects have been computationally constructed using computer aided design (CAD). Through the channels, turbulent water flow is fed to investigate the flow profile and rate. A micro-channel of dimensions $616.93 \times 1.14 \times 3750$ μm is used with fully turbulent SST modeled water at a temperature of 25°C. These channel dimensions are taken from the fluidic nozzle discussed earlier in this chapter. The fluid travels at an averaged volumetric flow rate of 4 ml/s at the inlet and 0MPa relative static pressure at the outlet. Given these values and the dimensions of the channel it is possible to calculate the hydraulic radius to be 2.28 μm, the average velocity of the

cross section to be 5687 m/s and the Reynolds number of 14526, putting the fluid firmly in the turbulent range.

9.9.1. Nominal Channel

First it is important to examine the flow through the feedback channel with correct dimensions and no defects, smooth walls and a flow of turbulent fluid, as would be found in the fluidic nozzle. As shown below (Figure 9-5) the flow is uniform throughout the feedback channel where the velocity is at its highest in the main part of the channel and slower at the edges where the highest amount of surface friction

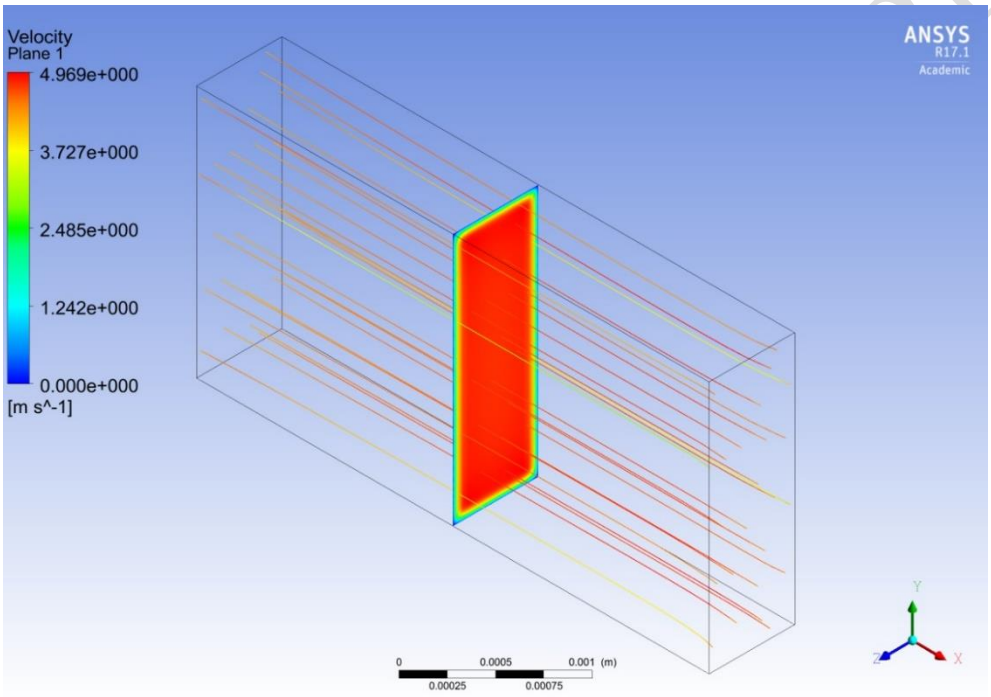

Figure 9-5: Fluid flow through smooth feedback channel

can be found.

9.9.2. High Surface Friction

The next situation investigated is the case for which the surface of the walls have a higher coefficient of friction (Figure 9-6 – Figure 8-7), expected to be produced if there was a rougher surface finish than anticipated. The higher friction channel has been modelled by geometrically changing the sides of the channel to simulate lines of different widths throughout, meaning that the water has to alter velocity to follow the wall boundary. This could be due to a number of factors, from a small amount of delamination, blistering, flow lines or from simply a polymer fill with an unsteady microstructure. Delamination is where a part of the wall is peeling off or splitting open, usually caused by shearing of the material or insufficient mould fill speed.

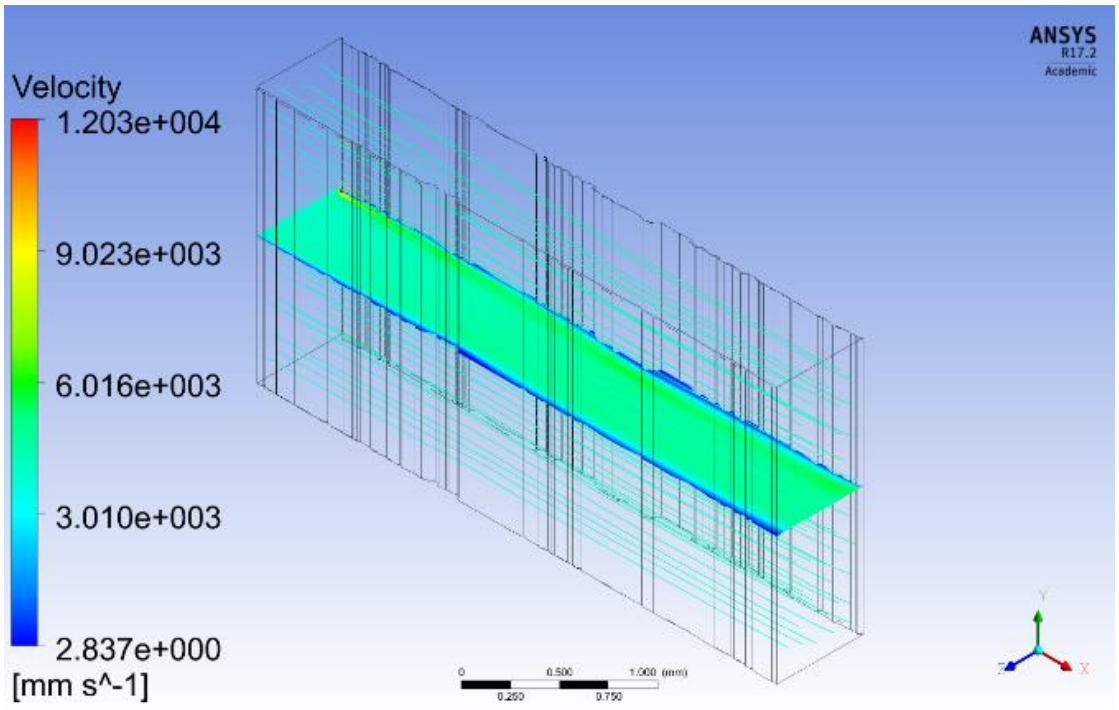

Figure 9-6: Fluid flow through channel with rough sides in full channel

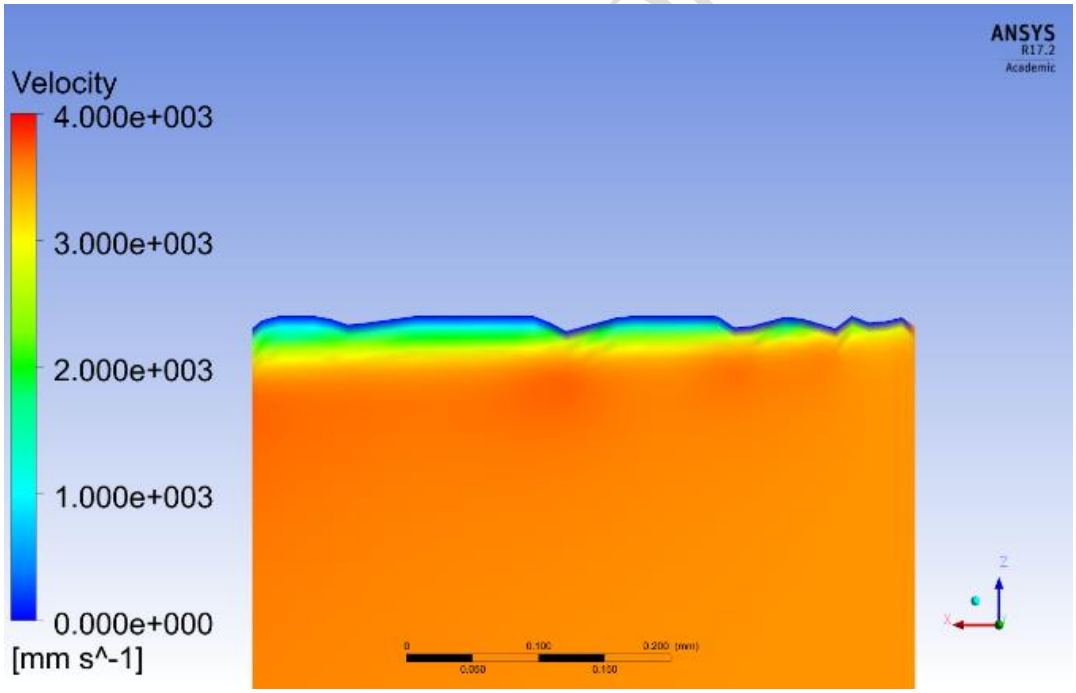

Figure 9-7: Fluid flow through channel with rough sides at the boundary

Blisters are the result of small amounts of heated air trapped in the mould, they are often caused by a low back pressure of insufficient material temperature. Flow lines are simply small wrinkles in the material where the material has inefficiently bonded and cooled at an uneven rate, caused primarily by a low temperature mould [80].

The flow of the water through the channel with a higher coefficient of friction is similar to that for smooth walls with a high velocity of fluid in the central part and

lower velocity nearer to the walls. The main difference is that the slower velocity distribution near to the walls is thicker and has a more pronounced curvature. The maximum velocity for this simulation is also lower, this is due to the higher value of surface friction creating a larger transient layer of flow and not allowing as great a velocity due to energy losses. This seemed a very minimal defect for this project, however if the velocity were to drop too low the oscillation frequency would lower, and the angle of flow emitted from the nozzle outlet would lessen and possibly lead to an out of specification nozzle.

9.9.3. Distortion

A defect that can occur in manufacturing is the warping of edges in the part being created (Figure 9-6). This could be due to a poorly distributed pressure throughout the flow meaning that the material does not have the ability to flow into the micro-features – in this case the edges – or poor cooling methods throughout the mould causing differential rates of shrinkage in the part. To simulate this, the channel edges

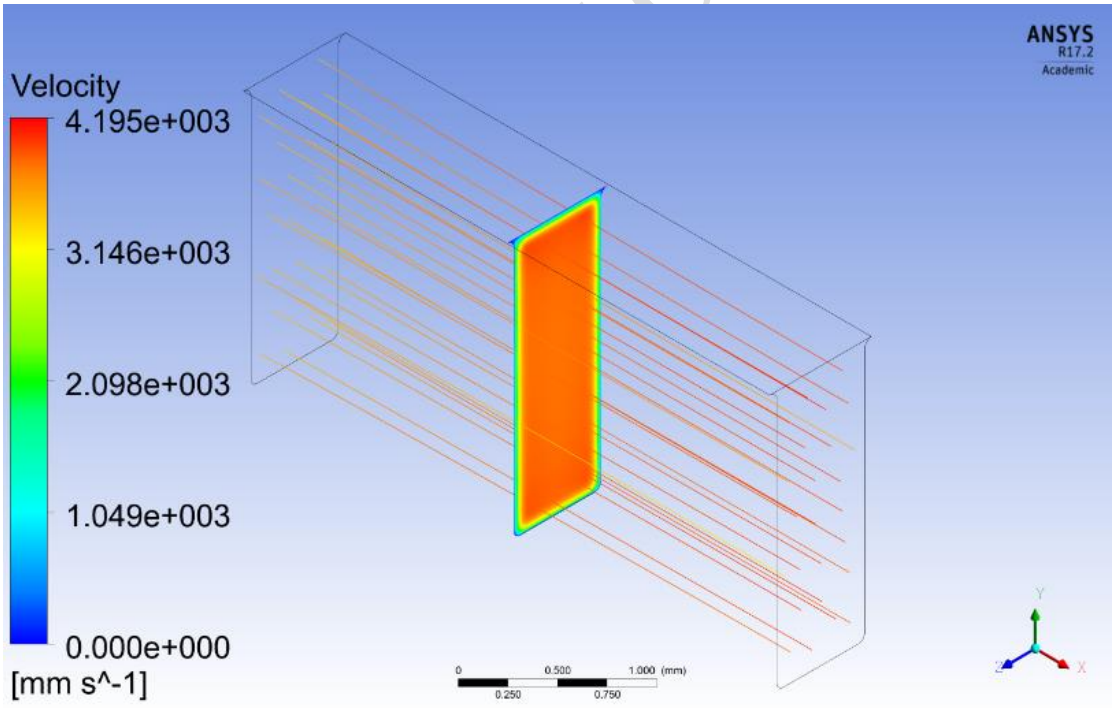

Figure 9-6: Fluid flow through channel with distorted edges

have been altered, the upper set becoming convex and the lower set concave [80].

The maximum velocity is affected greatly in this simulation where it has gone down by approximately 20%. This could be detrimental to the performance of the nozzle if it requires tight tolerances. It is also possible to see that the boundary layer for this

simulation is thicker than for the normal smooth wall simulation, particularly at the top of the channel, this is what is causing the large drop in maximum velocity [80].

9.9.4. Short Shot

The final defect simulated was for if the wall height on one side of the channel were incorrect, this could be due to an incorrect fit with the inner walls of the fluidic nozzle from a short shot or poor tolerances. The short shot could be caused by not enough mixture being allowed to enter the mould during the injection phase of production, or a pressure drop during the process. This has been modelled for two different mould fill orientations; a fill from both ends resulting in a micro-feature on each side (Figure 9-9) and a fill from the top or bottom with a one-sided micro-

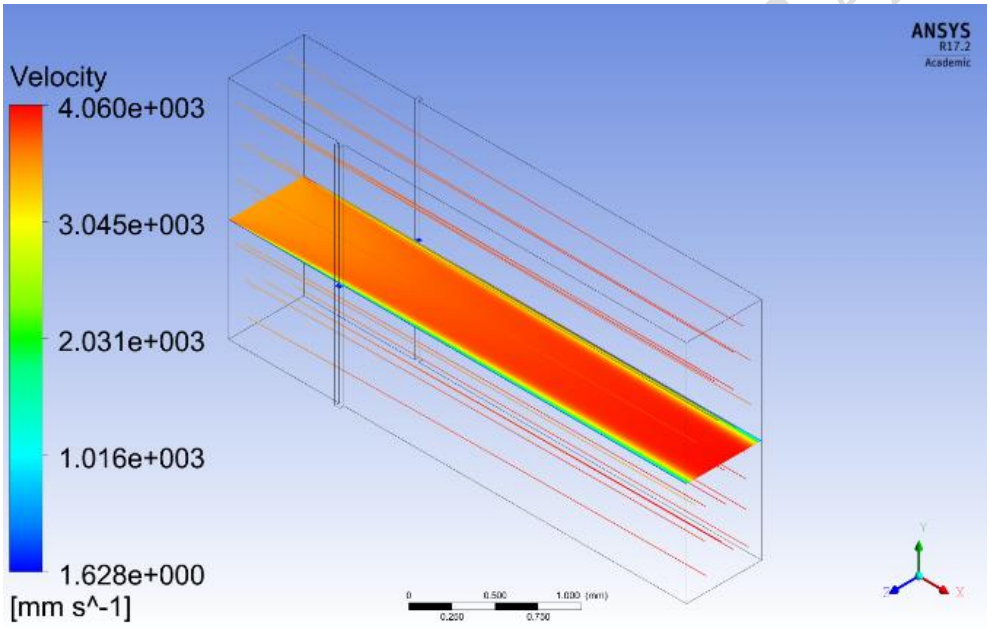

Figure 9-9: Fluid flow through channel with insufficient fill in horizontal direction

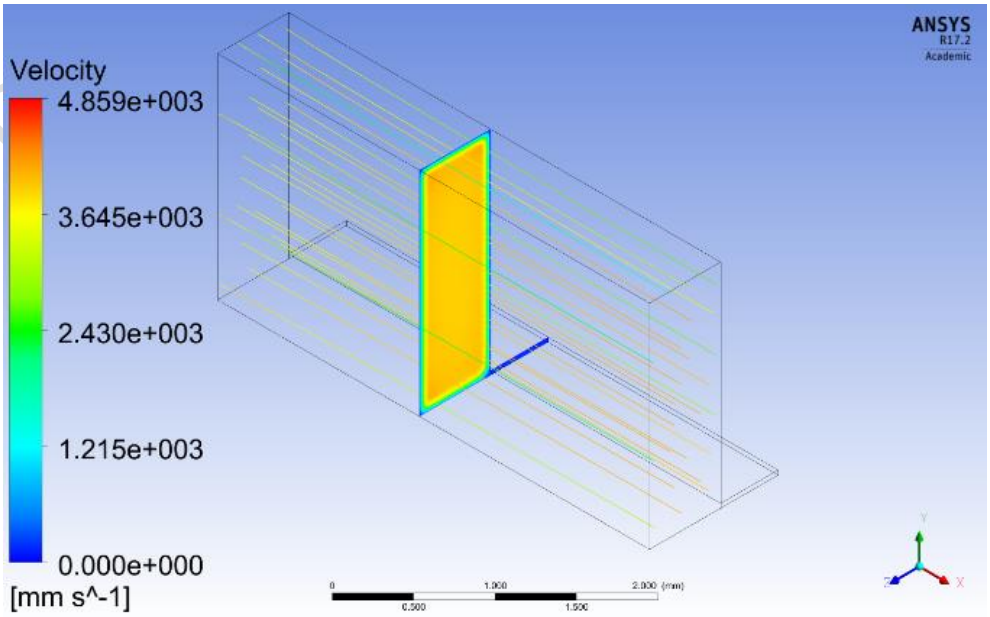

Figure 9-10: Fluid flow through channel with insufficient fill in vertical direction

feature (Figure 9-10) [80].

The fluid velocity is very minimally affected by this defect for both vertical and horizontal filling. There is a small amount of deflection in the flow for both cases around the deformity, however the remainder of the fluid is mostly unaffected. There is a small alteration in velocity and pressure for the vertically filled channel, the defect height in this case is taken as 2% of the main channel height and further investigation would be required to find the point at which the flow stream becomes further altered. This type of defect would not be particularly devastating to the fluid flowing through the channel unless a consistent flow is required and utilising vertical fill injection moulding [80].

9.9.5. Conclusion

By looking at how the different types of defects and different tolerances can affect the velocity and flow direction of the fluid it has shown the importance of ensuring that machinery is working properly when manufacturing micro-fluidic channels. Despite the majority of the channels still functioning with water flowing from one end to the other, the fluid does not have the same flow properties as in the nominal case. These minor deficiencies could cause parts to not meet the specification given by a manufacturer, forcing a redevelopment of a part or a loss of a manufacturing contract.

This study on defects in micro-channels through the injection moulding process was published in the International Journal of Mechanical and Mechatronics Engineering [81].

10. References

[1] S. Instruments, “1986 No. 1078 - Road Traffic - The Road Vehicles (Construction and Use) Regulations 1986,” 25 June 1986. [Online]. Available: http://www.legislation.gov.uk/uksi/1986/1078/pdfs/uksi_19861078_en.pdf. [Accessed 02 June 2019].

[2] J. S. Dismukes, “Windshield Cleaning Apparatus”. United States of America Patent US2114558, 19 April 1938.

[3] E. J. Martin, “Car-Window Cleaner”. United States of America Patent US1153095, 7 September 1915.

[4] G. E. Thum, “Windshield Cleaner”. United States of America Patent US1448508, 13 March 1923.

[5] H. Klatt, “Windshield Wiper, Washer and Cleaner”. United States of America Patent US1369817, 1 March 1921.

[6] S. R. Bumpass, “Windshield Washer and Wiper”. United States of America Patent US1932615, 31 October 1933.

[7] B. J. West, “Windshield Cleaning Device”. United States of America Patent US2162985, 20 June 1939.

[8] E. C. Horton, “Windshield Clearing System”. United States of America Patent US2260904, 28 October 1941.

[9] L. C. Neufeld, “Nozzle Structure for Windshield Cleaning Devices”. United States of America Patent US2622929, 23 December 1952.

[10] J. R. Oishei, “Windshield Washer System”. United States of America Patent US3199787, 10 August 1965.

[11] K. H. Carpenter, “Windshield Cleaning Device Utilizing an oscillatory Fluid Stream”. United States of America Patent US3423026, 21 January 1969.

[12] J. R. Frigon, “Windshield Washer Nozzle Device”. United States of America

Patent US3913167, 21 October 1975.

[13] X. Bousset, “Wiper System for Spraying a Cleaning and/or Deicing Fluid from the Region of a Windscreen Wiper”. France Patent US2014/0366301, 18 december 2014.

[14] S. Raghu, “High-Speed WIndshield Washer Nozzle System”. United States of Americca Patent US5820026, 13 October 1998.

[15] J. S. Murawa, “Pressure Sensitive Windshield Washer Nozzle”. United States of America Patent US6402052, 11 June 2002.

[16] K. Berning, D. E. Steerman, S. Sridhara and G. Russel, “Multiple Spray Devices for Automotive and Other Applications”. United States of America Patent US2003/0234303, 25 December 2003.

[17] A. L. Ludwig, “Windshield Assembly for Motor Vehicles and the Like”. United States of America Patent US3171683, 2 March 1965.

[18] K. Motoda, “Ultrasonic Wiper”. Japan Patent US4768256, 6 September 1988.

[19] D. R. M. Trevett and P. N. Trevett, “Clearing Precipitation”. Great Britain Patent US2013/0298419, 14 November 2013.

[20] Department for Transport, “Summary of the Requirements for Windscreeen Wipers and Washers on Road Vehicles,” 26 February 2015. [Online]. Available: https://www.gov.uk/government/uploads/system/uploads/attachment_data/file/408213/Information_Sheet_Windscreen_wipers_and_washers_on_vehicles.pdf. [Accessed 08 April 2016].

[21] T. E. Grimes, J. P. Baltz and R. T. Cedoz, “Ergonomic hand held paint spray gun”. United States of America Patent US5236129A, 27 May 1992.

[22] T. G. Funseth, S. L. Bullock, R. A. Humpal and D. Wu, “Spray nozzle body, agricultural spray boom and agricultural sprayer with such”. Europe Patent EP2957346A1, 20 June 2014.

[23] M. S. Maier, E. J. Gamble, J. W. Wilson, E. L. Calzadilla and G. F. Goetz,

"Nacelle air pump for vector nozzles for aircraft". United States of America Patent US5593112A, 06 December 1994.

[24] N. Reuss, "Apparatus for filling food product cups, multiple nozzle arrangement and dessert product". Europe Patent EP1602579A1, 01 June 2004.

[25] Pittsburgh Spray Equipment Co., "SIMPSON® Cleaning Pressure Washer Spray Nozzles Universal, 3600 PSI, Soap 3.0," Simpson, 13 July 2020. [Online]. Available: https://pittsburghsprayequip.com/products/simpson%C2%AE-cleaning-pressure-washer- spray-nozzles-universal-3600-psi-soap-3-0. [Accessed 20 August 2020].

[26] "Learn more about water jet cutting," Water Jet Sweden, 2019. [Online]. Available: https://www.waterjetsweden.co.uk/about/Learn-More-About-Waterjet-Cutting. [Accessed 20 August 2020].

[27] S. Wang, G. J. Dorr, M. Khashehchi and X. He, "Performance of Selected Agriculatural Spray Nozzles using Particle Image Velocimetry," *Journal of Agricultural Science and Technology,* vol. 17, no. 3, pp. 601-613, 2015.

[28] M. Fouvet and J. Rodrigues, "Sprayer device for a motor vehicle body spray paint booth". France Patent US6776843B2, 31 January 2000.

[29] C. Cerretrlli and K. Kirtley, "Boundary Layer Separation Control with Fluidic Oscillators," *Journal of Turbomachinery,* vol. 131, no. 4, 2009.

[30] D. Feikema and D. Culley, "Computational Fluid Dynamic Modelling of a Fluidic Actuator for Flow Control," *46th AIAA Aerospace Sciences Meeting and Exhibit,* pp. 1-13, 2008.

[31] G. W. A. Dummer and J. MacKenzie Robertson, "Design and Performance of Fluid Logic Components," in *Fluidic Components and Equipment*, London, Pergamon Press, 1968, p. 721.

[32] A. Kashani, H. Parizi and K. H. Mertins, "Multi-step spray modelling of a flat fan atomizer," *Computers and Electronics in Agriculture,* vol. 144, pp. 58-70, 2018.

[33] N. M. Morris, An Introduction to Fluid Logic, London: McGraw-Hill Inc., 1973.

[34] M. J. Moylan, Fluid Logic in Simple Terms, New york: Transatlantic Arts, 1968.

[35] J. M. Kirshner and S. Katz, Design Theory of Fluidic Components, New York: Academic Press, Inc., 1975.

[36] H. Hurvitz, "Suction Amplifier". United States of America Patent US3001539, 26 September 1961.

[37] B. M. Horton, "Negative Feedback Fluid Amplifier". United States of America Patent US3024805, 13 March 1962.

[38] B. C. Bobusch, R. Woszidlo, J. M. Bergada, C. N. Nayeri and C. O. Paschereit, "Experimental study of the internal flow structures inside a fluidic," *Experiments in Fluids,* vol. 54, p. 1559, 2013.

[39] M. Kim, D. Kim, E. Yeom and K. C. Kim, "Experimental study on heat transfer and flow structures of feedback-free sweeping jet impinging on a flat surface," *International Journal of Heat and Mass Transfer,* vol. 159, 2020.

[40] T. Eisner, For Love of Insects, Cambridge: Harvard University Press, 2005.

[41] E. W. Simões, R. Furlan, R. E. B. Leminski, M. R. Gongora-Rubio, M. T. Pereira, N. I. Morimoto and J. J. S. Avilés, "Microfluidic Oscillator for Gas Control and Measurement," *Flow Measurement and Instrumentation,* vol. 16, no. 1, pp. 7-12, 2005.

[42] M. N. Tomac, Internal Fluid Dynamics and frequency Characteristics of Feedback-free Fluidic Oscillators, Ohio: The Ohio State University, 2013.

[43] Engineering Toolbox, "Ethylene Glycol Heat-Transfer Fluid," Engineering Toolbox, 2003. [Online]. Available: https://www.engineeringtoolbox.com/ethylene-glycol-d_146.html. [Accessed 6 August 2019].

[44] "Dimensions of new Ford cars showing length, width and height," Automobile

Dimension, 2016. [Online]. Available: http://www.automobiledimension.com/ford-car-dimensions.html. [Accessed 20 June 2016].

[45] Laboratory for Optical and Computational Instrumentation, "ImageJ Welcome," University of Wisconsin-Madison, 20 May 2016. [Online]. Available: http://imagej.net/Welcome. [Accessed 23 May 2016].

[46] Iowa State University, "Selecting the Correct Nozzle to Reduce Spray Drift," 22 August 2001. [Online]. Available: https://www.google.co.uk/url?sa=t&rct=j&q=&esrc=s&source=web&cd=1&cad=rja&uact=8&ved=0ahUKEwios_3MxsrNAhVMLcAKHejPA0wQFggcMAA&url=https%3A%2F%2Fstore.extension.iastate.edu%2FProduct%2Fipm68-pdf&usg=AFQjCNHni4zVnuxp6hAg3lrPvO57GUVpng&sig2=MJC-2fimecnNRFkGW. [Accessed 15 February 2016].

[47] H. K. Versteeg and W. Malalasekera, "2.1 Governing equations of fluid flow and heat transfer," in *An Introduction to Computational Fluid Dynamics*, Harlow, England, Pearson Education M.U.A., 2007, pp. 9-20.

[48] T. Kambe, "Equation of Motion of a Viscous Fluid," in *Elementary Fluid Mechanics*, Tokyo, World Scientific, 2008, pp. 45-48.

[49] W. P. Graebel, "A.1 Vector Differential Calculus," in *Advanced Fluid Mechanics*, Michigan, Elsevier Inc., 2007, pp. 318-320.

[50] R. L. Panton, "26.2 Characteristics of Turbulent Flow," in *Incompressible Flow*, Austin texas, John Wiley & Sons, Incorporated, 2013, pp. 773-776.

[51] G. Haller, "An objective definition of a vortex," in *Journal of Fluid Mechanics*, Cambridge, 2005.

[52] R. L. Panton, "26.1 Types of Turbulent Flows," in *Incompressible Flow*, Austin, Texas, John Wiley & Sons, Incorporated, 2013, pp. 772-773.

[53] W. Frei, "Which Turbulence Model Should I Choose for My CFD Application?," COSMOL, 16 September 2013. [Online]. Available:

https://www.comsol.com/blogs/which-turbulence-model-should-choose-cfd-application/. [Accessed 19 April 2016].

[54] H. K. Versteeg and W. Malalasekera, "3.4 Characteristics of simple turbulent flows," in *An Introduction to Computational Fluid Dynamics*, Harlow, England, Elsevier Inc., 2007, pp. 52-61.

[55] H. K. Versteeg and W. Malalasekera, "3.7 Reynolds-averaged-Navier-Stokes equations and classical turbulence models," in *An Introduction to Computational Fluid Dynamics*, Harlow, England, Elsevier Inc., 2007, pp. 66-97.

[56] H. K. Versteeg and W. Malalasekera, "11 Methods for dealing with complex geometries," in *An Introduction to Computational Fluid Dynamics*, Harlow, England, Elsevier Inc., 2007, pp. 304-342.

[57] ANSYS Ltd., "ANSYS Fluent," ANSYS Ltd., 2016. [Online]. Available: http://www.ansys.com/Products/Fluids/ANSYS-Fluent. [Accessed 23 May 2016].

[58] S. M. Salim and S. C. Cheah, "Wall y+ Strategy for Dealing with Wall-bounded Turbulent Flows," in *International MultiConference of Engineers and Computer Scientists 2009 Vol II*, Hong Kong, 2009.

[59] ANSYS Inc., "Home," ANSYS Inc., 2017. [Online]. Available: http://www.ansys.com/en-GB. [Accessed 10 March 2017].

[60] T. Avraham, "Know Thy Mesh - Mesh Quality - part," Tom & Rajat communicating the physical world: Wonders of CFD, 1 February 2019. [Online]. Available: https://cfdisraelblog.wpcomstaging.com/2019/02/01/know-thy-mesh-mesh-quality-part-i/. [Accessed 2021 October 23].

[61] J. Danielewicz, B. Sneichowska, M. A. Sayegh, N. Fidorow and H. Jouhara, "Three-dimensional numerical model of heat losses from district heating network pre-insulated pipes buried in the ground," 14 August 2015. [Online]. Available: https://bura.brunel.ac.uk/bitstream/2438/11240/1/Fulltext.pdf. [Accessed 23 October 2021].

[62] R. L. Mott and J. A. Untener, “9.5 Flow in Noncircular Sections,” in *Applied Fluid Mechanics*, Harlow, Pearson Education Limited, 2016, pp. 228-232.

[63] R. L. Mott and J. A. Untener, “Appendix D: Variation of Viscosity with Temperature,” in *Applied Fluid Mechanics*, Harlow, Pearson Education Limited, 2016, pp. 510-516.

[64] F. Balduzzi, A. Bianchini, R. Maleci, G. Ferrara and L. Ferrari, “Critical issues in the CFD simulation of Darrieus wind turbines,” June 2015. [Online]. Available: https://flore.unifi.it/retrieve/handle/2158/1014162/590227/POSTPRINT.pdf. [Accessed 15 November 2021].

[65] CFD Intech, “Tutorial ANSYS CFX Part - 1/2 | Multiphase flow of a droplet in air,” YouTube, 29 April 2017. [Online]. Available: youtube.com/watch?v=-c4TmrtTQ80. [Accessed February 2019].

[66] CFD Intech, “Tutorial ANSYS CFX Part - 2/2 | Multiphase flow of a droplet in air,” YouTube, 29 April 2017. [Online]. Available: youtube.com/wwatch?v=KdFlwgLEnlo. [Accessed February 2019].

[67] S. T. Chang, C. Reitz, P. Farrell, A. Pierpoint and T. Tow, “Effects of Injection Pressure and Nozzle Geometry on Spray SMD and D.I Emissions,” *SAE Transactions*, vol. 104, pp. 975-984, 1995.

[68] R. Woszidlo, F. Ostermann, C. N. Nayeri and C. O. Paschereit, “The time-resolved natural flow field of a fluidic oscillator,” *Experiments in Fluids*, vol. 56, no. 125, 2015.

[69] I. M. Cohen, P. K. Kundu and P. S. Ayyaswamy, “Conservation of Mass,” in *Fluid Mechanics*, Burlington, Elsevier Science & Technology, 2007, pp. 84-86.

[70] V. Semião, P. Andrade and M. da Graça Carvalho, “Spray characterization: numerical prediction of Sauter mean diameter and droplet size distribution,” *Fuel*, vol. 75, no. 15, pp. 1707-1714, 1996.

[71] G. A. Matthews, P. Miller and R. Bateman, “Spray Droplets,” in *Pesticide Application Methods*, Chichester, John Wiley & Sons, Ltd., 2000, pp. 91-109.

[72] D. Guyot, C. O. Paschereit and S. Raghu, “Active Combustion Control Using a Fluidic Oscillator for Asymmetric Fuel Flow Modulation,” *International Journal of Flow Control,* pp. 155-166, 2009.

[73] J. W. Gregory, J. P. Sullivan, G. Raman and S. Raghu, “Characterization of the Microfluidic Oscillator,” *AIAA J,* vol. 45, no. 3, pp. 568-576, 2007.

[74] E. W. Simões, R. Furlan and M. T. Pereira, “Numerical Analysis of a Microfluidic Oscillator Flowmeter Operating with Gases and Liquids,” *Technical Proceedings of the Fifth International Conference on Modeling and Simulation of Microsystems,* pp. 36-39, 2002.

[75] V. Tesar, “Time-Delay Circuits for Fluidic Oscillators and Pulse Shapers,” *Fluid Mechanics and Thermodynamics: Theory, Methods and Applications,* vol. Energies, no. 12(16), 2019.

[76] J. W. Geregory and M. N. Tomac, “A review of Fluidic Oscillator Development and Application for Flow Control,” in *43rd Fluid Dynamics Conference,* San Diego, 2013.

[77] M. J. Moylan, “Logic devices in use,” in *Fluid Logic in simple terms,* New York, Transatlantic Arts, 1968, pp. 36-45.

[78] M. Koc and T. Ozel, “7.3 Taxonomy of micro-moulding processes,” in *Micro-Manufacturing: Design and Manufacturing of Micro-Products,* Hoboken, New Jersey, John Wiley & Sons, Inc., 2011, pp. 202-206.

[79] M. Koc and T. Ozel, “7.5 Micro-injection moulding,” in *Micro-Manufacturing: Design and Manufacturing of Micro-Products,* Hoboken, New Jersey, John Wiley & Sons, Inc., 2011, pp. 210-215.

[80] D. M. Bryce, “Defects and Remedies,” in *Polymer Injection Moulding: manufacturing process fundamentals,* Dearborn, Michigan, Society of Manufacturing Engineers, 1996, pp. 220-249.

[81] Z. L. Sheady, “Computational Fluid Dynamic Investigation into the Relationship between,” *International Journal of Mechanical and Mechatronics Engineering,* vol. 12, no. 3, p. 96, 2018.

[82] R. Grisso, S. D. Askew and D. McCall, “Nozzles: Selection and Sizing,” *Virginia Cooperative Extension publication 442-032,* no. 442-032, May 2013.

[83] H. J. Schmidt, R. Woszidlo, C. N. Nayeri and et al., “Separation control with fluidic oscillators in water,” *Experiments in Fluids,* vol. 58, no. 8, p. 17, 2017.